

PLASTICITY IN VISUAL CORTEX

STUDYING DEVELOPMENT AND EXPERIENCE-DEPENDENT
PLASTICITY OF VISUAL CORTEX: USING MODERN APPROACHES,
ANIMAL MODELS AND HUMAN POST-MORTEM TISSUE

By JUSTIN LARRY BALSOR, B.Sc

A Thesis Submitted to the School of Graduate Studies in Partial Fulfillment of the
Requirements for the Degree Doctor of Philosophy

McMaster University © Copyright by Justin Larry Balsor, June 2019

DOCTOR OF PHILOSOPHY (2016)

McMaster University

(Neuroscience)

Hamilton, Ontario

TITLE: Studying Development And Experience-Dependent
Plasticity Of Visual Cortex: Using Modern Approaches, Animal Models And
Human Post-Mortem Tissue

AUTHOR: Justin Larry Balsor, B.Sc (McMaster University)

SUPERVISOR: Dr. Kathryn M. Murphy

NUMBER OF PAGES: XIX, 299

Lay Abstract

Impaired visual experience early in life can cause lasting visual deficits in animals and humans. Even after correcting ocular impairment, poor vision often remains, which suggests early experience instills lifelong changes in the area of the brain that processes vision, called the visual cortex. Changes that take place in visual cortex affect the function of cortical cells. Most of these changes are executed by proteins that sit at the junction between cells. By inflicting visual impairments in young animals, and examining changes in protein expression in visual cortex cells, we can relate protein expression to experience-dependent changes. I examined expression of proteins in visually impaired kittens to investigate why some treatments might be more effective than others. I also examined protein levels in human brains to investigate why treatment during certain periods of development produce suboptimal recovery.

Abstract

When the visual system is confronted with adverse early-life experiences, maladaptive plasticity permits development of poor vision in a disorder called amblyopia. Patch therapy is the common treatment for amblyopia, by which occluding the good eye manipulates residual plasticity to improve acuity in the poor eye. Unfortunately patch therapy does not work for everyone and improvements are often transient. Animal models of amblyopia have highlighted the neurobiology after the initial insult, but little is known about the response to treatment. Since synaptic proteins are the interface between neuronal structure and function, it is imperative that neuroscientists study the amblyopic synaptic proteome to better map intervention strategies in humans.

In the first part of this thesis I modernize 3 approaches for examining central visual pathway. First I combine neuroanatomical tracing with modern tissue clearing to examine central visual pathway connectivity. Next, I improved a manual fractionation protocol for enriching synaptic protein expression in cortical tissues. Third, I present a series of analytical techniques for multi-dimensional statistics to interpret protein expression in cortical tissue samples.

In the second part of this thesis I used these techniques to examine a set of commonly studied synaptic plasticity mechanisms in a cat model of amblyopia. I identified the neurobiological plasticity phenotype of patch therapy and treatment alternatives. I then examined expression of 23 synaptic and non-neuronal proteins in post-mortem tissue samples from human visual cortex across development to identify neuroplasticity states.

These chapters identify options for improved or augmented therapies by identifying the plasticity phenotypes in animal models of amblyopia, and across human development. Together these tools identify potential successes and failures of existing behavioural interventions, such as binocular vision, as well as the causes of suboptimal treatments in human development, such as early periods of protein heterogeneity.

Acknowledgements

I would first like to thank my thesis supervisor and mentor, Dr. Kathryn Murphy. I learned many lessons under her tutelage that have been instrumental in my academic development. Some of these lessons include phrases such as “cheap and cheerful”, “making the sausages” and “italian wedding soup”. I am grateful for your dedication and guidance.

I would also like to thank my supervisory committee members, Dr. Ram Mishra and Dr. Laurie Doering, as well as Dr. David Jones. Their insightful, thought-provoking and often challenging questions helped mould these projects into a thesis I can be proud of. I would also like to thank the Ontario government for providing funding support for this research.

There are a number of lab members who provided me with much support over the years. I am grateful to Dr. Kate Williams for our many discussions regarding the handsomeness of cats and theories on what to do in the event of a zombie apocalypse. I appreciate the lessons I learned from Dr. Simon Beshara, including what *not* to do if you break expensive glassware. I am also grateful to Steven Mancini, who was a good friend to me towards the end of this process. And of course, Coco, who reminded me of the importance of standing up and stretching my legs.

Thank you to my friend Dr. Ali Hashemi, who has been a friend since the beginning. What a wild ride! I am happy to call you my colleague once more.

Importantly, I would like to thank my parents, Deanna and Bradley Balsor, who I could always rely on to ask “Is it done yet?”, but also to offer words of encouragement after I inevitably replied “Not yet”. Thank you to my grandparents Anne-Marie and Larry Balsor, and Anna and Orlando Verrecchia, who were constantly curious and interested in what I was doing in the lab for all these years. To my brothers, Phil and Nate, I finally did it. Told ya’!

And finally, thank you to Dr. Caitlin Siu. When I began this journey, you were a friend who sat across from me in lab. As this journey comes to a close, I am proud to call you my wife. None of this would have been possible without you by my side. In this, as in all things, you are my inspiration. I like you and I love you.

And to all the rest who helped me along the way, thank you.

Table of Contents

Chapter 1. General Introduction	1
Preamble	2
1.1 Amblyopia	3
Quality of life.....	3
Susceptibility	3
Standard treatment.....	4
1.2 Cortical Plasticity - Animal models	5
Central Visual Pathway - Retina.....	5
Central Visual Pathway - Connections to midbrain and thalamus	7
Anatomical Organization of Visual Cortex - Cortical Layers	8
Functional Organization of Visual Cortex - Cortical Columns	9
Ocular dominance plasticity and neuronal morphology.....	10
Animal models of amblyopia.....	11
1.3 Synaptic plasticity - animal models	12
Glutamatergic plasticity mechanisms.....	12
GABAergic plasticity mechanisms.....	14
Excitatory:Inhibitory Balance.....	15
Other plasticity mechanisms.....	15
1.4 Translating plasticity - From animal models to amblyopia treatments	17
Pharmacological interventions to manipulate plasticity	17
Behavioural interventions to manipulate plasticity	18
Biologically inspired human interventions.....	20

1.5 Human development- Challenges and Opportunities	21
1.6 Summary of my contributions	22
Preamble Chapter 2	24
Preamble Chapter 3	26
Preamble Chapter 4	27
Preamble Chapter 5	29
Preamble Chapter 6	30
Chapter 2. Anatomical labeling of the central visual pathway	31
2.1 Introduction	33
2.2 Methods	34
2.3 Results	42
2.4 Discussion.....	60
2.5 References	64
Chapter 3. Protocol for a high-throughput semi-automated preparation for filtered synaptosomes	66
3.1 Introduction	68
3.2 Materials and Equipment List.....	71
3.3 Protocol & Main Findings	74
3.4 Notes.....	87
3.5 References	88
Chapter 4. A primer on high-dimensional data analysis workflows for studying visual cortex development and plasticity	90
4.1 Introduction	92
4.2 Past work using high-dimensional analysis.....	94
4.3. Using PCA & tSNE to study experience-dependent changes in visual cortex: Data reduction, feature identification, clustering, plasticity phenotypes	100
4.4: Using sparse high-dimensional clustering to study human visual cortical development: Clusters, features, and plasticity phenotypes.....	124
4.5 Extensions and Discussion	153
Supplemental Analysis- Bootstrap analysis using custom R code	155
4.6 References	157

Chapter 5. Classification of visual cortex plasticity phenotypes following treatment for amblyopia	160
5.1 Introduction	162
5.2 Experimental Procedure	164
5.3 Results	176
5.4 Discussion.....	196
5.5 Supplemental Material.....	202
5.6 References	213
Chapter 6. Expression of synaptic and non-neuronal proteins reveal parallel plasticity states across human visual cortex development	220
6.1 Introduction	223
6.2 Experimental Procedure	225
6.3 Analysis	229
6.4 Results	234
6.5 Discussion.....	259
6.6 References	264
Chapter 7. General Discussion	270
7.1 Summary of main findings	271
7.2 Methodological Approach	273
7.3 Significance	276
7.4 Future Directions	279
References	283

List of Figures

Chapter 1. General Introduction	1
Figure 1. Representation of common organizational schemes along the central visual pathway.	6
Chapter 2. Anatomical labeling of the central visual pathway	31
Figure 1. Schematic overview of the steps from eye injection to imaging the cleared unfolded and flattened cortex.	39
Figure 2. WGA CF® dye labeling in flat-mounted cat retina.	42
Figure 3. WGA CF® dye labeling in LGN coronal series of sectioned tissue.	44
Figure 4. WGA CF® dye labeling in single LGN section at 1200µm.	45
Figure 5. Analysis of WGA CF® dye labeling in single LGN section.	46
Figure 6. WGA CF® dye labeling in sectioned superior colliculus.	48
Figure 7. Aligning WGA CF® dye labeling in right superior colliculus.	50
Figure 8. Analysis of clearing rates in flattened rat cortex.	52
Figure 9. Confocal image of WGA CF® dye in PACT cleared LGN.	53
Figure 10. WGA CF® dye labeling in the whole cleared LGN after left-eye injection.	55
Figure 11. Analysis of WGA CF® dye labeling in whole cleared superior colliculus.	56
Figure 12. Grey level analysis of retinae, sectioned SC and LGN, sectioned cortex and cleared cortex.	57
Figure 13. WGA CF® dye labeling in cleared unfolded and flattened cat cortex.	60
Chapter 3. Protocol for a high-throughput semi-automated preparation for filtered synaptosomes	66
Fig 1. Overview of process for preparing synaptoneuroosomes using either the manual hand or new high-throughput, semi-automated protocol, including a comparison of the primary steps in the processes from homogenization to filtration, and low speed centrifugation.	76
Fig 2. Volume of filtered homogenate tissue collected using Ultrafree-MC SV centrifuge tubes.	79
Fig 3. Total protein concentration for the hand or high-throughput techniques measured in (A) homogenate and (B) synaptoneurosome tissue fractions prepared from cat and rat cortical tissues.	80

Fig 4. Synaptoneurosome enrichment of PSD95 expression comparing across (A) different lengths of filtration or (B) hand versus new high-throughput preparation.. 84

Fig 5. Comparison of β -tubulin and PSD95 expression in whole homogenate and synaptoneurosome (A) with matching enrichment (B).86

Chapter 4. A primer on high-dimensional data analysis workflows for studying visual cortex development and plasticity 90

Figure 1. Interpreting PCA dimensions with either thousands or tens of genes or proteins:95

Figure 2. Applying tSNE to human brain cells identifies cell type clusters.96

Figure 3. Hierarchical clustering of samples in a correlation matrix.99

Figure 4. Protein analysis workflow for $p < 10$ and $p \approx n$101

Figure 5. Initial output of hierarchical clustering the Normal distance matrix of proteins.104

Figure 6. Correlation matrices for protein expression in Normal and MD animals. . 105

Figure 7. Scree plot of the percentage of explained variance captured by each principal component.107

Figure 8. The basis vectors for dimensions 1-3 showing the protein vector amplitudes.109

Figure 9. Correlation between the plasticity features (columns) identified using the basis vectors for PCA dimensions 1-3.111

Figure 10. tSNE output when run on NewFeatures identified by PCA.113

Figure 11. Within group sum of squares for hierarchical clustering of tSNE coordinates in Figure 10.114

Figure 12. K-means clustering applied to tSNE reduced data.115

Figure 13. Boxplot for the GABAA α 3:GABAA α 1 feature that identified subclusters with expression different from normal.118

Figure 14. Correlation matrix for plasticity phenotypes between the subclusters of the data.119

Figure 15. Legend for the features comprised in the plasticity phenotype and the colour-code.120

Figure 16. Example plasticity phenotype for the Normal subcluster.121

Figure 17. Example of the orderly progression of plasticity phenotypes across subclusters.122

Figure 18. Identifying features of the plasticity phenotypes in the subclusters that are different from normal.	123
Figure 19. Protein analysis workflow for $p > 20$ and $p \approx n$	126
Figure 20. Top-down, bottom-up and sparse subspace clustering.	132
Figure 21. Robust and sparse k-means clustering (RSKC) applied to 23 proteins from the human data set.	136
Figure 22. Adjusted weights for the proteins from RSKC.	138
Figure 23. Parallel coordinates of the protein expression in each cluster.	139
Figure 24. Protein expression motifs for the 6 clusters.	140
Figure 25. Protein expression per cluster.	141
Figure 26. Scree plot of the percentage of explained variance captured by each principal component.	142
Figure 27. The correlation (A) and \cos^2 (B) matrix showing the relationship between each protein and the 23 principal component dimensions.	143
Figure 28. Sum of \cos^2 across the first 3 dimensions.	144
Figure 29. Sum of \cos^2 across dimension 1.	145
Figure 30. Ranking of proteins using RSKC reweighted values relative to \cos^2 representation.	146
Figure 31. Biplot shows the protein vectors along dimension 1 (horizontal axis) and dimension 2 (vertical axis).	147
Figure 32. Biplots demonstrate the relationship between proteins and samples.	148
Figure 33. Amplitude of each protein about the second principal component.	149
Figure 34. Examination of extracted feature correlation with PCA dimensions.	150
Figure 35. Heatmap of the significant features identified in Figure 34.	152
Figure 36. Average plasticity phenotype for each of the 6 clusters representing human visual cortical development.	152

Chapter 5. Classification of visual cortex plasticity phenotypes following treatment for amblyopia **160**

Figure 1. Study design diagram	165
Figure 2. Analysis Workflow.....	168
Figure 3. Expression of synaptic proteins in the different regions of visual cortex... 177	

Figure 4. Indices for pairs of receptor subunits and modeling of predicted decay kinetics for a population of NMDARs and GABAARs.....	181
Figure 5. Visualizing pairwise correlations between proteins.....	184
Figure 6. Identifying plasticity features using principal component analysis.....	187
Figure 7. Expression of plasticity features identified using principal component analysis.....	188
Figure 8. Clustering of samples with similar plasticity features identified using t-Distributed Stochastic Neighbor Embedding (t-SNE) and k-means clustering ..	190
Figure 9. Visualizing pairwise correlations between treatment subclusters.....	192
Figure 10. Visualizing the plasticity features and phenotypes for each subclusters ..	194
Figure 11. Significant plasticity features.....	195
Figure 3-1. Glutamatergic protein variance to mean ratios.....	202
Figure 4-1. Predicted decay kinetics of NMDAR and GABAAR across normal cat V1 development ..	203
Figure 8-1 Within group sum of squares with variable cluster sizes.	204

Chapter 6. Expression of synaptic and non-neuronal proteins reveal parallel plasticity states across human visual cortex development **220**

Figure 1. Comparison of samples grouped by RSKC cluster algorithm (A-F) or age bins (G-J).	236
Figure 2. Protein development by age (A) and by cluster (B)	238
Figure 3. Feature sorting according to sparse clustering.....	243
Figure 4. Principal component analysis identifies 3 dimensions of interest.	244
Figure 5. Examination of Principal Component Analysis for feature identification..	246
Figure 6. Examination of Principal Component Analysis for feature extraction and reduction.....	250
Figure 7. Feature extraction identifies a set of biological features	252
Figure 8. Association between protein sums and functional indices identify developmental changes that emerge during each cluster.	254
Figure 9. Plasticity motif of indices and protein sums separated by cluster.	255
Figure 10. Indices of receptor subunit pairs for NMDAR and GABAAR predict receptor decay kinetics across development.	258

Chapter 7. General Discussion	270
References	283

List of Tables

Chapter 1. General Introduction	1
Chapter 2. Anatomical labeling of the central visual pathway	31
Chapter 3. Protocol for a high-throughput semi-automated preparation for filtered synaptosomes	66
Chapter 4. A primer on high-dimensional data analysis workflows for studying visual cortex development and plasticity	90
Table 1. Observations (n)	100
Table 2. Variables (p)	100
Table 3. Subclusters identified from the tSNE plot	116
Table 4. Observations (n)	125
Table 5. Variables (p)	125
Chapter 5. Classification of visual cortex plasticity phenotypes following treatment for amblyopia	160
Table 1: List of primary antibody concentrations	167
Table 2: The number of animals, cortical tissue pieces, and WB measurements for each condition and V1 region.....	169
Table 3: Formulas and Pearson’s R correlation between the features and principal components.	173
Table 2-1. The number of Western blot measurements for each cortical region in Normal animals.	205
Table 2-2. The number of Western blot measurements for each cortical region in MD animals.	206
Table 3-1. Table of p-values comparing protein expression in each treatment condition against 5wk Normal animals and 5wk MD animals.	207
Table 4-1. Table of p-values comparing the values for each plasticity feature in treatment conditions against 5wk Normal animals or 5wk MD animals.	208
Table 5-1. Pearson’s R values in each treatment condition comparing the strength of association between each protein.....	209

Table 6-1. Pearson’s R correlations between newly identified plasticity features and PCA dimensions.	210
Table 7-1 p-values comparing the each newly identified plasticity feature in treatment conditions against 5wk Normal animals and 5wk MD animals.....	210
Table 9-1 Pearson’s R values comparing the strength of association between each treatment subcluster.	211
Table 9-2 Bonferroni corrected p-values between each treatment subcluster.	211
Table 11-1. p-values for each identified plasticity feature within subclusters compared against the Normal animals from cluster 1.....	212
Chapter 6. Expression of synaptic and non-neuronal proteins reveal parallel plasticity states across human visual cortex development	220
Table 1: List of proteins included in this chapter.	225
Table 2: Cases used in this study.....	227
Table 3: Comparison of protein expression levels against preceding cluster.....	240
Table 4: Summary of cluster-identifying proteins across the first 3 PCA dimensions.....	248
Chapter 7. General Discussion	270
References	283

List of Abbreviations

2D	two dimensional
AMPA	α -amino-3-hydroxy-5-methyl-4-isoxazolepropionic acid receptor
ABTS	2,2'-azino-bis(3-ethylbenzothiazoline-6-sulphonic acid)
ANOVA	analysis of variance
β -tubulin	beta-tubulin
BCA	bicinchoninic acid (assay)
BD	binocular deprivation
BV	binocular vision
CI	confidence interval
CP	critical period
CTB	cholera toxin B
CVP	central visual pathway
DAB	3,3'-Diaminobenzidine
DE	dark exposure
DR	dark rearing
DTT	dithiothreitol
EDTA	ethylenediaminetetraacetic acid
EEG	electroencephalogram
EGTA	ethylene glycol tetraacetic acid
E:I	excitatory:inhibitory balance
EPSC	excitatory post-synaptic current
fMRI	functional magnetic resonance imaging
GABA	gamma-aminobutyric acid
GABA _A α 1/ α 1	gamma-aminobutyric acid A receptor subunit alpha 1
GABA _A α 3/ α 3	gamma-aminobutyric acid A receptor subunit alpha 3
GAPDH	glyceraldehyde 3-phosphate dehydrogenase
GFP	green fluorescent protein

GluA	glutamate receptor ionotropic AMPA receptor
GluN	glutamate receptor ionotropic NMDA receptor
GluN2A/NR2A/2A	glutamate receptor ionotropic NMDA receptor subunit 2A
GluN2B/NR2B/2B	glutamate receptor ionotropic NMDA receptor subunit 2B
HD	high dimensional
HEPES	4-(2-hydroxyethyl)-1-piperazineethanesulfonic acid
HOM	homogenate
HRP	horseradish peroxidase
IP	intraperitoneal
IPSC	inhibitory post-synaptic current
IV	intravenous
k	number of clusters
LGN	lateral geniculate nucleus of the thalamus
LTD	long term depression
LTBV	long term binocular vision
LTP	long term potentiation
MBP	myelin basic protein
MD	monocular deprivation
MIN	medial interlaminary nucleus
NMDAR	N-methyl-D-aspartate receptor
NgR	Nogo-66 receptor
NIR	near infrared
OD	ocular dominance
PBS	phosphate-buffered saline
PBS-T	phosphate-buffered saline with Triton-X
PACT	passive clarity technique
PC	principal component
PCA	principal component analysis
PFA	paraformaldehyde

PMSF	phenylmethanesulfonyl fluoride
PNNs	peri-neuronal nets
PSD-95	post-synaptic density protein 95
PVDF-FL	polyvinylidene difluoride
PV+	parvalbumin-positive
RGC	retinal ganglion cell
RO	reverse occlusion
ROI	region of interest
RSKC	robust and sparse K-means clustering
SC	superior colliculus of the midbrain
SDS	sodium dodecyl sulfate
SDS-PAGE	sodium dodecyl sulfate polyacrylamide gel electrophoresis
SEM	standard error of the mean
SPARCL	sparse clustering
sRIMS	sorbitol-based refractive index matching solution
STBV	short term binocular vision
SVD	singular value decomposition
Syn	synapsin I
SYN	synaptoneurosome
TMB	3,3',5,5'-Tetramethylbenzidine
TNF- α	tumor necrotic factor- α
tSNE	t-distributed stochastic neighbor embedding
Ube3A	ubiquitin protein ligase E3A
V1	primary visual cortex
VMR	variance to mean ratio
WB	western blot
WGA	wheat-germ agglutinin
WSS	within group sum of squares

Declaration of Academic Achievement

Chapter 2 is a manuscript to be submitted to the Journal of Neuroscience Methods. This chapter was a collaboration between myself and Dr. Murphy. I was the lead on designing the experiment, myself and Dr. Murphy performed the experiment, collected the data and analyze the data, and I wrote the manuscript with Dr. Murphy.

Chapter 3 is a chapter that was published by Springer Nature Protocols. It was published in the Neuroscience series entitled ‘Synaptosomes’, in the chapter ‘Making synaptosomes’. This chapter was a collaboration between myself and Dr. Murphy. I was the lead on performing the experiments, analyzing the data, and I wrote the manuscript.

Balsor J.L., Murphy K.M. (2018) Protocol for a High-Throughput Semiautomated Preparation for Filtered Synaptoneurosomes. In: Murphy K. (eds) Synaptosomes. Neuromethods, vol 141. Humana Press, New York, NY

Chapter 4 is a chapter that will be submitted to the Journal of Neuroscience Methods. This chapter was a collaboration between myself and Dr. Murphy. I was the lead on designing and performing the experiments, analyzing the data and I wrote the manuscript. A pre-print copy of this manuscript is available on bioRxiv pre-print server at:

Balsor, J. L., Jones, D. G., & Murphy, K. M. (2019). A primer on high-dimensional data analysis workflows for studying visual cortex development and plasticity. bioRxiv, 554378.

Chapter 5 is a manuscript that was accepted to the special issue of Neural Plasticity entitled *Role of Visual Cortical Plasticity in the Development and Treatment of Amblyopia and Other Neurodevelopmental Disorders*. This chapter was a collaboration between myself, Dr. David Jones and Dr. Murphy. I was the lead on designing the experiment, Dr. Brett Beston helped to collect the data, I analyzed the data with Dr. Jones and Dr. Murphy, and I wrote the manuscript with Dr. Murphy. A pre-print copy of this manuscript is available on bioRxiv pre-print server at:

Balsor, J., Jones, D. G., & Murphy, K. M. (2019). Classification of visual cortex plasticity phenotypes following treatment for amblyopia. bioRxiv, 554576.

Chapter 6 is a manuscript in preparation for submission to Journal of Neuroscience. This chapter is a collaboration between myself, Dr. David Jones, and Dr. Kathryn Murphy. I was the lead on designing the experiments, analyzing the data, and I wrote the manuscript. Data were collected by various students including Dr. Caitlin Siu, Dr. Joshua Pinto, Dr. Kate Williams and Dr. Brett Beston.

Chapter 1. General Introduction

Preamble

Vision is the most heavily relied upon sensory system for humans navigating the world around us. The quality of our vision changes, however, depending on early visual experience. Abnormal visual experience in childhood can result in permanent visual impairments, including visual disorders like amblyopia. Those visual impairments have significant socioeconomic impacts as kids with amblyopia have difficulties with tasks such as reading or making eye-contact with peers, that is likely to affect self-esteem, the ability to learn and to perform academically (Nelson et al., 2008). Children with uncorrected visual impairments are therefore less likely to pursue post-secondary school education or careers that rely on those abilities, in addition to experiencing an overall decrease in quality-of-life (van de Graaf et al., 2007; McBain et al., 2014). Although many treatments for childhood vision disorders like amblyopia have been explored through visual manipulation, perceptual training and pharmacological intervention, there is little consensus as to what treatment leads to lasting visual recovery.

Over the past fifty years, researchers have used animal models to investigate the underlying causes of amblyopia along the visual pathway. Together these studies point to a collection of neurobiological mechanisms in the primary visual cortex (V1) that underlie those experience-dependent visual impairments. Little is known however, about how therapies for visual impairments impact those neurobiological mechanisms in V1. Even less is known about how to translate those neurobiological mechanisms for use in human therapies.

This thesis addresses these gaps in the field by answering questions about how treatment for amblyopia affects plasticity mechanisms in V1, and how to begin to translate those findings in animal models onto normal human development. In this introduction I will discuss the maladaptive cortical response to early visual impairments and classic treatments for amblyopia. I will then explain how animal models have been instrumental in our understanding of experience dependent plasticity mechanisms as they pertain to amblyopia, and how we can take advantage of this knowledge to reinstate plasticity and treat amblyopia. Finally, I will outline current treatment therapies in animal models and explain how we can translate these findings for interpreting persistent amblyopia in humans.

1.1 Amblyopia

Quality of life

Amblyopia, more commonly known as lazy-eye, is a visual disorder that typically presents in young children, and negatively impacts both visual function and quality of life. The clinical diagnosis for amblyopia includes the presence of a visual deficit that impacts the acuity of either one, or both eyes, even after correcting the original visual insult. This disorder afflicts ~2-5% of children (Wu and Hunter, 2006; Friedman et al., 2009; Maurer and McKee, 2018), and constitutes the leading cause of monocular visual impairment in children and young adults worldwide (Gunton, 2013). Monocular acuity deficits affect a multitude of visual tasks, including contrast sensitivity, accommodation, binocular vision, and higher-order motor and visual tasks (Birch, 2013). These deficits are more pronounced in central than peripheral vision (Tytla et al., 1988; Bowering et al., 1993; 1997), and lead to poor performance on real-world visuomotor tasks (Grant and Moseley, 2011) and day-to-day activities such as reading (Kelly et al., 2015). Aside from the visual deficits, the psychological and social tolls of untreated amblyopia range from peer discrimination to poor image of the self, and poor school performance (Packwood et al., 1999; Choong et al., 2004; Chua and Mitchell, 2004; Webber and Wood, 2005; Rahi et al., 2006; Webber et al., 2008; Horwood:2005gc; O'Connor et al., 2010).

Susceptibility

The exact cause of amblyopia is unknown, however it is clear that this disorder stems from inadequate visual experience during the first years of life, and risk factors for amblyopia include misalignment of retinal images (strabismus), unequal refractive power between the two eyes (anisometropia), or visual deprivation (e.g. cataracts) (Ellemberg et al., 2000; Maurer and Lewis, 2001; Birch, 2013). The period of susceptibility to amblyopia is restricted to a developmental window that extends to around 8 years of age (Daw, 1998; Mitchell and MacKinnon, 2002; Simons, 2005), and reversal of the effects of amblyopia becomes more difficult outside this window (Birch, 2013).

Human development has long been characterized by a series of stages (Piaget 1952, Erikson, 1959), and the development of vision is no exception (Lewis and Maurer, 2005; Siu &

Murphy 2018, 2018). Even studies investigating the development of visual cortex use developmental stages (Pinto et al., 2010; Williams et al., 2010; Siu et al., 2015; 2017). One of these developmental stages is defined by the increased susceptibility to amblyopia (Lewis and Maurer, 2005). Other stages are marked by the development of visual perceptual abilities, which progress through a series of stages that extend well into the fourth decade of life (Kovács et al., 1999; Owsley, 2011; Hartshorne and Germine, 2015). Modern interventions for amblyopia are inspired by the protracted time course of development of human visual abilities, and have produced varying degrees of success in treating both young children within the window of susceptibility to plasticity, as well as older adult amblyopes.

Standard treatment

For over 200 years the best treatment for amblyopia has been patching therapy: applying a patch over the good eye to eliminate the suppressive action, and permit experience-induced recovery of acuity in the open amblyopic eye. If amblyopia is diagnosed early and treatment is provided, patching therapy can be an effective intervention strategy for recovering lost acuity (Wallace et al., 2006). There are several challenges with patching therapy. First, not all children are receptive to patching therapy, and many fail to show improvements despite even the most aggressive patching therapy (Woodruff et al., 1994; Repka et al., 2003; Birch et al., 2004; Repka et al., 2004; Stewart et al., 2004; Repka et al., 2005; Birch and Stager, 2006; Wallace et al., 2006). Second, even if treatment starts on time and compliance is monitored, children can still present with persistent visual deficits, implying that even the best amblyopia treatments fail to provide optimal recovery (Birch, 2013). Third, most amblyopic children that actually succeed in recovering acuity are prone to regression, whereby the recovered acuity is lost within the first year after treatment (Holmes et al., 2004; Bhola et al., 2006).

Over the last 50 years our knowledge of the anatomy and function of the visual system has grown, and with it so has our understanding of the causes of visual acuity deficits such as the ones found in amblyopia. The prolonged development of human visual cortex, measured through anatomical and neurobiological markers as well as visual milestones, would suggest that various forms of plasticity persist well into adulthood. The visual systems of animals like cats and non-human primates share homologies with visual systems of humans, and that makes them good

models for identifying biological changes that might explain the poor acuity after amblyopia treatment. This includes our understanding of how neural circuits of the central visual pathway are shaped or molded by experience, called neural plasticity. Unfortunately the translation of effective treatments for amblyopia is lagging, in part due to the slow translation of neural plasticity in animal models into effective human therapies. This introduction will present an overview of animal models for amblyopia, our understanding of the causes of amblyopia, and how intervention for human amblyopes might be improved.

1.2 Cortical Plasticity - Animal models

Central Visual Pathway - Retina

Light signals are processed in the eye, where photons get converted into electrochemical signals that travel along the central visual pathway to the brain (Figure 1A). There the signals are used to interpret physical characteristics of real world objects, such as size, shape, color, texture, location and motion information. However the only neural portion of the eye directly connected to the central nervous system is the retina. After light passes through the cornea, it is filtered through the aqueous humor (anterior chamber), the lens and the vitreous humor (posterior chamber), before contacting the various layers of the retina (Figure 1B). Light photons enter the retina through the ganglion cell layer and strike two classes of photoreceptor cells, rods and cones. In a process called photo-transduction, both classes of photoreceptor convert light signals into neural signals (Kuffler, 1953) that are passed between the 5 cell types spread across the layers of the retina (Polyak, 1941; 1957)(Fig 1B). In the outer plexiform layer, photoreceptors synapse onto bipolar cells, and in the inner plexiform layer, the bipolar cells in turn synapse onto retinal ganglion cells (RGCs). Finally, RGCs bring the visual signal out of the retina through the optic disk and along the optic nerve (reviewed in Masland, 2012; Seung and Sümbül, 2014; Spillmann, 2014).

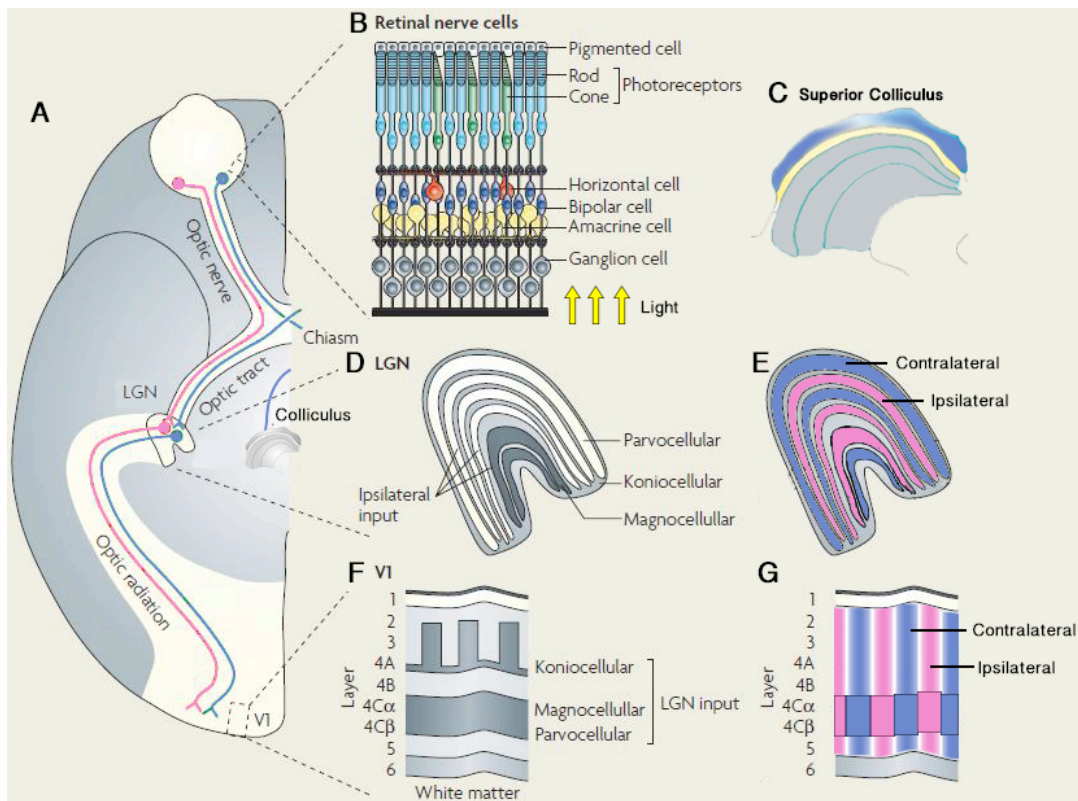


Figure 1. Representation of common organizational schemes along the central visual pathway.

A. Overview of the central visual pathway depicting retinal afferents that innervate the ipsilateral (pink) or contralateral (blue) hemispheres. B. The layers of the retina and associated cell types, arranged with photoreceptors at the top and ganglion cells at the bottom. Note that light (yellow arrows) first enters the retina through the ganglion cell layer, but is only photo-transduced into an electrical signal by the photoreceptors at the back of the retina. Neurons in the optic nerve project to the superior colliculus (C) and lateral geniculate nucleus (LGN) (D,E). The LGN primarily projects to layer 4 (IV) of the primary visual cortex (V1) (F,G). LGN is divided into 3 types of layers: parvocellular, magnocellular and koniocellular (D), which remain segregated as they project to the different layers of V1 (F). Similarly the pattern of contralateral and ipsilateral afferents in the LGN (E) is preserved as columns of ocular dominance in V1 (G). Figure 1 is modified from (Solomon and Lennie, 2007).

Though the retina contains more than 60 different cell types the major classes include the photoreceptors, bipolar cells and ganglion cells, as well as horizontal and amacrine cells, which have cell bodies located in the inner nuclear layer, but synapse in the outer and inner plexiform layers, respectively (Masland, 2012). Horizontal and amacrine cells create lateral connections between photoreceptors and bipolar cells.

The spatial arrangement of photoreceptors, bipolar cells and ganglion cells are not uniformly distributed across the retina, and because of this the degree of convergence from photoreceptor to ganglion cell differs depending on retinal eccentricity. In non-human primates and humans, the center of vision is focused by the eye onto the fovea, an area of the retina known

for processing high visual acuity. In animals with fovea-like vision, including cats that have an area centralis (Kuffler, 1953; Curcio et al., 1990; Roorda and Williams, 1999; Roorda et al., 2001), the fovea is marked by a low degree of convergence from the many cone photoreceptors (Steinberg et al., 1973) to the high density of retinal ganglion cells (Stone, 1978). Low convergence from one cell type to another maintains small receptive field sizes and high visual acuity (Cleland et al., 1979; Wässle et al., 1990; Sjöstrand et al., 1999). As retinal eccentricity increases, densely packed cones are exchanged for sparsely packed rods, and higher convergence from photoreceptor to RGC results in poorer visual acuity in visual periphery.

Regardless of retinal eccentricity, neighbouring ganglion cells share neighbouring receptive fields, and the degree of convergence from photoreceptor to ganglion cell establishes the size of these receptive fields. While not all mammals have a fovea-centralis like human and non-human primates, carnivores like the cat possess a similar fovea-like retinal area centralis with a high density of photoreceptors with low convergence on ganglion cells. This topographic arrangement of neighbouring receptive fields innervating neighbouring RGCs is referred to as retinotopy, and is maintained at all stages of the central visual pathway.

Central Visual Pathway - Connections to midbrain and thalamus

Retinal ganglion cells exit the retina through the optic disk in a nerve bundle called the optic nerve, that projects to the superior colliculus of the midbrain (SC, Figure 1C) or along the optic tract to the lateral geniculate nucleus of the thalamus (LGN, Figure 1D,E), as well as other sites. The SC controls oculomotor responses (reviewed in (Wurtz et al., 1980; Gandhi and Katnani, 2011) and early anatomical lesion studies in tree shrews concluded that superficial SC layers were responsible for visual processing (Casagrande et al., 1972; Harting et al., 1973; Casagrande and Diamond, 1974), while deeper layers guide orientation/movement of the eyes and head toward stimuli (Harting et al., 1973). Tracer studies in primates and cats further revealed that most cells across the surface of the SC are innervated by the contralateral eye (Figure 1C- blue), and receive few ipsilateral connections (Lane et al., 1971; Cynader and Berman, 1972; Kaas et al., 1974). Curiously, labelling RGC projections to SC revealed labelling in superficial layers of both hemispheres of the SC (Hendrickson et al., 1970; Tigges and Tigges, 1970; Lund, 1972a; 1972b; Tigges and O'Steen, 1974; Hubel et al., 1975), with superficial label

density highest in the contralateral hemisphere (Graybiel 1975) and only small islands of label in the ipsilateral hemisphere (Graybiel 1975; Wässle and Illing, 1980; Illing, 1989). The same superficial layers of SC receive feedback projections from layer V of V1 (Lund et al., 1975).

In the LGN, RGC afferents terminate in alternating, eye-specific laminae in both cats, (Guillery and Kaas, 1971; Shatz, 1983; Anderson et al., 1988) and primates (Kaas et al., 1978). The number and patterning of laminae differs across species, but the anatomical and functional mapping of retinal output to LGN inputs is highly conserved from cats (Cleland et al., 1971; Hamos et al., 1987) to primates (Lee et al., 1983; Conley and Fitzpatrick, 1989). Cats have 3 major LGN subdivisions: A, A1 and C that process stimulation from contralateral, ipsilateral then contralateral retinae, respectively (Guillery and Kaas, 1971). Meanwhile, humans and non-human primates have 6 LGN laminae: the contralateral eye innervates layers 1, 4 and 6, and the ipsilateral eye layers 2, 3 and 5 (Figure 1E). LGN laminae in humans and non-human primates are also divided by function. The outermost laminae (3-6) are parvocellular layers containing cells with smaller receptive fields, that process medium wavelength colour information, while the innermost laminae (1 and 2) are magnocellular layers containing cells with larger receptive fields, that process contrast and motion, but are achromatic (Wiesel and Hubel, 1966; Derrington et al., 1984; Kaplan and Shapley, 1986; Michael, 1988; Jacobs, 2008) (Figure 1D). In between each magno- and parvocellular layer exists a third type of layer called koniocellular (Kaas et al., 1978; Casagrande, 1994; Hendry and Yoshioka, 1994). The koniocellular layers are believed to process information from short wavelength cones (blue light) (Martin et al., 1997; Hendry and Reid, 2000; Tailby et al., 2008a; 2008b). All layers of the LGN project to primary visual cortex, and in turn the LGN receives feedback from V1 (Guillery and Sherman, 2002; Briggs et al., 2016).

Anatomical Organization of Visual Cortex - Cortical Layers

The visual cortex itself is divided into 6 layers. The supragranular layers (I-III) are the layers where inter-cortical connections occur between visual association and other areas. Layer I does not contain many neurons, but does contain cell neuropil, and is called the molecular layer. Layers II and III, the external granular and external pyramidal layer, contain mostly pyramidal

cells. Layer II/III contains most of the connections with other cortical areas (cortico-cortical areas).

The internal granular layer (IV), or the input layer, is where most afferents from LGN axons terminate (Figure 1F). Layer IV is divided into A, B and C. Layer IVC is further subdivided into IVC α and IVC β , where the magnocellular and parvocellular LGN laminae terminate, respectively (Chatterjee and Callaway, 2003)(Figure 1F). The koniocellular neurons primarily terminate in layer IVA(Casagrande et al., 2007; Klein et al., 2016). The koniocellular neurons project not only to layer IVA, but also to supragranular “blobs” or “puffs”. In layer V and VI, pyramidal cells receive the information from layer IV and supra granular layers, and send information out of the cortex. Most of these neurons are excitatory, but modulatory inhibitory circuits govern their behaviour as well. For example in layer IV there is a thick neuropil of inhibitory parvalbumin-positive (PV+) inhibitory interneurons (del Río and DeFelipe, 1994), that are exquisitely positioned to modulate feedforward responses in the visual cortex (Pouille and Scanziani, 2001; Self et al., 2012) and across cortical networks (Agetsuma et al., 2018). Beyond the input layer IV, the streams of visual processing intermingle extensively.

In mammals with a region of specialized vision, such as the fovea (primate) or area centralis (cat), the largest amount of V1 cortical area is reserved for processing the central field of vision (Tusa et al., 1978), and the small receptive field sizes are maintained in neurons in the central visual field representation of V1. This preserves high visual acuity for central vision (Hubel & Wiesel, 1962). Since monocular deprivation (MD) affects central visual processing the most (Dews and Wiesel, 1970), the cortical deficits present in amblyopia are likely located in this cortical region.

Functional Organization of Visual Cortex - Cortical Columns

Much of what is known about the structure and function of the visual cortex, from its organization to the impact of early experience on visual function, comes from the work of David Hubel and Torsten Wiesel. By projecting bars of moving light onto a screen while simultaneously recording the extracellular responses of neurons in cat V1, Hubel and Wiesel were able to map receptive field properties of V1 neurons (Hubel & Wiesel, 1962). They discovered that the cells they were recording from responded preferentially to stimuli of a particular orientation (0-180°),

called the orientation selectivity, and preferred one eye over another, called ocular dominance (OD). Neighbouring V1 neurons were likely to have similar orientation and ocular preference, and later it was confirmed that neighbouring cells in the input layer IVC of visual cortex in both cats (LeVay et al., 1978) and primates (Wiesel et al., 1974) extend as columns throughout cortical layers (Figure 1G). The sudden transitions between these OD columns take place more gradually outside layer IVC of V1, where binocular information begins to intermingle.

Ocular dominance plasticity and neuronal morphology

Visual experience alters the response properties of V1 cells in cats (Wiesel and Hubel, 1963). The OD columns were already present in the cortex of very young, visually inexperienced animals and OD columns formed even in the absence of visual stimulation. However, the quality of vision is important for maintenance of OD columns across development, since cats that were monocularly deprived (MD) of visual stimulation shifted OD preference in favour of the non-deprived eye (Wiesel and Hubel, 1965). The capacity for this OD shift, called OD plasticity, was greatest in younger animals, while mature animals were more resistant to experience-dependent changes (Hubel and Wiesel, 1970). The window for ocular dominance plasticity was outlined in cats from as early as 3 weeks of age, peaks by 5 weeks, and steadily declines past 8 weeks of age and into adulthood (Olson and Freeman, 1980). It was possible to induce the ocular dominance shift in adult animals, but it was harder to initiate and required longer periods of deprivation (Jones et al., 1984). The physiological shift in OD preference following early MD (Movshon and Dürsteler, 1977; Shatz et al., 1978; Crair et al., 1997) was accompanied by visual acuity deficits (Dews and Wiesel, 1970; Mitchell et al., 1977; Giffin & Mitchell, 1978), and the more severe the deprivation, the worse the acuity deficit. Therefore, the acuity deficits that arise after early MD are directly related to the physiological response property known as OD plasticity.

The physiological changes that occur after MD during the critical period (CP) proceed through two stages; first a weakening of responses from the deprived eye (Gordon & Stryker 1996; Hensch et al., 1998; Trachtenberg et al., 2000; Frenkel & Bear, 2004), followed closely by a slow strengthening of non-deprived eye response (Sawtell et al., 2003; Frenkel & Bear, 2004; Kaneko et al., 2008). The structural changes that accompany MD-induced OD shifts occur in a similar cascade of events, beginning with an early mobilization and diminished density of

dendritic spines (Mataga et al., 2004; Oray et al., 2004; Tropea et al., 2010; Yu et al., 2011; Djurasic et al., 2013). After these early spine changes, there follows a loss of neuronal afferents from the deprived eye (Antonini and Stryker, 1993; 1996), and then a later expansion of afferents from non-deprived eye (Antonini et al., 1999). Even short periods of deprivation, on the scale of hours, are sufficient to cause rapid physiological (Freeman and Olson, 1982; Trachtenberg et al., 2000; Schwarzkopf et al., 2007), proteomic (Williams et al., 2015) and anatomical changes (Antonini and Stryker, 1996). Sensory deprivation experiments such as these have become the preeminent model for studying CP plasticity and understanding the physiological and anatomical basis for juvenile plasticity is a goal of modern neuroscience.

Animal models of amblyopia

Visual impairments in animal models of amblyopia are typically administered by MD. These animal models recapitulate the physiological and anatomical changes that accompany early adverse experiences in humans, including the transient recovery of acuity following patching therapy. In an extreme form of behavioural intervention, cats that received MD to the peak of the CP were reverse occluded by suturing shut the non-deprived eye and re-opening the initially deprived eye (Movshon, 1976a). This reverse occlusion (RO) treatment demonstrates some recovery of vision in the initially deprived eye (Movshon, 1976a; Giffin and Mitchell, 1978). However, like in humans, this recovered vision is lost soon after treatment stops and binocular vision (BV) is restored (Mitchell et al., 1984). The challenges of patching therapy are further complicated in that vision of the initially non-deprived eye may also be affected, resulting in bilateral amblyopia after patching therapy (Murphy and Mitchell, 1986; 1987).

The loss of recovered acuity after patching therapy remains a mystery. RO restores much of the anatomical and physiological changes of MD. Indeed 18 days of RO shifts the physiological response back to normal, while longer lengths of RO have little effect (Blakemore and Van Sluyters, 1974; Movshon, 1976b; Mitchell et al., 1977; Giffin and Mitchell, 1978; Mitchell, 1988; Mitchell and Gingras, 1998). RO even rescues some anatomical changes, namely restoring the size of axonal branches from the initially deprived eye (Antonini et al., 1998). If anatomical and physiological changes cannot fully explain the loss of acuity after RO, then what are the neurobiological changes that lead to bilateral amblyopia?

1.3 Synaptic plasticity - animal models

Glutamatergic plasticity mechanisms

Visual information first reaches visual cortex by means of excitatory thalamocortical axons terminating in layer IVc of V1. Here neurotransmission begins through the release of glutamate, which binds to alpha-amino-3-hydroxy-5-methyl-4-isoxazole receptors (AMPA) and N-methyl-d-aspartate receptors (NMDAR). This glutamatergic binding to either AMPARs or NMDARs triggers an early ~2ms (AMPA) (Kleppe & Robinson, 1999) or later ~190-380ms (NMDAR) (Monyer et al., 1992) phase of excitatory post-synaptic currents (EPSC). The subunit composition of glutamatergic receptors modulates receptor kinetics, and by extension, the ease with which synaptic plasticity can occur. For example, most AMPARs contain the GluA2 subunit, which makes the AMPAR impermeable to calcium, restricting calcium-dependent LTP (Hollmann et al., 1991). GluA2-containing AMPAR expression increases with experience (Herrmann, 1996) and after blocking cell activity using TTX (Gainey et al., 2009). This fast acting glutamatergic receptor is associated with rapid signal processing in the visual system and homeostatic plasticity, so changes in AMPAR expression after MD explain some of the system resistance to recovery.

Similar to AMPA receptors, NMDA receptors are considered a functional unit controlling synaptic plasticity. Pharmacological inactivation of NMDARs prevents the ocular dominance shift in young kittens (Bear et al., 1990). NMDARs are tetrameric glutamate receptors that contain two obligatory GluN1 subunits paired with two GluN2 (A-D) and/or GluN3 subunits (Monyer et al., 1994). The contribution of NMDAR activity to synaptic plasticity is tightly regulated by NMDAR subunit composition. There is a well-documented experience-dependent shift in NMDAR currents in visual cortex, that shortens the duration of EPSCs across development (Flint et al., 1997). This shift in the receptor currents is delayed by visual deprivation (Carmignoto & Vicini, 1992), and is directly regulated by changes in the NMDAR composition (Quinlan et al., 1999b). Only recently has the effect of including more 2A subunits in NMDAR been suitably quantified as a shift in NMDAR decay kinetics away from the slow 333ms contributed by diheteromeric 2B NMDAR (2B:2B) to the faster decay kinetics from

triheteromeric NMDAR (2A:2B) (50ms) or the diheteromeric NMDAR (2A:2A) (36ms) (Tovar et al., 2013; Sun et al., 2017). Shifting to faster NMDAR kinetics reduces the window for coincidence detection in LTP (Erreger et al., 2005), but indicates classic Hebbian plasticity has strengthened connections between neurons. Furthermore, the change in NMDAR currents is bidirectional, and environmental manipulations such as dark rearing and light exposure can adjust synaptic transmission. Dark rearing prolongs the length of EPSCs while light exposure shortens them (Philpot et al., 2001). Similarly, the shift in receptor subunit composition can be manipulated by experience: dark rearing increases the relative contribution of GluN2B, and light exposure increases the GluN2A (Quinlan et al., 1999a).

Aside from classic Hebbian forms of plasticity, AMPAR and NMDAR are also involved in homeostatic plasticity mechanisms. One example of this is the insertion of AMPAR to synaptic membranes of silent (dormant) synapses (Rumpel et al., 1998). Once synapses are activated the strength of the signal required to effect further change through LTP or LTD is gated by the balance between 2A and 2B, a synaptic property dubbed the 'sliding modification threshold' of a synapse, also referred to as metaplasticity (Quinlan et al., 1999a; Philpot et al., 2001). With increased 2B expression in juvenile visual cortex, the likelihood of LTP is higher because of the prolonged decay kinetics of 2B-dominated NMDAR and increased calcium entry (Jones et al., 1999), leading to more calcium-dependent LTP processes (Philpot et al., 2001). After MD the delicate synaptic environment becomes skewed in subunit compositions of AMPA and NMDAR subunits. The weakened deprived eye response is mediated by decreased GluA2 (Heynen et al., 2003; Lambo and Turrigiano, 2013) and increased GluN2B (Chen and Bear, 2007), and the strengthened non-deprived eye response is driven by increased GluA2 (Lambo and Turrigiano, 2013) and decreased GluN2B (Smith et al., 2009). The weakening of deprived eye responses via AMPAR internalization (Yoon et al., 2009) can be prevented by pharmacologically blocking NMDAR activity, and reducing OD plasticity (Kleinschmidt et al., 1987; Gu et al., 1989; Bear et al., 1990).

The balance between NMDAR and AMPAR is important for visual processing. First, NMDARs are necessary for establishing orientation selectivity (Ramoia et al., 2001), and the timing of the developmental shift from 2B to 2A coincides with the CP for OD plasticity

(Fagiolini et al., 2003). Furthermore, the rapid response properties of AMPARs imbue synapses with stimulus-driven feedforward visual processing abilities, while the slower NMDAR are involved in feedback stimulus modulation (Self et al., 2012).

In human visual cortex development, the timing of these receptor subunit shifts are very prolonged, for example, the NMDAR subunits continue to shift from 2B to 2A into adulthood (~40years) (Siu et al., 2017), well after the window of susceptibility for amblyopia (Lewis and Maurer, 2005). Our lab has characterized two aspects of these subunit shifts in MD cats, and classified the changes as an early homeostatic unsilencing of synapses (Beston et al., 2010). This can occur after reduced activity in cortical cells, which increases GluA2 relative to GluN1 (Gainey et al., 2009), or after MD, which delayed the shift from more 2B to more 2A (Beston et al., 2010).

GABAergic plasticity mechanisms

Regulation of excitatory transmission occurs in part through GABAergic activation of ionotropic GABA_A receptors, which hyperpolarize the neuronal membrane. The GABA_A receptor is the most abundant inotropic GABAR in the visual cortex, and the subunit composition affects the duration and intensity of hyperpolarization. GABA_A subunits have a large number of possible combinations of subunits, each grouped into families of α (1–6), β (1–3), γ (1–3), δ , ϵ , π , θ or σ (Bonnert et al., 1999; Whiting et al., 1999). The most abundant of these heteropentameric GABA_A receptors contain 1 γ subunit, 2 β subunits and 2 α subunits. There is a developmental shift in the expression of the α subunits like the shift that occurs for GluN2 subunits. Early in development there are more GABA_A $\alpha 3$ ($\alpha 3$) then a transition to more GABA_A $\alpha 1$ ($\alpha 1$) during the CP in rats (Bosman et al., 2002) cats (Chen et al., 2001) macaque monkeys (Hendrickson et al., 1994) and humans (Pinto et al., 2010). Functionally, the developmental shift speeds up the receptor kinetics (Gingrich et al., 1995), and the relative abundance of each subunit alters the speed from more diheteromeric $\alpha 3$ ($\alpha 3:\alpha 3$ -129ms) to more diheteromeric $\alpha 1$ ($\alpha 1:\alpha 1$ - 42ms) (Eyre et al., 2012).

The timing of the GABA_A subunit shift is especially important as it overlaps with the end of the CP in cats, monkeys and humans (Hendrickson et al., 1994; Chen et al., 2001; Pinto et al., 2010). The transition to the faster $\alpha 1$ subunit is necessary for ocular dominance plasticity

(Hensch et al., 1998; Fagiolini et al., 2004), regulates gamma oscillations and controls long-range cortical signalling (Cardin et al., 2009). The CP can even be induced in rodents through modulation of GABA_A agonists (Fagiolini & Hensch, 2000). Expression of GABA_A receptors is mediated by visual experience (Hendry et al., 1994), and in our lab, we demonstrated an accelerated transition from $\alpha 3$ to $\alpha 1$ in V1 of MD cats, suggesting premature development of the inhibitory system following early abnormal visual experience (Beston et al., 2010). Some of this inhibitory regulation of critical period has been traced to inputs from the LGN. For example, mice lacking the GABA_A $\alpha 1$ subunit failed to demonstrate an OD shift after MD, suggesting that thalamocortical neurons containing the GABA_A $\alpha 1$ subunit are involved in consolidating the ocular dominance shift in visual cortex (Sommeijer et al. 2017). Expression of both excitatory and inhibitory mechanisms are necessary for onset and closure of the CP.

Excitatory:Inhibitory Balance

Together these excitatory and inhibitory molecular mechanisms govern long term potentiation (LTP), long term depression (LTD), synaptic scaling, and changes in the excitatory:inhibitory (E:I) balance (Kirkwood and Bear, 1994a; 1994b; Hensch et al., 1998; Heynen et al., 2003; Fagiolini et al., 2004; Turrigiano and Nelson, 2004) that contribute to experience dependent changes in amblyopia (Hess and Pointer, 1985; Li et al., 2007; Hensch and Quinlan, 2018). Critically, GABAergic inhibition is essential for both the opening and close of the critical period (Hensch et al., 1998; Fagiolini & Hensch, 2000) and there is ample evidence to suggest that the balance between excitation and inhibition regulates the amount of available plasticity across development (Fagiolini et al., 2004, reviewed in Hensch 2005). Manipulating either mechanism can increase or decrease the amount of experience-dependent plasticity in the cortex.

Other plasticity mechanisms

There are hundreds of pre-synaptic proteins, and thousands of post-synaptic proteins, and many, but not all of the synaptic proteins are involved in regulating experience-dependent plasticity. In fact, the list of proteins regulating plasticity has extended beyond the classic view of the synapse. The experience dependent changes that shape neural connections are typically consolidated by extra-synaptic brakes on plasticity that increase at the close of the CP (e.g.

Dityatev et al., 2010). For example, increased electrical activity in cortical neurons increases oligodendrocyte-mediated myelination around active synapses, compacting the myelin sheath and restricting motility (Wake et al., 2011). A receptor for the myelin signaling molecule NogoA, the Nogo-66 receptor (NgR), couples with neurotrophin receptor-75 to form a complex, which prevents neurite growth (Hu and Strittmatter, 2004). Interfering with this complex restores juvenile-like plasticity by permitting OD shifts in cortex of adult animals (McGee et al., 2005), but does not rescue visual acuity (Stephany et al., 2018).

Another extra-cellular factor that both permits plasticity and consolidates the fast electrical signals are peri-neuronal nets (PNNs). These multi-protein complexes initially are degraded by a brief upregulation of proteases at the beginning of MD in the mouse animal model (Mataga et al., 2004; Oray et al., 2004). As the CP draws to a close, PNNs form around the fast spiking PV+ inhibitory interneurons in the cortex (Cabungcal et al., 2013a), increase in expression at the close of the CP (Cabungcal et al., 2013b), and increase expression of Otx2 (Bernard 2016) and when PNN are pharmacologically degraded, even in adult rats, juvenile-like plasticity is restored (Pizzorusso, 2002; Pizzorusso et al, 2006; Carulli et al., 2010). This restoration of plasticity has been linked with increased spine motility (Mataga et al., 2004; Oray et al., 2004).

However, extra-synaptic factors such as astrocytes can still play a role in experience-dependent plasticity. Tumor necrotic factor- α (TNF- α), a cytokine produced by glial cells and released on glutamate stimulation (Sawada et al., 1989), is involved in synaptic plasticity (Stellwagen and Malenka, 2006). TNF- α causes AMPA receptor insertion on the membrane of the post-synaptic neuron, while the absence of TNF- α causes endocytosis of AMPA receptors (Beattie et al., 2002). The astrocytic release of TNF- α also regulates experience dependent visual plasticity (Kaneko et al., 2008).

These are just some examples of extra-synaptic mechanisms that control plasticity within cortical neurons. There are many other neurochemicals involved in regulating synaptic plasticity, including monoamines, CaMKII, ERK1/2 and Otx2. In fact, many of the plasticity mechanisms outlined in this section are further regulated by post-translational modifications (e.g. phosphorylation state) to synaptic and extra-synaptic proteins. Many of the changes in these proteins and neurochemicals have been quantified in the classic model of monocular deprivation.

For example, there is a larger impact of amblyopia on central visual acuity in amblyopes, it is not surprising that the greatest impact of MD on these molecular plasticity mechanisms in V1 occurs in the cortical representation of central visual field (Murphy et al., 2004; Beston et al., 2010). The field lacks a complementary understanding of the molecular changes following treatment for amblyopia.

1.4 Translating plasticity - From animal models to amblyopia treatments

Persistent amblyopia is challenging to treat because diagnosis and treatment typically begin near the close of the CP for human vision when visual cortex is less susceptible to experience-dependent change and there are more molecular brakes on plasticity. Two targets for amblyopia therapies have emerged and focus on experimentally reinstating a critical-period-like state of plasticity (reviewed in Bavelier et al., 2010; Sengpiel, 2014) by either reinstating the excitatory-inhibitory balance that triggers the onset of the CP or reducing the brakes on plasticity that emerge in adulthood. These two primary targets have been addressed through pharmacological and behavioural interventions.

Pharmacological interventions to manipulate plasticity

Pharmacological interventions have been successful in targeting CP-like plasticity in animal models by reducing the plasticity-limiting factors, or ‘brakes’. These brakes tend to be located outside the synapse, for example, in myelin sheaths or PNNs, both of which restrict neural and dendritic motility and limit plasticity (eg. McGee et al., 2005; Pizzorusso et al, 2006; Syken et al., 2006; Carulli et al., 2010)). Interfering with the myelin-binding Nogo-R(McGee et al., 2005) or degrading PNNs with chondroitin-sulphate proteoglycans (Pizzorusso et al, 2006) restores juvenile-like plasticity. Alternatively, pharmacological interventions can reinstate conditions that initiate CP-like plasticity by increasing plasticity-promoting factors, such as synaptic expression of GABA (Hensch et al., 1998; Fagiolini & Hensch, 2000). Drugs that modulate or mimic GABA can fine-tune the balance between excitation and inhibition to restore juvenile-like plasticity in adult animals (Maya-Vetencourt et al., 2008).

Another approach targets bidirectional regulators of plasticity, like the GluN2A:GluN2B ratio of NMDAR subunits (Quinlan et al., 1999a; Philpot et al., 2001; 2003; Fagiolini et al., 2004). This approach is more difficult to address pharmacologically because of the high degree of similarity between these two receptor subunits, but drugs are being developed that selectively target one subunit over the other (Lind et al., 2017).

Since multiple plasticity mechanisms are affected after MD, treatments should not focus on targeting a single plasticity mechanism. Instead, treatments that regulate multiple plasticity mechanisms are more likely to be effective in restoring good vision. For example, modulating visual experience as a means of treating amblyopia not only targets multiple plasticity mechanisms, but it is relatively noninvasive. The latter consideration is especially important when considering the clinical population of children where invasive therapies are avoided.

Behavioural interventions to manipulate plasticity

Patching therapy remains the most common behavioural treatment for amblyopia despite the transient nature of recovery. The intervention itself is relatively non-invasive, with as little as 2 hours of patching therapy a day providing effective treatment for moderate cases of amblyopia (Repka et al., 2003), and more aggressive treatments (>6 hours/day) are no more effective than patching full-time (Holmes et al., 2003a; 2003b). Patching therapy such as this is the basis of RO in animal models, which restores some of the physiological and anatomical hallmarks of MD (Blakemore and Van Sluyters, 1974; Movshon, 1976b; Mitchell et al., 1977; Blakemore et al., 1978; Giffin and Mitchell, 1978; Swindale et al., 1981; Mitchell, 1988; Antonini et al., 1998; Mitchell and Gingras, 1998). The labile nature of recovered acuity in amblyopia animal models still cannot be explained (Mitchell et al., 1984; Murphy and Mitchell, 1986; 1987), which has prompted clinicians and researchers to begin searching for other behavioural interventions.

Manipulating visual experience by raising animals in enriched environments with increased visual, social and physical stimuli prolongs the window of plasticity in rats and mice (Sale et al., 2009; Greifzu et al., 2014) and promotes OD plasticity into adulthood. This environmental manipulation is a great example of a single manipulation that both attenuates a molecular brake on plasticity, by decreasing both the density of PNNs (CP-brake) and GABAergic inhibition (CP-trigger) in the visual cortex (Sale et al., 2009; Greifzu et al., 2014). However, there are concerns

regarding the difficulty in mapping such a treatment onto a therapeutic intervention for humans since we already exist in a very enriched, visually stimulating world.

On the other extreme lies dark rearing (DR) and dark exposure (DE), wherein exposing animals to complete darkness at various stages of development has proven equally effective in restoring cortical plasticity (He et al., 2006; Duffy and Mitchell, 2013). Like environmental enrichment, it is difficult to map dark rearing onto an effective treatment for human amblyopes. However, short periods of darkness have proven effective in reinstating CP-like plasticity into adulthood. DE has shown recent promise as a treatment to reinstate plasticity outside the CP in MD rats (Montey & Quinlan, 2011) and cats (Duffy et al., 2013; Mitchell et al., 2016). Manipulations such as dark exposure, or even binocular deprivation (BD), are based the premise that correlated binocular information reduces inter-ocular acuity differences and enables the good eye to better teach the deprived eye. Decreased activity in both eyes should remove the suppressive action from the non-deprived eye while enhancing plasticity in the deprived eye (Cooper and Bear, 2012). Indeed there is an increase in the juvenile subunit of the NMDA receptor (2B) with DE (Yashiro et al., 2005; He et al., 2006). BD also restores the physiological response and spine density on thalamocortical axons in rodents (He et al., 2006; Montey & Quinlan, 2011; Stodieck et al., 2014) and rescues thalamic soma size and neurofilament density in cats (Duffy et al., 2015; 2018), thereby reversing decreased spine density and shrunken LGN soma size observed with MD. Despite the seemingly juvenile-like plasticity state, this treatment fails to promote good recovery of visual acuity by itself, and must be combined with training (Montey et al., 2013; Eaton et al., 2016). Further examination of the synaptic mechanisms underlying recovery of vision in DE and BD animals is still necessary.

Studies such as these that target *both* eyes have shifted the theory behind the causes and treatments for amblyopia away from monocular impairment toward a new understanding of the importance of binocular interactions (Birch, 2013). Perhaps the most important example of this is the work of Kind et al., who demonstrated that *coordinated* BV provides optimal restoration of physiological responses after MD, as well as recovers good acuity (Kind et al., 2002). Just a few hours of intermittent BV during MD have been proven to prevent the physiological effects of MD (Schwarzkopf et al., 2007), results in some recovered acuity after MD (Mitchell, 1991), and helps

improve the recovery after RO (Faulkner et al., 2006). Indeed, our lab has found that BV provides good recovery of visual acuity in MD cats following a range of deprivation lengths throughout the CP (Murphy et al., 2015).

Therefore, binocular interactions are an important consideration for behavioural interventions to yield proper recovery after MD. Pharmacological and behavioural alternatives to treat amblyopia will continue to emerge, but until the molecular mechanisms regulating the successes and failures of each intervention are understood, progress toward effective therapies for humans will be slow.

Biologically inspired human interventions

The success of perceptual learning in animal models have made their way into human trials. Perceptual learning has shown marked improvement in visual abilities of the amblyopic eye (reviewed in Levi and Li, 2009), many of which transfer outside the testing environment (eg. Levi et al., 1997; Li and Levi, 2004; Levi and Polat, 2005). Importantly, these improvements appear to last, demonstrating retained acuity improvements as long as 12 (Polat et al., 2004) or even 18 months after treatment (Zhou et al., 2006). When perceptual learning is combined with patching therapy this improvement is greater still (Li et al., 2005).

Alternative approaches to treating amblyopia as a binocular disorder have emerged, and initially showed great promise for improving treatment outcome (Li et al., 2013; Tsirlin et al., 2015). Special displays permit video game play through the dichoptic presentation of visual stimuli that use active perceptual learning to implement a modern approach to training (reviewed in Hess and Thompson, 2015). These displays re-balance the contrast of an image such that the visual stimulus is matched between each eye, and have transported training opportunities outside the doctor's office into the iPhone and iPad (Hess et al., 2011; Birch et al., 2015; Vedamurthy et al., 2015; Webber et al., 2016). Unfortunately, these techniques were no more effective than a few hours of patching therapy (Holmes et al., 2016; Kelly et al., 2016), and poor outcomes were attributed to low compliance. The recent failure of the BRAVO technique (Gao et al., 2018) has some clinicians questioning binocular treatments for amblyopia (Holmes, 2018). Nevertheless, binocular treatments continue to emerge, and benefits include improved amblyopic eye acuity, but also binocular abilities such as stereoacuity and depth of suppression (Kelly et al., 2018).

1.5 Human development- Challenges and Opportunities

The average age of diagnosis for amblyopia is less than 3 years of age (Birch and Holmes, 2010), and patching therapy remains the number one treatment prescribed for amblyopes. When patching therapy fails to promote recovery, there is no consensus on how to proceed with treatment. This is in part because there is a gap between animal findings of CP plasticity and translating those findings into effective human treatments. Understanding development of human visual cortex, and how it is affected by adverse early life experiences, like amblyopia, is challenging due to the limitations in studying human brain development.

The longstanding view of human visual cortex development is that synaptic maturity is reached in the first few years of life, based on anatomical milestones including synapse counts (Huttenlocher et al., 1982) and development of intra-cortical horizontal connections (Burkhalter et al., 1993). That view has been difficult to reconcile with the protracted development of visual abilities that continue developing well past adulthood and into aging. Just like our understanding of the neural basis of amblyopia, our understanding of development of human visual cortex has progressed dramatically in recent years. Studies by our lab and others have begun to investigate the expression of the same cellular processes that govern animal CP plasticity across the course of human development (Pinto et al., 2010; Williams et al., 2010; Siu et al., 2015; 2017). These studies highlight the variability in early human stages of development and the protracted development of plasticity mechanisms.

The glutamatergic, GABAergic and extra-synaptic environment is involved in regulating susceptibility to early life adversity in animal visual cortex, and major changes in these systems tend to occur during the CP in animal models (Fagioloni et al., 2003; 2004). In our investigations, we have found the timing of some important functional shifts, including those inhibitory mechanisms that initiate the CP, occur precisely as predicted. For example, the shift from immature $\alpha 3$ to mature $\alpha 1$ occurs at the beginning of the visual CP (Pinto et al., 2010). Extra-synaptic brakes on plasticity, such as the increase in intracortical myelin (Siu et al., 2015), and the expression of ubiquitin ligase Ube3A (Williams et al., 2010) both continue developing until the mid-30s. Even more surprisingly, transitions in NMDAR subunit expression from more 2B to more 2A are protracted and extend well beyond 40 years of age (Siu et al., 2017). In fact,

measuring the expression of a set of 4 proteins that mark the presence of synapses (synapsin I, synaptophysin, PSD95 and gephyrin) we were able to align the development of rat visual cortex with the development of human visual cortex (Pinto et al., 2015). This age alignment perfectly identified matching sets of visual milestones between the two species. These major visual milestones in human visual cortex development correspond to a host of anatomical and neurobiological changes (for review Siu & Murphy, 2018).

Aside from the few studies listed here, little effort has been made to synthesize the development of these proteins across the human lifespan. Investigation of the development of multiple synaptic protein systems in human visual cortex, including glutamatergic, GABAergic and extra-synaptic proteins, would undoubtedly provide valuable information for mapping animal models onto human stages of development to improve therapy.

1.6 Summary of my contributions

This thesis presents an analysis of both classic and modern amblyopia treatments, and the effect that these treatments have on synaptic proteins in V1 of an animal model for amblyopia. I also present a data-driven approach to quantifying states of human V1 development using a subset of the synaptic proteome. In chapters 2 and 3 I present two techniques that modernize the study of central visual pathway in the cat animal model for amblyopia. First, I combined traditional neural tracing techniques with modern tissue clearing (Chapter 2), and second, I introduced semi-automated homogenization and filtration steps to the classic fractionation of synaptosomes (Chapter 3). My modern synaptosome approach is amenable for use on animal and human tissues and enables probing tissue multiple times for high-throughput analyses of the synaptic proteome. Next, I designed a modern, high-dimensional analysis workflow that can be used to compare multiple treatment conditions or investigate trends across stages of development (Chapter 4). This analysis workflow includes techniques such as principal component analysis (PCA), t-distributed stochastic neighbour embedding (tSNE) analysis, and sparse clustering (Sparcl). Using this workflow, I identified unique treatment effects on protein expression patterns after RO, BD and BV in cat V1 (Chapter 5). I also used this workflow to identify 6 overlapping stages of human visual cortex development across 23 synaptic proteins and multiple plasticity mechanisms (Chapter 6). These innovations in my approach have immense utility for clinical

neuroscience as amblyopia research progress toward newer treatments. This thesis also highlights the importance of understanding development from a data-driven perspective while shifting our understanding of the human visual cortical development away from discrete developmental stages toward overlapping states of plasticity.

Preamble Chapter 2

Amblyopia has the greatest effect on acuity in the central visual field of humans and animals. Even after the original deficits are corrected (e.g. cataract), impaired acuity persists. The changes following amblyopia are not restricted to the optics of the eye, and are found all along the central visual pathway. Indeed, the anatomical effects of early MD in animal models range from shrunken soma size in the lateral geniculate nucleus of the thalamus (Movshon, 1976b), to shrunken arbors of axons that terminate in layer IV of the visual cortex (Antonini et al., 1996). The expansion of afferents serving the non-deprived eye is perhaps the most well studied anatomical effect of MD. This effect is most easily viewed when visual cortex is unfolded and flattened because this presents ocular dominance columns in a single, unbroken sheet of cortical tissue.

Early studies of visual cortex anatomy traced the pattern of connections from retina to V1 using anterograde tracers (Grafstein 1971; Wiesel et al., 1974; Anderson et al., 1988). Since then, many different labels have been used to study this pattern of connections, but all suffer from the same curse; ultimately tissues must be sectioned to investigate fine details like axonal arborization or the spatial arrangement of ocular dominance columns. Despite costly advancements in microscopes that improve cellular resolution and imaging depth, imaging multiple tissue sections remains quite laborious, is notoriously difficult, and is prone to errors aligning adjacent sections. Because of these limitations, tissue clearing to remove optical obstruction and increase light penetration into tissue has seen a resurgence of interest (Richardson & Lichtman, 2015).

These techniques might prove useful for studying the arrangement of ocular dominance in the visual cortex of animal models for amblyopia. It remains to be seen whether these modern tissue clearing techniques are compatible with classical anterograde tracers. Furthermore, many tissue clearing papers still resort to tissue sectioning in order to expedite the clearing process. It seems logical that using common techniques like unfolding and flattening the visual cortex (Anderson et al., 1988) that have proven useful in originally identifying ocular dominance columns (Murphy et al., 1995) could benefit tissue clearing. The question remained whether

cleared tissue would maintain modern fluorescent tracers, and if these could be used in conjunction with tissue unfolding and flattening.

To test this we combined eye injection with fluorescent tracers neural (WGA CF dyes®), cortical unfolding and flattening, and the modern Passive clarity technique (PACT), to label and image the central visual pathway of the cat. This approach would be beneficial for examining macroscopic patterns in cleared tissue in MD animals to better understand the changes that take place during recovery from amblyopia.

Preamble Chapter 3

The molecular mechanisms of synaptic plasticity that are affected by early monocular deprivation (e.g., Beston et al., 2010), are likely the same mechanisms that recover following treatment for amblyopia. These include NMDAR and GABA_AR receptor subunits, which present in very low abundance in synapses of the visual cortex. It is therefore difficult to accurately quantify the expression of these subunits in our tissue samples. One technique to address this issue is a tissue preparation that enriches tissue samples for synaptic entities, called synaptosomes (Quinlan et al., 1999). These tissue preparations are based on the premise that receptor proteins are embedded in cell membranes, and thus have greater weight than other synaptic entities. Therefore, there are a variety of techniques to procure synaptosomes, and some are more effective than others.

The cortical tissue examined in our lab is our most precious resource. Whether these samples come from frozen human visual cortex or animal samples obtained after complicated rearing paradigms, the tissue cannot be used frivolously. I therefore sought to create a technique that maximizes experimenter resources. I improved on the crude fractionation approach developed by (Hollingsworth et al., 1985), and used in my lab for many years (Pinto et al., 2010; Beston et al., 2010; Williams et al., 2010). My goals were to decrease the amount of time spent performing the tissue preparation while increasing reliability in the procedure and increase sample yield and protein enrichment.

Preamble Chapter 4

When investigating normal development or the effect of rearing conditions on plasticity mechanisms, the common approach is to measure only a few variables in a single experiment. However, plasticity mechanisms rarely change in isolation, and typically these changes affect the entire system. Standard analyses such as ANOVA and t-tests report significant differences among groups, but begin to fail as the number of comparisons increases. This is because it gets exponentially more difficult to keep track of the myriad of changes after analyzing only a few variables, and it is even more difficult to make sense of the effect of multiple changes on a system.

This is not a new challenge faced by systems neuroscientists, and just as the methods for acquiring large amounts of data have improved (eg. genetic assays, large scale western blot assays), so too have data analysis techniques to make sense of these large data sets. In order to make large data sets easier to handle, a common approach is to reduce the number of variables. There are two approaches to variable reduction. The first approach is to select only the most important variables and ignore the remaining variables that do not pass a threshold criteria (feature selection). The second approach is to transform the data set into a new set of features based on the high-dimensional relationships across multiple variables (feature transformation). In fact, it is more common to perform some combination of these two approaches. After the number of variables have been reduced, the next step is to group similar samples together based on the variables within a group.

There are many different techniques to consider for feature selection, feature transformation, and clustering of data. Most of these techniques are typically used to explore genetic data in animals and humans so that subsequent experiments can be performed after the most important features have been identified. These techniques are rarely used in neuroscience for analyzing the entire system response to experimental manipulation or to track changes across development. In Chapters 5 of this thesis I present an analysis of 5 different rearing conditions in cats, measuring expression of 7 different synaptic proteins across 3 cortical areas. In chapter 6 of this thesis I present an analysis of human development across 31 individuals, measuring expression of 23 different synaptic proteins. Both of these investigations of plasticity

mechanisms in visual cortex were not amenable to standard tests of significance, and when considering high-dimensional analyses, I was faced with many options to consider for feature selection, feature transformation and sample clustering. This chapter presents the considerations I employed in the course of creating my analysis workflow that was used in Chapters 5 and 6.

Preamble Chapter 5

This chapter is the successor to Beston et al., 2010, which quantified changes across a panel of glutamatergic and GABAergic proteins in cat visual cortex across normal development and in response to various lengths of monocular deprivation. This project was motivated by the alarming lack of information surrounding the molecular changes in glutamatergic or GABAergic mechanisms following classic treatments for amblyopia like reverse occlusion. The timeliness of this chapter comes from a spike in interest surrounding modern amblyopia treatments, including dark exposure and binocular experience. Dark exposure was implemented in my study by binocularly depriving the animals of visual input through bilateral lid suture, while binocular experience was reinstated by simply removing the sutures from the initially MD eye.

The greatest innovation that I contributed in this chapter was my implementation of modern statistical analyses to process the wealth of data that was produced (see Chapter 4). Across just 9 of the animals included in the bulk of the analyses (5wk Normal, 5wk MD, reverse occlusion, binocular deprivation and binocular vision), measuring the 7 proteins across three cortical areas caused the data to grow exponentially to include ~1,510 data points. In order to identify system changes, I used principal component analysis (PCA) to convert protein expression into biologically relevant indices representing synaptic function (feature transformation). Then I used the popular dimensionality reduction technique t-stochastic neighbour embedding (tSNE) to reduce the data to two dimensions. Finally, using hierarchical clustering I identified 6 clusters that parse treatment effects into 13 groups. By correlating system changes across all biologically relevant indices I identified those treatments that reinstated the entire system closest to a 5 week normal animal since this represented the peak of the critical period. My creation of plasticity phenotypes enabled visualization, at a glance, of the state of plasticity for each treatment condition, which simplified comparisons with normal development.

Preamble Chapter 6

This chapter complements the characterization of a collection of GABAergic (Pinto et al., 2010) and glutamatergic (Siu et al., 2017) proteins expression in human V1 across development. The motivation for this chapter was to map the approach developed and implemented in Chapters 4 and 5 onto normal human development in an attempt to better understand the changes in synaptic plasticity mechanisms across development.

Investigation of human development takes one of two approaches to classifying data. The canonical theory of human development proceeds according to successive stages, first proposed by cognitive psychologists like Jean Piaget and Erik Erikson. These theories were based on the developmental progression along a series of behavioural milestones. Approaches like this have been used in mapping development of visual sensitive periods based on the appearance of visual abilities (Lewis & Maurer, 2005). Conversely, advancements in EEG and fMRI technologies allow repeated investigations of in-vivo structural and functional cortex, which has blurred the lines between stages and instead proposes continuous development. Either of these *a priori* assumptions about the development of human visual cortex hinders analysis of the true nature of human development because they restrict interpretations of the data.

As the number of proteins analyzed by our lab has grown past 20 synaptic and non-neuronal proteins, it has become more and more challenging to reconcile the different courses of protein development with one another, especially when attempting to infer function from protein expression. Therefore I turned to modern, high-dimensional data analysis techniques to take a data-driven approach to investigating the course of human development. Using this approach I was able to identify the proteins that set the course for development define 6 states of human V1 development. Approaches such as this are the first step toward truly effective translation of animal findings to humans. By taking a systems-level approach to understanding the series of protein changes across the human lifespan we can synthesize the ever-growing repository of data that exists for experience-dependent changes in visual cortex and design effective, biologically inspired therapies for amblyopia.

Chapter 2. Anatomical labeling of the central visual pathway

Abstract

Background: The pattern of connections from the retina to the visual cortex are typically studied by injecting anterograde tracers to the eye, and physically sectioning tissues along the central visual pathway. Super bright fluorescent dyes conjugated to lectins have recently been used to study the central visual pathway, but have failed to label the primary visual cortex. The creation of near-infrared, small, bright, water-soluble fluorescent probes conjugated to wheat-germ agglutinin (WGA CF® dyes (Biotium Inc)) are compatible with widely available laboratory scanners. It was unknown whether these dyes would label all stages of the central visual pathway, or if they could be easily visualized after physical tissue sectioning or optical tissue clearing.

New Method: We implemented a simple and reliable protocol that combines eye injection of a new anterograde tracer (WGA CF® dyes), cortical unfolding and flattening, physical tissue sectioning and PACT optical tissue clearing (Yang et al. 2014) to visualize the central visual pathway in the cat.

Results: Following an eye injection with WGA CF® dyes we found label in retinal ganglion cells, anterograde transport of label to the LGN and superior colliculus. Importantly, we provide evidence of bright label remained in the cleared LGN and SC, as well as trace amounts of transneuronal transport to V1 in cleared cortical tissue.

Comparison with existing methods: The bright WGA CF® dye labeling was easily imaged in cat cortex using both the low magnification fluorescent scanner and confocal microscopy. Furthermore, resecting tissues and using the unfolded and flattened cortex reduced the clearing time for PACT from weeks (whole rodent brains) to just a few days (unfolded rodent cortex).

Conclusions: This modern protocol labels the central visual pathway quickly, plus the WGA CF® dye remains in cleared tissues, and is compatible with cutting-edge techniques (super-resolution). These advantages make this protocol ideal for studies about development and plasticity of the visual system that span questions from macro- to nano-scales.

2.1 Introduction

The anatomical features of the central visual pathway are readily visualized after an eye injection of an anterograde tracer, including subcortical projections to the LGN and SC, and geniculocortical projections when the tracer is transported transneuronally (Mesulam and Mufson 1980; Itaya and Van Hoesen 1982; Williams and Chalupa 1982; Anderson et al. 1988). Wheat-germ agglutinin (WGA) conjugated with horseradish peroxidase (HRP) has been used to label the visual pathway because WGA is selectively taken up by neurons and packaged into vesicles for active anterograde and transneuronal transport (Gonatas 1979; Itaya and Van Hoesen 1982). For example, injection of WGA-HRP in the posterior chamber of the eye labels the details of the retinogeniculate projection and the stripe-like pattern of eye-specific inputs to the visual cortex of the cat (Anderson et al. 1988). Although WGA-HRP labels fine details, only one eye's connections can be labeled making it hard to compare the arrangement of ipsilateral and contralateral eye projections in the same structure.

Recent studies have taken advantage of bright, fade resistant, multi-color fluorescent dyes conjugated with WGA (e.g., WGA-Alexa Fluor® dyes) to label the projections from the eye to the LGN or SC (Kuwajima et al. 2013; Renier et al. 2014) but have not observed label in the visual cortex. Furthermore, the dyes used in those studies were from the visible spectrum because near-infrared (NIR) Alexa Fluor® dyes need an additional negative charge to improve solubility and quantum yield, but that charge leads to higher non-specific binding. A different class of fluorescent dyes based on rhodamine chemistry, CF® dyes (Biotium Inc), has been developed and includes NIR dyes that are small, water-soluble, bright and photostable. Furthermore, the NIR dyes are readily imaged with standard laboratory scanners (e.g., LI-COR Odyssey) that can quickly scan a large number of anatomical slides at one time.

Here we describe a protocol that uses eye injection with NIR WGA CF® dyes to label the central visual pathway and a laboratory NIR scanner to visualize the pattern of labeling in the LGN, SC and visual cortex. Also, we show that the WGA CF® dye can be combined with a passive tissue-clearing technique (PACT - Yang et al. 2014) to take advantage of the NIR dyes for visualizing labeled pathways in full thickness tissue samples from the LGN, SC or visual cortex.

2.2 Methods

2.2.1 Materials and Equipment List

Reagents

PPC Vet Isoflurane (1-chloro-2,2,2-trifluoroethyl difluoro-methyl ether)

WGA CF® dye: 5% Fluorescent Wheat Germ Agglutinin (WGA)

WGA CF®680 Wheat Germ Agglutinin (Biotium, CA, USA, #29029)

WGA CF®770 Wheat Germ Agglutinin (Biotium, CA, USA, #29029)

1M PBS

Fixative: 2% Paraformaldehyde (PFA)

16% PFA (Electron Microscopy Sciences, PA, USA, #15710)

1M PBS

Acrylamide Hydrogel Solution: 4% Acrylamide with 0.25% photoinitiator

40% Acrylamide Solution (BIORAD, ON, CAN, #1610140)

Photoinitiator 2,20 -Azobis[2-(2-imidazolin-2-yl) propane]dihydrochloride
(Wako Chemicals, USA, #VA-044)

1M PBS

Clearing Solution: 8% SDS Detergent

Sodium dodecyl Sulfate (SDS) (BIOSHOP, ON, CAN, #SDS001)

0.1M PBS

NaOH (as required to adjust pH to 7.5)

Sorbitol-based Refractive Index Matching Solution (sRIMS (Yang et al. 2014)):

70% sorbitol (w/v) with 0.01% sodium azide

D-Sorbitol (Sigma Aldrich, MO, USA, #S1876)

Sodium Azide (Sigma Aldrich, MO, USA, #S2002)

0.02 M PBS

NaOH (as required to adjust pH to 7.5)

PBS-T: PBS with 0.1% TritonX

Triton™X-100 (Sigma Aldrich, MO, USA, X100)

Tools

50µL Microsyringe (Hamilton Co., #1705)
BD Syringe with Luer Lock (1ml)
BD Syringe with Luer Lock (3ml)
BD Needle Tip (21G)
Razor Blade (#22)
Beaker (500ml)
Large Petri Dish
Cotton Swabs
Glass Slides (4"x3" 2 per sample for flattening)
Slide spacers (can use broken glass slide pieces; 1mm thick)
Binder Clips (1-1/4"; 2 per sample)
Extra large plastic vial (must accommodate width of glass slides)
Glass Mason Jars
Fine paint brushes
PVDF-P Immobilon Membranes (Sigma Aldrich, MO, USA, #IPVH00010)
Fluoroshield Mounting Medium (Sigma Aldrich, MO, USA, #F6182-20ML)
Imaging Chamber
 Rubber Gasket Material (1/16" thick)
 Ultra Blue ® Silicone Gasket Maker (Permatex)
 Glass slides (4"x3"; x2)
 Freezing Mounting Medium (TissueTek, Ted Pella Inc, CA, USA, #27209)

Equipment

ScanMaker i900 flatbed scanner (Microtek, CA, USA)
Odyssey Infrared Scanner (LiCor Biosciences, Lincoln, NE)
Zeiss Confocal 680

2.2.2 Protocol

1. Animals

We used two adult cats to develop the protocol for using eye injections with WGA CF® dyes to label the central visual pathway (2.2.ii) and adult rats (n=2 cortical hemispheres) to test the tissue clearing on unfolded and flattened cortical tissue. All procedures were approved by McMaster Animal Research Ethics Board.

2. WGA Injection (0.5 Hr per injection)

The WGA CF® dye was injected into the posterior chamber of the cat eye (Figure 1A). One cat received an injection into one eye, and the tissue was cleared using the modified PACT protocol (Yang et al. 2014) described in sections 2.2.vi-2.2.vii, while the other cat had a different WGA CF® dye injected into each eye and the tissue was sectioned (Fig. 1).

Before starting surgery, 25µl of 5% WGA CF® dye was loaded into a 50µl Hamilton microsyringe. It is helpful to pre-wet the Hamilton syringe to facilitate dye loading by removing the plunger, dipping the end of the plunger into distilled water, putting it back into the syringe, and moving it up and down a few times to improve suction for loading 25µl. We ensured that 25µl was reliably loaded by testing the calibration of the syringe beforehand.

We injected 25µl of 5% WGA CF® dye (WGA CF® 680R or WGA CF® 770) in PBS into the posterior chamber of the cat eye using the same steps as previous studies (Anderson et al. 1988; Murphy et al. 1995). Each eye received two injections, the first one on day 1 and the second one on day 3 of the protocol. Briefly, gaseous anesthetic (isoflurane, 1.5–5%, in oxygen) was used to induce and maintain anesthesia. The eye was stabilized and rotated nasally by placing a temporary suture through the conjunctiva at the lateral edge of the eye-opening, clipping the two ends of the suture with a hemostat, and gently pulling the hemostat nasally to access the sclera. Next, the sclera was exposed by blunt dissection of the conjunctiva to visualize the whiter band of the ora serrata, just anterior to the retina. A guide hole was made onto the ora serrata with a 26 gauge needle by rotating the needle and applying gentle pressure. A drop or two of vitreous will come out the end of the needle. The guide needle was removed, and the Hamilton microsyringe needle was inserted ~5mm into the hole, pointing towards the back of the eye and angled away from the lens. The WGA CF® dye was injected slowly over about 4 minutes, using

a series of 5 μ l steps, and waiting for about 45 seconds between steps, including waiting 45 seconds after the last step before removing the needle. The needle remained in the eye for the full duration of the injection. The eye injection was repeated two days later, inserting the Hamilton microsyringe through the existing guide hole. Animals survived for two more days and then were perfused on day 5 of the protocol.

3. Perfusion and Cortical Flattening (5.5 Hrs)

All animals were euthanized with Euthanyl (120 mg/kg rat IP, 165 mg/kg cat IV) and perfused transcardially with 0.1M PBS (4°C) until circulating fluid was clear (~4 mins). The brain was removed from the skull, and the cerebral hemispheres were resected and placed in 0.1M PBS (4°C) before flattening. The rat cortex was unfolded and flattened by removing the basal ganglia from under the cortex, making 3 cuts to relieve the intrinsic curvature (1 anterior and 2 posterior), then flattening the sheet of cortex by sandwiching it between 2 glass slides with 1mm glass spacers placed at either end (Olavarria and Van Sluyters 1985) (Figure 1C).

The visual cortex from the cat was unfolded and flattened using procedures that have been described previously (Anderson et al. 1988; Murphy et al. 1995; Olavarria and Van Sluyters 2014). First, the white matter was wiped away using cotton swabs wetted with PBS. Next two cuts were made in the sheet of cortical tissue, a medial and a lateral cut, to relieve the intrinsic curvature of the cortex (Figure 1C asterisks). Because we were focusing on the visual cortex, the frontal cortex was trimmed (Figure 1C-dashed lines), and the visual cortex was gently flattened by placing it between two large glass slides with 1mm spacers at either end (Anderson et al. 1988) (Figure 1D). The slides and flattened cortex were held together with two binder clips, and placed in cold fixative for 30 minutes (2% PFA, 25°C). Also, tissue samples containing the superior colliculus and lateral geniculate nuclei (LGN) were removed from the perfused cat brains. The colliculi were gently flattened between 2 glass slides while the LGNs were left free floating in 2% PFA (4°C). After 30 minutes in 2% PFA, flattened tissues were floated off the slides, and left free-floating in cold 2% PFA (4°C) for 5 hrs. Tissue that was going to be sectioned was placed in 30% sucrose overnight (4°C) which was long enough for the samples to sink and then be sectioned that following day.

4. Tissue Sectioning and Imaging

Tissue samples from the cat injected with two WGA CF[©] dyes were sectioned on a freezing microtome at a thickness of 50 μ m (Figure 1E). The cortex and superior colliculus were sectioned tangential to the surface while the LGN was sectioned coronally. All sectioned samples were collected in PBS, mounted onto subbed slides and coverslipped using fluoroshield mounting medium (Sigma-Aldrich, MO, USA) (Figure 1F). Once the mounting medium was dry the slides were on the LI-COR Odyssey Infrared Scanner (LI-COR Biosciences; Lincoln, NE) with the coverslip side down and scanned at the maximum resolution (21 μ m/pixel) and the laser focus was offset to 0.1mm to account for the thickness of the coverslip. All slides from a site were scanned at the same time and both the red (700nm) and green (800nm) laser channels scanned. The scan intensity was kept at the default settings.

5. Retinal Whole Mounts and Imaging (0.5 Hr)

Whole mounts of the cat retinae were done to assess if the retinal ganglion cells were labeled. The anterior chamber of the eye, including cornea, iris, and lens, was removed, the vitreous humor was wiped out, and four cuts were made through the full thickness of the sclera and retina to allow the tissue to lie flat. A few drops of PBS were applied to keep the retina wet, and the retina was gently separated from the pigment epithelium using fine paint brushes, then a cut was made through the back of the optic disk to free the retina and float it out of the eyecup. The retinae were floated onto a hydrophobic membrane (e.g., PVDF-P Immobilon), and covered with a second piece of the membrane. That sandwich was placed between two glass slides and retinae were flattened using the weight of the top slide. Slides were left for 15 minutes in 2% PFA. The flattened retinae were rinsed, free-floating, in cold PBS (4°C) for 30 minutes. Then the retinae were mounted onto subbed slides, allowed to air dry, and coverslipped with Fluoroshield mounting medium. Finally, the retinal whole mounts were imaged using the Odyssey Infrared Scanner (LI-COR Biosciences; Lincoln, NE).

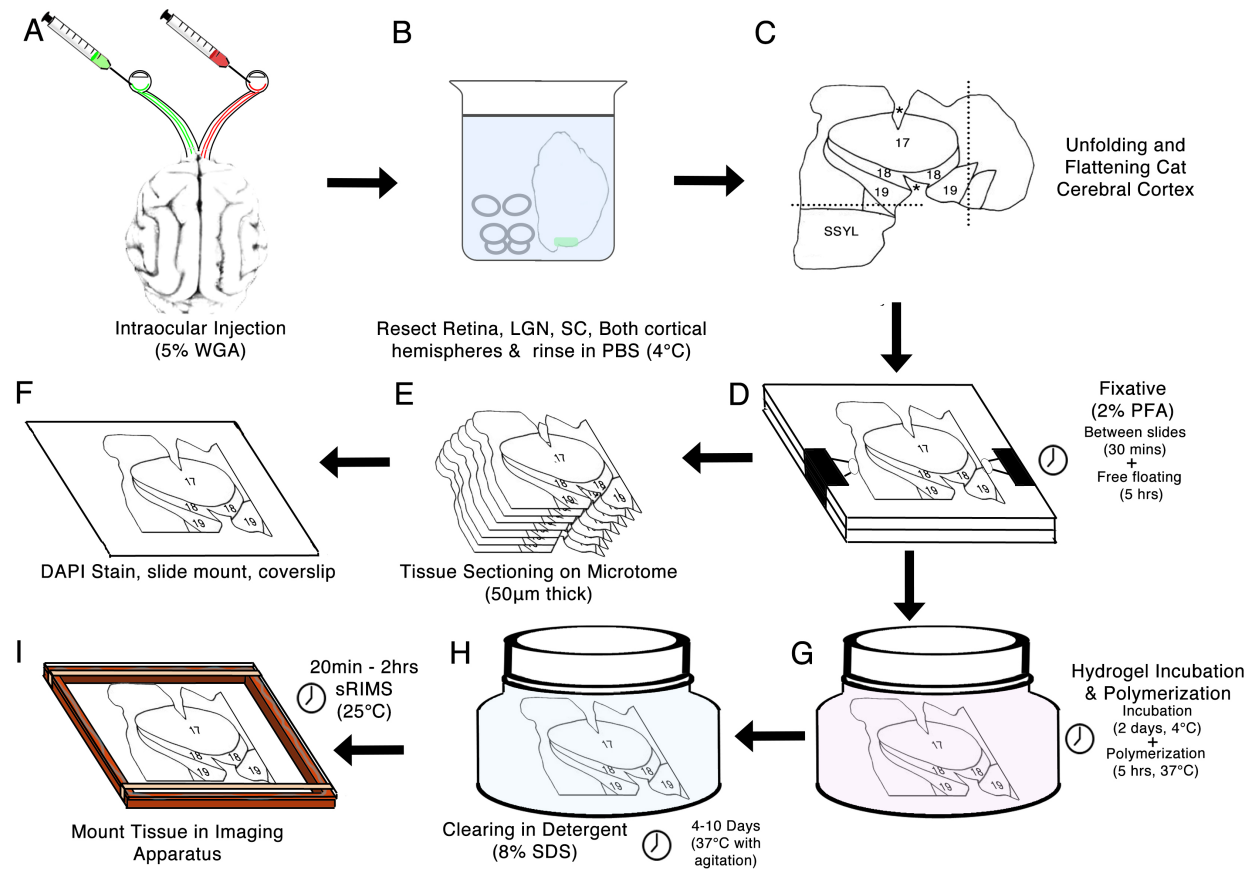


Figure 1. Schematic overview of the steps from eye injection to imaging the cleared unfolded and flattened cortex.

(A) Either one (red) or both (red right, green left) cat eyes were injected with fluorescent 5% WGA-CF™ dye (25µl) on days 1 and 3. (B) Resected LGN and Colliculus (cartoon ovals) as well as the cortical hemispheres were rinsed in cool PBS before unfolding cortex (C). Unfolding and flattening cat cortex with visual areas 17, 18, 19 and SSYL (suprasylvian sulcus) indicated. Two cuts were made (asterisks) to relieve the intrinsic curvature so the cortex can be flattened and extra tissue outside V1 (dashed lines) was cut away. (D) Cortical hemispheres and LGN were fixed in 2%PFA while being pressed between two glass slides, assembled with 1mm spacers and held together by clips. Colliculi were free floated in fixative. Flattened tissues were removed from glass slides and left to free float in PFA for an additional 5 hrs at 4°C. The tissue from the cat that received injections of two different dyes, one in each eye, progressed to tissue sectioning (E,F). The tissue from the cat that received a single injection in a single eye progressed to tissue clearing (G-I). (E) Tissues were sectioned on a freezing microtome at 50µm thickness before (F) applying mounting medium, slide-mounting and coverslipping. (G) Flattened cortex was placed in hydrogel to incubate for 2 days at 4°C, and hydrogel polymerized by placing in 37°C for 5 hours. (H) Clearing took place in SDS 8% at 37°C over the course of 4-10 days, depending on the size of cortical sheet being cleared. (I) After clearing and PBS-T washes (not pictured), samples incubated in sRIMS for 20 min - 2 hrs (until transparent). Tissues were then transferred to imaging apparatus (see Methods) for scanning with an Odyssey Infrared Scanner (Li-cor Biosciences; Lincoln, NE).

6. Tissue Clearing -- Hydrogel Incubation and Polymerization (2 Days + 5 Hrs)

The clearing protocol was adapted from the passive clarity technique (PACT) developed by Yang et al., 2014. Post-fixed samples were transferred to glass jars containing acrylamide hydrogel solution and protected from light to preserve tracer fluorescence. Samples were left to incubate in cool acrylamide hydrogel solution for two days at 4°C to ensure sufficient tissue penetration. Tissue can incubate for a few hours longer, but the cool temperature is imperative to

avoid premature polymerization. Next, all oxygen must be displaced from the containers to allow sufficient polymerization of the hydrogel monomer solution. Instead of degassing the samples before polymerization, as in the original PACT protocol describes (Yang et al. 2014), we displaced oxygen by overfilling the glass container with hydrogel solution, similar to the use of gelatin capsules for the polymerization of the resin during tissue embedding (e.g., Micheva and Smith 2007). Polymerization of the hydrogel monomer solution was done by transferring the filled tissue containers to a hot water bath (37°C, 5 hrs, Figure 1G). Polymers were drained from glass containers, and tissues were briefly rinsed in PBS-T (5 min) to remove the visible polymerized solution.

7. Tissue Clearing -- Detergent steps (4-14 days, depending on tissue)

Tissue was submerged in clearing solution and transferred to a warm water-bath (37°C, slight agitation, Figure 1H). The clearing solution was refreshed every day until samples were transparent (4 days for rat cortex, ten days for cat cortex). Tissue should be inspected daily to avoid over-clearing, which can damage the tissue. After tissue clearing, excess SDS micelles were removed by rinsing samples in PBS-T over the course of one day (2-3 wash changes).

8. Tissue Clearing -- Analysis of Cortical Clearing Rate

To assess the uniformity and rate of clearing for the cortical sheet we started with unfolded rat cortex and scanned the samples every 4-8 hours to assess the optical density (OD) (Fig. 2). A chamber was made to hold the flattened cortex in the imaging medium (e.g. sRIMS). The chamber was made out of a 1/16" thick rubber gasket (e.g. Gasket Material, Moen, M6158, Oakville, ON) adhered to a glass slide with Ultra Blue® Silicone Gasket Maker (Figure 1F). To avoid interrupting the clearing process, the flattened cortical sheet was placed into the imaging chamber filled with SDS (8%) and sealed by outlining the top surface of the gasket with a temporary sealant (eg. TissueTek mounting medium, Ted Pella Inc, CA, USA), a second glass slide gently placed on top to serve as the coverslip. A stepped neutral density filter was scanned with the tissue on a flatbed scanner (ScanMaker i900, Microtek, CA, USA) using VueScan imaging software (Hamrick Software, FL, USA) version 9.0.96. All images were converted into grey levels using the green color channel in Photoshop (Adobe, Inc., San Jose, CA). Mean gray values were obtained for each step of the neutral density filter using the measure tool, and those

values were used to create optical density calibration curves. The cortices were aligned in register to facilitate comparisons between clearing time points. Alignments were done using a template of the flattened rat cortex that outlined the frontal, somatosensory and visual areas. The mean gray values were taken for each area and aligned with the optical density calibration curve to determine the mean optical density of each regions

9. Tissue Clearing -- Imaging Tissue (1.5-3 Hrs per piece)

Before imaging the cleared tissue, each section was incubated in sorbitol-based refractive index matching solution (sRIMS) until transparent (30 min-2 hrs, depending on tissue size). Tissues can be incubated in sRIMS for a few hours after transparency is achieved, enabling more extended imaging sessions, but storage in sRIMS is not advised as a precipitate will form inside the tissue. If short-term storage is required, we recommend storing samples at room temperature in PBS. The tissue samples were individually loaded into the imaging chamber filled with sRIMS and sealed as described previously. To visualize the fluorescent WGA CF™ dye at low magnification, the tissue sample was scanned in the imaging chamber on the flatbed of the Odyssey Infrared Scanner (LI-COR Biosciences; Lincoln, NE). Cleared tissue were imaged using similar parameters as the sectioned tissue (2.2.iv), only the offset was adjusted to accommodate thickness of the slides (1mm) and cleared tissue (~0.5mm). To visualize the fluorescent WGA CF™ dye at high magnification, whole cleared LGN was transferred to sRIMS and imaged using the Zeiss 680 confocal imager and the CLARITY imaging objective.

10. Analysis of Label Intensity

All samples were analyzed using Adobe Photoshop and ImageJ (Schindelin et al. 2012). Images were converted to greyscale to measure the intensity of label and analyzed using the 3D surface plot plugin. For analyzing label intensity in ROIs, surface plots were created for each channel. Sometimes images were slightly shifted in the x-y plane between 700nm and 800nm channels, so minor transformations were made in Adobe Photoshop, and aligned using blood vessels.

2.3 Results

2.3.1 WGA CF® Dye Eye Injection Labels Retinal Ganglion Cells

To determine the efficacy of WGA CF® dye as a tracer for visualizing the visual pathway, we injected the dye into the posterior chamber of the cat eye and evaluated the appearance of tracer in multiple structures from the retina to visual cortex. First, we made a whole mount of each cat retina and scanned them using the appropriate wavelength on the LI-COR Odyssey NIR scanner. Those rapid, low magnification scans showed a pattern of labeling indicative of labeled retinal ganglion cells (Figure 2). The labeled cells were apparent across each retina, with the area centralis appearing brighter than the surrounding regions in both cases. Even areas of the retina with fainter labeling had a clear mosaic pattern of fluorescently-labeled cells (Figure 2 insets), the size and arrangement of which were in agreement with the previously documented density of RGC in the cat retina (Schall and Leventhal 1987). Thus, WGA CF® dye injected into the posterior chamber of the cat eye was taken up by retinal ganglion cells.

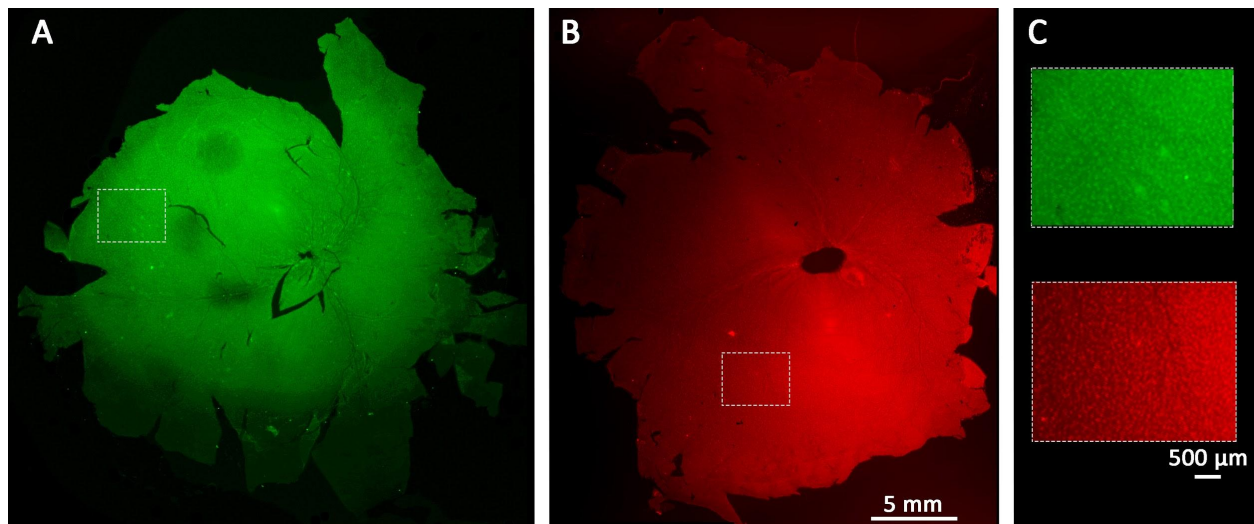


Figure 2. WGA CF® dye labeling in flat-mounted cat retina.

Low magnification fluorescent scans of flat-mounted cat retina following intra-vitreous injections of a green (A) and red (B) WGA CF® dye. Label is visible across the left (A, green) and right (B, red) retinæ. Throughout the retina there is a hexagonal mosaic pattern of labeled retinal ganglion cells (inset). Scale bars for A,B= 5mm, for regions of interest in C =500μm.

2.3.2 Rapid Low Magnification Imaging of Anterogradely Transported WGA CF® Dye to the LGN and SC

WGA CF® Dye Labeling of LGN Features and the Medial Interlaminar Nucleus

To identify the pattern of labeling in the LGN, we imaged the sectioned tissue in the animal injected with a different dye into each eye. The large scan area of the LI-COR Odyssey (LI-COR Biosciences; Lincoln, NE) enabled all of the LGN sections to be imaged at once. That rapid and simultaneous image acquisition eliminated variation that can occur after multiple separate scans and improved consistency during batch processing of images.

The pattern of labeling from the left (Figure 3A) and right eye injections (Figure 3B) throughout the anterior (top) to posterior (bottom) extent of the LGN is shown in Figure 3. LGN laminae were identified in sectioned tissue by the labeling pattern from the ipsilateral (uncrossed) versus contralateral (crossed) eye. Ipsilateral fibers appeared to be slightly darker than contralateral fibers in both hemispheres, and that intensity seemed slightly darker laterally. The laminae of cat LGN A, A1, and C are easily distinguished as early as 300 μ m A-P and remain well-defined until 1400 μ m A-P. The C laminae (C, C1, and C2) were most distinct at ~1000 μ m A-P as well-defined, alternating layers in the merged image (Figure 3C). A band of a vertically oriented label was also present from 650 μ m to 1400 μ m A-P, representing the medial interlaminar nucleus (MIN).

The LGN labeling was shown for a single section to illustrate the fine details that were apparent with the WGA CF® dye (Figure 4). The segregated pattern matched previous observations of LGN laminae (Anderson et al., 1988; Polley and Guillery 1980). Importantly, scanned images to reveal retinal inputs from both eyes were taken of the same section at the same time. Studying both inputs in the same section removed the need to react adjacent sections for different tracers (e.g., H3 proline versus HRP) and instead allowed visualization of inputs from both eyes in all sections, thereby eliminating waste tissue and effectively doubling tissue utility.

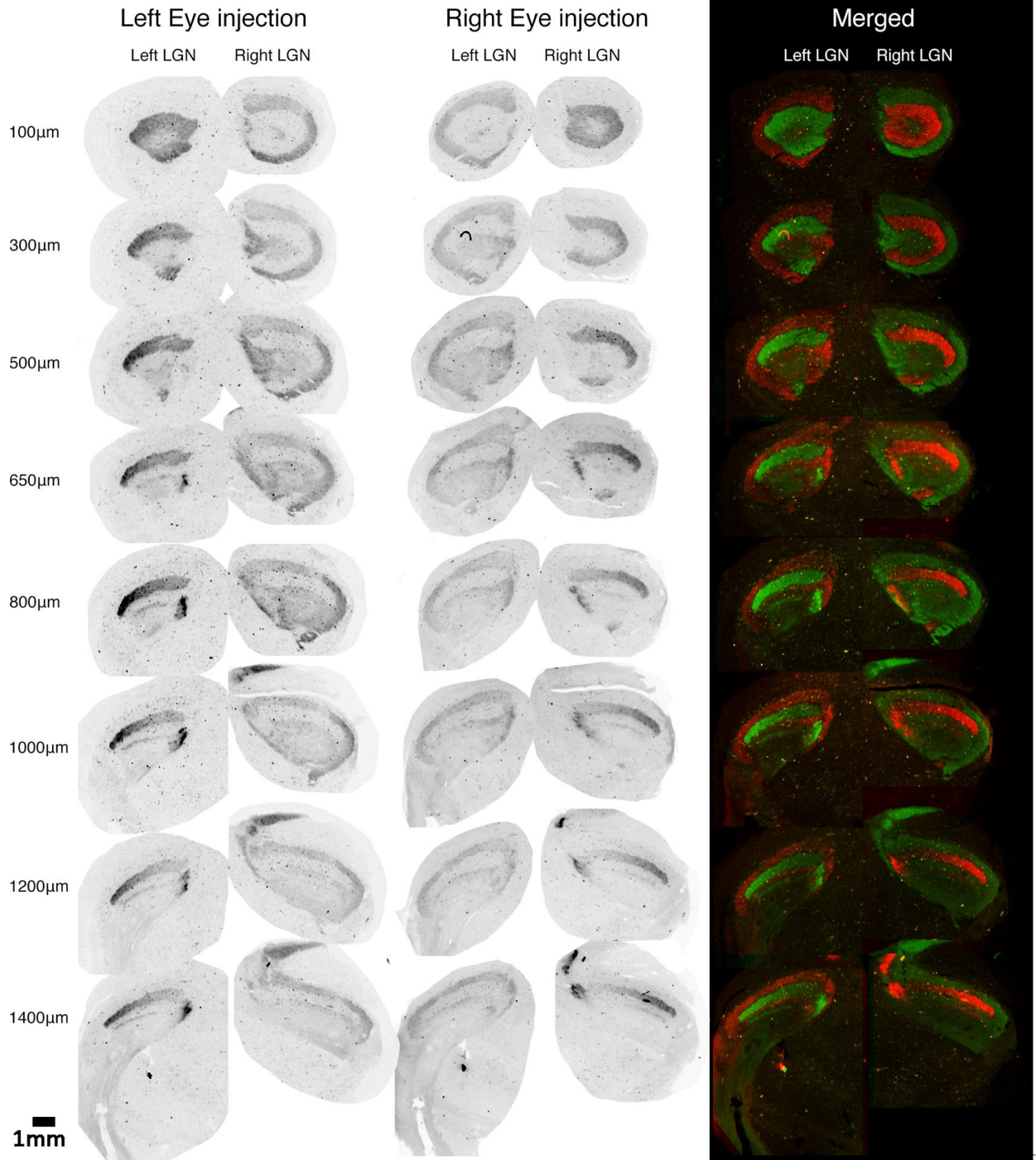


Figure 3. WGA CF® dye labeling in LGN coronal series of sectioned tissue.

Tissue was sectioned coronally and anterior tissue are at the top of the figure, posterior at the bottom and the section depth of the tissue section is presented on the left (μm). Presented sections are $\sim 200 \mu\text{m}$ apart. Low magnification fluorescent scans of the cat LGN sectioned showing label from an injection into the left eye (A) or right eye (B), and the merged (C) images of left (green) and right (red) eye injections. Fluorescent scans for the left eye injection were imaged using 800 nm light, and right eye injection using 700 nm light. Merged images were pseudo-coloured (C) and minor adjustments were made to align channels using blood vessels. Importantly, scans were taken in the same section, not adjacent sections, to reveal truly interleaved layers. Scale bar for all sections is 1mm.

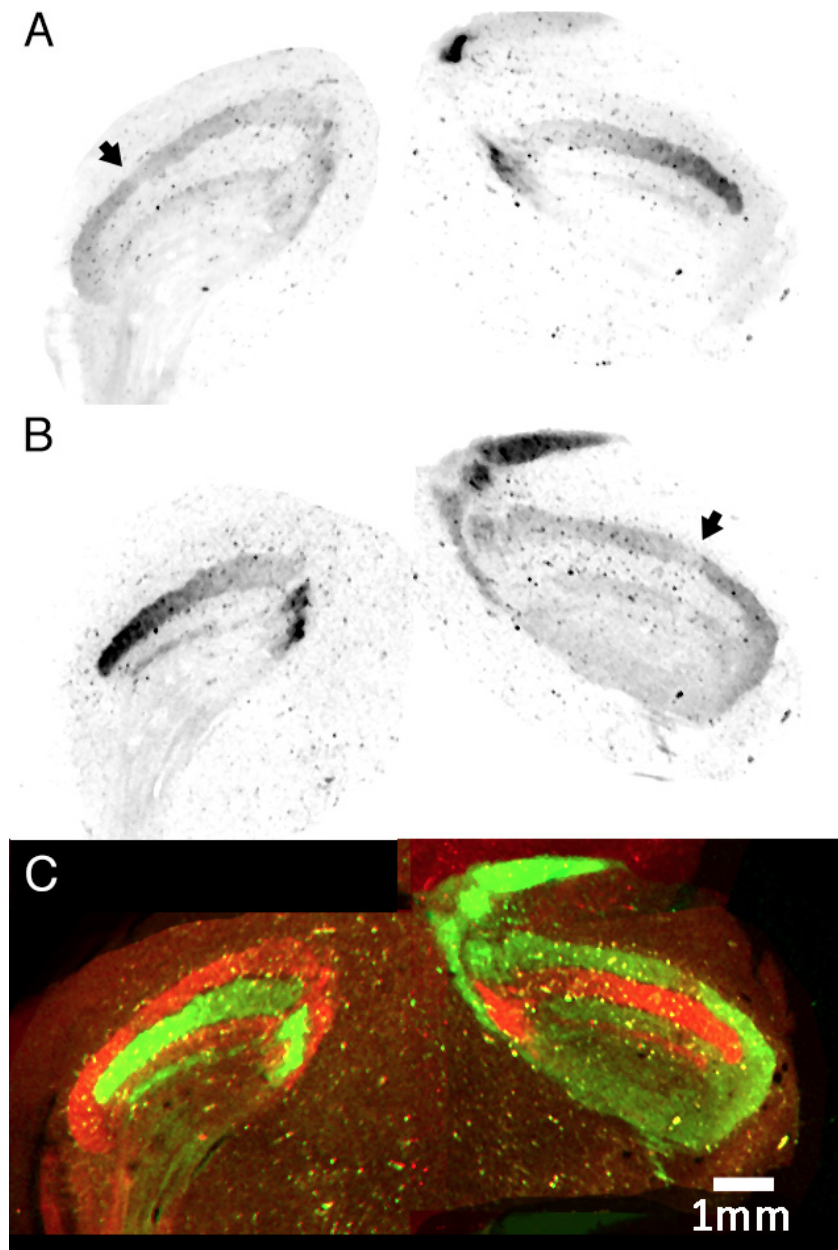


Figure 4. WGA CF® dye labeling in single LGN section at 1200µm.

Low magnification fluorescent scans reveal the right-eye injected tracer (red -700nm) (A) and left-eye injected tracer (green-800nm) (B). Images were overlaid and merged (C) to demonstrate interdigitation of layers in cat LGN. Dark labelling was observed for contralateral “crossed” layers A, C and C2 (A left, B right) as well as ipsilateral “uncrossed” layers A1 and C1 (A right, B left), which matches previous observations (Guillery et al. 1980; Anderson et al. 1988). Black arrow indicates the gap in labelling caused by the optic disk. Merged images were pseudo-colour coded and aligned using blood vessels to demonstrate interdigitation of LGN layers. Scale bar is 1mm.

Heatmap analysis of label intensity confirmed the presence of the laminar boundaries (Figure 5). The grey level images were converted into heatmaps representing the fluorescent

label intensities (blue - background, red to yellow - label color-coded for intensity) and here even fine details such as the gap for the optic disk representation (yellow arrows Figure 5B, F) were visible. The analysis also confirmed the presence of stronger label intensity throughout the ipsilateral layers of LGN since the lateral portion (Figure 5D left, 7H right) had more intense label than medial portion (Figure 5D right, Figure 5H left).

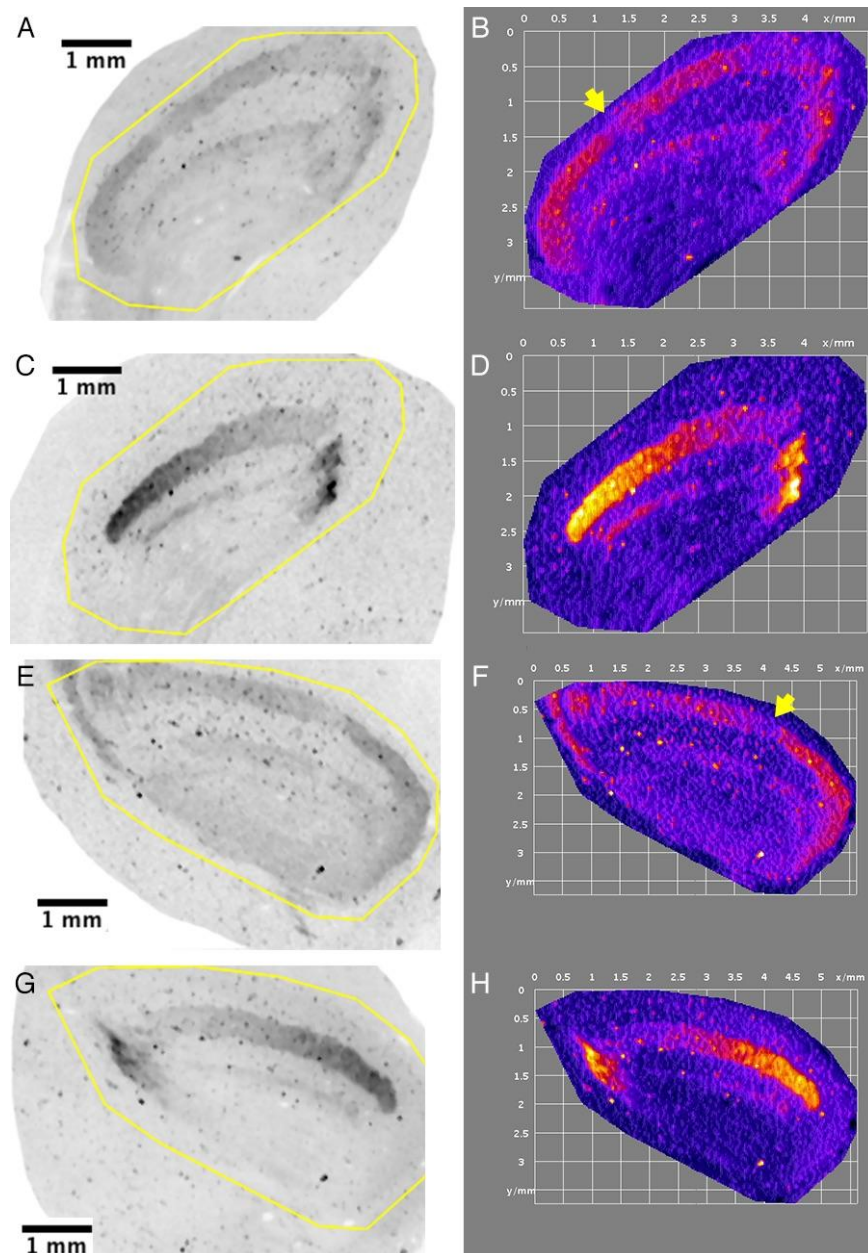


Figure 5. Analysis of WGA CF® dye labeling in single LGN section.

Identical sections as presented in Figure 5. Yellow line (A,C,E,G) outlines the ROI that was converted to a heat map of label intensity (B,D,F,H). Cool colours (blue) represent light label intensity, while warm colours (red) represent more intense labelling. This analysis was useful in identifying the gap in Layer A (yellow arrows) that

represented the optic disk (B,F). There is also a more intense label presence in ipsilateral labeling of the outer segments of layer A1 indicated by bright yellows in D and H. Scale bar is 1mm.

WGA CF® Dye Labeling of Contralateral and Ipsilateral Inputs to the SC

The superior colliculus is typically sectioned in the same A-P plane as LGN, and this was how Ann Graybiel first identified the small 'islands' of ipsilateral fibers (Graybiel 1976). These islands or patches were later identified when superior colliculus was sectioned in the dorsal-ventral (D-V) plane by Illing in 1989 (Illing 1989). In practice, only a few sections demonstrate this patchiness, which is in agreement with the depth of label observed in sections of SC spanning just a few hundred microns (Graybiel 1976).

Here we present a montage of 2 superficial sections (100-200 μ m) used to create the overlaid image in Figure 6. The SC receives most of its input from the contralateral hemisphere, and this was clear when considering the vast amount of green label observed in the right superior colliculus (Figure 6A). The opposite situation was observed in the left hemisphere with the red label (Figure 6B). There was, however, labeling in the ipsilateral hemisphere that appeared as a series of small, irregularly sized but regularly spaced patches. Yellow boxes in each image were drawn around an ROI containing some of this patchy label distribution (Figure 6A left, Figure 6B right) with arrows pointing at three neighboring patches within the ROI. Similarly, two boxes were drawn around ROI in each panel around an area that appears to have complementary lack of label from the contralateral hemisphere and are devoid of labeling (Figure 6A right, Figure 6B left). When the two ROI panels within a hemisphere were overlaid, the label from the ipsilateral hemisphere indeed appeared to nicely fill the voids left in the contralateral hemisphere (Figure 6C).

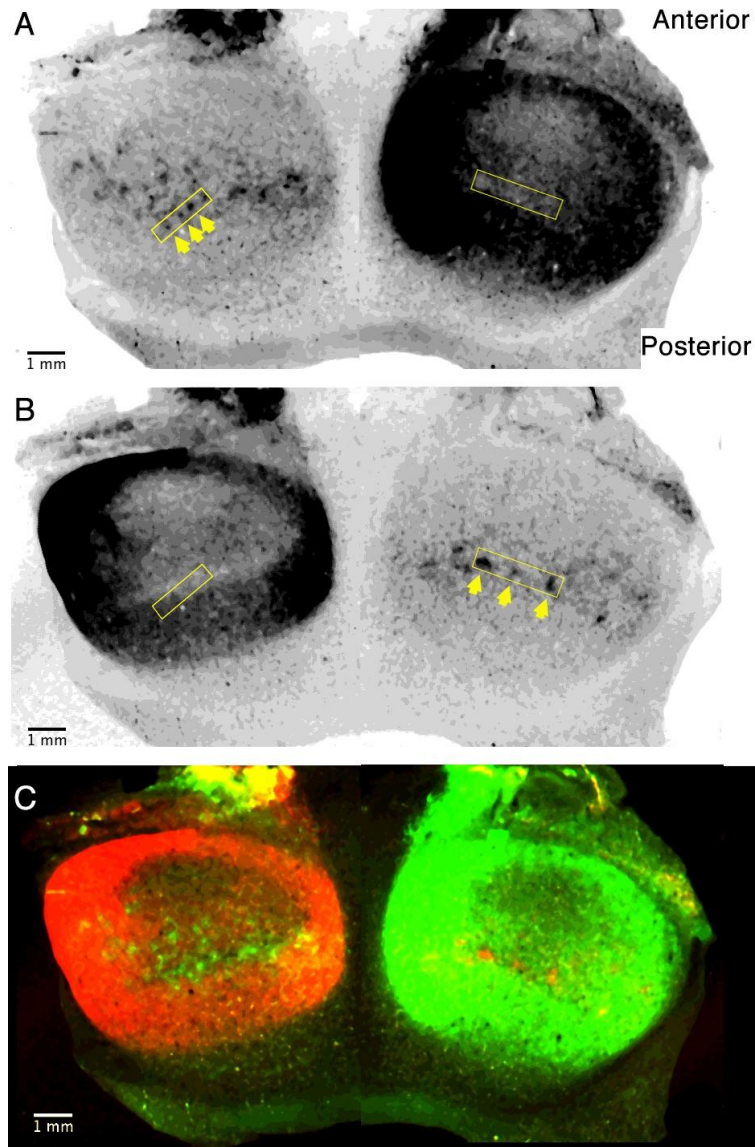


Figure 6. WGA CF[®] dye labeling in sectioned superior colliculus.

Low magnification fluorescent scans of colliculus (100-200 μ m D-V) imaged to reveal left-eye injected tracer (green- 800nm) (A) and right-eye injected tracer (red -700nm) (B). Images were overlaid and merged (C) to demonstrate interdigitation of patches in ipsilateral, uncrossed fibres of cat superior colliculus (A-left, B, right) fill the gaps in label of the contralateral, crossed fibers (A-right, B-left). Minor adjustments were made to align channels using blood vessels. Importantly, scans were taken in the same section, not adjacent sections, to reveal truly interleaved layers. Scale bar is 1mm.

To analyze the intervening patterning of crossed and uncrossed afferents in SC, we compared the intensity of label in matching ROIs for both channels (Figure 7A). The yellow box marked the same ROI on the right-hand side of Figure 6A and 6B. The three yellow arrowheads in Figure 7D match the arrowheads from Figure 6B (right) used to denote intense patches of labeling. Grayscale images were converted to heat maps demonstrating areas of high (yellow)

and low (blue) label intensity (Figure 7 B, E). It was difficult to discern changes in label intensity from the contralateral label (Figure 7 B), but waxing and waning of the ipsilateral label were easily identified (Figure 7E). The image view was rotated $\sim 90\text{deg}$ into the plane of the image, and 35 degrees CCW around the X-Y axis (Figure 7C, F) to help visualize maxima and minima in label intensity. These two panels were vertically aligned using the blood vessel (Figure 7G, white arrow). Each of the local maxima in the ipsilateral hemisphere (Figure 7D yellow arrows, Figure 7G bottom, peaks) aligned with the local minima in the contralateral hemisphere (Figure 7G top, troughs), as indicated by double-headed yellow arrows.

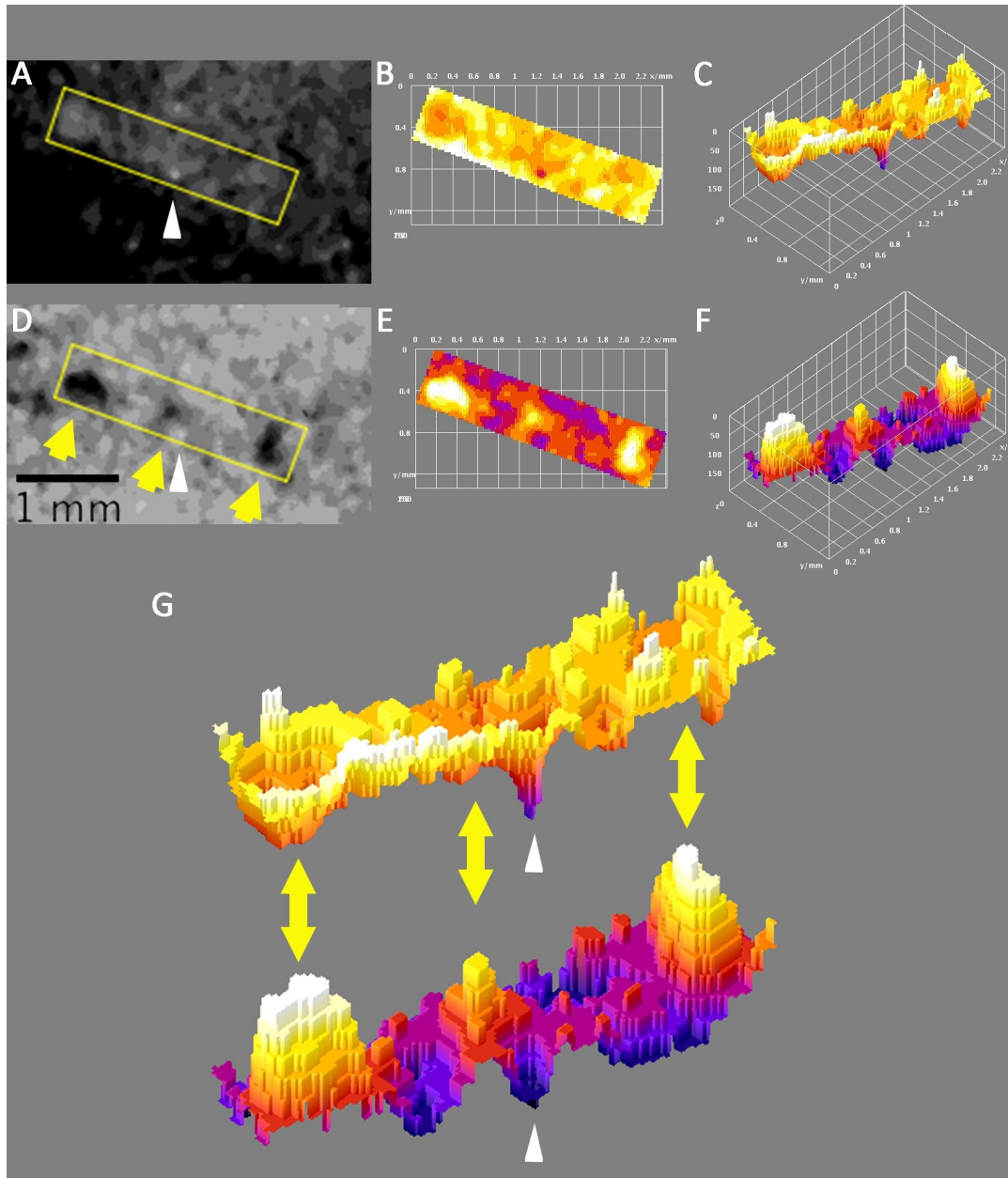


Figure 7. Aligning WGA CF® dye labeling in right superior colliculus.

Yellow boxes represent the same ROIs from contralateral (A-C) and ipsilateral (D-F) injections to superior colliculus. White arrow represents blood vessel with no label in either channel, which was used to align ROIs. Grayscale images were converted to heat maps, with the same conventions as Figure 5 (B,E). Heatmaps were rotated so that label intensities were also plotted in the vertical z-dimension, and aligned with x-y coordinates (C,F). The contralateral superior colliculus (G-top) was aligned above the ipsilateral colliculus (G-bottom), and the peaks in ipsilateral label aligned with the troughs in contralateral label. Blood vessel (white arrow) is the same as in A, D, and recognizes zero label in either channel. Scale bar is 1mm.

2.3.3. Investigation of WGA CF® Dye Labeling in PACT Cleared Tissue

Measurement of flattened cortical clearing rate using PACT

To test the PACT protocol for use with unfolded and flattened cortex, we began by assessing if the rate of tissue clearing and if the clearing was uniform across the unfolded tissue sample. During clearing, we measured the optical density in 3 cortical regions in the unfolded and flattened rat cortex by repeatedly scanning the tissue on a flatbed scanner (ScanMaker i900, Microtek Inc). This imaging was done in the clearing solution (8% SDS) to avoid interrupting tissue clearing. The change in optical density reflected the rate of lipid removal. Figure 8 shows the optical densities in visual, somatosensory and frontal cortex measured repeatedly over the 4 days of tissue clearing (Figure 8A) and illustrates the change in optical density from opaque (black) at the start of clearing (Figure 8B top) to translucent (whitish) (Figure 8B middle), to transparent at the end (clear) (Figure 8B bottom). The average optical density and standard error of the mean (SEM) for each region were plotted for each time point, and an exponential decay was fit to these data ($y = a + b \cdot \exp(-x/T)$). The decay functions provided excellent fits: visual (black; $y = 0.15 + 1.22 \cdot \exp(-x/12.09)$; $r(250) = 0.99$, $p < 0.0001$), frontal, (red; $y = 0.16 + 1.17 \cdot \exp(-x/10.05)$; $r(250) = 0.99$, $p < 0.0001$), and somatosensory (grey, $y = 0.16 + 1.26 \cdot \exp(-x/15.04)$; $r(250) = 0.99$, $p < 0.0001$). This decay function served as a measure of the rate of clearing. First, we noticed that after 96 hours of clearing, all cortical regions reached the same level of transparency (~ 0.1 OD, ANOVA ($F_{92,9} = 2.6487$, $p > 0.05$)). Next, we used τ from the decay function to quantify when the tissue had reached 87.5% of the maximum transparency (3τ). We found that the three cortical regions took slightly different lengths of time to reach the same level of transparency: visual 30.2 hrs, frontal 36.3 hrs, and somatosensory 45.1 hrs. The rate of PACT clearing for the flattened rat cortex was similar to or faster than previously identified times to clear 2mm thick sagittal sections of rodent brains (48 hours- (Yang et al. 2014)). The current results suggest that somatosensory cortex might take about 10-15 hours longer to clear than the other regions (ANOVA ($F_{2,9} = 7.7911$, $p < 0.05$; Tukey HSD $p < 0.05$)). The basal ganglia, however, is tightly adhered under the somatosensory cortex and is difficult to remove completely during the unfolding process. As a result, some of the basal ganglia remained after unfolding and

flattening, which was visible as a honeycomb-like matrix (Figure 8B middle-outline). The results showed that although rates of clearing in unfolded and flattened rat cortex can vary slightly among cortical areas, ultimately all regions achieve a similar level of transparency.

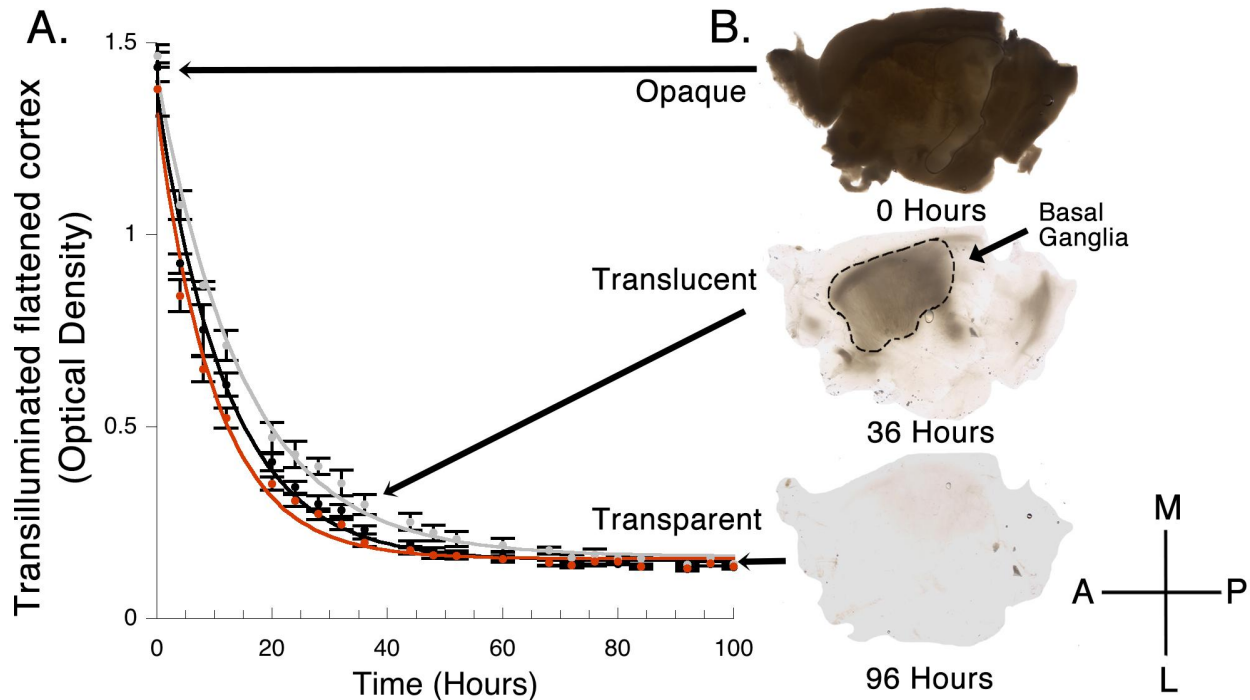


Figure 8. Analysis of clearing rates in flattened rat cortex.

(A) The optical densities of three cortical areas measured repeatedly over 4 days. Exponential decay curves were fit to the data for frontal (red), visual (black) and somatosensory (grey) cortex. (B) Sample images showing the amount of light transmitted through the unfolded and flattened rat hemisphere at different points in the PACT process. Arrows point to the corresponding optical density measured for the tissue. The top image shows very little light transmission through the tissue prior to starting the clearing (~1.4 O.D.), the middle image shows the translucent appearance after 36 hrs of clearing, and the bottom images show the transparent appearance after 96 hrs of clearing. The basal ganglia was still visible under the somatosensory cortex at 36 hrs but most of the other regions (frontal and visual) were almost transparent.

The unfolded and flattened adult cat visual cortex took ~10 days to become clear. Visual inspections were performed multiple times a day to determine when tissue has reached the appropriate level of transparency. Interestingly, clearing the subcortical visual areas, including separate pieces of the LGN and SC took a few days longer (14 and 21 days respectively).

Packets of WGA CF® Dye Remain Inside Retinogeniculate Axons in PACT Cleared LGN

To evaluate the anterograde transport of WGA CF® dye, we obtained high magnification images from a small piece of PACT cleared LGN tissue (~3mm x 2mm x 1mm) using confocal imaging and the CLARITY immersion lens (Methods). We visualized multiple packets of bright

fluorescent labeling (Figure 9A) and then determined the location of the label. First, we looked in blood vessels and did not find any fluorescent label (Figure 9B, Black Arrow) indicating that the WGA injection to the eye did not leak into the bloodstream. Second, we looked at the label in large axons of retinal ganglion cells. We saw label visible as strings along the axon wall, presumably being actively transported by actin filaments (Figure 9B). Finally, we looked at the appearance of label in fine processes of retinal ganglion cell axons and observed patterns of labeling that included synapse-like processes (Figure 9C). Those synapse-like structures appeared as very bright, small (~15nm) accumulations of the fluorescent label (Figure 9C). The high magnification confocal imaging confirmed that WGA CF® dye remained inside the axons of post-fixed neuronal tissue even after extended lipid removal with mild detergents.

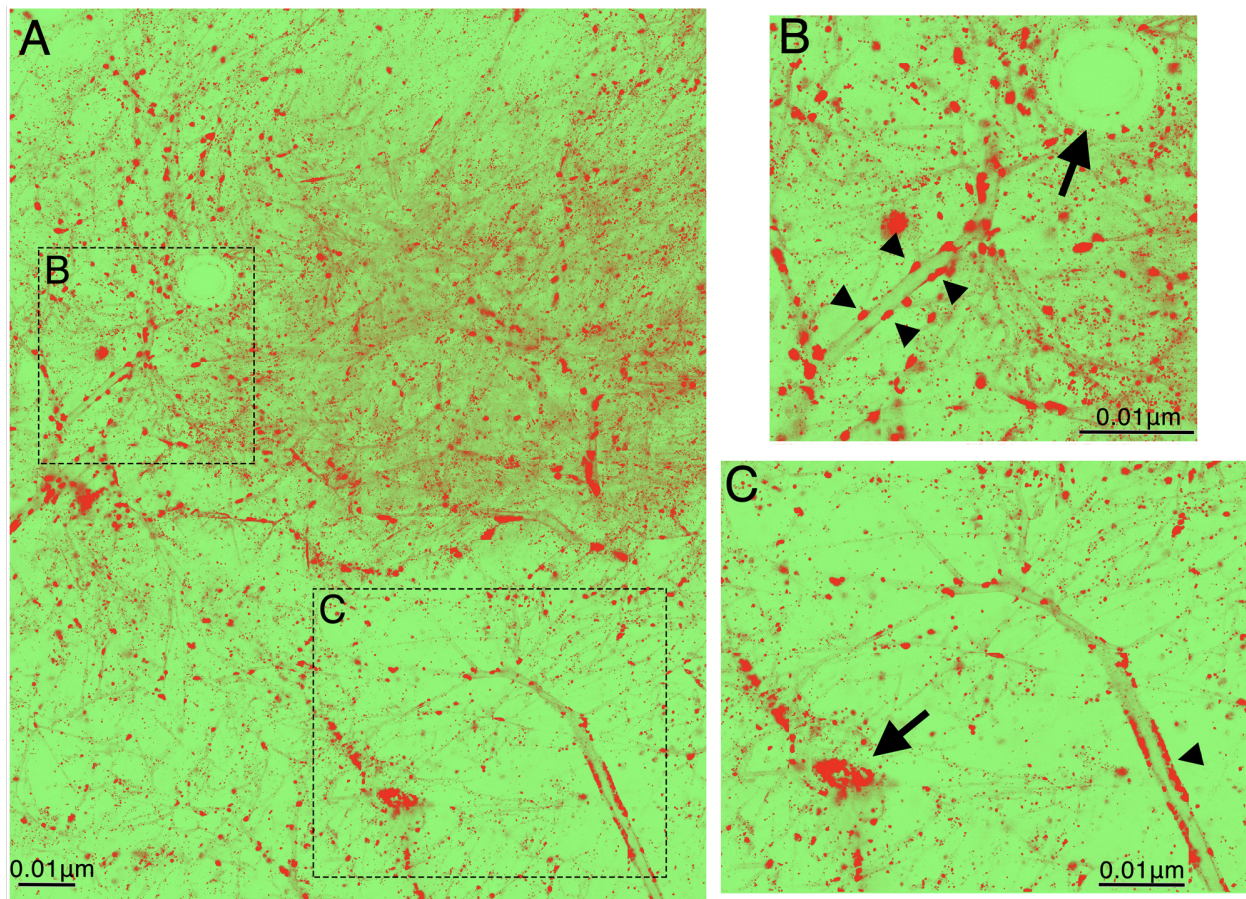


Figure 9. Confocal image of WGA CF® dye in PACT cleared LGN.

High magnification confocal image of tissue mounted in sRIMS (A). Packets of WGA CF® dye (red) are found throughout the axonal process in the sample that are visible on the light green background. (B) No WGA CF® dye was found inside blood vessels (arrow points to a large circular opening cut across a blood vessel). In contrast, axonal processes were lined with lots of WGA CF® dye packets, especially along the edges of large retinal ganglion cell axons (small black arrowheads). (C) WGA CF® dye appeared as strings of label along the axon wall in large diameter (small black arrowhead) and more isolated packets of label in the finer processes. In addition, there

were sites with accumulation of label that were presumably gathering near synapses (~15 nm wide) (C, large arrowhead).

Imaging the Whole Cleared LGN After an Eye Injection with a WGA CF® dye

After the high magnification imaging had confirmed that the WGA CF® dye transported to the LGN remained inside the axons after PACT tissue clearing we wanted to examine low magnification imaging of the whole LGN. We wished to determine if there was sufficient label in the LGN for the LI-COR near-infrared scanner to image it and identify any details of the laminar pattern of labeling. Additional high resolution imaging could be done with a light sheet microscope, however, it is an expensive piece of equipment requiring specialized training to operate and many universities do not have one. For those reasons we wanted to test the quality of low magnification imaging of cleared tissue from the central visual pathway.

Different patterns of fluorescent label were observed when the cleared ipsilateral (left) and contralateral (right) LGNs were imaged at low magnification (Figure 10). The ipsilateral LGN had most of the label restricted to the more ventral region of the LGN, where we expected to find layer A1 (Figure 10 Left- layer A1), while labeling in the contralateral hemisphere was confined to the dorsal region of the LGN, where we expected to find layer A (Figure 10 right- layer A). Thus, the WGA CF® could be imaged at low magnification in the whole cleared LGN, however, the lamination was far less detailed than found in the sectioned tissue. In addition, the anterior sections of the LGN are dominated by contralateral inputs that cover the entire surface of the LGN (Figure 5 A, B, C 100µm), and that pattern of contralateral dominance does not segregate into distinct layers until more posterior sections. Thus, we expected that imaging the whole LGN would obscure the finer details of the retinogeniculate projection such as the C laminae.

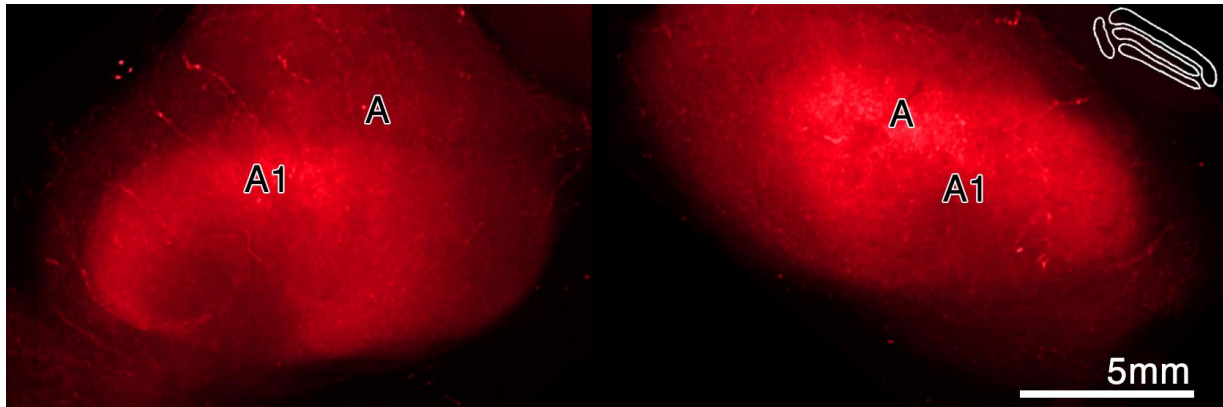


Figure 10. WGA CF® dye labeling in the whole cleared LGN after left-eye injection.

Low magnification scan of the whole LGN mounted in sRIMS. The bright label in left and right LGN reveals the larger layers of uncrossed (left A1) and crossed (right A) fibres from the injected eye. Thinner layers C, C1, and C2 appear to be obscured by tissue thickness. Inset depicts the major layers of the right LGN, stacked vertically as A, A1 and C laminae. Scale bar is 5mm.

Imaging the Whole Cleared SC After an Eye Injection with a WGA CF® dye

After confirming that WGA label transported to the SC, and identifying a pattern of interdigitated labeling from the the ipsilateral and contralateral eye, we tested whether that label remained after clearing the flattened SC tissue. As was the case for the LGN, label stayed in the cleared SC, with more label observed in the contralateral (Figure 11A-left ROI) than the ipsilateral hemisphere (Figure 11A-right ROI). The pattern of labeling in the cleared contralateral SC, was marked by a large swathe of label across the entirety of SC. In contrast, there was a faint pattern of waxing and waning of fluorescence in the contralateral hemisphere (Figure 11A, left ROI) evident by faint patches of weaker label expression (Figure 11A- yellow arrows) surrounded by the swathe of darker label. That pattern matches what was seen in the superficial layers of the sectioned SC.

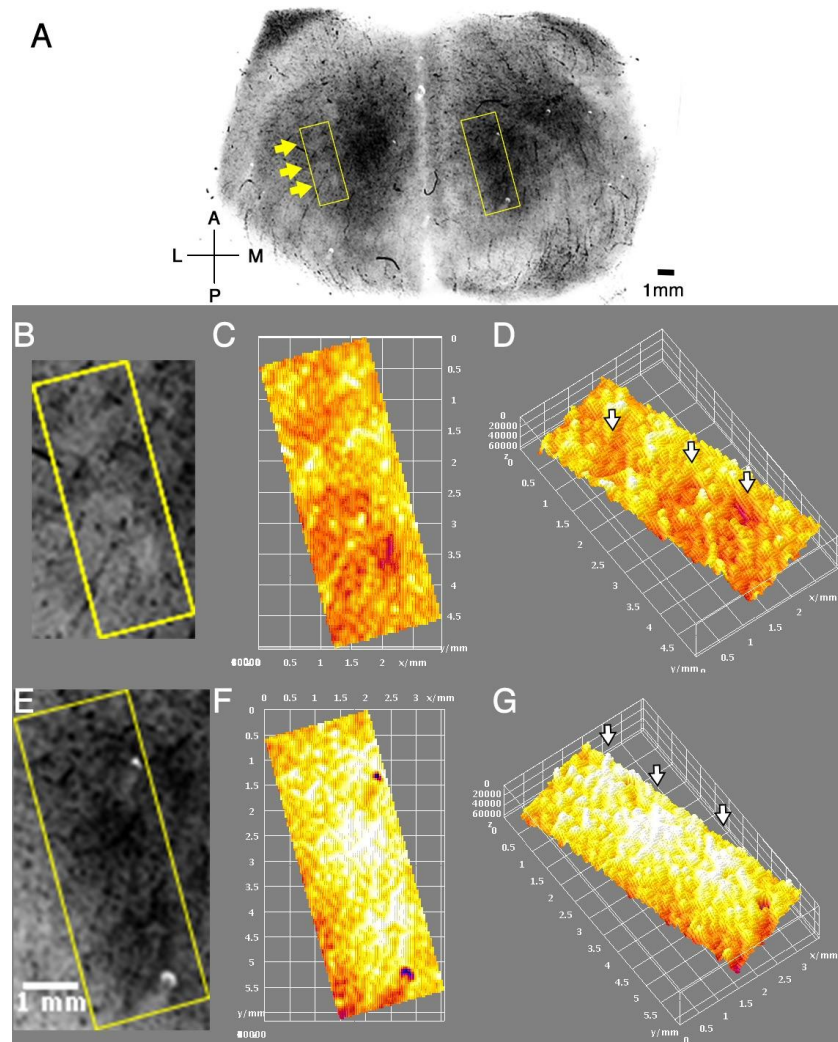


Figure 11. Analysis of WGA CF® dye labeling in whole cleared superior colliculus.

A. Low magnification image of the flattened left and right hemispheres from a cleared superior colliculus. Yellow boxes outline two regions of interest in the contralateral (**B-D**) and ipsilateral (**E-G**) hemispheres of superior colliculus. Higher magnification images of the left (**B**) and right (**E**) regions of interest outlined in **A**. Grayscale images were converted to heat maps (**C,F**), where areas of high label intensity are colored white, and low intensity are colored red. Heatmaps were rotated so that label intensities were visualized in the vertical z-dimension in **D** and **G**. White arrows in **D** denote valleys of low label intensity, and white arrows in **G** denote peaks of high label intensity.

Closer inspection of the ROIs identified some small fluctuations in label intensity with fainter patches of reduced label in the contralateral SC (Figure 11B-D) and darker patches with more label in the ipsilateral SC (Figure 11 E-F). When the grayscale images of the contralateral SC were converted to heat maps and rotated to highlight the label intensity, the patches of reduced label intensity appeared as valleys (Figure 11D-white arrows). When the same approach was applied to the ipsilateral SC, patches of intense label appeared as small peaks in label intensity (Figure 11G- white arrows). However, the change in fluorescence amplitude between

regions of low label to regions with greater label were much smaller than observed in the sectioned tissue (see Figure 9). Similarly, the range of grey levels in the entire cleared SC was much smaller than observed in sectioned tissue. Thus, similar to the low magnification imaging the cleared LGN, the WGA CF[®] dye was readily imaged through the cleared SC but the fine details of the ipsilateral and contralateral projections could not be visualized.

2.3.4. Investigating Transneuronal Transport of WGA CF[®] Dye

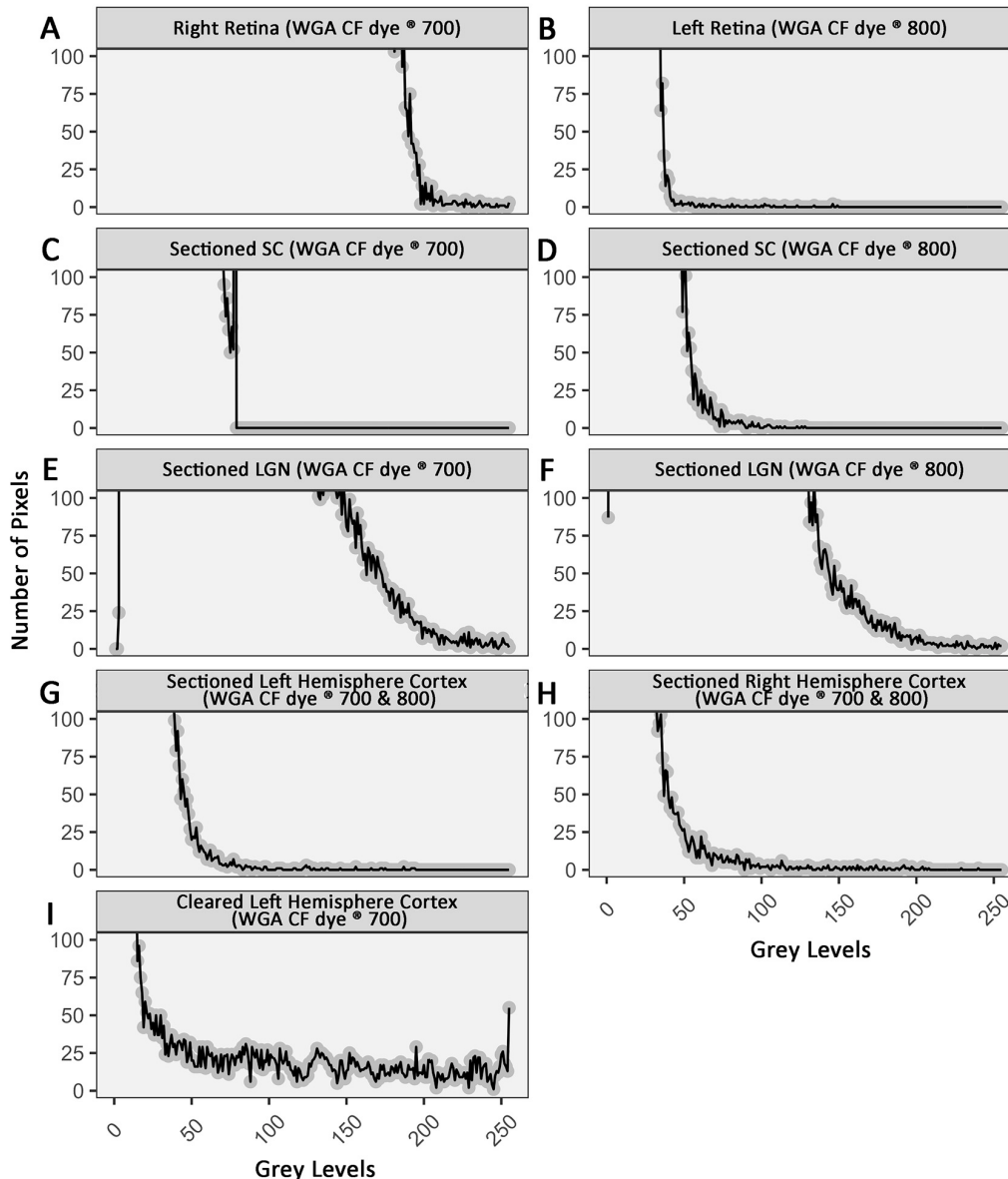


Figure 12. Grey level analysis of retinæ, sectioned SC and LGN, sectioned cortex and cleared cortex.

Histograms of grey levels in the retinæ (A,B) and across all sections of the SC (B,C), LGN (E,F), and Cortex (G,H). Histograms were also plotted for the single image of cleared cortex (I). The y-axis of all plots were matched and set to 100 pixels in order to demonstrate the differences in the number of pixels (visible fluorescence) found in sectioned cortex (G,H) relative to cleared cortex (I).

To determine the extent of label transport to the retinae, LGN and SC, we performed an analysis of the grey level histograms contained in the unprocessed, raw images for these tissues. The right retinae, which was injected with 700nm wavelength tracer, had far more grey levels (0- to 225 grey levels) than the left retina, which was injected with 800nm wavelength tracer (0 to 50 grey levels, Figure 12 A,B). The difference was likely due to the brightness of each tracer, since near-infrared wavelength light is much less bright than light in the visible spectrum. The difference in brightness was not an issue for the sectioned SC which had a wide range of grey levels in both the left SC (700nm - 0 to 75 grey levels) and the right SC (800nm - 0 to 75nm) hemispheres (Figure 12 C,D) . Similarly, the sectioned LGN tissue had a wide range of grey levels for laminae with projections contralateral to the right eye (700nm - 0 to 225 grey levels) and contralateral to the left eye (800nm - 0 to 225 grey levels; Figure 12 E,F).

We investigated the extent of transneuronal WGA CF® dyes by performing the same grey level analysis in sectioned unfolded and flattened cat V1 (Figure 12 G,H) and in cleared tissue (Figure 12 I). The intensity of visible label in sectioned visual cortex was very low, and did not match that of previous reports using other anterograde tracers (e.g. Murphy et al. 1995). Furthermore, the range of grey levels after fluorescent imaging of the sectioned cortex (~0 to 75 grey levels, Figure 12 G,H) was much lower than that observed after imaging the sectioned retina, SC or LGN, supporting the notion that little label was transported to the cortical tissue. A major difference between the current tracer (WGA CF® dyes) and classic tracers (WGA-HRP) is the ability to convert the HRP into a chromogenic substance to amplify reportability and visibility of the tracer (for example TMB, DAB, ABTS). Such techniques that might increase the visibility of WGA CF® dyes are not yet available, as they are for other amplifiers of fluorescent reporters (anti-GFP). Therefore, the sectioned visual cortex was not included in further analyses.

We wondered whether WGA CF® dyes might be visible in cleared tissue, even if they were not visible in thin sections. We imaged cleared tissue in the hopes that the alignment of ocular dominance columns could serve to amplify the underlying fluorescent signal of trace amounts of WGA CF® dye. The cleared unfolded and flattened V1 was prepared for scanning at low magnification by incubating the samples in refractive index matching solution (sRIMS) until optically clear. Next, the cleared tissue was placed in an imaging chamber (Methods) and the

chamber was filled with sRIMS. Lids were carefully sealed with Freezing Mounting Medium (TissueTek, Ted Pella Inc, CA, USA, #27209), and sealed imaging chambers were placed on the fluorescent flatbed Odyssey Scanner (LI-COR Inc). The scan intensity of the 700nm channel was left at the default intensity, while the resolution was set to 21 μ m and the offset was adjusted to 1.25mm to account for the thickness of the slides and tissue (scan area outlined in Figure 13A). When we looked more closely at the pattern of the fluorescent label, we saw an alternating pattern of similarly sized bright and dark patches (Figure 13 B&C). A regular pattern of waxing and waning of the fluorescent intensity was found in the cleared V1. The patch-like organization of fluorescent labeling was similar to the pattern of cat ocular dominance patterns visualized with WGA-HRP (Anderson et al. 1988). The range of grey levels in cleared tissue ranged from 0 to 255 (Figure 12 I), and this was a much wider range of grey levels than observed after imaging the physically sectioned visual cortex. The likely reason for more visible tracer, and thus more grey levels in cleared tissue, was the alignment of tracer within ocular dominance columns, which were aligned with the vertical imaging plane of the fluorescent flatbed scanner.

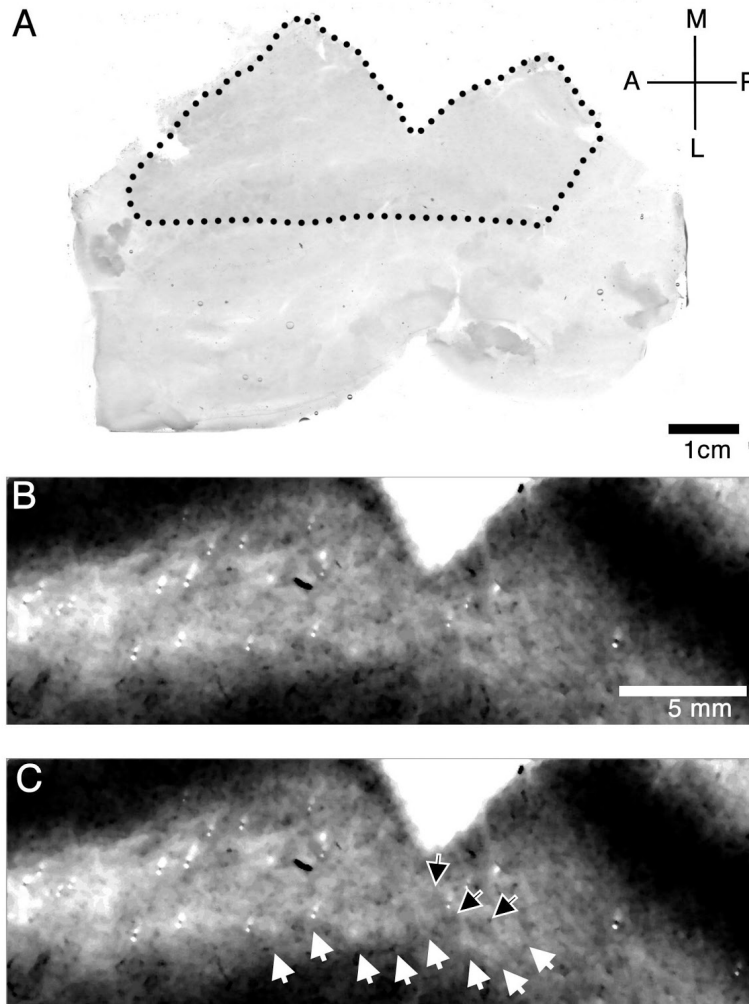


Figure 13. WGA CF® dye labeling in cleared unfolded and flattened cat cortex.

(A) Low magnification image of the large piece of transparent flattened cortex scanned on a ScanMaker i900 (Microtek Inc) to identify V1 (dotted line). M, medial, L, lateral, A, anterior, P, posterior. Scale bar =1cm. (B & C) A slightly higher magnification image scanned through the full thickness of the cleared V1 on an Odyssey infrared fluorescent scanner (LI-COR Biosciences; Lincoln, NE). Brighter patches represent WGA CF® dye labeled inputs from the injected eye (C, white arrows), while the interdigitated darker patches (C, black arrows) are presumably areas with inputs from the other eye. Scale bar is 5mm.

2.4 Discussion

We developed a protocol for tracing the central visual pathway of both eyes using WGA CF® dyes that was fast, simple, affordable, and compatible with passive tissue clearing (PACT, (Yang et al. 2014)). We showed that the features of the visual pathway could be imaged with a standard NIR fluorescent flatbed scanner because of the bright and photostable properties of the dyes. Furthermore, we showed that WGA CF® dye remained inside axons in cleared tissue, and

even low magnification imaging of cleared tissue identified some of the eye-specific features of projections to the LGN, SC and visual cortex.

WGA CF® dye labeling of the central visual pathway

We showed that the WGA CF® dyes were taken up by retinal ganglion cells, and that it was easy to visualize the hexagonal arrangement of labeled cells in retinal whole mounts, with notably stronger intensity of label in the area centralis. In the LGN, the WGA CF® dyes labeled the eye-specific laminae along the full anterior-posterior extent of the nucleus. Low-magnification analysis of the LGN confirmed that the protocol could label fine details including the pattern of A and C layers, as well as the gap in labelling for the representation of the optic disk, and the eye-specific segments of the medial interlaminary nucleus (Figures 4 and 5) (Guillery and Kaas 1971; Guillery et al. 1980; Sretavan and Shatz 1986; Anderson et al. 1988). In addition, the appearance of WGA CF® dye at high magnification as packets along the inside edge of retinal ganglion cell axons was similar to previous studies that used the dyes to study axonal transport in live neurons (Pesaresi et al. 2015) suggesting active and specific anterograde transport of WGA CF® dye from the retina to LGN. The pattern of transported dye in the SC was visible as strong contralateral labeling with regular waxing and waning to create a patch-like pattern. That contralateral pattern was interdigitated by the distinct puffs arising from ipsilateral eye afferents (Figures 6 and 7), similar to previous reports of islands of label (Graybiel 1976; Illing 1989). Tangential sectioning and analysis of the double-labeled SC showed that the ipsilateral puffs fell in the less intensely labeled contralateral patches suggesting an ocular dominance-like pattern of inputs to the SC. The new protocol is therefore suitable for rapidly visualizing the pattern of retinal projections to the LGN and SC.

WGA CF® dye remained after clearing

The expression of fluorescent WGA CF® dyes in sectioned LGN and SC tissues confirmed transport of the dye from retinal ganglion cells to terminals. It was unclear, however, if the WGA CF® dye would remain after tissue was cleared because previous studies using other dyes have had variable success after clearing tissue (Kuwajima et al., 2013). In this case, we were unsure whether label would remain because PACT is a gentle tissue clearing protocol that preserves

structural integrity of cleared tissue by crosslinking a hydrogel matrix between acrylamide polymers and fixed tissue contents, before washing out unfixed cell components such as lipids, which are a large component of neural membranes (LeVine et al. 1972; Nicolson 1974; Mesulam 1982; Yang et al. 2014) before forming crosslinks with the N-acetyl-D-glucosamine and N-acetylneuraminic acid residue in neural membranes (Mesulam 1982). Therefore it was unclear whether crosslinked WGA molecules would be removed via lipid extraction (SDS washing).

The efficacy of WGA for neuronal tracing is often increased through conjugation with other molecules (eg. HRP, Alexa-fluor), yet whether those molecules remain in membranes after tissue clearing has not been evaluated. Here we have shown that WGA CF dye indeed remains inside the axons of retinal ganglion cells after PACT clearing (Figures 9, 10 and 11).

Furthermore, imaging with the LiCOR Odyssey scanner detected WGA CF® dye throughout all layers of cleared tissue. The low magnification full thickness scanning of the dye obscured finer details of the LGN, such as the alternating C1 and C2 layers (Figure 10), and also obscured finer features of the SC, such as the pattern of islands in the SC (Figure 11). Nevertheless, there was still good evidence for preserved label in more robust features, such as the alternating A and A1 laminae of the LGN, and the intense swathe of contralateral label in the SC.

Transneuronal Transport of WGA CF® dye

Here we assessed transneuronal transport of the WGA CF® dyes by examining unfolded and flattened V1 sections but did not find evidence of neural labeling. The range of available grey levels supported the notion that little label transported to visual cortex. Classic studies using WGA-HRP or CTB require additional steps to increase tracer visibility in a single tissue section (Matteau et al., 2003). For example, the protocols to visualize HRP amplify the signal and with the TMB reaction a birefringent crystal is formed that can be further amplified by using cross-polarized darkfield illumination. The current sections were imaged by scanning with a laboratory NIR scanner without any additional steps to amplify the fluorescent signal. It is possible that the signal intensity could be increased by using a type of antigen retrieval or fluorescent signal amplification, similar to how anti-GFP directly targets the fluorescent molecule in order to amplify fluorescence. Unfortunately, antigens that might detect the fluorescent component of WGA CF® dyes do not exist.

On the other hand, examination of cleared cortical tissue after a single eye-injection revealed similarly spaced blobs as previous reports (e.g., Wiesel et al. 1974; Murphy et al. 1995). This was surprising, since the fluorescent images were taken by imaging throughout the entire thickness of cleared tissue. Unlike our examination of LGN and SC, where fine details were obscured by out-of focus fluorescence, here the intensity of the WGA CF® dye appears to be amplified by out of focus fluorescence. This was likely a byproduct of aligning ocular dominance columns through the tissue thickness, which might explain why blobs were visible in cleared V1 and not in sectioned V1. Nevertheless, the range of grey levels in this tissue was less than that observed in any of the other sectioned or cleared tissue samples, suggesting that very little tracer was transported to V1 in the first place.

Conclusions

The protocol outlined here combines anterograde transneuronal pathway tracing using a bright WGA CF™ dye, cortical unfolding and flattening, and passive tissue clearing (PACT). This provided a simple, inexpensive method to take advantage of modern neuroanatomical techniques, including tissue clearing for studying development and plasticity of axonal projections along the central visual pathway. Here we showed that the WGA CF® dyes are transported along the visual pathway so that fine details of the LGN and SC are easily visualized, even at low magnification. The current study extends the repertoire of fluorescent labeled WGA dyes for tracing the central visual pathway by showing the specificity of the anterograde labeling with the WGA CF® dyes and the compatibility of the dyes with PACT clearing. The WGA label used here transports quickly, is not toxic, does not kill labeled neurons or the animal, and does not require the implementation of biosafety protocols. Thus, the WGA CF® dye is a simple alternative for labeling the projections from the eye to subcortical sites and V1.

2.5 References

- Anderson PA, Olavarria J, Van Sluyters RC. The overall pattern of ocular dominance bands in cat visual cortex. *Journal of Neuroscience*. Society for Neuroscience; 1988 Jun 1;8(6):2183–200.
- Gonatas NK. The use of lectins and cholera toxin for the detection of surface carbohydrates of cultured neurons and neuroblastoma. *Journal of Histochemistry and Cytochemistry*. 1979 Aug;27(8):1165–6.
- Graybiel AM. Evidence for banding of the cat's ipsilateral retinotectal connection. *Brain Res*. 1976 Sep 17;114(2):318–27.
- Guillery RW, Geisert EE, Polley EH, Mason CA. An analysis of the retinal afferents to the cat's medial interlaminar nucleus and to its rostral thalamic extension, the "geniculate wing". *J Comp Neurol*. 1980 Nov 1;194(1):117–42.
- Guillery RW, Kaas JH. A study of normal and congenitally abnormal retinogeniculate projections in cats. *J Comp Neurol*. 1971 Sep;143(1):73–100.
- Illing RB. The mosaic of the uncrossed retinal projection in the superior colliculus of the cat. *Exp Brain Res*. 1989;74(3):641–4.
- Itaya SK, Van Hoesen GW. WGA-HRP as a transneuronal marker in the visual pathways of monkey and rat. *Brain Res*. 1982 Mar 18;236(1):199–204.
- Kuwajima T, Sitko AA, Bhansali P, Jurgens C, Guido W, Mason C. ClearT: a detergent- and solvent-free clearing method for neuronal and non-neuronal tissue. *Development*. 2013 Mar;140(6):1364–8.
- LeVine D, Kaplan MJ, Greenaway PJ. The purification and characterization of wheat-germ agglutinin. *Biochem J*. 1972 Oct;129(4):847–56.
- Matteau, I., Boire, D., & Ptito, M. (2003). Retinal projections in the cat: a cholera toxin B subunit study. *Visual neuroscience*, 20(5), 481-493.
- Mesulam MM. Tracing neural connections with horseradish peroxidase. 1982.
- Mesulam MM, Mufson EJ. The rapid anterograde transport of horseradish peroxidase. *NEUROSCIENCE*. 1980;5(7):1277–86.
- Micheva KD, Smith SJ. Array Tomography: A New Tool for Imaging the Molecular Architecture and Ultrastructure of Neural Circuits. *Neuron*. 2007 Jul;55(1):25–36.
- Murphy KM, Jones DG, Van Sluyters RC. Cytochrome-oxidase blobs in cat primary visual cortex. *Journal of Neuroscience*. 1995 Jun;15(6):4196–208.
- Nicolson GL. The interactions of lectins with animal cell surfaces. *Int Rev Cytol*. 1974;39:89–190.
- Olavarria J, Van Sluyters RC. Unfolding and flattening the cortex of gyrencephalic brains. *Journal of Neuroscience Methods*. 1985 Nov;15(3):191–202.

- Olavarria J, Van Sluyters RC. Unfolding and flattening the cortex of gyrencephalic brains. *Journal of Neuroscience Methods*. 2014 Aug 21;15(3):1–12.
- Pesaresi M, Soon-Shiong R, French L, Kaplan DR, Miller FD, Paus T. Axon diameter and axonal transport: In vivo and in vitro effects of androgens. *NeuroImage*. Elsevier Inc; 2015 Jul 15;115(C):191–201.
- Polley EH, Guillery RW. An anomalous uncrossed retinal input to lamina a of the cats dorsal lateral geniculate nucleus. *NEUROSCIENCE*. 1980;5(9):1603–8.
- Renier N, Wu Z, Simon DJ, Yang J, Ariel P, Tessier-Lavigne M. iDISCO: a simple, rapid method to immunolabel large tissue samples for volume imaging. *Cell*. 2014 Nov 6;159(4):896–910.
- Schall JD, Leventhal AG. Relationships between ganglion cell dendritic structure and retinal topography in the cat. *J Comp Neurol*. Wiley-Blackwell; 1987 Mar 8;257(2):149–59.
- Schindelin J, Arganda-Carreras I, Frise E, Kaynig V, Longair M, Pietzsch T, et al. Fiji: an open-source platform for biological-image analysis. *Nat Methods*. 2012 Jul 1;9(7):676–82.
- Sretavan DW, Shatz CJ. Prenatal development of cat retinogeniculate axon arbors in the absence of binocular interactions. *Journal of Neuroscience*. 1986 Apr;6(4):990–1003.
- Wiesel TN, Hubel DH, Lam DM. Autoradiographic demonstration of ocular-dominance columns in the monkey striate cortex by means of transneuronal transport. *Brain Res*. 1974 Oct 18;79(2):273–9.
- Williams RW, Chalupa LM. Prenatal development of retinocollicular projections in the cat: an anterograde tracer transport study. *Journal of Neuroscience*. 1982 May;2(5):604–22.
- Yang B, Treweek JB, Kulkarni RP, Deverman BE, Chen C-K, Lubeck E, et al. Single-cell phenotyping within transparent intact tissue through whole-body clearing. *Cell*. 2014 Aug 14;158(4):945–58.

Chapter 3. Protocol for a high-throughput semi-automated preparation for filtered synaptosomes

Abstract

One of the simplest techniques for the isolation and application of synaptosomes involves fractionation of synaptoneuroosomes through filtration and low speed centrifugation¹. This approach however, is limited by two essential stages of the synaptoneurosome tissue preparation: the manual homogenization and filtrations are both laborious and slow. We have updated this traditional technique to include modern bench-top homogenizers and centrifugal filter units to simplify these labor intensive stages, to make each stage faster and to reduce the variability between samples. Here we outline our protocol to produce filtered synaptoneuroosomes that reduces sample preparation time, increase the amount of tissue recovered and most importantly, increases protein enrichment.

Keywords: Synaptoneuroosomes, synaptic proteins, high-throughput, centrifugal filtration

3.1 Introduction

3.1.1 General Introduction

Synaptosome preparations enrich brain tissue samples for synaptic proteins, making it an important tool for studying proteins involved in synaptic development and plasticity²⁻⁸. Two types of protocols are used to enrich for the synaptic fraction; the use of a sucrose or Percoll gradient to make synaptosomes^{9,10}, or filtration procedures to make synaptoneuroosomes^{1,11}. What makes these synaptosome or synaptoneurosome preparations useful for studying synaptic development and plasticity is the approximate twofold enrichment of synaptic proteins^{1,12}. That enrichment improves the signal-to-noise so that synaptic proteins can be accurately quantified even when the synaptosome or synaptoneurosome is prepared from a small brain sample (e.g. ~30 mg). Furthermore, low abundance synaptic proteins (eg. PICK and GRIP) that are difficult to reliably quantify in homogenate samples can be routinely studied with synaptoneuroosomes¹³.

Our research uses filtered synaptoneuroosomes to study synaptic development and plasticity in visual cortex of animals and humans. We have also developed a high-throughput, semi-automated protocol for preparing synaptoneuroosomes because many aspects of synaptic function can be studied with this preparation. For example, we have examined both pre- and post-synaptic proteins involved in establishing nascent synapses and mediating experience dependent strengthening or weakening of connections¹³⁻²¹. Our studies, as well as ones from other labs have found that using a synaptoneurosome preparation can uncover synapse-specific aspects of neurodevelopment and plasticity^{12,14}. Indeed, our lab has used synaptoneuroosomes to highlight similarities and differences between the total pool of synaptic proteins found in homogenate samples and the amount concentrated at the synapse by the synaptoneurosome^{14,19,21}.

This chapter will focus on describing the protocol we developed for high-throughput and semi-automated preparation of synaptoneuroosomes that is ideal to process large numbers of samples quickly, inexpensively, and with high reliability¹⁸.

3.1.2 Synaptoneurosome Steps

All filtered synaptoneurosome preparations are made using two steps: tissue homogenization and fractionation (Chapter 1 of Springer Methods book). The simple protocol

described by Hollingsworth et al. (1985) helped to popularize the use of filtered synaptoneurosomes. That method describes manual homogenization with a glass-glass Dounce tissue grinder, followed by 5 μ m filtration and low speed centrifugations. Two challenges emerge when trying to scale up any of the manual protocols for making synaptoneurosomes. First, these protocols are very slow because each sample is prepared by hand, one at a time. Second, substantial sample-to-sample variability can be introduced because both homogenization and filtration steps are done by hand. Many groups have tried to improve the quality of the synaptoneurosome preparation by introducing new methods for tissue lysing²²⁻²⁴, fractionation²⁵, or adjusting the filter pore size^{11,25}. Yet, all of those protocols still use hand processing for tissue lysing and/or filtering, so they continue to have sample-to-sample variability and are not easily scaled up for large projects. We have addressed these problems by developing a new high-throughput, semi-automated protocol to prepare filtered synaptoneurosomes¹⁸.

3.1.3 Tissue Homogenization

Synaptoneurosome protocols with manual steps for tissue homogenization (e.g. glass-glass Dounce tissue grinders) use qualitative descriptions to explain how to lyse the sample. In practice, these protocols are difficult to reproduce since only the number of strokes is quantified, and most other aspects of the tissue lysing, such as how fast or how much pressure to use with each stroke, are difficult to describe. New protocols however, use modern bench-top homogenizers to grind, homogenize and lyse tissue samples¹⁸. These homogenizers can prepare multiple samples at a time, using built-in programmable steps that lead to highly reproducible preparation of many samples.

3.1.4 Sample Fractionation

Tissue fractionation protocols typically include syringe filtration steps to remove larger extra-synaptic components from the homogenate. These are followed by low speed centrifugations to further separate heavier synaptic fractions from the lighter supernatant. The manual syringe filtrations vary according to the number of filtrations, the size of the filter pores, and the qualitative description of how to carry out the steps. In addition, syringe filters such as Swinnex holders, have about 1ml of dead space, so at least 1.5ml of sample has to be loaded to

recover enough filtrate to continue the protocol. This loss of sample is problematic when using small, valuable samples that do not generate enough homogenate for subsequent filtration. We eliminated these problems by replacing the manual filtration steps with centrifugal filtration units, where even a small volume of homogenate is reliably filtered. Each centrifugal filtration unit is loaded with up to 500µl of homogenate, and then spun with a known g-force in a centrifuge to collect the filtered sample needed to prepare the synaptoneurosome. There is no dead space where sample volume can be lost, and many samples can be filtered at once, leading to reliable high-throughput filtration.

Here we detail the steps to prepare filtered synaptoneurosomes using our new protocol¹⁸. The protocol explains how to implement our semi-automated, high-throughput procedure and compares samples prepared with this new protocol versus older manual protocols to illustrate the optimizations that lead to improved reliability, enhanced protein yield, greater synaptic enrichment, and faster preparation of synaptoneurosomes.

3.2 Materials and Equipment List

3.2.1 Laboratory Equipment

Peristaltic Pump

Biosafety cabinet (equipped with drain)

1.5 ml Micro centrifuge vial (7x tissue piece)

1 on crushed dry ice

6 on wet ice

-80°C freezer

Weigh boats

Scale

Scoopula

2 ml Lysing Matrix-D tube (1x tissue piece, MP Biomedical, Cat. #116913050)

Bench-top Homogenizer (FastPrep 24 Tissue and Cell homogenizer, MP Biomedicals, Cat. #116004500)

2 ml Ultrafree-MC SV Centrifugal Filter Units with Microporous Membrane (1x tissue piece, Millipore, Cat # UFC30SV00)

Centrifuge (e.g. Sorvall legend Micro 21R)

96 well sample assay plate

Pipettor (volumes between 0.5µl and 200µl)

Biological Incubator (capable of 45°C)

Absorbance Reader (e.g. iMark Plate reader, BioRad)

Heating Block

3.2.2 Chemicals and Reagents for Synaptoneurosome Tissue Preparation

Animal Perfusion and Tissue Collection

PO4 Solution (0.2M): Make stock ahead of time

4L dH2O

30.8g NaOH

117.1g Monobasic NaH2PO4

PBS: Make fresh, store at 4°C

50ml 10x saline

450ml dH₂O

500ml PO₄ Solution (0.2M)

Euthanyl (sodium pentobarbital) (150 mg/kg rat, 165 mg/kg cat)

Synaptoneurosome Preparation

Homogenization Buffer Recipe yields 50 ml (3ml x tissue piece)

5ml HEPES (10mM)

5ml EDTA (2mM)

5ml EGTA (2mM)

125µl DTT (0.5mM)

500µl Leupeptin (10mg/L)

500µl Soybean Trypsin Inhibitor (50mg/L)

50µl Microcystin (100nM)

33.825 ml H₂O

i. Check the pH level of the combined ingredients, and adjust to pH 7.5

ii. Add 50µl PMSF

iii. Put solution on wet ice until added to frozen tissue. Can be frozen at -20°C for later use.

Stock HEPES (10mM):

100 ml dH₂O

2.38g HEPES powder (N-2-Hydroxyethylpiperazine-N'-2-Ethanesulfonic Acid,

Bishop, Cat #Hep 001)

Stir until powder is dissolved. Aqueous HEPES can be aliquoted and frozen at

-20°C, and thawed for use in Homogenization Buffer.

Stock EDTA (2mM):

100 ml dH₂O

0.5844g EDTA powder (Ethylenediaminetetraacetic acid disodium salt dihydrate,

Sigma, Cat# E-1644)

Stir until powder is dissolved. Aqueous EDTA can be aliquoted and frozen at -20°C, and thawed for use in Homogenization Buffer.

Stock EGTA (2mM):

90 ml dH₂O

10 ml NaOH

Stir until powder is dissolved.

To the above solution, add 0.768g EGTA powder (Ethylene-bis(oxyethylenenitrilo)tetraacetic acid, Sigma, Cat #E4378). Stir until powder is dissolved. Aqueous EGTA can be aliquoted and frozen at -20°C, and thawed for use in Homogenization Buffer.

Stock SDS solution (10%): (20µl x tissue piece)

10 grams of SDS Powder (Sodium Dodecyl Sulfate, Bioshop, Cat#SDS001)

100ml dH₂O

Stock SDS solution (1%): (boiling, 100µl x tissue piece)

100ml of Stock SDS solution (10%) (see above)

Add 900ml of dH₂O

BCA Assay and preparing tissue for Western blotting

Albumin Standards

Dilute stock albumin (2 µg/ml) to the following concentrations using saline/dH₂O:

1 µg/ml, 0.5 µg/ml, 0.25 µg/ml

BCA working solution

50 ml Reagent A (Pierce™ BCA protein Assay Reagent A, Thermo Fisher Scientific, Cat# 23223)

1 ml Reagent B (Pierce™ BCA protein Assay Reagent B, Thermo Fisher Scientific, Cat#23224)

Sample loading buffer (M260 NextGel® Sample loading buffer 4x, Amresco LLC, Solon, OH, USA)

Laemmli buffer (Cayman chemical company, Ann Arbor, MI, USA)

3.3 Protocol & Main Findings

Animal Perfusion and Tissue Collection

Here we describe the perfusion and tissue collection protocols that we use for our studies of visual cortex. If perfusion is not a suitable option for your experiment we provide an alternative protocol with modified filtration steps in a subsequent chapter (Siu Chapter of Springer Methods book).

3.3.1 Animal Perfusion

1. Euthanize the animal using the protocol approved by your institutional animal ethics committee.
2. Use transcardial perfusion to clear blood from the animal. Insert the needle from the peristaltic pump into the left ventricle of the heart, cut the right atrium with scissors and begin the perfusion with cold 0.1 M phosphate buffered saline (PBS) at a rate of 50-100 ml/min, for about 4 minutes, or until circulating fluid becomes clear.
3. Quickly remove the brain from the skull and immerse in cold PBS.

3.3.2 Tissue Collection

1. Cut samples from the desired location with sharp iris scissors or a surgical blade. For example, the samples we cut from rat cortex are typically 3x3x1 mm to yield ~500mg of tissue that is ready for synaptoneurosome preparation.
2. Quickly transfer tissue pieces to pre-cooled centrifuge vials. Label the vial with the needed identifiers, and place vial back on dry ice to rapidly freeze the sample.
3. Then store the frozen samples at -80°C , or begin with the synaptoneurosome preparation.

3.3.3 Synaptoneurosome Preparation

In this chapter, we describe our published protocol¹⁸ for the high-throughput and semi-automated preparation of filtered synaptoneurosome, and compare this protocol with the manual hand preparation popularized by Hollingsworth et al., 1985 (Fig. 1). The primary steps needed to make filtered synaptoneurosome, homogenization and filtration, as well as a set of low speed centrifugations, are outlined in Fig 1. An approximation of how long it takes to prepare a single

sample at each of these 3 steps is also outlined in Fig 1. Homogenization and filtration following the manual hand preparation each took about 5 minutes to prepare just one sample, and when scaling to 24 samples, just these 2 steps add a minimum of 4 hours to a tissue preparation protocol. Furthermore, the manual hand preparation requires at least 2 experimenters, because while one person is homogenizing and filtering tissue, the other is needed to clean the glass-glass Dounce homogenizers, as well as clean and assemble the Swinnex filter holders between samples. In contrast, one experimenter can easily perform the new high throughput, semi-automated steps, in under 10 minutes and the single experimenter is able to homogenize and filter all 24 samples at once.

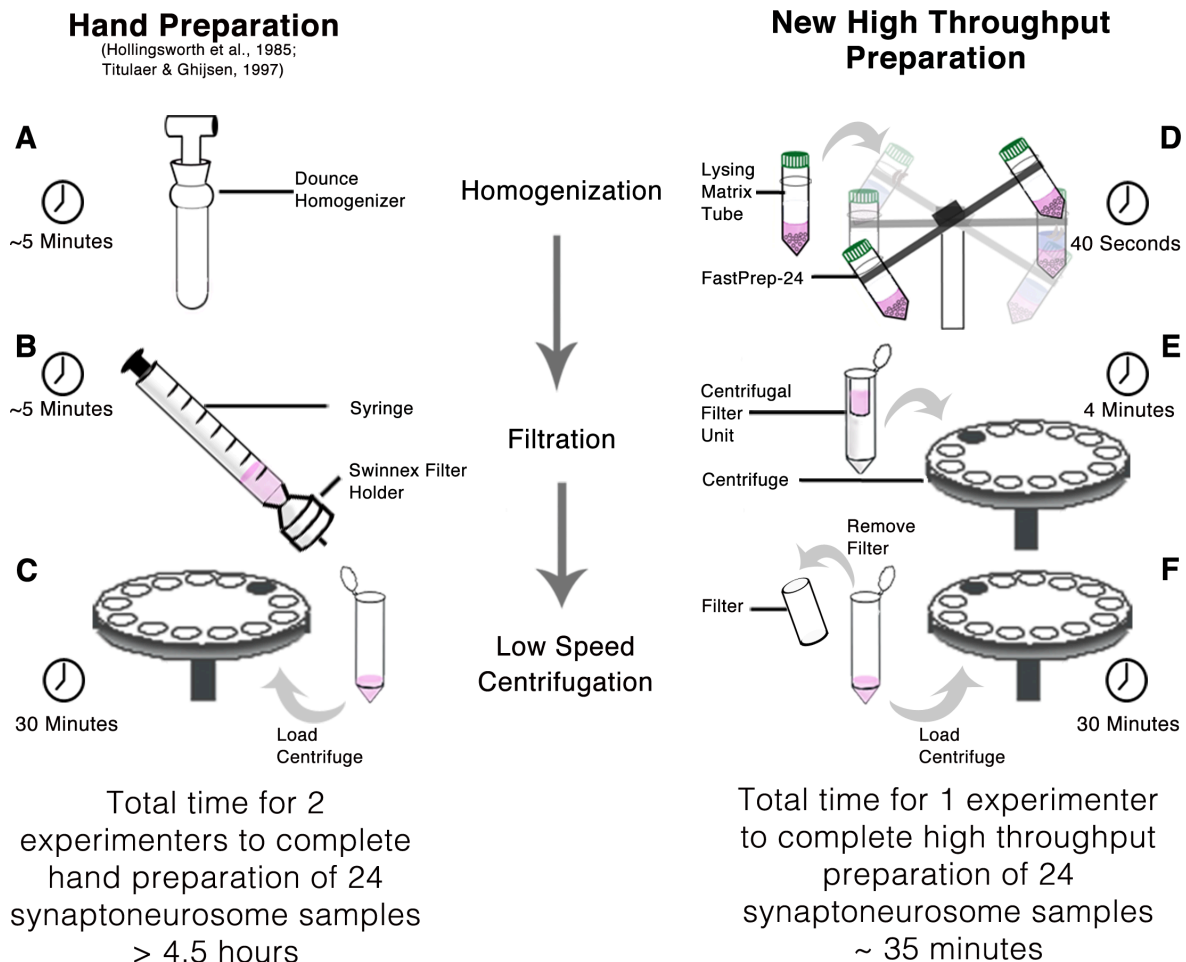


Fig 1. Overview of process for preparing synaptoneurosomes using either the manual hand or new high-throughput, semi-automated protocol, including a comparison of the primary steps in the processes from homogenization to filtration, and low speed centrifugation.

(A) The hand preparation began with two experimenters working together to homogenize samples one at a time using glass-glass Dounce homogenizers. (B) The resultant homogenate was then filtered by applying hand-pressure to a syringe, and forcing homogenate through hydrophobic membranes held in place by the Swinnex filter holder. (D) The high-throughput preparation began with one experimenter placing samples in lysing matrix tubes, and running samples in the Fast-Prep® -24 Tissue and Cell Homogenizer for 40 s. (E) The resultant homogenate was then transferred to centrifugal filter units, and centrifuged for 4 minutes. The filter component of the centrifugal filter unit was removed before low speed centrifugation. (C and F) In both the hand and high-throughput preparations, samples were centrifuged at low speed for 30 minutes. To prepare 24 samples with the hand preparation, the total time require was 4.5 hours and two experimenters were required. To prepare 24 samples with the high-throughput preparation, the total time require was 35 minutes, and only one experimenter was required.

3.3.4 Synaptoneurosomes Preparation - Preliminary Steps

Our protocol significantly speeds up the process and decreases the number of experimenters required to make synaptoneurosomes from fresh frozen tissue, but it is still

important to work quickly to prevent tissue thawing. Therefore, we include these steps to reduce the likelihood of tissue thawing before samples are introduced to homogenization buffer. [Note 1].

1. Thaw homogenization buffer on ice. Homogenization buffer can be made ahead of time, and it can now be taken out to thaw, but homogenization buffer must remain cold when adding to tissue pieces. Turn on the centrifuge ahead of time, and allow sufficient time to cool to operating temperature of 4°C.
2. Label all 1.5 ml centrifuge vials. 3 vials are required for each sample, with separate vials designated for 'Homogenate', 'Supernatant' and 'Synaptoneurosome', respectively. (e.g. for sample R123, one vial each is labelled as R123 HOM, R123 SUP and R123 SYN). Place these on ice.
3. Pipette 10µl of 10% SDS solution into each 'Homogenate' and 'Supernatant' vial. Place these vials on ice. [Note 2]
4. Label 1 Lysing Matrix-D tube for each sample. (e.g. for sample R123, write 'R123' clearly on both tube side and cap). Place on ice.
5. Label 1 Ultrafree-MC SV Centrifugal Filter Unit for each sample.
6. Obtain either freshly sectioned tissue samples, or fresh frozen tissue samples, and place vials containing the tissue samples on crushed dry ice.

3.3.5 Synaptoneurosome Preparation - Homogenization

Modern bench-top homogenizers lyse tissue samples using built-in programmable steps. For example, in this protocol, tissues are homogenized at an angular velocity of 6m/s for a duration of 40 s. Furthermore, the Lysing Matrix-D described in this protocol is specifically designed by MP Biomedicals for use with soft brain tissues. Controlling the lysing matrix and the lysing intensity results in a highly reproducible preparation of many samples.

1. Remove the tissue section from the original vial, weigh the sample on a balance, and record the weight. Quickly transfer the sample to the labeled Lysing Matrix-D tube and add cold homogenization buffer to the Lysing Matrix-D tubes. The amount of homogenization buffer required in each vial depends on sample size. Use a ratio of 1ml of homogenization buffer to 0.05g of tissue to determine the volume of homogenization buffer required for each

sample. Record the amount of homogenization buffer added. Cap tubes, and place on ice. [Note 3].

2. Secure Lysing Matrix-D tubes in FastPrep-24 Tissue and Cell Homogenizer. Set the FastPrep-24 to a speed of 6m/s, set the duration to 40 s, and run the FastPrep-24.

3. Inspect vials to ensure samples are completely homogenized. Check for visible chunks of tissue resuspended in the homogenization buffer. If the tissue is not fully homogenized, run all samples for a second time at 6m/s for a duration of 40 s.

4. Remove 90 μ l of homogenized tissue from lysing matrix tubes and transfer it to the labelled 'Homogenate' vial. Gently vortex the sample, and place vial on ice.

3.3.6 Synaptoneurosome Preparation - Micro-MC Spin Tube Filtration

The syringe filtration component of tissue fractionation is replaced with centrifugal filter units in our protocol. The product description for Ultrafree-MC SV Centrifugal Filter Units outlines a range of allowable parameters that can be used with these filter units. First, the recommended speed of 12,000 x g is a qualitative description of the force applied to pass homogenate tissue through the microporous membranes. We optimized the filtration time by measuring the amount of filtrate collected across the range of minutes recommended by Millipore (1-4min). We determined that 4 minutes yields a significantly higher recovery 334 μ l (SEM 22 μ l, n = 4) (Fig 2) of the total original homogenate (500 μ l) than 1 (average 183 μ l, SEM 62 μ l, n=4) or 2 minutes (average 180 μ l, SEM 59 μ l, n=4) (p<0.05). Here we describe our protocol for filtering the homogenate tissue through these filter units.

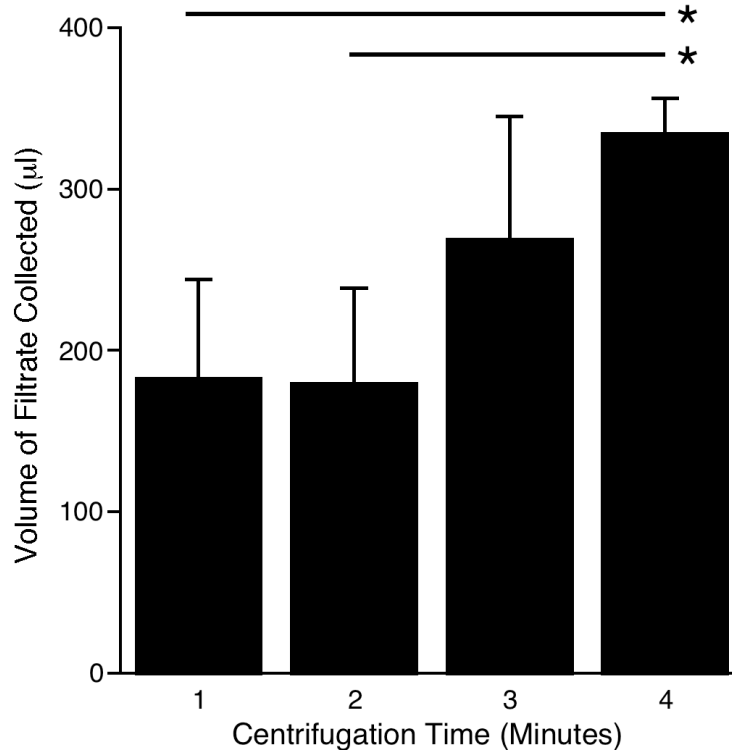


Fig 2. Volume of filtered homogenate tissue collected using Ultrafree-MC SV centrifuge tubes.

Identical amounts of homogenate tissue (500µl) were loaded into filter units of the centrifuge filter units (Millipore) and the percent volume of filtrate was compared across one minute filtration intervals (1-4 min). Centrifugal filtration for 4 minutes yielded greater sample recovery (average 335µl, SEM 22µl, n = 23) than either 1 (average 183µl, SEM 62µl, n=4) ($p < 0.05$) or 2min (average 180µl, SEM 59µl, n=4) ($p < 0.05$).

1. Using a 3 ml syringe equipped with an 18 5/8 G needle tip, take up the remaining homogenate from the Lysing Matrix D-tube and transfer to Ultrafree-MC SV Centrifugal Filter Units. [Note 4]
2. Place the newly filled filter spin tubes in the centrifuge. Set the centrifuge speed to 12,000 x g, the duration for 4 minutes, and run the centrifuge.
3. When complete, remove and inspect the filters to ensure no visible tears occurred. Be sure to note any relevant details pertaining to the condition of the filters. Dispose of empty filter units.
4. Gently vortex all samples.
5. Place the filter spin tubes (now without filters) in the centrifuge. Set the centrifuge speed to 1,000 x g, set the duration for 20 minutes and run the centrifuge.

3.3.7 Synaptoneurosome Preparation - Supernatant

The following sections describe the set of low speed centrifugations that separate heavier synaptic fractions from the lighter supernatant. For the following steps it is imperative that the

remaining tissue in the centrifuged vials is not disturbed since this concentrated pellet now contains all resealed synaptoneurosome entities.

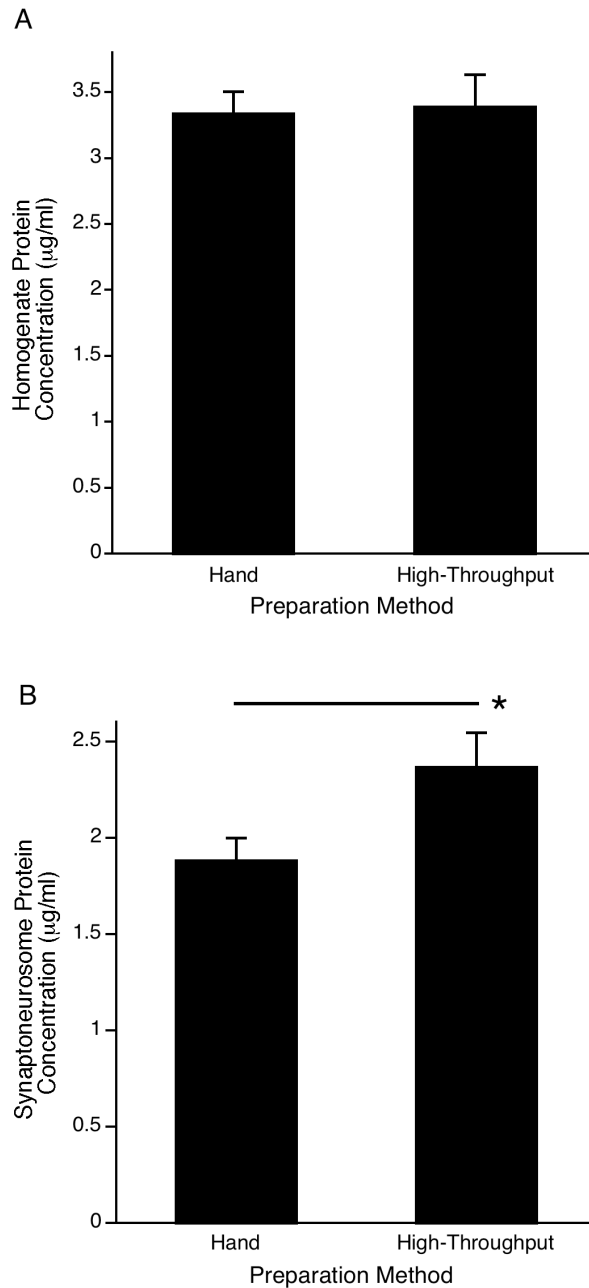


Fig 3. Total protein concentration for the hand or high-throughput techniques measured in (A) homogenate and (B) synaptoneurosome tissue fractions prepared from cat and rat cortical tissues.

(A) There was no difference between total protein concentration measured by BCA assay in the homogenate samples prepared using either the hand (3.34µg/ml, SEM 0.16 µg/ml, n = 50) or high throughput technique (3.43 µg/ml, SEM 0.24 µg/ml, n = 24). (B) There was greater total protein concentration in the synaptoneurosome samples prepared using the high-throughput technique (2.4µg/ml, SEM 0.18µg/ml, n=23) than in the hand preparation (1.88 µg/ml SEM 0.13µg/ml, n=88; p<0.05).

1. Transfer 90 μ l of supernatant tissue from the top of the centrifuged filter vial into the respective 'Supernatant' vial. Vortex the supernatant vial and place the sample on ice.
2. Carefully take up the remaining supernatant material surrounding the pellet with a pipette and expel it into a waste beaker.

3.3.8 Synaptoneurosome Preparation - Synaptoneurosome

1. Turn on the heating block, place vial containing 25 ml of SDS solution (1%) inside the heating block, and bring to a boil.
2. Add 1 ml cold homogenization buffer to 'Synaptoneurosome' vial to re-suspend each pellet and vortex each sample until the pellet has dissolved entirely. Place the vials on ice until ready to proceed to the next step.
3. Place 'Synaptoneurosome' vials in the centrifuge in a counterbalanced fashion. Set the centrifuge speed to 1,000 x g, set the duration for 10 minutes and run the centrifuge.
4. A pellet should once again be collected in the bottom of the vial. Use a pipette to discard the remaining supernatant, being careful not to disturb the pellet.
5. The 'Synaptoneurosome' vials should contain little more than a pellet at this point. Using a pipette, add 100 μ l of boiling SDS solution (1%) to each of the 'Synaptoneurosome' vials, and gently vortex until the pellet is resuspended.
6. 'Homogenate', 'Supernatant' and 'Synaptoneurosome' samples are now prepped. Place all vials in the heating block for a duration of 10 minutes, then store at -20°C.

3.4 BCA Assay and preparing tissue for Western blotting

The total protein concentration from both homogenate and synaptoneurosome tissue can be obtained following bicinchoninic acid (BCA) assay guidelines (Pierce, Rockford, IL, USA). This provides a highly accurate measurement of the total protein available in a tissue preparation before investing in Western blotting. We measured the total protein by performing BCA assays of whole homogenates and synaptoneurosome prepared from rat cortex. We compared total protein concentration between samples prepared following traditional hand preparation using glass-glass Dounce homogenizers or with the new high-throughput FastPrep-24 Tissue and cell homogenizer. We found similar total protein concentrations in whole homogenates prepared by

hand (average = 3.34 $\mu\text{g/ml}$, SEM 0.16 $\mu\text{g/ml}$, $n = 50$) as those prepared using the high throughput preparation (3.43 $\mu\text{g/ml}$, SEM 0.24 $\mu\text{g/ml}$, $n=24$) (Fig 3A). The total protein concentration was greater ($p<0.05$) when synaptoneurosomes were centrifuged using the Ultrafree-MC centrifugal filtration units (2.37 $\mu\text{g/ml}$, SEM 0.18 $\mu\text{g/ml}$, $n = 23$) than when samples were pressure filtered by hand (1.88 $\mu\text{g/ml}$, SEM 0.13 $\mu\text{g/ml}$, $n = 88$) (Fig 3B).

We briefly describe here the BCA protocol to compare total protein concentration between the semi-automated and manual tissue preparations at either the whole homogenate stage or after creating synaptoneurosome.

1. Leaving one column of wells blank, pipette 3 μl each of the 4 different albumin protein standards (e.g. 0.25, 0.5, 1, 2) in order to establish the profile for experimenter pipetting variability. Do this 3 times for each standard. Since multiple samples are loaded multiple times, create a map of your assay plate by assigning samples to specific wells.
2. Gently vortex samples once more before pipetting 3 μl each of 'Homogenate', 'Supernatant' and 'Synaptoneurosome' for each sample. Do this 3 times for each sample.
3. In all wells, add 300 μl of the BCA solution. Place the lid on the protein assay plate, and place the plate in the incubator at 45°C for 45 minutes.
4. Quantify the colorimetric change in the samples by scanning the plate in the iMark Microplate Absorbance Reader (Bio-Rad Laboratories, Hercules, CA, USA). Use the information obtained from this assay to determine total protein concentration in each sample. In an excel spreadsheet, first plot the protein concentration of the 4 pipetted albumin standard (i.e., 0.25 $\mu\text{g/ml}$, 0.5 $\mu\text{g/ml}$, 1 $\mu\text{g/ml}$, and 2 $\mu\text{g/ml}$) against the net light absorbance at the designated wavelength of your spectrophotometer (e.g., 562nm). Plotting a line of best fit will determine the strength of the relationship between protein concentration and absorbance with the function $y=mx+b$. We have stringent guidelines for this step in the protocol and require a minimum correlation of $r^2=0.99$ between the values for these two variables for all protein standards. If $r^2=0.99$ is not achieved, the assay must be re-done.
5. Next, obtain the average absorbance (nm) from the three runs of each sample, and identify total protein concentration ($\mu\text{g/ml}$) by dividing this average by the slope of the function, and adding any linear shift in the function (y-intercept). In this protocol an ideal

final concentration for diluted tissue samples is $1\mu\text{g}/\mu\text{l}$. Use the information about the average protein concentration obtained from the plate reader to dilute samples down to $1\mu\text{g}/\mu\text{l}$. It helps to start with a common volume of tissue (eg. $80\mu\text{l}$) from each 'Homogenate', 'Supernatant' and 'Synaptoneurosome' vial, and transfer this to new vials for use with Western blotting. Dilute samples with Sample loading buffer (4x) and then with laemmli buffer (1x) to weigh samples down for loading into the wells on SDS-PAGE gels, and to equate protein volume across samples.

3.5 Check for synaptic enrichment

We quantified the expression of a specific post-synaptic anchoring protein for glutamatergic receptors, post-synaptic density 95 (PSD95), in both whole homogenate and synaptoneurosome for each sample. We then performed a typical enrichment check by dividing the expression of PSD95 in the synaptoneurosome fraction by the PSD95 expression in the homogenized fraction (Synaptoneurosome/Homogenate). We calculated the amount of enrichment after 1,2,3, and 4 minutes of centrifugal filtration, and found the best enrichment after 4 minutes (Fig 4A). Since 4 minutes of centrifugation produced the greatest amount of synaptic

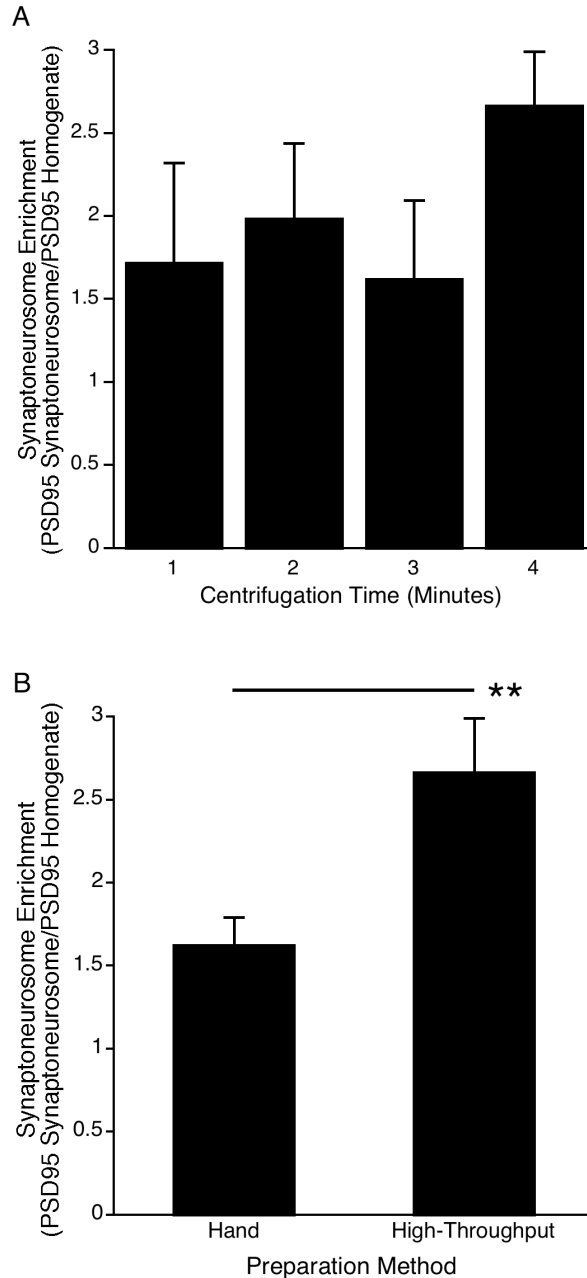


Fig 4. Synaptoneurosomes enrichment of PSD95 expression comparing across (A) different lengths of filtration or (B) hand versus new high-throughput preparation.

(A) Centrifugal filtration for 4min led to better enrichment for PSD95 than 1, 2, or 3 mins (average for 1–3 min was 1.8 X's enrichment, SEM 0.3, n = 12; average for 4 min was 2.7 X's enrichment, SEM 0.3, n = 23) ($p < 0.05$). (B) There was significantly greater enrichment of the synaptoneurosomes prepared using the high-throughput (2.7 X's enrichment, SEM 0.3, n=23) than the hand preparation (1.6 X's enrichment, SEM 0.2, n=24) ($p < 0.01$).

filtrate (Fig 2A) as well as the greatest enrichment, we compared PSD95 enrichment in this subset of samples versus those prepared through traditional manual preparations. We found less than two-fold enrichment (Fig 2B, average 1.6, SEM 0.2, n = 24) in the manual preparation but an average of 2.7-fold enrichment (SEM 0.3, n = 23) using the new high-throughput preparation, with some samples having up to 5 times greater PSD95 expression in the synaptoneurosomes than the homogenate. Importantly, these high enrichment values were obtained using very small tissue samples (25mg) that were orders of magnitude smaller than tissue samples required for the traditional preparation (1000mg)¹.

The synaptoneurosomes fraction is dominated by synaptic proteins, since cytosolic proteins are removed as supernatant at each successive stage of the tissue fractionation protocol. Therefore it is imperative that protein expression is not normalized against classic housekeeping proteins typically used as loading controls in Western blotting experiments, since these proteins are expected to be depleted by the synaptoneurosomes preparation. To demonstrate this, we compared the expression of a classic housekeeping protein, β -tubulin, against PSD95 expression in a subset of homogenate and synaptoneurosomes samples prepared through both the hand and high-throughput techniques (Fig 5). We found greater average β -tubulin expression in the homogenate fraction (1.12) than the synaptoneurosomes (0.06; $p < 0.001$ Fig 5A. light gray), while the opposite is true for PSD95 expression, which again demonstrates higher protein expression in the synaptoneurosomes (0.155) versus the homogenate (0.11; $p < 0.05$ Fig 5A dark grey). This confirms the low expression of β -tubulin in homogenate versus synaptoneurosomes reported by others¹². In fact, an enrichment check performed for β -tubulin produces an anti-enrichment for β -tubulin, while standard enrichment is demonstrated for PSD95 (Fig 5B). It is vital that loading controls are used properly when analyzing a synaptoneurosomes preparation, since normalizing protein expression against a house-keeping proteins that demonstrates anti-enrichment (i.e. enrichment values less than 1) will lead to artificially inflated measurements of expression for proteins of interest.

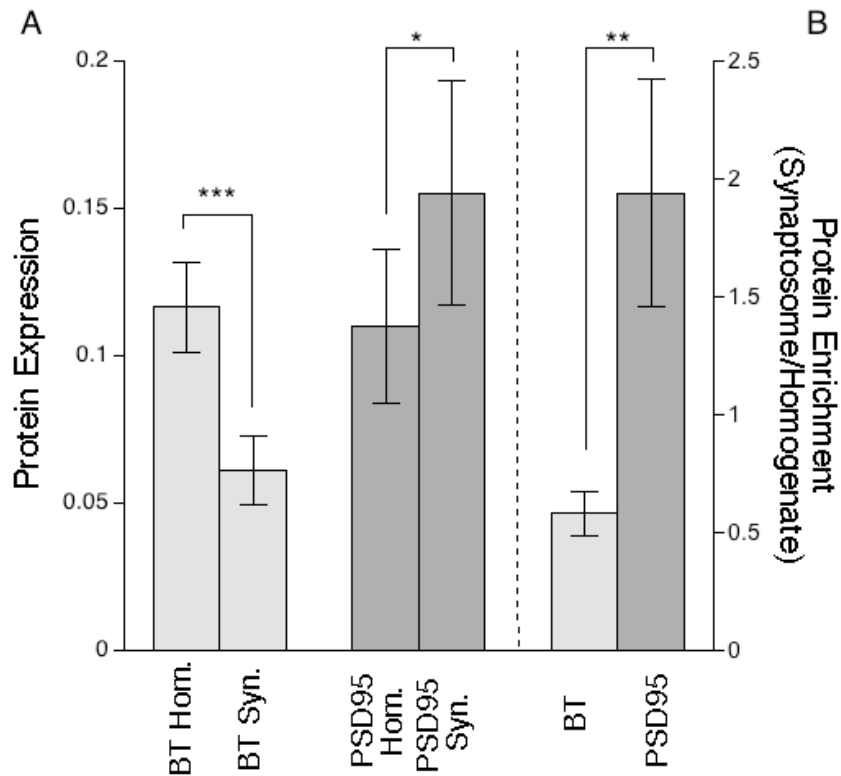


Fig 5. Comparison of β -tubulin and PSD95 expression in whole homogenate and synaptoneuroosomes (A) with matching enrichment (B).

(A) There was less β -tubulin expression in the synaptoneurosome (0.06, SEM= 0.01) than in the whole homogenate sample (0.12 , SEM= 0.02; $p < 0.001$), while PSD95 had greater expression in the synaptoneurosome (0.16 , SEM=0.04) than in the homogenate (0.11 , SEM=0.03) sample. This lead to protein enrichment (>1 X) for PSD95 (1.9X , SEM=0.48) and protein depletion of β -tubulin (0.58 X, SEM=0.10, $p < 0.05$) in the synaptoneurosome fractions.

3.4 Notes

1. One purpose of the homogenization buffer is to slow the process of protein denaturing. There are a variety of homogenization buffers available for purchase, but here we include our in-house design since this combination of calcium chelators and protease inhibitors has proven successful for our Western blotting purposes. Be sure to modify this recipe to suit your own needs.

2. After applying heat, SDS solution coats proteins with an even electric charge, so that electrophoretic separation of proteins is based primarily on size of unfolded proteins. If this is undesirable for your synaptoneurosome preparation, skip this step.

3. Be aware of the total volume of homogenization buffer being added to each Lysing Matrix-D Tube. The current protocol uses smaller pieces of tissue, and the maximum volume these tubes accommodate is 2ml. If you are sectioning larger pieces that require more homogenization buffer, MP Biomedicals make larger lysing matrix tubes that can be used with a larger shaker unit for the Fast-Prep 24 Tissue and cell homogenizer. Ensure you have the proper lysing matrix (Lysing Matrix-D) that is specifically designed for use on soft tissues like cortical tissue, since all parameters in this protocol were designed for use with soft tissue.

4. We advise having extra filter spin tubes ready in case there is excess homogenized tissue. Again be aware of the total volume that these filtration units can accommodate to avoid overfilling vials. These particular units accommodate 500 μ l in the filter unit.

3.5 References

1. Hollingsworth, E. B. et al. Biochemical characterization of a filtered synaptoneurosome preparation from guinea pig cerebral cortex: cyclic adenosine 3':5'-monophosphate-generating systems, receptors, and enzymes. *Journal of Neuroscience* 5, 2240–2253 (1985).
2. Suzdak, P. D. et al. A selective imidazobenzodiazepine antagonist of ethanol in the rat. *Science* 234, 1243–1247 (1986).
3. Suzdak, P. D., Schwartz, R. D., Skolnick, P. & Paul, S. M. Ethanol stimulates gamma-aminobutyric acid receptor-mediated chloride transport in rat brain synaptoneurosomes. *Proc Natl Acad Sci USA* 83, 4071–4075 (1986).
4. Morrow, A. L., Pace, J. R., Purdy, R. H. & Paul, S. M. Characterization of steroid interactions with gamma-aminobutyric acid receptor-gated chloride ion channels: evidence for multiple steroid recognition sites. *Mol. Pharmacol.* 37, 263–270 (1990).
5. Weiler, I. J. et al. Fragile X mental retardation protein is translated near synapses in response to neurotransmitter activation. *Proc Natl Acad Sci USA* 94, 5395–5400 (1997).
6. Wu, L. et al. CPEB-Mediated Cytoplasmic Polyadenylation and the Regulation of Experience-Dependent Translation of β -CaMKII mRNA at Synapses. *Neuron* 21, 1129–1139 (1998).
7. Quinlan, E. M., Olstein, D. H. & Bear, M. F. Bidirectional, experience-dependent regulation of N-methyl-D-aspartate receptor subunit composition in the rat visual cortex during postnatal development. *Proc Natl Acad Sci USA* 96, 12876–12880 (1999).
8. Quinlan, E. M., Philpot, B. D., Huganir, R. L. & Bear, M. F. Rapid, experience-dependent expression of synaptic NMDA receptors in visual cortex in vivo. *Nat Neurosci* 2, 352–357 (1999).
9. HEBB, C. O. & Whittaker, V. P. Intracellular distributions of acetylcholine and choline acetylase. *The Journal of Physiology* 142, 187–196 (1958).
10. Cohen, R. S., Blomberg, F., Berzins, K. & Siekevitz, P. The structure of postsynaptic densities isolated from dog cerebral cortex: I. overall morphology and protein composition. *The Journal of Cell Biology* 74, 181–203 (1977).
11. Weiler, I. J. & Greenough, W. T. Potassium ion stimulation triggers protein translation in synaptoneurosomal polyribosomes. *Molecular and Cellular Neuroscience* (1991).
12. Heynen, A. J., Quinlan, E. M., Bae, D. C. & Bear, M. F. Bidirectional, Activity-Dependent Regulation of Glutamate Receptors in the Adult Hippocampus In Vivo. *Neuron* 28, 1–10 (2000).
13. Murphy, K. M., Tcharnaia, L., Beshara, S. P. & Jones, D. G. Cortical development of AMPA receptor trafficking proteins. *Front Mol Neurosci* 5, 65 (2012).
14. Murphy, K. M., Beston, B. R., Boley, P. M. & Jones, D. G. Development of human visual cortex: A balance between excitatory and inhibitory plasticity mechanisms. *Dev. Psychobiol.* 46, 209–221 (2005).

15. Beston, B. R., Jones, D. G. & Murphy, K. M. Experience-dependent changes in excitatory and inhibitory receptor subunit expression in visual cortex. *Front Synaptic Neurosci* 2, 138 (2010).
16. Williams, K., Irwin, D. A., Jones, D. G. & Murphy, K. M. Dramatic Loss of Ube3A Expression during Aging of the Mammalian Cortex. *Front Aging Neurosci* 2, 18 (2010).
17. Pinto, J. G. A., Hornby, K. R., Jones, D. G. & Murphy, K. M. Developmental changes in GABAergic mechanisms in human visual cortex across the lifespan. *Front Cell Neurosci* 4, 16 (2010).
18. Murphy, K. M., Balsor, J., Beshara, S., Siu, C. & Pinto, J. G. A. A high-throughput semi-automated preparation for filtered synaptoneurosomes. *Journal of Neuroscience Methods* 235, 35–40 (2014).
19. Pinto, J. G. A., Jones, D. G., Williams, C. K. & Murphy, K. M. Characterizing synaptic protein development in human visual cortex enables alignment of synaptic age with rat visual cortex. *Front Neural Circuits* 9, 3 (2015).
20. Beshara, S., Beston, B. R., Pinto, J. G. A. & Murphy, K. M. Effects of Fluoxetine and Visual Experience on Glutamatergic and GABAergic Synaptic Proteins in Adult Rat Visual Cortex. *eNeuro* 2, ENEURO.0126–15.2015 (2015).
21. Siu, C. R., Beshara, S. P., Jones, D. G. & Murphy, K. M. Development of Glutamatergic Proteins in Human Visual Cortex across the Lifespan. *J. Neurosci.* 37, 6031–6042 (2017).
22. Chandler, L. J. & Crews, F. T. Calcium- versus G protein-mediated phosphoinositide Hydrolysis in rat cerebral cortical synaptoneurosomes. *Journal of Neurochemistry* 55, 1022–1030 (1990).
23. Villasana, L. E., Klann, E. & Tejada-Simon, M. V. Rapid isolation of synaptoneurosomes and postsynaptic densities from adult mouse hippocampus. *Journal of Neuroscience Methods* 158, 30–36 (2006).
24. Chang, J. W. et al. Synaptoneurosomes micromethod for fractionation of mouse and human brain, and primary neuronal cultures. *Journal of Neuroscience Methods* 211, 289–295 (2012).
25. Titulaer, M. N. & Ghijsen, W. E. Synaptoneurosomes. A preparation for studying subhippocampal GABAA receptor activity. *Methods Mol. Biol.* 72, 49–59 (1997).

Chapter 4. A primer on high-dimensional data analysis workflows for studying visual cortex development and plasticity

Abstract

New techniques for quantifying large numbers of proteins or genes are transforming the study of plasticity mechanisms in visual cortex (V1) into the era of big data. With those changes comes the challenge of applying new analytical methods designed for high-dimensional data. Studies of V1 can take advantage of the known functions of many proteins for regulating experience-dependent plasticity to link high-dimensional analyses with neurobiological functions. Here we discuss two workflows and provide example R code for analyzing high-dimensional changes in a group of proteins using two data sets. The first data set includes measurements for 7 synaptic proteins from an animal model for amblyopia. The second data set includes 23 neural proteins and 31 ages (20d-80yrs) from human post-mortem samples of V1. Each data set presents different challenges, and we describe using PCA, tSNE, and various clustering algorithms including sparse high-dimensional clustering (RSKC). Also, we describe a new approach for identifying high-dimensional features and using them to construct a plasticity phenotype that identifies neurobiological differences among clusters. We include an R package “v1hdexplorer” that aggregates the various coding packages and custom visualization scripts written in R Studio.

4.1 Introduction

More than 30 years ago, Artola & Singer (Artola and Singer 1987) introduced the field of visual neuroscience to the central roles that NMDA and GABA_A receptors play in regulating plasticity in the visual cortex (V1) and Tsumoto et al. (Tsumoto et al. 1987) showed the enhanced contribution of NMDARs during the critical period (CP). Thousands of experiments followed those studies, targeting specific pre- and post-synaptic proteins and providing an in-depth understanding of how neural proteins enhance or reduce experience-dependent development and plasticity in V1. More recently, proteomic and genomic studies are surveying thousands of proteins and genes to explore novel mechanisms regulating development and plasticity in V1 (Carlyle et al. 2017; Nowakowski et al. 2017).

The shift from studying a few proteins to quantifying tens to thousands of proteins is changing our understanding of visual cortical development and plasticity but it also poses new challenges for data analysis. Here we describe two workflows for using high-dimensional analyses to study the development and plasticity of neural proteins (or genes) in V1. We take advantage of insights gained from previous studies about the role of different proteins in development and plasticity to select a set of proteins to study. Furthermore, working at the level of proteins, we can apply the same techniques to studying V1 in animal models (section 4.3) and humans (section 4.4).

Our aim is to describe the workflows and provide examples for applying high-dimensional analysis of protein (or gene) data using the statistical software R. The examples address how to use the workflow to discover experience-dependent or lifespan changes in plasticity mechanisms. Also, we describe a novel approach for exploring and comparing the neurobiological features that characterize different rearing conditions or age groups that we call the *plasticity phenotype*. The goal of building the plasticity phenotype is to connect the high-dimensional analyses with biologically meaningful insights into V1 plasticity.

Getting started

The first challenge in developing the workflows was to determine which high-dimensional analyses were appropriate for the experimental designs of our studies. Our experiments include many proteins with known roles in neuroplasticity, and often the tissue samples come from

multiple cortical regions. That experimental design has more variables (p) than conditions (n), so the data sets are $p > n$ and are by definition high-dimensional. The data sets are also described as *sparse* because the data points do not fill the space and thus the distance between samples in the high-dimensional space is uneven. This sparse structure means that special consideration is needed in selecting methods for data analysis. First, the methods must support the discovery of clusters that differ on only a few proteins or combinations of proteins (features). Second, those discoveries need to guide meaningful insights into how V1 develops and changes with different forms of visual experience. To this end, we developed workflows that lead to the construction of plasticity phenotypes using features identified by high-dimensional analyses. Also, we implemented a visualization for the plasticity phenotype that facilitates the intuitive exploration of the data.

Here we describe and compare two approaches suitable for analyzing a set of plasticity proteins (or genes) (p) and comparing among rearing conditions (n) or developmental stages (n).

The intent of this paper is not to review high-dimensional analyses or to determine the “best” analysis, but rather to demonstrate and discuss two workflows appropriate for high-dimensional clustering of the data and classifying plasticity phenotypes in the developing visual cortex.

Contributions of this paper:

1) We provide two workflows with examples for identifying clusters in a sparse data set ($p \approx n$ or $p > n$). With each workflow we discuss selection of the analysis steps.

2) We explore different techniques and discuss selecting a clustering method that is appropriate for the data set and research questions.

3) We combine tools for partitioning data into clusters and identifying features. The features are then used to create the plasticity phenotype which aids in discovering biologically meaningful interpretations of the data.

4) We aggregated the various packages and custom visualization code used in this paper into an R package “v1hdexplorer” that is available for download using the function `install_github("balsorjl/ v1hdexplorer")`.

The rest of this paper is organized as follows. In section 4.2, we review some of the high-dimensional data analysis methods that have been used in recent papers studying cortical development. In sections 4.3 and 4.4, we present the workflows with examples using PCA and tSNE, or sparse high-dimensional clustering, and describe how to build and use the plasticity phenotypes. Section 4.5 provides a brief summary and discussion.

4.2 Past work using high-dimensional analysis

Principal Component Analysis: The most commonly used high-dimensional analysis for exploring gene or protein expression in the brain has been principal component analysis (PCA) (Hotelling 1933, Jolliffe and Cadima 2016). PCA transforms the gene or protein data, which is likely to include correlated genes or proteins, into a linear set of uncorrelated principal components that capture successively less of the variance in the data. Thus, individual cases can be visualized and analyzed within the transformed lower-dimensional space and that is often helpful for identifying clusters in the data (Figure 1). For example, a recent survey of human brain development using RNA and protein expression used PCA to reduce the dimensionality of the data and identify differences among brain regions (Carlyle et al. 2017). That analysis highlighted the separation of cerebellar samples from the other brain regions, but it was challenging to interpret the biological significance of the components that differentiate the regions.

The unitless dimensions of PCA components make it hard to identify the biological correlates when thousands of genes or proteins have been quantified and this often leads to the use of pseudo-units (e.g. pseudoage). In contrast, when a targeted set of genes or proteins with known functions are studied then the basis vectors for each component (the weights for each protein) can be used to attach biological significance to otherwise unitless dimensions. For example, after applying PCA to the expression of 7 synaptic proteins from animals reared with normal vision or monocular deprivation (MD), we used the basis vectors to infer that PC1 reflected the sum of the proteins, PC2 an aspect of the excitatory:inhibitory balance, and PC3 the maturational state of the subunit expression (Beston et al. 2010, Balsor et al. 2019; Figure 1B).

In section 4.3, we describe a two-step process for using PCA; first, the typical step for dimension reduction, and second, a new step that expands each dimension using the basis vectors

to identify the biologically relevant features that account for variance in the data. Those features become the building blocks for the *plasticity phenotype* and facilitate interpretation by linking the features with known functions for regulating experience-dependent plasticity. Also, the overall pattern of features can be used to provide robust phenotypic information about the biological correlates that identify clusters in the data. Thus, the plasticity phenotypes help to discover meaningful insights into how V1 matures during normal development or is changed by abnormal visual experience.

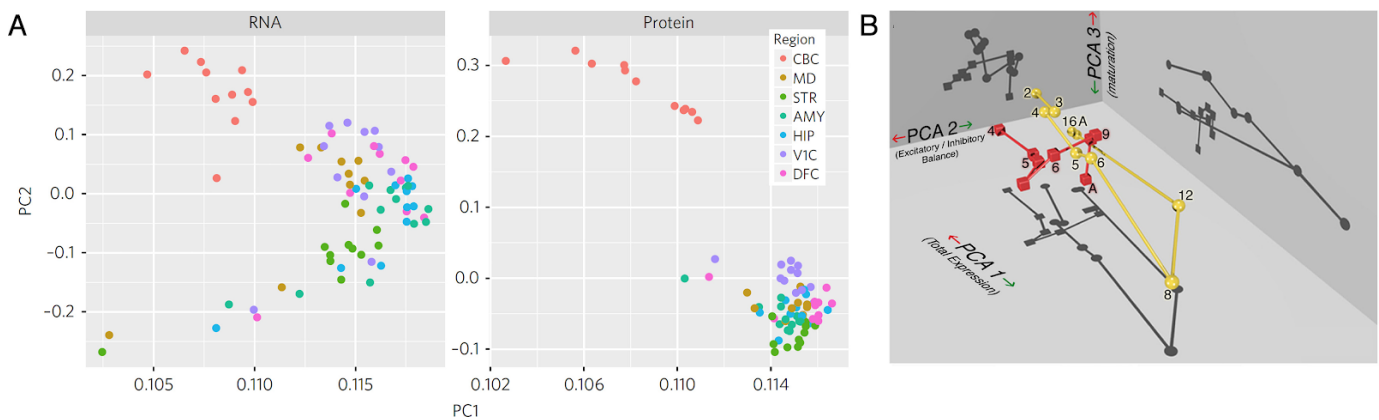


Figure 1. Interpreting PCA dimensions with either thousands or tens of genes or proteins:

(A) Scatter plots for the first two dimensions from a PCA analysis of RNA (5141 genes) or protein (6529 proteins) expression for postmortem tissue samples from 7 regions of the human brain. The plots show a clear separation of cerebellum samples (CBC) from the other brain regions. It is challenging, however, to interpret the biological correlates that differentiate among the regions because the very large number of genes or proteins were reduced to just 2 unitless components. Reprinted with permission from Becky C. Carlyle et al: Springer Nature, Nature Neuroscience, A multiregional proteomic survey of the postnatal human brain, Carlyle et al., 2017 (B) A plot of the first 3 dimensions from a PCA analysis of 7 proteins and 3 regions for normally developing (yellow spheres) or monocularly deprived animals (red spheres). The shadows projected on the three walls help to visualize differences between normal (circles) and deprived (squares) animals. Age (in weeks) is displayed beside each symbol and the connecting lines link the points by age. The biological correlates for each dimension were determined using the basis vectors -- PCA 1 reflects the sum of the protein expression, PCA 2 reflects an aspect of the E:I balance, and PCA 3 reflects the maturation of receptor composition. Reprinted from Beston et al., 2010.

t-Distributed Stochastic Neighbor Embedding: Another popular method for transforming and visualizing high-dimensional data is t-Distributed Stochastic Neighbor Embedding (t-SNE, (Maaten and Hinton 2008)). tSNE measures the shortest distance between pairs of data points, then calculates pairwise probability estimates of similarity across *all* dimensions. Often, these estimates are mapped onto 2-dimensional (2D) space by scaling the distance between data points and positioning similar data points closer together. The new mapping preserves local and global patterns thereby representing the relationships among data

points that may highlight clusters in the data. The artificial scaling makes it easier to identify clusters by either color-coding points based on a known attribute (e.g. cortical area), or by applying a clustering method to the tSNE XY coordinates. Furthermore, the unsupervised nature of tSNE is particularly useful when exploring data without strong a priori knowledge of the expression patterns that may differ among the conditions.

For example, a combination of PCA and tSNE was used to analyze the data from a recent study of single-cell mRNA expression in the developing human brain ((Nowakowski et al. 2017), Figure 2A). In this example, PCA was used to reduce the dimensionality of the data and then tSNE to further reduce the dimensions and visualize clusters (colour-coded dots) of samples (Figure 2B-D). Next, the tSNE plots were used to show clustering by lineage (e.g. CP or GZ) (Figure 2C) and cell type (e.g. DLX1 for MGE derived cells) (Figure 2D).

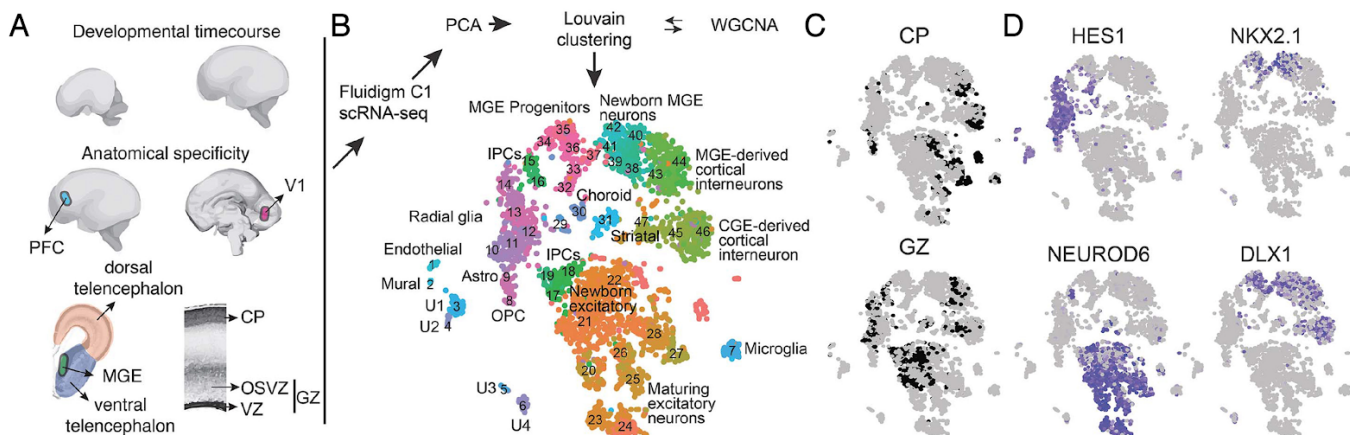


Figure 2. Applying tSNE to human brain cells identifies cell type clusters.

(A) Schematic illustrating sample collection over time, region, and lamina. (B to D) Scatterplot of 4261 cells after principal components analysis and t-stochastic neighbor embedding (tSNE), coloured by (B) cluster, (C) cortical lamina source, and (D) maker gene expression. From Nowakowski, T. J., Bhaduri, A., Pollen, A. A., Alvarado, B., Mostajo-Radji, M. A., Di Lullo, E., ... & Ounadjela, J. R. (2017). Spatiotemporal gene expression trajectories reveal developmental hierarchies of the human cortex. *Science*, 358(6368), 1318-1323. Reprinted with permission from AAAS.

This is a powerful workflow for analyzing and visualizing complex gene or protein data. It is a good illustration of a common approach that starts by reducing the dimensions down to 1-5 components and using those eigenvalues as input to the cluster analysis. However, care is needed when using dimension reduced data as input to clustering because the orthogonal components from PCA may not contain the features need to partition the data into clusters (Chang 1983).

In section 4.3, we describe a modified workflow that uses tSNE to visualize clusters and PCA to select features for constructing plasticity phenotypes but does not use the transformed eigenproteins as the input to the tSNE analysis. We demonstrate this workflow using a data set comparing protein expression in V1 among a set of rearing conditions where animals had either normal visual experience, monocular deprivation (MD) or MD plus a subsequent treatment. We present the steps for this new workflow (section 4.3) and explain how it can be used to explore and interpret cluster composition based on rebranding each sample by their plasticity phenotype.

Other clustering approaches: In addition to PCA and tSNE, there are many other algorithms that can be used to discover the natural clustering of samples based on similar patterns of features. These techniques often employ partitional or hierarchical methods to separate data points into clusters. Partitional clustering refers to an immediate division of data points into non-overlapping clusters, while hierarchical clustering nests closely related samples into a tree-like structure to identify clusters. Hierarchical clusters are built through a top-down (divisive) or bottom-up (agglomerative) approach: top-down begins with all the data in a single cluster that is recursively divided into smaller clusters, or bottom-up begins with each data point in individual clusters that are recursively merged. Hierarchical clustering continues until a designated threshold is met, usually the number of clusters (k). One of the strengths of that approach is the use of a dendrogram to graphically represent clusters by ordering samples with similar features nearby in a tree structure. For example, the matrix in Figure 3B used hierarchical clustering to order the strength of pairwise correlations between brain areas for a set of 123 proteins that are differentially expressed across human development (Figure 3B; (Carlyle et al. 2017)). The strength of the correlations was colour-coded, and the hierarchical ordering made it easy to see the clustering of cerebellar samples based on their poor correlations (blue) with the other areas. It can be difficult, however, to see more subtle differences in the pattern of correlations among the other areas and to select a height in the tree to define more subtle clustering.

The other major class of clustering algorithms, partitional, does not impose hierarchical structure to the data and instead finds all of the clusters at the same time as a partition of the data. K -means is the best known and most widely used partitional clustering method. It starts by partitioning samples into k clusters where the number of clusters is chosen using the gap statistic

to estimate the number of clusters in the data set (Tibshirani et al. 2001). The data are then iteratively repartitioned into different clusters to minimize the within-cluster sum of squares. Since this method is not hierarchical, the clusters cannot be represented in a dendrogram, so K-means or other partitional clustering methods (e.g. Louvain, Infomap, etc) are often visualized using tSNE. For example, in the workflow diagram from Nowakowski et al. (2018) the color-coded clusters in the tSNE plot were identified using Louvain partitional clustering.

Many clustering approaches work well when there is good separation among the features in the protein or gene data set. In contrast, when samples differ on a small fraction of the features or there are more subtle changes in protein expression the typical clustering methods begin to fail and other approaches such as sparse clustering algorithms are needed. The advantage of sparse clustering is that it uses an adaptive selection of a subset of features within hierarchical or K-means clustering and the selection of features is iteratively optimized using a regression-style analysis (e.g. lasso) (Witten et al. 2009).

Finally, whether clustering is done with hierarchical, partitional, or sparse algorithms the same challenge remains -- how to link the holistic exploration of the data with the biological features that differentiate the groups. In previous studies, the task of pinning down those features was often done by sorting through the clusters using a series of plots and univariate analyses aimed at finding proteins or genes that are over- or under-represented in a group (Carlyle et al. 2017; Luo et al. 2017). That approach, however, focuses on measurements from just one variable per sample and thereby loses sight of differences that arise from higher order combinations of protein or gene expression. That problem prompted us to develop a method for discovering combinations of proteins that represent high-dimensional features and then use those features to construct the *plasticity phenotype*. While the idea of a phenotype is not new, our approach to extracting features from the protein data and using them to analyze and visualize the plasticity phenotypes is a novel application in this field of study.

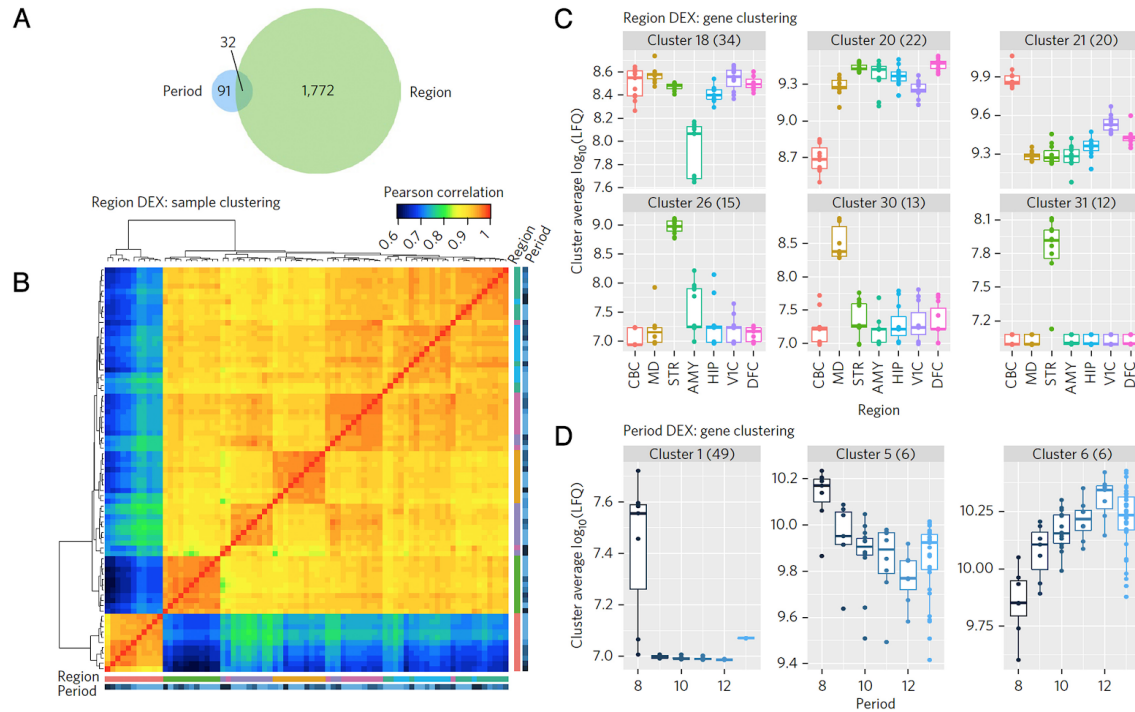


Figure 3. Hierarchical clustering of samples in a correlation matrix.

a. Venn diagram showing the number of genes that were significantly and differentially expressed across developmental periods (left, blue) or brain regions (right, green). **b.** Hierarchical clustering revealed major divisions between brain regions, but less distinct classification based on developmental period. **c-d.** Exploring clusters by region (**c**) reveals region-specific enrichment or depletion and exploring across developmental periods (**d**) reveals developmentally enriched period of protein expression shortly after birth (period 8). Each data point is shown as a dot. Reprinted with permission from Becky C. Carlyle et al: Springer Nature, *Nature Neuroscience*, *A multiregional proteomic survey of the postnatal human brain*, Carlyle et al., 2017.

Example data sets and preparation of the data

In this paper, we used two data sets of neural protein expression in V1 obtained using Western blotting and quantification with densitometry. Each data set was organized into a matrix with n rows of observations (e.g. cases, cortical regions, and number of Western blot runs) and p columns of variables (e.g. # of proteins). The first data set included results from animal studies examining changes in glutamatergic and GABAergic receptor subunit expression during normal development, monocular deprivation (MD), or treatment after MD (Beston et al. 2010, Balsor et al, 2019). The second data set was from a series of studies examining the development of human V1 by measuring expression of a collection of neural plasticity proteins in postmortem tissue samples from cases that range in age from neonates to older adults (Murphy et al. 2005; Pinto et al. 2010; Williams et al. 2010; Pinto et al. 2015; Siu et al. 2015; 2017).

Prior to beginning the high-dimensional analyses described in this paper it is important to inspect and organize the raw data set. First, if using Western blotting ensure that the quantification of the bands did not include artifacts (e.g. bubbles, spots) or poorly labeled bands that could skew the results. Those data points should be omitted, and the missing data can be filled by imputation. A variety of imputation functions have been implemented in R and a package *impute* was developed for microarray data that imputes missing gene or protein expression data using a nearest-neighbor analysis (Hastie et al. 2001).

4.3. Using PCA & tSNE to study experience-dependent changes in visual cortex: Data reduction, feature identification, clustering, plasticity phenotypes

The first workflow describes using PCA to identify features and then clustering of the features with tSNE. A novel aspect of this approach is using the features to construct plasticity phenotypes and applying those phenotypes to rebrand and compare the clusters.

The data set comes from two animal studies of visual cortical development and plasticity (Beston et al. 2010; Balsor et al. 2019) with an $n \times p$ matrix comprised of $n=567$ rows of observations and $p=7$ columns of protein variables (Tables 1&2). The final matrix had 3,969 cells of data and after omitting 602 cells with poor labelling, the final number of data points was 3,367.

Table 1. Observations (n)

Categories	Specific	Total
Rearing Condition	Normal (9), MD (8), Reverse Occlusion (1), Binocular Deprivation (1), Binocular Vision (5)	24
Regions	Central (2), Peripheral (8 or 10), Monocular (2)	12 or 14
WB Runs	1,2	2
	Sum	567

Table 2. Variables (p)

Categories	Specific	Total
Protein	Synapsin I (Syn), GluN1, GluN2A, GluN2B, GluA2, GABA _{Aα1} , GABA _{Aα3}	7

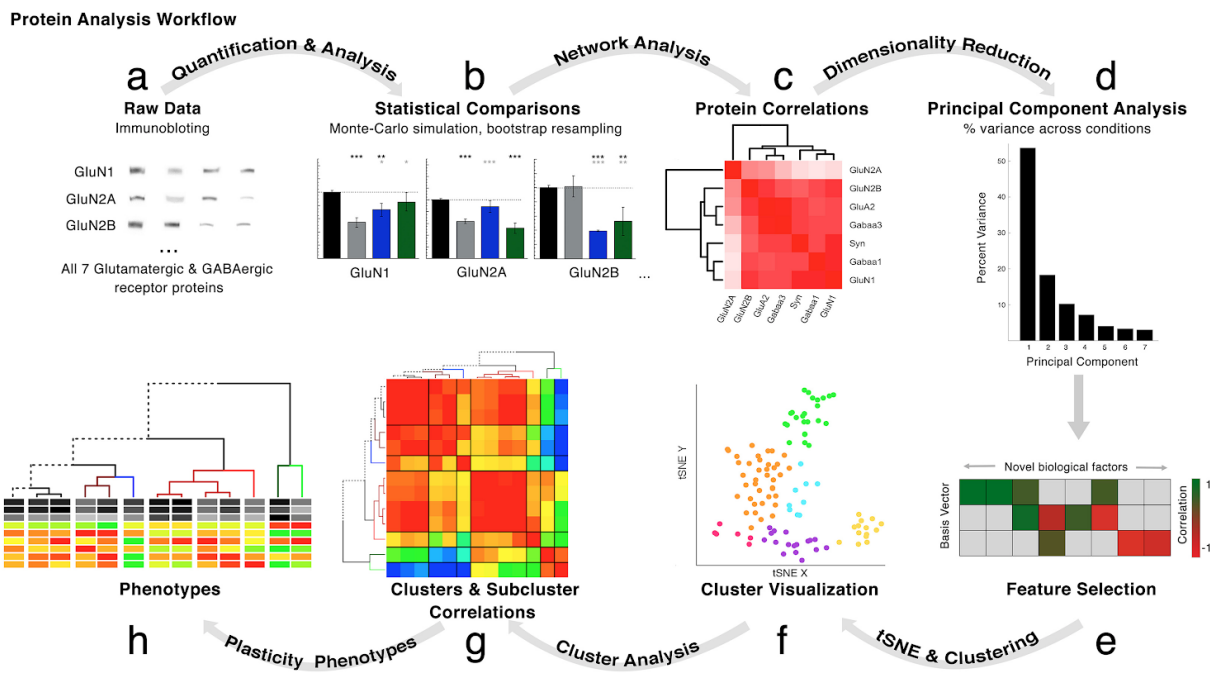


Figure 4. Protein analysis workflow for $p < 10$ and $p \cong n$.

a. Protein expression was collected across 7 proteins using immunoblotting ($N=4232$). **b.** Standard univariate analyses to identify significant differences among the 9 rearing conditions. **c.** Network analyses calculated using Pearson's R between the 7 proteins in each rearing condition. **d.** PCA to explore and **e.** transform features. **f.** tSNE to represent the data in low-dimensional space (2D), then clustering algorithms were applied to the low-dimensional representation of the data. Clusters were annotated and subclusters identified (coloured dots) using known information about the tissue samples (rearing conditions). **g.** Network effects assessed using Pearson's R correlations between clusters & subclusters **h.** Plasticity phenotypes to visualize similarities/differences among subclusters.

4.3.i) Quantification and analysis

The natural first step in the analysis workflow is to find extremes in protein expression that identify significant differences between conditions. Using a series of univariate analyses, however, becomes overwhelming very quickly as the number of genes or proteins quantified increases (Figure 4B). Furthermore, such an approach does not realize the potential of the high-dimensional data set since it is not inclusive of the full repertoire of proteins available. Instead, holistic approaches that examine all proteins can identify patterns in the data that suggest how the biological functions might have changed.

Next, we describe using pairwise correlations and hierarchical clustering to visualize patterns in the data using a 2D correlation heatmap. The organization of positive and negative

correlations provides insight into the network of protein expression in visual cortex and how different visual rearing conditions changed the pattern.

4.3.ii) Network analysis

Visualizing pairwise correlations between proteins was the first step to beginning a holistic analysis of the data. The order of the proteins was sorted by hierarchical clustering so that proteins with similar patterns of correlations were nearby. A dendrogram was used to visualize the tree of protein clusters in the data (Figure 4C).

The analysis was done in R Studio using a series of packages available for download at the Comprehensive R Archive Network (CRAN). These packages include: *Harell Miscellaneous*, *stats*, *dendextend*, *seriation*, and *gplots*.

First, the data file was read in to an object called `my.data`.

```
my.data <- read.csv (file="data.csv", header=TRUE, fill=TRUE, blank.lines.skip=FALSE) (1)
```

Then the data were parsed into subsets representing each of the rearing conditions. The following R coding example (2) demonstrates how to parse the data for the Normal rearing condition (Normal):

```
#Subset protein expression for normal animals: (2)
Normal <- as.matrix(subset(my.data, Rearing Condition=="Normal",
select=c(GluN1,GluN2A,GluN2B,Gabaa1,Gabaa3,GluA2,Syn)))
#Repeat for all rearing conditions
```

A correlation matrix was calculated for each subset of data. There are many packages in R that can calculate Pearson's R correlations. We used the *rcorr* function in the *Harell Miscellaneous* package (*Hmisc*, (Harrell and Dupont 2008)) since it computes a matrix of Pearson's R or Spearman's Rho rank correlation coefficients for all possible pairs of columns of a matrix. The following coding example (3) calculates the Pearson's R for the Normal subset of data:

```
#Compute the Pearson's R for all columns p for the subset 'Normal' (3)
NormalCor<-rcorr(Normal, type =c("pearson"))
#Save the Normal correlation matrix values as a data matrix called 'NormalCorMat'
NormalCorMat<-as.matrix(NormalCor$r)
```

The matrix of Pearson's R correlations was then converted into distance values since those values will be used for the hierarchical clustering. The distance matrix is the inverse of the correlation matrix, so that values represent dissimilarity rather than similarity. This step is necessary for generating the dendrograms that will represent cluster hierarchies. The conversion

from a correlation matrix into a distance matrix was done in R using the `dist` function in the `stats` package (Team 2015).

This coding example (4) converts the correlation matrix for Normal animals (`NormalCorMat`) to a distance matrix:

```
Normal.distance <- dist(as.matrix(NormalCorMat), method = "euclidean") (4)
```

The distance matrix for the proteins was used for hierarchical clustering with the `hclust` function in the `stats` package. Clusters were visualized using a dendrogram to show the branching pattern and distances between proteins. Proteins with similar patterns of correlations were separated by shorter branch distances (y-axis) and fewer branch points.

This coding example (5) calculated the hierarchical clustering of the `Normal.distance` matrix and generated the dendrogram in Figure 5:

```
#Compute hierarchical clusters using the ward.D2 method (5)
```

```
Normal.cluster = hclust(Normal.distance, method = "ward.D2")
```

```
#Compute dendrogram without reordering branches
```

```
Normal.Dendrogram<-as.dendrogram(Normal.cluster) #converts clusters to dendrogram  
plot(Normal.dd)
```

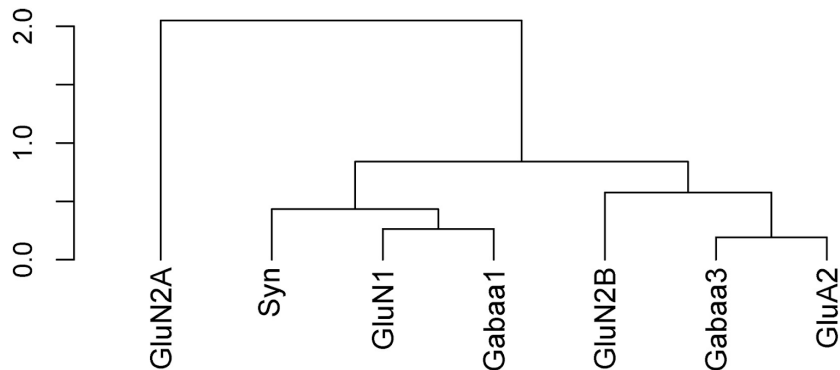


Figure 5. Initial output of hierarchical clustering the Normal distance matrix of proteins.

The distance (y-axis) represents how closely related proteins are, with smaller values indicating a smaller distance and therefore a higher correlation. In this dendrogram, GluN2A is the most dissimilar to all other proteins. Depending on the height of the cut level, this dendrogram can be parse into any number of clusters (k).

The last step was to create the colour-coded correlation matrix with surrounding dendrogram in Figure 6 using the `heatmap.2` function from the `gplots` package (Warnes et al. 2016). The correlation matrix (`NormalCorMat`) and dendrogram (`NormalDendrogram`) were the inputs for this example code (6). The colour scheme of the correlation matrix was adjusted by selecting an appropriate colour palette using the `col` parameter, and the limits of the correlation matrix were adjusted to represent the range of Pearson's R correlations using the `breaks` parameter.

```
heatmap.2(NormalCorMat,
Colv=NormalDendrogram, Rowv=NormalDendrogram,
revC=TRUE, breaks=seq(-1,1,length.out=51),
margins =c(6,6), cexRow=1.5, cexCol=1.5, col=redbluecolours,
dendrogram="both", trace="none", density.info='histogram',
key.xlab=NA, key.ylab=NA, key.title="Pearsons' R",
lhei=c(1.75,8), lwid=c(3,8), keysize=.75, par(cex.main=10), srtCol = 65,
key.xtickfun=function() {
breaks <- parent.frame()$breaks
return(list(
at=parent.frame()$scale01(c(breaks[1],0,
breaks[length(breaks)])),
labels=c(as.character(breaks[1]),0,
as.character(breaks[length(breaks)]))
))
})
```

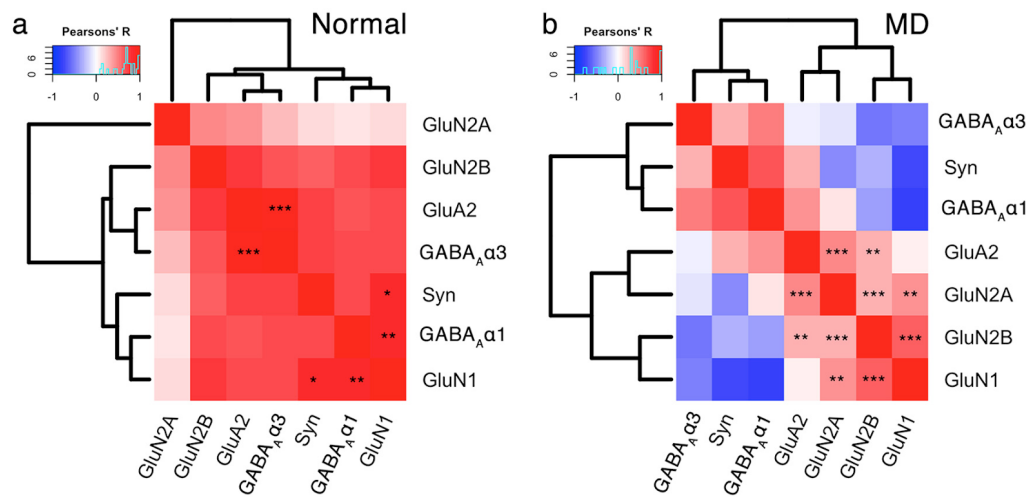


Figure 6. Correlation matrices for protein expression in Normal and MD animals.

a. The output of the coding example for the Normal animals reveals most proteins have positive correlations with each other. **b.** The same code was used on the subset of MD data to create a correlation matrix, distance matrix and dendrogram. The MD plot shows that the excitatory proteins are positively correlated with one another, the inhibitory are positively correlated with one another, but excitatory proteins are negatively correlated with inhibitory proteins.

The examples above illustrate the information that can be readily visualized in a 2D correlation heatmaps. This analysis helped to identify the pairs of proteins (e.g., GluN1 and GABA_Aα1) that had different relationships after abnormal visual experience.

A final note: the dendrogram package *dendextend* (Galili 2015) provides additional control for dendrogram attributes such as line style, thickness, and colour. Also, the *seriation* package (Hahsler et al. 2008) allows rotation of child branches to improve visualization. For example, in the MD heatmap above the first branch separates positive and negative correlations and using the *seriation* package that branch could be rotated so the blue cells are on the top left and the red cells on the top right. This control can be helpful for highlighting the pattern of correlations for particular proteins in the study.

4.3.iii) Dimension reduction

The next part of the analysis workflow uses PCA to explore the high-dimensional nature of the data. We have implemented a two-step procedure that starts by reducing the dimensionality of the data and then uses the basis vectors for those dimensions to identify candidate biological features that capture the variance in the data.

A note of caution: many implementations of PCA do not work well when there are empty cells in the matrix. There are a variety of approaches that can be used, including imputation to fill in the empty cells, removing runs where data are missing for one or more proteins, or averaging across runs. In this example, we averaged protein expression across runs.

This section is not an overview of PCA and we encourage readers to go to the online tutorials to learn more about applying PCA to biological data. It is important, however, to emphasize that our use of PCA is a data-driven approach to protein analysis because the variables (p) were *only* protein expression and did not include any of the categorical information such as treatment condition, cortical area or age.

This coding example (7) starts by extracting the columns (3-9) from `my.data` that contained protein expression.

```
Protein<- my.data[,3:9] (7)
#Column 1 and 3 contain the Condition and cortical area; here we select proteins 1-7 by calling
#columns 3:9
```

The first step for performing PCA was to center and scale the data so that proteins with abundant expression did not obscure proteins with smaller but still significant variations in expression. Each protein was scaled and centered producing a standard deviation of ± 1 , and a mean of zero. Scaling data in R was done using the following example (8) of the base function *scale*:

```
data.scaled <- scale(Protein, center = TRUE, scale = TRUE) (8)
```

There are a variety of packages in R to do PCA, and here we used the *PCA* function in the *FactoMineR* package (Lê et al. 2008). That package produces eigenvalues and comes with excellent visualization tools to aid exploration of the relationships between principal components and features in the data set.

First, we ran PCA on the scaled data set `data.scaled` and saved the result as the object `pca`.

```
pca <- PCA(data.scaled, ncp=m, scale.unit=FALSE, graph = FALSE) (9)
#scale.unit can be set to TRUE if data set was not scaled in earlier steps
#graph can be set to TRUE to visualize the data set in the new PCA dimensions
```

Principal components (PC) returned by this function are the set of orthogonal vectors in the object `pca` identifying the variance in `data.scaled`. The eigenvalues represent the magnitude of the variance captured by each PC vector, and the eigenvalue is largest for PC1 and successively less for each subsequent PC. An in-depth explanation of PCA and eigenvectors can be found here (Jolliffe and Cadima 2016).

The eigenvalues for each PC were identified by consulting the `pca` object as follows:

```
eig.val <- get_eigenvalue(pca) (10)
```

The first step of dimension reduction was to identify how much variance was captured by each PC, then rank the PCs from largest to smallest, and lastly, retain the set of PCs that capture a significant amount of the variance. Start with a Scree plot (Figure 7) showing the amount of variance explained by each of the PC dimensions. The following coding example (11) demonstrates how to consult the `pca` object to create a scree plot.

```
fviz_eig(pca, addlabels = FALSE, ylim = c(0, 60), xlim=c(0.5,7.5), ncp=7, barfill="grey", (11)
barcolor="grey", geom="bar")+
scale_y_continuous(expand =c(0,0))+scale_x_discrete(expand =c(0,0))+
theme(axis.line.y=element_line(), axis.line.x=element_line(), panel.grid=element_blank())
```

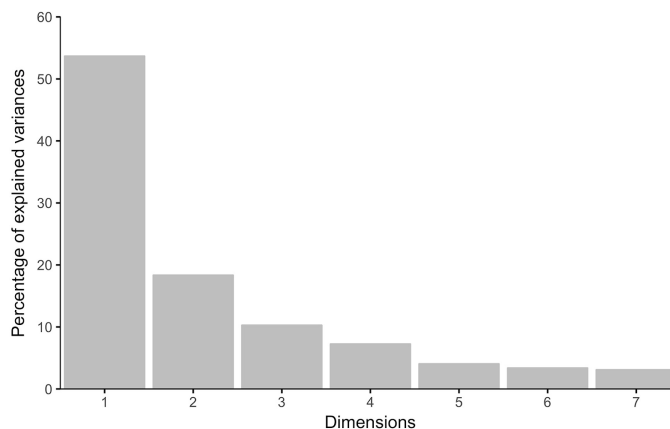


Figure 7. Scree plot of the percentage of explained variance captured by each principal component.

The amount of cumulative explained variance over the first 3 dimensions is >80%. Typically, the first 3 dimensions are used at the cutoff value for reducing dimensionality. The remaining 4 dimensions each contain <7% variance.

The Scree plot (Figure 7) shows the decreasing magnitude for the variance explained by the 7 PC vectors. A variety of methods have been used to identify the significant dimensions (Minka

2001; Hoyle 2008) and here we used the simple rule to retain successive dimensions until the amount of variance explained was $\geq 80\%$. In this example, Dim1-3 explained 82% of the variance.

Once the significant dimensions were identified they were used to select candidate plasticity features driving the variance of each dimension. The 3 significant PC vectors can be represented by the weighted contribution from each the 7 proteins that together make up the basis vectors (Figure 8). Those were used to understand which proteins drove the variance in the data. That information was stored as XY coordinates in the `pca` object and it was called with the following coding example (12).

```
#Identify the amplitudes of protein features relative to PCA 1 (12)
VarCoordDim1<-data.frame(pca$var$coord[,1])
setDT(VarCoordDim1, keep.rownames = TRUE)[]

#Plot the amplitudes of protein features relative to PCA 1 in a histogram
ggplot(data=VarCoordDim1,aes(rn,pca.var.coord...1.))+
  geom_col(colour="black")+
  scale_y_continuous(expand =c(0,0),name="Amplitude (Basis Vector 1)",lim=c(0,0.75),
breaks=c(0,0.25,0.5,0.75))+
  scale_x_discrete(limits=VarCoordDim1$rn)+
  theme(axis.line.y=element_line(),axis.line.x=element_line(),panel.grid=element_blank(),
  axis.text.x = element_text(angle=45,hjust =1,size=12),axis.text.y =
element_text(angle=0,vjust=0.5,size=12),
  axis.title.x=element_text(size=14,face="bold"), axis.title.y=element_text(size=14,face="bold"),
  panel.grid.major = element_blank(), panel.grid.minor = element_blank())
# Run the same code for PCA 2 and 3 to produce histograms of protein amplitude about the remaining 2
dimensions
```

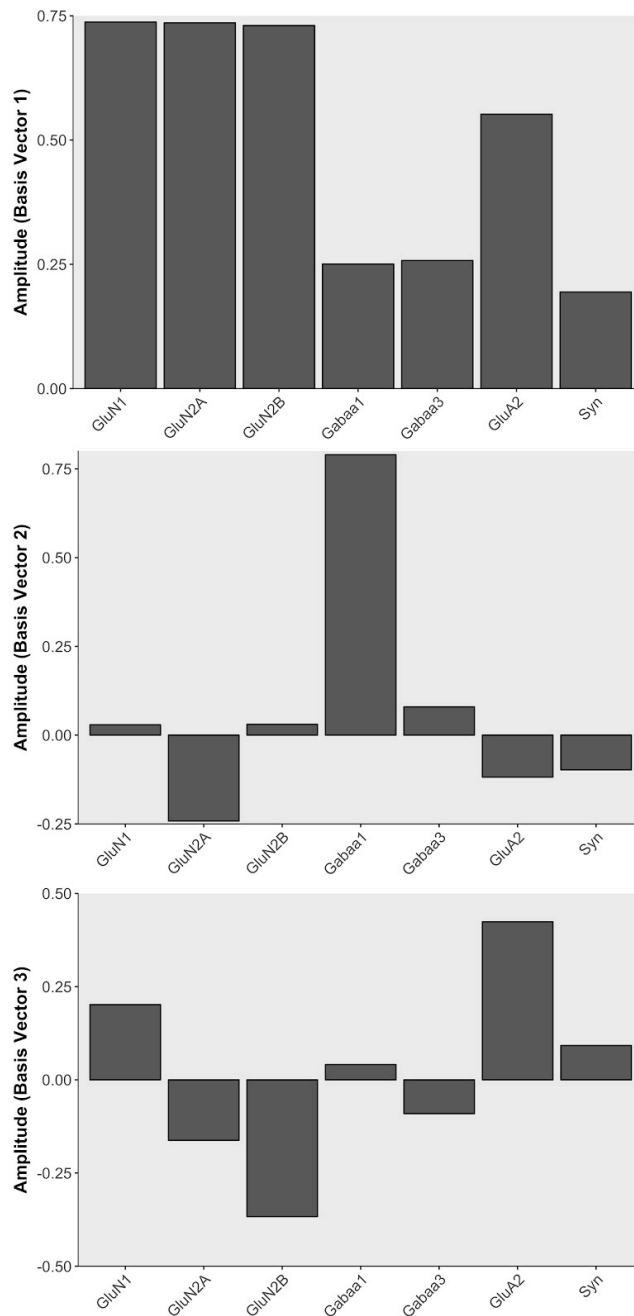


Figure 8. The basis vectors for dimensions 1-3 showing the protein vector amplitudes.

The vectors were used to identify candidate plasticity features. For example, the basis vector for PCA 1 showed that all proteins move in the same direction suggesting that this dimension reflects protein sums (top). The basis vector for PCA2 showed that GluN2A and GABA_Aα1 contribute in opposite directions, suggesting that this dimension reflects a balance between those proteins (middle). The basis vector for PCA3 reflected a balance between GluN2B and GluA2 (bottom).

We used multiple steps to identify candidate plasticity features from each of the basis vectors. Starting with PC1, we noticed that the weights for all the proteins were positive, so 3

candidate features were made using the sum of all proteins, the sum of the glutamatergic proteins, and the sum of the GABAergic proteins. Next PC2 and PC3 were inspected, these basis vectors had both positive and negative weights suggesting that along these dimensions the expression of some proteins increased while others decreased. This inspection revealed some pairs of proteins (e.g., GluN2A:GluN2B) that are known to change in opposite directions with different forms of visual experience. This step also identified novel pairings (e.g., GABA_A α 1:GluN2A) that were also included as candidate features. Continuing this approach, we identified 9 candidate features from the 3 basis vectors, and it is important to note that all were combinations of proteins rather than individual proteins. Thus, this approach to using PCA can be described as an initial dimension reduction followed by expansion into candidate plasticity features. Importantly, the expansion steps will identify both novel features and ones that have been well studied thereby facilitating interpretation of the results within a biologically relevant framework.

4.3.iv) Feature selection

The features were validated by determining the correlation between each of the 9 candidate features and the 3 dimensions. This was done by calculating the 9 candidate features for all of the samples using the protein expression data and correlating those with the eigenvalues for the 3 dimensions. Bonferroni correction was done to adjust the significance level for the multiple correlations and features that were significantly correlated with a dimension became the plasticity features used in subsequent stages of the workflow.

The validation of candidate features was done in R, by storing the new features in a matrix `NewFeatures`, centering and scaling those data, then correlating the eigenvalues with the `NewFeatures` matrix. The function `corr.test` from the `psych` package (Revelle 2011) was used for that step. The strength of the significant correlations was visualized with a custom 2D matrix created using the `geom_tile` function from the `gplots` package (Warnes et al. 2016).

The new features were centered, scaled and stored as a new data matrix:

```
NewFeatures <- scale(NewFeatures, center = TRUE, scale = TRUE) (13)
```

Next, the coordinates for all data points in PCA space were stored in another matrix by consulting the `pca` object as follows:

```
PCA.scores<-pca$ind$coord (14)
```

Finally, the correlations between the two matrices `PCA.scores` and `NewFeatures` were determined and visualized using the following R coding example (15):

```
Corr.scores<-corr.test(PCA.scores[,1:3],NewFeatures,use="pairwise",
method="pearson",adjust="none") (15)
```

```
#produce Pearson's R correlations for only the first 3 dimensions
Corr.scores$p[1:3,]
```

```
#Run a bonferroni correction on the correlation matrix: Corr.scores.bf<-corr.test(PCA.scores[,
1:3],NewFeatures,use="pairwise",method="pearson",adjust="bonferroni")
Corr.scores.Rval<-Corr.scores.bf$r #Pearson's R values between PCs 1-3 & New features
Corr.scores.bfpval<-Corr.scores.bf$p #Bonferroni corrected p-values
```

```
#Before creating the following plot, consult the table of bonferroni corrected p-values (Corr.scores.bfpval),
and omit corresponding cells in the table of R values (Corr.scores.Rval) for which the p-value falls below
significance. The line in the code na.value="grey" will fill leave these cells empty.
```

```
ggplot(Corr.scores.Rval, aes(x = variable, y = Dimension)) +
  geom_tile(data = Corr.scores.Rval, aes(fill = value,width=0.95, height=0.95))+
  scale_fill_continuous(low="red",high="darkgreen",limits=c(-1, 1),
breaks=c(-1,0,1),labels=c(-1,0,1),na.value="grey",name="Correlation")+
  theme(panel.background = element_rect(fill = 'gray95'),
        axis.text.x = element_text(angle=65,hjust=1),panel.grid.major = element_blank(), panel.grid.minor =
element_blank()+
  scale_x_discrete(expand=c(0,0),name="Protein Indices",labels=index.ord
)+scale_y_discrete(expand=c(0,0),limits = rev(unique(sort(j$Dimension))))+coord_fixed(ratio=1)
```

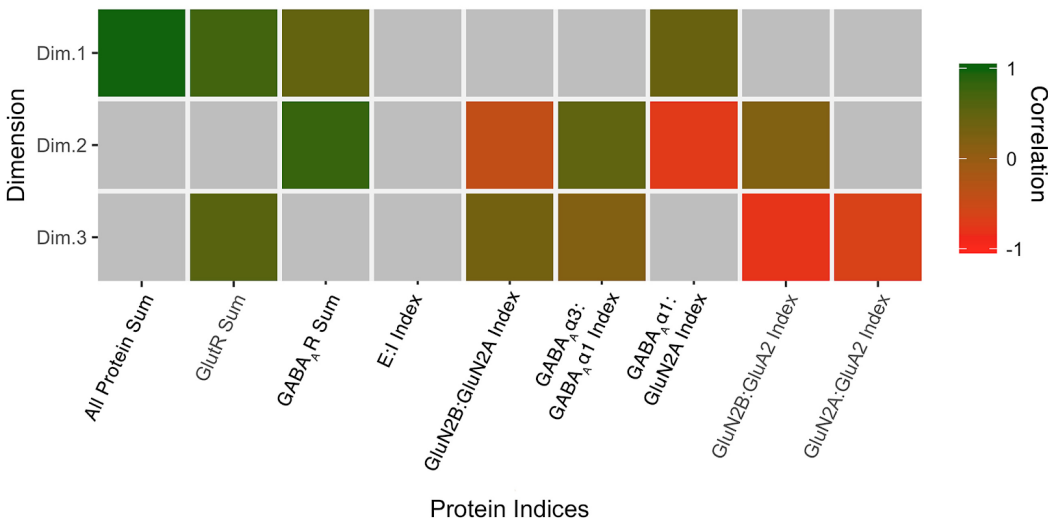


Figure 9. Correlation between the plasticity features (columns) identified using the basis vectors for PCA dimensions 1-3.

Coloured cells are significant, grey cells are non-significant. Bonferroni corrected correlations (green = positive, red = negative).

The plot of correlations between the 3 significant PCA dimensions and the candidate features was used to validate the selection of features for input to the next stage of the analysis workflow (tSNE and clustering). In the example above, all of the candidate features except a measure of the E:I balance was significantly correlated with at least one of the dimensions. Interestingly, none of the features were correlated with all 3 dimensions demonstrating that multiple plasticity features are necessary to capture the variance in the data.

The whole collection of plasticity features was combined to form the plasticity phenotype that became the input to the next step in the analysis workflow.

A final note: the new plasticity features can be analyzed using univariate statistics to determine if there are significant differences among rearing conditions. That analysis is particularly important when feature selection identifies combinations of proteins that are not typically studied since they may provide new insights into the neurobiological mechanisms that differentiate among groups reared with various forms of visual experience.

4.3.v) tSNE and clustering

This step used tSNE analysis to preserve both the global and local arrangement of the plasticity features. Also, tSNE is a good way to visualize clusters because it artificially scales the distance between data points with similar patterns of features.

In this example, the inputs to tSNE were the validated plasticity features (NewFeatures) without the information that identified the source of the sample (e.g., cortical region, rearing condition, or age).

The following coding example (16) demonstrates how to perform a tSNE analysis using the *tsne* function from the *tsne* package (Donaldson and Donaldson 2010).

```
tsne <- Rtsne(NewFeatures, dims = 2, perplexity=25, verbose=TRUE, max_iter = 5000) (16)
```

```
## plotting the results without clustering
```

```
d_tsne_1 = as.data.frame(tsne$Y)
```

```
#append the condition information to the tsne coordinates
```

```
d_tsne_1 = data.frame(d_tsne_1,Labels)
```

```
plot_t<-ggplot(d_tsne_1, aes(x=V1, y=V2, color="black")) +
  geom_point(size=4) + guides(colour=guide_legend(override.aes=list(size=4))) +
  xlab("tSNE2") + ylab("tSNE1") +
  theme_light(base_size=20) +
  theme(axis.text.x=element_blank(),
```

```
axis.text.y=element_blank() +
theme(panel.background = element_rect(fill="white", colour="lightgrey"
,size=1,linetype="solid")) +
theme(legend.position = "bottom")
plot_t
```

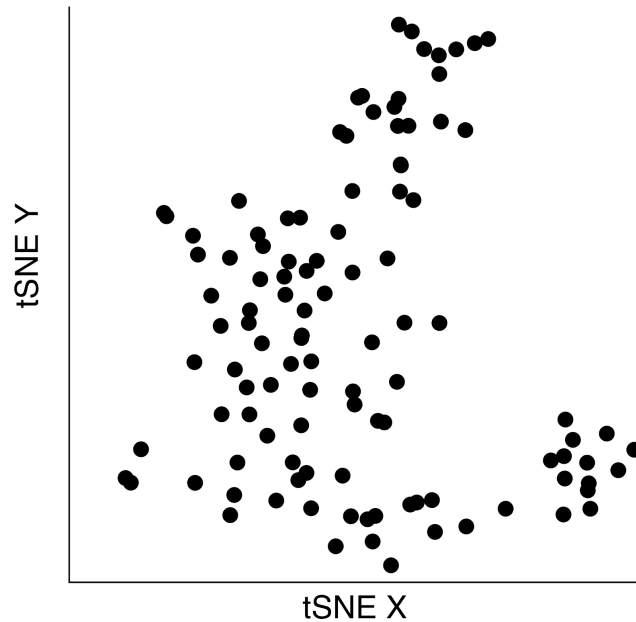


Figure 10. tSNE output when run on NewFeatures identified by PCA.

The dimensions for X and Y in tSNE have no units, but the distance between objects is scaled to position similar samples nearest to one another.

The first step in the tSNE analysis reduced the plasticity features from each sample to tSNE XY coordinates (Figure 10). Those coordinates were used as the input to K-means clustering analysis to identify and then visualize clusters in the data set.

Both K-means and hierarchical clustering algorithms require the number of clusters k as a parameter. A good method for choosing the number of clusters is to measure the within groups sum of squares (WSS) for a range of k , plot that information and then determine the inflection point.

In the example data set there were 9 rearing conditions (e.g. normal, monocular deprivation etc) so we chose a range for k of 2 to 15 clusters, which encompassed the number of conditions.

The following coding example (17) determined the WSS and plotted it for the k clusters:

```
wss <- (nrow(d_tsne_1)-1)*sum(apply(d_tsne_1,2,var))
for (i in 2:15) wss[i] <- sum(kmeans(d_tsne_1,
                                centers=i)$withinss)
plot(1:15, wss, type="b", xlab="Number of Clusters",
     ylab="Within groups sum of squares")
```

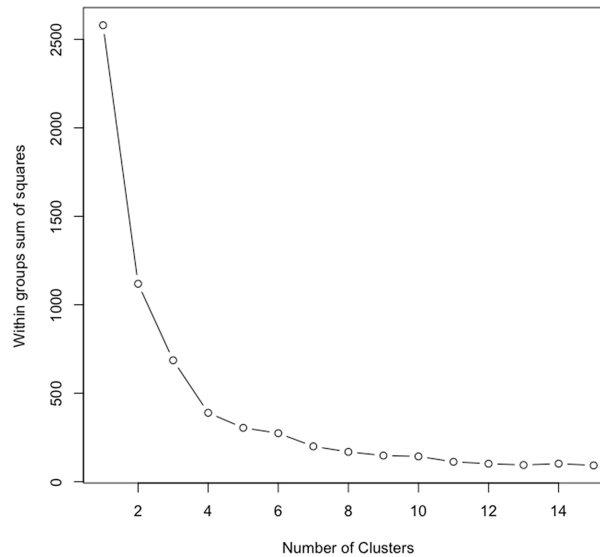


Figure 11. Within group sum of squares for hierarchical clustering of tSNE coordinates in Figure 10.

Sum of squares decreases as cluster number (k) increases. Increasing k has little effect on sum of squares after a certain threshold is met. In this plot it appears that 6 or 7 clusters represents that threshold point. To accurately identify optimal cluster number using this “elbow method” we apply an exponential decay function to the curve and identify the 3τ , the point where 85% of the change has occurred.

The optimal number of clusters was selected by fitting an exponential decay curve to the WSS data the finding the number of clusters corresponding to point where the curve plateaued (4τ) ($k=6$). This approach is called the “elbow method”, where 4τ is the point of inflection, or elbow, of the curve.

Next, K -means clustering for $k=6$ was done on the output from the tSNE analysis (Figure 12a). The clusters were assigned different colours to visualize the samples in each cluster. Some clusters (green and yellow) were spatially separated on the tSNE plot, while others (e.g., orange and blue) were adjacent. The following coding example (18) plots the clusters identified in the tSNE representation of the data as different colors, but these colors can be manipulated to represent other characteristics of the data (e.g. cortical area, treatment condition).

```
kmeans.clusters=kmeans(d_tsne_1[,-1],6)
kmeans.clusters <- as.factor(kmeans.clusters$cluster)
ggplot(d_tsne_1, aes(d_tsne_1$V1, d_tsne_1$V2, color = kmeans.clusters)) + geom_point()
```

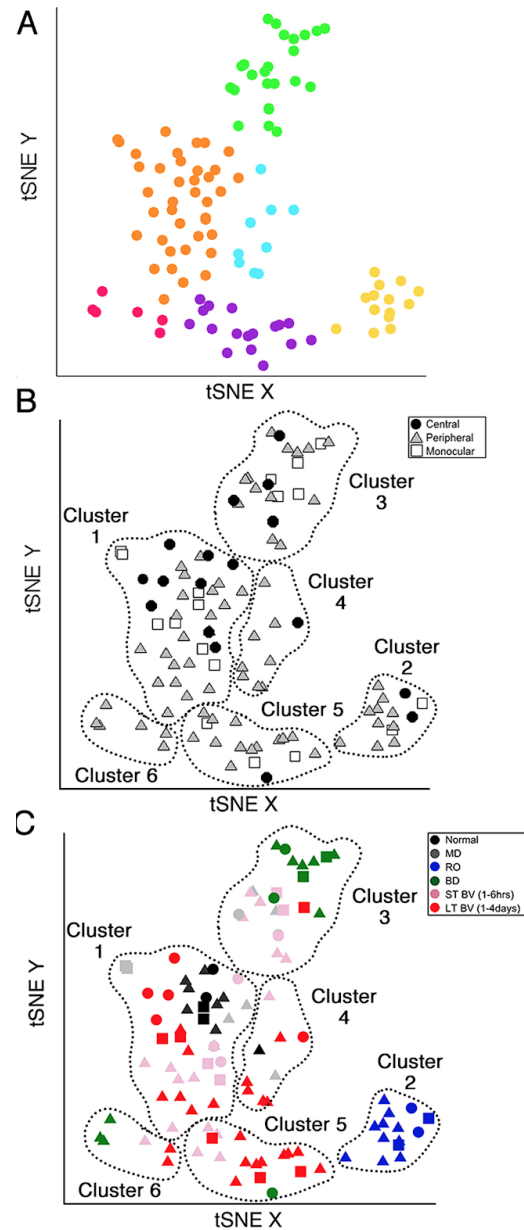


Figure 12. K-means clustering applied to tSNE reduced data.

a. The clusters were colour-coded to visualize the 6 clusters identified in the data. **b.** Samples were annotated for cortical region (black circles=central, grey triangles=peripheral, white squares=monocular) and dashed lines were drawn around the clusters identified in a. **c.** Samples were colour-coded according to the rearing condition, the shapes were the same as in b.

The number of samples in each cluster ranged from 5 (magenta) to 38 samples (orange). We annotated each sample based on the visual cortical region (central, peripheral, or monocular) (Figure 12b) and rearing condition (Figure 12c) to analyze cluster composition and determine if the clustering reflected one of those parameters. For example, cluster 2 contained samples from

only one rearing condition (reverse occlusion) and cluster 1 contained almost all of the normally reared cases but it also had samples from other rearing conditions. Thus, this step identified clusters and provided some evidence that the rearing condition was driving changes in the plasticity phenotypes. The tSNE clustering, however, did not reveal which features from the phenotypes were separating the samples into different clusters or grouping them into the same cluster.

Annotating each sample by the cluster, visual cortical region, and rearing condition was an essential first step for using the plasticity phenotypes to identify and explore *subclusters* in the data. That process identified 13 subclusters in the example data set (Table 3).

Table 3. Subclusters identified from the tSNE plot

Subcluster	Rearing Condition	tSNE Cluster	Region		
			C	P	M
Normal 1 _{C,P,M}	Normal	1	X	X	X
LTBV1 _{C,P,M}	Long term BV recovery	1	X	X	X
MD1 _{P,M}	Monocular deprivation	1		X	X
STBV1 _{C,P,M}	Short term BV recovery	1	X	X	X
RO2 _{C,P,M}	Reverse occlusion	2	X	X	X
STBV3 _{C,P,M}	Short term BV recovery	3	X	X	X
MD3 _{C,P}	Monocular deprivation	3	X	X	
BD3 _{C,P,M}	Binocular deprivation	3	X	X	X
LTBV4 _{P,M}	Long term BV recovery	4		X	X
LTBV5 _{P,M}	Long term BV recovery	5		X	X
STBV5 _P	Short term BV recovery	5		X	
LTBV6 _P	Long term BV recovery	6		X	
BD6 _P	Binocular deprivation	6		X	

A final note: In this workflow, dimensionality reduction and feature selection were performed before tSNE analysis and clustering. Although this is a common approach for analyzing high-dimensional data in neuroscience it is important to remember that PCA preserves the features with variance that is aligned with the orthogonal dimensions. Thus, features with more subtle but important variance away from the PCA dimensions will not be included in

subsequent clustering (Chang 1983). We will return to this issue in section 4.4 where we present a second analysis workflow to handle data with more subtle differences in the features.

4.3.vi) Identifying and exploring subclusters

In this section, we describe how to analyze and visualize subclusters using the features that comprise the plasticity phenotypes.

First, the features and tSNE results were combined in R by appending the object containing the tSNE dimensions and clusters (`d_tsne_1`) to the plasticity features (`NewFeatures`). Now each sample had both the clustering information from the tSNE analysis and the feature data from PCA. Next, the data were organized into subsets according to the subclusters. For example, all of the data points for Normal samples in cluster 1 were subset as follows:

```
Sub.Normal1<- subset(Feature, group=="Normal 1") (19)
mean.Norm1 <- mean(Sub.Normal1)
N.Norm1 <- length(Sub.Normal1)
# repeat for the remaining subclusters of data
```

Next, univariate analyses were done to compare plasticity features between subclusters. Boxplots were made with the *boxplot* function in the *vioplot* package (Adler 2005) and bootstrap tests were used to determine which subclusters were significantly different from the normal subcluster (Supplemental Information).

The significant deviations from normal were colour-coded in the boxplot to facilitate visualizing subclusters where a feature had above (red) or below (blue) normal expression. To include the colour-coding of boxes a column with the information from the significance tests was added to the subset data (e.g., `Sub.Normal1`). For example, clusters that were significantly greater than `mean.Norm1` were identified with the label ‘red’, clusters that were significantly less than `mean.Norm1` with the label ‘blue’, and those that were not significantly different than `mean.Norm1` with the label ‘grey’. That updated collection of subset data were stored in an object called `Clusters.Subsetted`, and the original cluster designation was stored as `Subset.Names`. The following coding example (20) was used to create boxplots of the subsetted data for the feature `GABAAα3:GABAAα1`.

```
boxplot(Clusters.Subsetted.GluN2A.GABAa1, names=Subset.Names) (20)
,col=c("grey",Bootstrap.Colour) ,ylim=limits ,las=2, pchMed=15, colMed="black", rectCol="white",
outline=FALSE)
```

```
stripchart(Clusters.Subsetted ~ Cluster.ID, vertical = TRUE, data = data, method = "jitter", add = TRUE,
pch=20, col=rgb(0,0,0,0.5),opacity=0.5,cex=0.75)
```

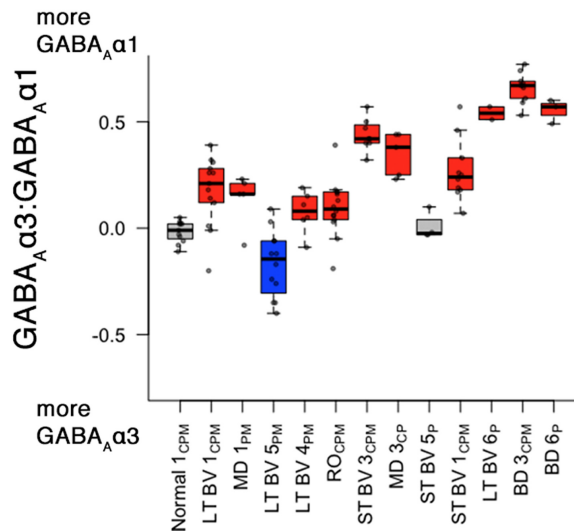


Figure 13. Boxplot for the $GABA_{A\alpha 3}:GABA_{A\alpha 1}$ feature that identified subclusters with expression different from normal.

The original 6 clusters were divided into 13 subclusters, annotated by the original conditions. Boxplots were drawn around the mean expression on the $GABA_{A\alpha 3}:GABA_{A\alpha 1}$ balance. Boxes were coloured relative to normal (red for significantly above, and blue for significantly below). Scatterplots were drawn on top of each boxplot showing the observations within each cluster.

The boxplots were useful for highlighting significantly different subclusters for individual features. For example, the plot above identified 8 subclusters that were significantly greater than normal (red). However, it is daunting trying to synthesize all of the significant differences for 9 features and 13 subclusters using just that approach. Instead, we calculated the pairwise correlations between subclusters using the plasticity phenotypes, ordered the subclusters using hierarchical clustering and visualized these in a 2D heatmap. The steps were the same as explained in coding examples (2)-(6), except the input data for the plasticity phenotypes was `NewFeatures` and the 13 subclusters identified in `Clusters.Subsetted`.

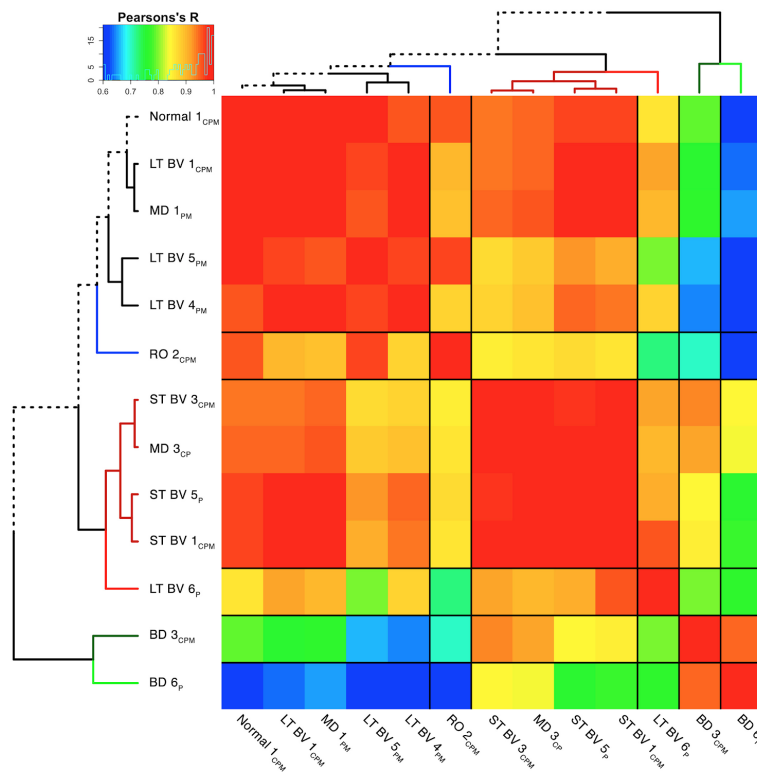


Figure 14. Correlation matrix for plasticity phenotypes between the subclusters of the data.

Matrix of Pearson's R correlations between the means across 8 plasticity features in each subcluster. Clusters were reordered according to the surrounding dendrogram. The dendrogram positioned similar clusters close together, and moved dissimilar samples to the periphery. Inset demonstrates counts across the range of Pearson's correlations, while the color gradient ranges from low positive correlations (blue) to high positive correlations (red).

The correlation matrix for the plasticity phenotypes showed the strength of similarity or dissimilarity among the subclusters. Here, the surrounding dendrogram ordered subclusters for some rearing conditions (e.g., LTBV) on the same branch as the Normal subcluster, while other conditions (e.g., BD) were far from the Normal branch. This analysis revealed which subclusters had similar plasticity phenotypes but did not clarify if that was based on the entire pattern of the features in the phenotype or if a smaller number of features drove the clustering.

4.3.vii) Construct and visualize plasticity phenotypes to identify similar and different features among subclusters

In the last step for this workflow we describe visualizing the plasticity phenotypes, ordering them using the dendrogram from the hierarchical clustering, and comparing phenotypes to identify differences among rearing conditions.

A display was created to show each of the feature and the whole pattern of the plasticity phenotype so that it was easy to compare the subclusters for similarities and differences visually (Figure 15). The visualization had a series of colour-coded horizontal bands where each band represented a feature, and together the 9 bands represented the average plasticity phenotype for a subcluster.

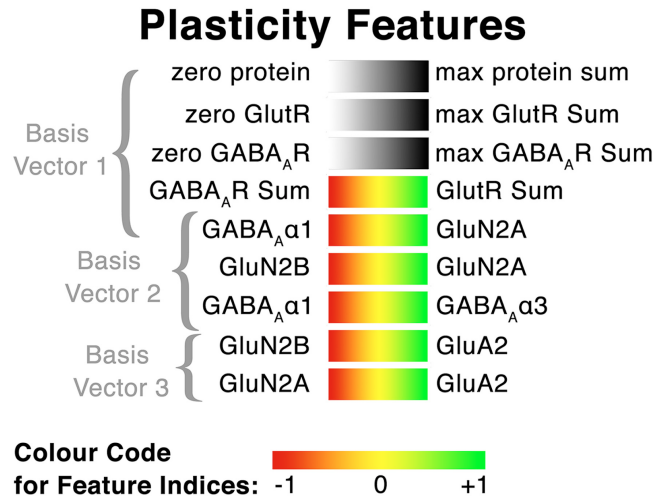


Figure 15. Legend for the features comprised in the plasticity phenotype and the colour-code.

The top three bars (from protein amplitudes about PCA basis vector 1) represent protein sums and use greyscale (white to black) for zero to the maximum protein sum. The next 6 bars represent the feature indices identified with the basis vectors from PC2 and PC3 and use a colour-scale (red to yellow to green) for the shift from one protein to the other.

The plasticity phenotypes were visualized in R, using the *geom_tile* function in the *ggplot2* package (Wickham 2010). First, the feature mean was determined for each subcluster then the limits of the colour scales were set by finding the maximum and minimum expressions for a feature across all subclusters. Finally, the subcluster mean was converted to the corresponding RGB score. The following coding example (21) was used to map the mean for each feature in the Normal condition onto a color scale:

```
GluN2A:GABAAa1.min<-min(subcluster.means)
GluN2A:GABAAa1.max<-max(subcluster.means) (21)
```

```
GluN2A:GABAAa1.range<-(abs(GluN2A:GABAAa1.min)+GluN2A:GABAAa1.max)/2
GluN2A:GABAAa1.mid<- GluN2A:GABAAa1.max-GluN2A:GABAAa1.range
```

```
GluN2A:GABAAa1.col<-scale_colour_gradient2(low="green",mid="yellow",high="red",
midpoint=GluN2A:GABAAa1.mid,
breaks=c(GluN2A:GABAAa1.min,GluN2A:GABAAa1.mid, GluN2A:GABAAa1.max),
```

```
labels=c("Below Normal","Normal","Above Normal"),
limits=c(GluN2A:GABAAa1.min,GluN2A:GABAAa1.max))
```

```
Mat.col.Norm<- Mat.col$map(Mat.mean.Norm)
```

That list of colour-codes for each subcluster was stored in a new matrix called `Colour.Table`. The matrix will be consulted in the code below (22) to call the correct colour for each horizontal bar in the plasticity phenotype.

```
Normal1plot<-ggplot() + (22)
  scale_x_continuous(name="Normal1") +
  scale_y_continuous(name=NULL) +
  theme(axis.text.x=element_blank(),axis.ticks.x=element_blank(),axis.text.y=element_blank(),axis.ticks.y=element_blank(),
        panel.background = element_rect(fill = "white", colour = "white"))+
  geom_rect(mapping=aes(xmin=x1, xmax=x2, ymin=y1, ymax=y2), color="white", alpha=0)+
  geom_rect(data=d,xmin = 1, xmax = 9, ymin = 18, ymax = 19.75, color="black", fill =Colour.Table[3,3])
  +geom_rect(data=d,xmin = 1, xmax = 9, ymin = 16, ymax = 17.75, color="black", fill)
Normal1plot
```

```
#The coordinates must refer to the cell containing colour information for the #desired feature in a particular subset of data
#repeat the above code beginning at colour.table [,] to create as many features as desired.
```

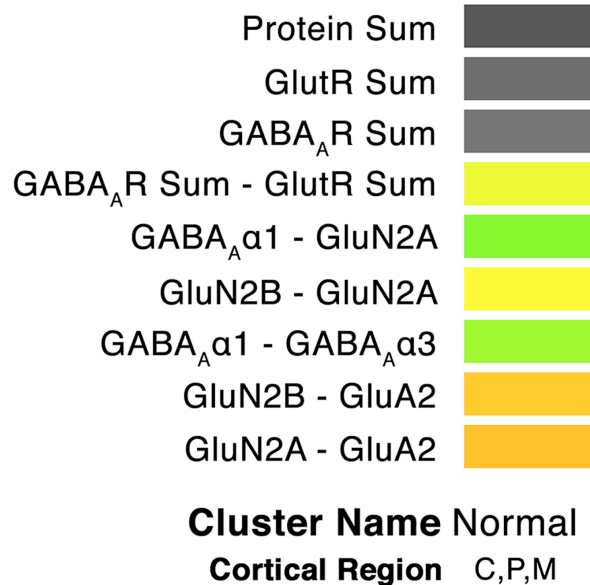


Figure 16. Example plasticity phenotype for the Normal subcluster.

The top three bars depict high levels for the protein sums, while the next 6 bars represent the balance between the protein pairs for that feature using a green-to-red colour scale. The greenish bars indicate features that are biased toward first protein (e.g., GABA_Aα1 versus GluN2A), reddish bars are biased toward the second protein (e.g., GluN2A versus GluA2) and yellow bars reflect roughly equal expression of the two proteins (e.g., GluN2B versus GluN2A).

The figure below (Figure 17) illustrates the power of this tool for visualizing the features and patterns in the plasticity phenotypes that group or separate subclusters.

The subclusters in this example were ordered using the same hierarchical clustering dendrogram as in Figure 14, and the average plasticity phenotype for a subcluster was displayed at the end of its branch in the tree. The figure provides a strong visual impression of the phenotypic similarity among subclusters located nearby in the tree (e.g., normal and LTBV) and differences for subclusters that are further away (e.g., normal and BD). Thus, this tool supports linking the output of high-dimensional analyses with neurobiologically meaningful insights. For the example data set, the visualization revealed the patterns of neural proteins changes driven by different forms of visual experience.

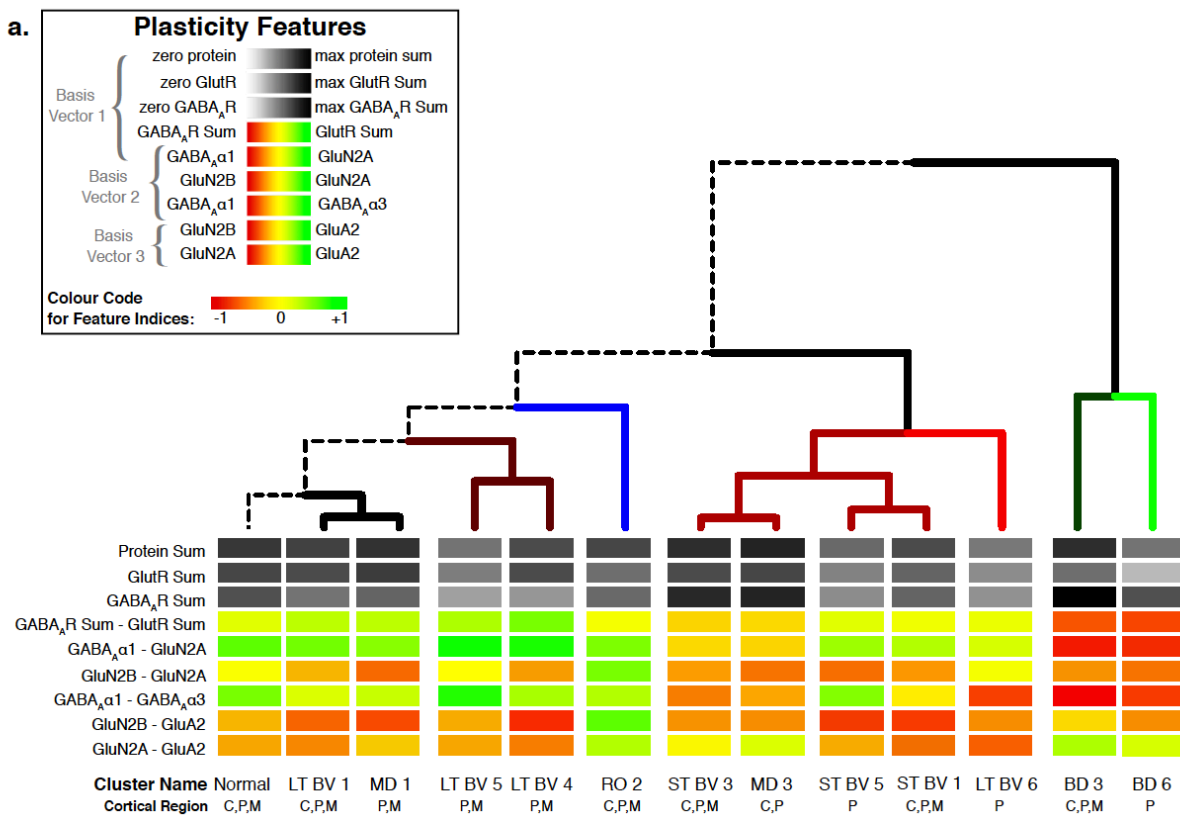


Figure 17. Example of the orderly progression of plasticity phenotypes across subclusters.

The subclusters are noted below the phenotypes, and are arranged according to the dendrogram

Finally, features in a subcluster that are significantly different from normal can be easily visualized by color-coding each bar red for features that are above or blues for ones that are

below normal (Figure 18). We performed a Bootstrap analysis comparing expression of each feature to the Normal subcluster of data points and colored each bar with a mean expression significantly greater than the normal subcluster red, and each bar with a mean expression significantly less than the normal cluster blue. Features that did not significantly differ from Normal subcluster were left empty. The result of that analysis is below.

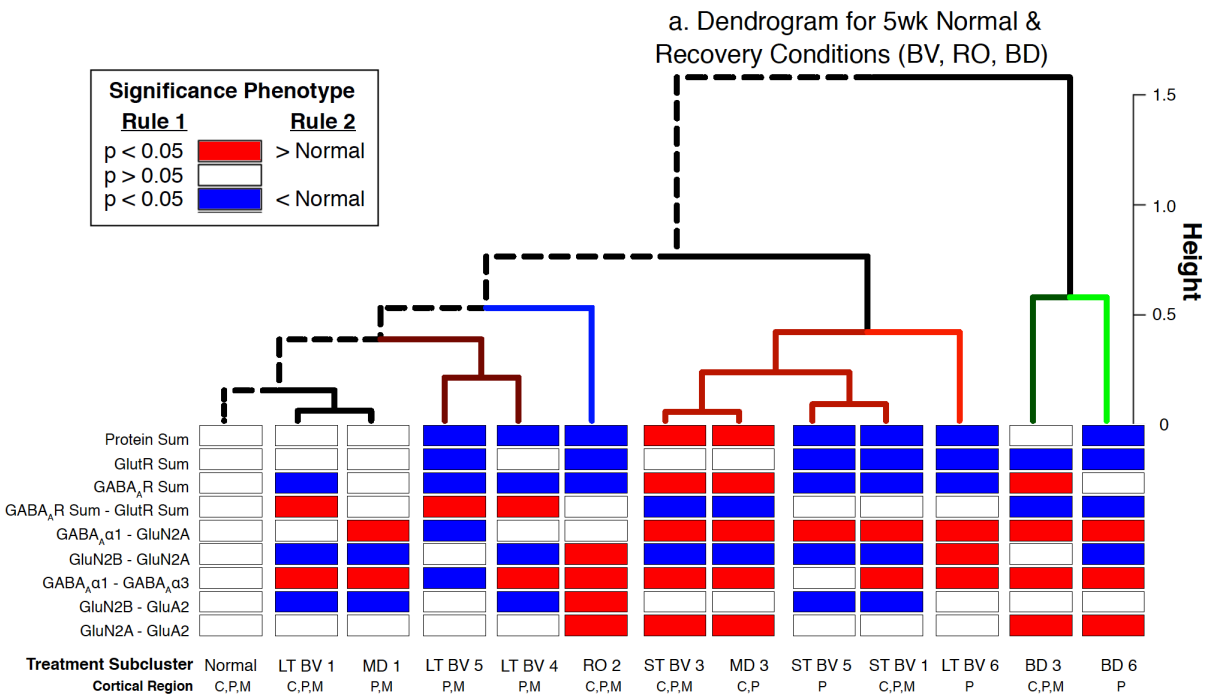


Figure 18. Identifying features of the plasticity phenotypes in the subclusters that are different from normal.

The subclusters are noted below the phenotypes, and are arranged according to the dendrogram. The features in each subcluster phenotype are color-coded to indicate if the feature is significantly greater than (red) or less than (blue) the 5wk normal condition (left most phenotype).

Attaching significance to the color bars makes the visual inspection for cluster-defining features even easier. For example, bootstrap analysis reveals that for the subcluster labelled RO the top three factors were significantly greater than normal, while the bottom 4 factors were significantly less. In figure 17 this was represented as a collection of grey bars stacked above mostly green, but a quick inspection of the phenotype for RO in figure 18 reveals that the significant decreases were in total protein expression (top 3 blue bars) and the significant increases were in the plasticity indices (bottom 4 red bars). The most notable finding from this

new presentation of the phenotypes was that the feature most likely to be not significantly different from normal was the bottom most feature (GluN2A:GluA2 balance), which is formatted as a series of white boxes across the bottom of 7 of the different subclusters.

4.4: Using sparse high-dimensional clustering to study human visual cortical development: Clusters, features, and plasticity phenotypes

The goal of testing sparse high-dimensional clustering methods was to determine if they reveal age-related clusters in the expression of proteins in human visual cortex that provide meaningful insights into the neurobiological development of human cortex.

The second workflow describes the application of sparse high-dimensional clustering, transformation and identification of features using PCA, and exploration of cluster composition using plasticity phenotypes (Figure 19). This workflow moved away from using tSNE and instead applies sparse high-dimensional clustering for analyzing the protein data. In the first workflow (4.3), PCA was used to identify significant features in the data set, and those features were used as the input for the clustering algorithm. In the second workflow (4.4), clusters were first identified in a high-dimensional space, and then PCA was used to further explore significant relationships between the protein features. Importantly, PCA can be used either before or after clustering, provided that the features that are used as the input to the clustering algorithm are significantly correlated with the original data set (as in 4.3.iv).

The data set used here was from a series of studies examining the development of synaptic and nonsynaptic proteins in human visual cortex (Murphy et al. 2005; Pinto et al. 2010; Williams et al. 2010; Pinto et al. 2015; Siu et al. 2015; 2017). The data set created a $n \times p$ matrix comprised of $n=403$ rows of observations and $p=23$ columns of protein variables (Tables 4 & 5). The data were collected from the same tissue samples, across a series of different experiments, and each experimental data set was stacked vertically creating an initial matrix of 9,269 cells and an initial $N=1,831$ data points. The empty cells created by stacking experimental data sets (7,438 empty cells) were reduced by converting protein expression across the 23 protein variables to a sample average for each of the 31 samples, creating a final matrix of 713 cells and a final $N=651$ data points.

Table 4. Observations (*n*)

Categories	Specific	Total
Age	2 days - 79 years	31
WB Runs	2-5	2-5

Table 5. Variables (*p*)

Categories	Specific	Total
Proteins	Gad65 Gad67, VGAT, GABA _A α1, GABA _A α2, GABA _A α3, CB1, Gephyrin, PSD95, Gephyrin from whole homogenate (Gephyrin.HOM), PSD95 from whole homogenate (PSD95.HOM), Synapsin I, Synaptophysin, GluA2, GluN1 (NR1), GluN2A (NR2A), GluN2B (NR2B), Classic-MBP, Golli-MBP, Integrinβ3, GFAP, Ube3A, Drebrin	23

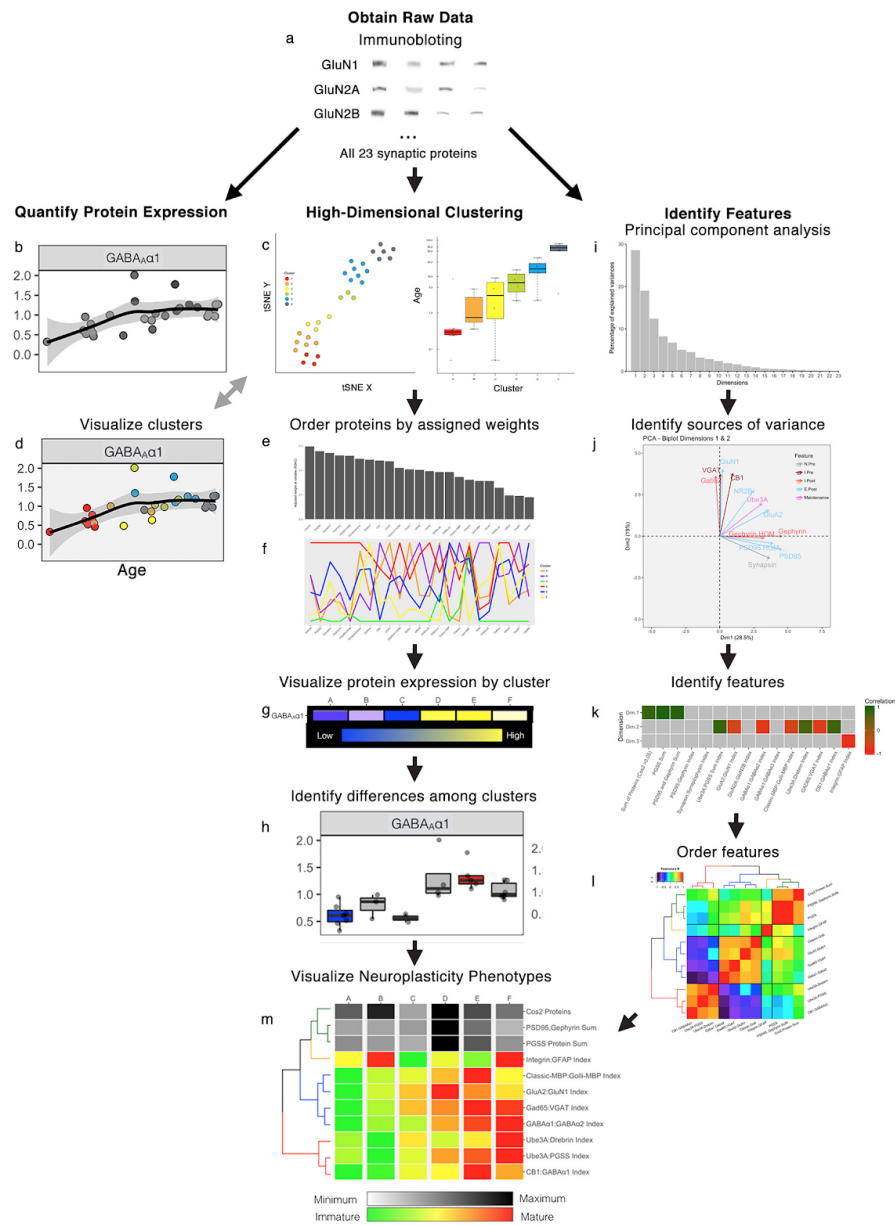


Figure 19. Protein analysis workflow for $p > 20$ and $p \cong n$.

a. Protein expression was collected across 23 proteins using immunoblotting ($N_{\text{final}}=651$). **b.** Developmental trajectory of each protein visualized using scatterplots. **c.** We explored multiple high-dimensional clustering methods to identify underlying patterns across 23 proteins. A tSNE representation of the data was used to visualize the results of each clustering attempt (left), and boxplots of cluster median age were used to visualize developmental separation of clusters (right). **d.** Cluster information was fed into the developmental trajectories to color clusters in scatterplots. **e-f.** The weights attached to each protein after high-dimensional clustering were used to order the protein variables and used to make a parallel coordinates plot of the average scaled protein expression for each cluster. **g.** Protein motifs of the same scaled data in **f** were created as a simple visual inspection tool to identify differences across clusters. **h.** Boxplots of clusters with significantly high or low expression relative to the full course of development. **i.** Principal component analysis (PCA) was performed to identify significant dimensions. **j.** Biplots of protein

vectors visualize variables with the greatest variance. **k.** Identify candidate features and transform the data using the results of PCA and biplot analysis. **l-m.** Correlation matrix of new plasticity features and the surrounding dendrogram (**l**) were used to order the presentation of neuroplasticity phenotypes (**m**).

4.4.i) Challenges identifying clusters in a data set with many features

Clustering of high-dimensional data is challenging because of sparsity in the data set, and for that reason, it is common to use dimension reduction (e.g., PCA) as the first step to identify a smaller number of features that are correlated among the points and drive variance in the data. Then the subsequent clustering focuses on those features. That approach, however, breaks down when the features that differentiate clusters are not orthogonal (Chang 1983). For example, in the current data set, subtle developmental shifts were identified where some proteins are correlated with certain features, while other proteins are correlated with other, non-orthogonal features. These are important considerations when studying cortical development because even a small change in protein expression can have a significant impact on neurobiological function and those changes may be missed by some approaches to high dimensional data analysis.

To overcome the problem that dimension reduction may prune off too much information, or miss more subtle changes in protein expression, we tested a set of sparse clustering algorithms using our human V1 development protein data set as the input. Those algorithms were designed to cluster high-dimensional data with strong sparsity, and here we show that a recent application (RSKC- Kondo et al. 2016) based on the adaptive sparse clustering algorithm from Witten & Tibshirani (2010) performed best for clustering the developmental changes in protein expression. The Witten & Tibshirani algorithm was explicitly designed for sparse clustering of high-dimensional data when the structure of the data set is either $p \approx n$ or $p > n$. That is the structure of the data set used here ($p=23$, $n=31$) and that is generally the case for genomic or proteomic studies of human brain development where measurements are made for many genes or proteins (p) from a smaller number of cases (n).

It is important to note that sparsity in the context of high-dimensional cluster analysis does not mean empty cells in the data set but rather that for any pair of points in a high-dimensional space there are probably a few dimensions that separate them. Standard clustering algorithms like those used in section 4.3 work well for separating data points based on larger differences in feature expression, which exist along orthogonal sets of dimensions. Information for identifying

clusters, however, can come from more subtle differences in feature expression, which exist along non-orthogonal sets of dimensions. Those features are less likely to be captured by clustering algorithms suited for a low-dimensional space. Hence the need to use a clustering algorithm that can adaptively search all sets of dimensions for both the local, non-orthogonal sets of dimensions, as well as global, orthogonal sets of dimensions.

4.4.ii) Sparse high-dimensional clustering to identify communities in the data

Here we describe and compare four sparse high-dimensional clustering methods for analyzing the development of human visual cortex. High-dimensional clustering is an active area of statistics research (e.g., Lakshmi et al. 2017) with many new algorithms and approaches published yearly but the more commonly used ones are reviewed in Parsons et al., 2004.

The 4 clustering methods that we tested were selected because they were developed to find clusters in sparse high-dimensional data. The first two methods, CLIQUE (Agrawal et al. 1998) and PROCLUS (Aggarwal et al. 1999), use projected clustering to discover dense regions, or subspaces of correlated points and find clusters in the corresponding subspace. The CLIQUE algorithm is a bottom-up approach moving from lower to higher dimensionality subspace, but it does not strictly partition points into unique clusters so a data point may be assigned to more than one cluster. CLIQUE is also prone to classifying points as outliers and excluding them from the analysis. PROCLUS was developed to address the partitioning problem and uses a 3-step top-down approach to projected clustering based on medoids. The steps involve initializing the number of clusters (k) and the subspace search size (number of dimensions to consider), then iteratively assigning medoids to find the best clusters for the local dimensions, and a final pass to refine the clusters. PROCLUS has better accuracy than CLIQUE in partitioning points into clusters but the *a priori* selection of cluster size is not easy and demands an iterative approach to finding clusters. Furthermore, by restricting the subspace search size, some essential features may be omitted from the analysis.

Both CLIQUE and PROCLUS were developed for large data sets, 2-3 orders of magnitude larger than the data set used here and that higher information content can lessen the partitioning, outlier, and feature omission problems. For our purposes, we also needed to test sparse

clustering designed for smaller data sets where $p \approx n$ or $p > n$, but that also met the criteria introduced above:

- I. use as many features as possible to identify clusters
- II. group all of the samples into distinct clusters containing at least 3 samples
- III. do not exclude points as outliers

The sparse hierarchical clustering method SPARCL was developed by Witten & Tibshirani (2010), and clusters data points using an application of the lasso regression method to select local subsets of features adaptively. Those subsets are applied by scaling the weight of each variable, the proteins in our data set, to reflect the impact of each protein on the features and the reweighted proteins are the input to K -means hierarchical clustering. In our application, all of the reweighted proteins were part of the clustering but it is possible to drop variables from the clustering component of this approach. The adaptive feature selection of SPARCL focuses on the subset of proteins that underlie the differences among clusters and that process is similar to removing noise from the data. Finally, SPARCL makes it easier to draw meaningful conclusions about why data points are in a cluster because clustering is determined using the subset of features responsible for differences among the data points.

The Witten & Tibshirani sparse clustering algorithm has many strengths for analyzing data sets with $p \approx n$ or $p > n$; however, it can form clusters containing just one observation (Witten and Tibshirani 2010). A recent extension, Robust and Sparse K -means Clustering (RSKC), addresses the issue of small clusters by assuming that those are caused by outlier data points. RSKC uses the same clustering framework as SPARCL, except that it is ‘*robust*’ to outliers (Kondo et al. 2016). RSKC iteratively identifies clusters in the data, then identifies clusters with a small number of data points (e.g., $n=1$) and flags these data points as potential outliers. The outliers are temporarily removed from the analysis, and clustering proceeds as outlined above for SPARCL. Once all clusters have been identified, the outliers are re-inserted in the high-dimensional space and grouped with the nearest neighbour cluster. Thus, RSKC identifies meaningful clusters in the data and includes all of the data points.

Applications

Here we compare four high-dimensional clustering approaches (PROCLUS, CLIQUE, SPARCL, RSKC) using a subset of the proteins in the human visual cortex develop data set. Then describe the application of RSKC to the full set of proteins in the data set.

First, we tested the two density projection clustering methods that use either top-down (PROCLUS) or bottom-up (CLIQUE) clustering methods with all of the observations ($n=31$) and 7 of the proteins from the human visual cortex development data set. The outputs were plotted in 2D using tSNE, and the data points were colour-coded according to the clusters identified by each method. Finally, to determine if the clusters represented developmental changes in the data set we plotted boxplots showing the median ages for each cluster.

PROCLUS: The PROCLUS clustering method was implemented in RStudio using the *ProClus* function in the *subspace* package (Hassani et al. 2015). We explored clusters between $k=2-9$ and the example code below is for $k=2$ clusters.

The data file was read into an object called `my.data2` and the clustering function *ProClus* was called. tSNE was run on `my.data2` to visualize the data points in 2D and the points were color-coded using their cluster identification determined from *ProClus*. The results were saved in `my.proclus.tsne` and that object was used to create the tSNE plots.

```
ProClus.clusters.k2 <- ProClus(my.data2,k=2) (23)
#identify the row ID for samples in each cluster (e.g. ProClus2[[1]]$objects identifies cluster 1 rowIDs)
rows.2.1<-ProClus.clusters.k2[[1]]$objects
rows.2.2<-ProClus.clusters.k2[[2]]$objects

#subset the same rows from the original data file
proclus2.1<-cbind(my.data2[c(rows.2.1),c(1:4)],"Cluster"=1)
proclus2.2<-cbind(my.data2[c(rows.2.2),c(1:4)],"Cluster"=2)

#create a new data.frame that contains the clusters
ProClus.2.df<- rbind(proclus2.1,proclus2.2)
ProClus.2.df$Cluster<-as.factor(ProClus.2.df$Cluster)

#Perform a tSNE analysis to create a 2D representation of the data
my.proclus.tsne<-Rtsne(my.data2, dims = 2, perplexity=25, verbose=TRUE, max_iter = 5000)

#Plot the 2 Clusters and set each cluster to a different colour
colours.clus2<-c("#FF0000","#0000FF")
colours.clus2.all <- colours.clus2[as.numeric(ProClus.2.df$Cluster)]
cols2 <- c("1" = "#FF0000", "2" = "#0000FF")

#Visualize the clusters using the tSNE plot
```

```
ggplot(my.proclus.tSNE, aes(V1, V2)) +
  theme(axis.text.x=element_blank(),axis.ticks.x=element_blank(),axis.text.y=element_blank(),axis.ticks.y=element_blank(),
        panel.background = element_rect(fill = NA, colour = "white"),panel.border = element_blank(),
        axis.line = element_line(),
        legend.direction="vertical",legend.position = c(0.1, 0.8),legend.background = element_rect(fill = NA,
        colour = NA), legend.title.align=0.5)+
  labs(x="V1",y="V2")+
  geom_point(data=proclus2.1,colour="#FF0000",size=8,aes(V1,V2))+
  geom_point(data=proclus2.2,colour="#0000FF",size=7,aes(V1,V2))+
  geom_point(size=1,shape=20,colour="black")
```

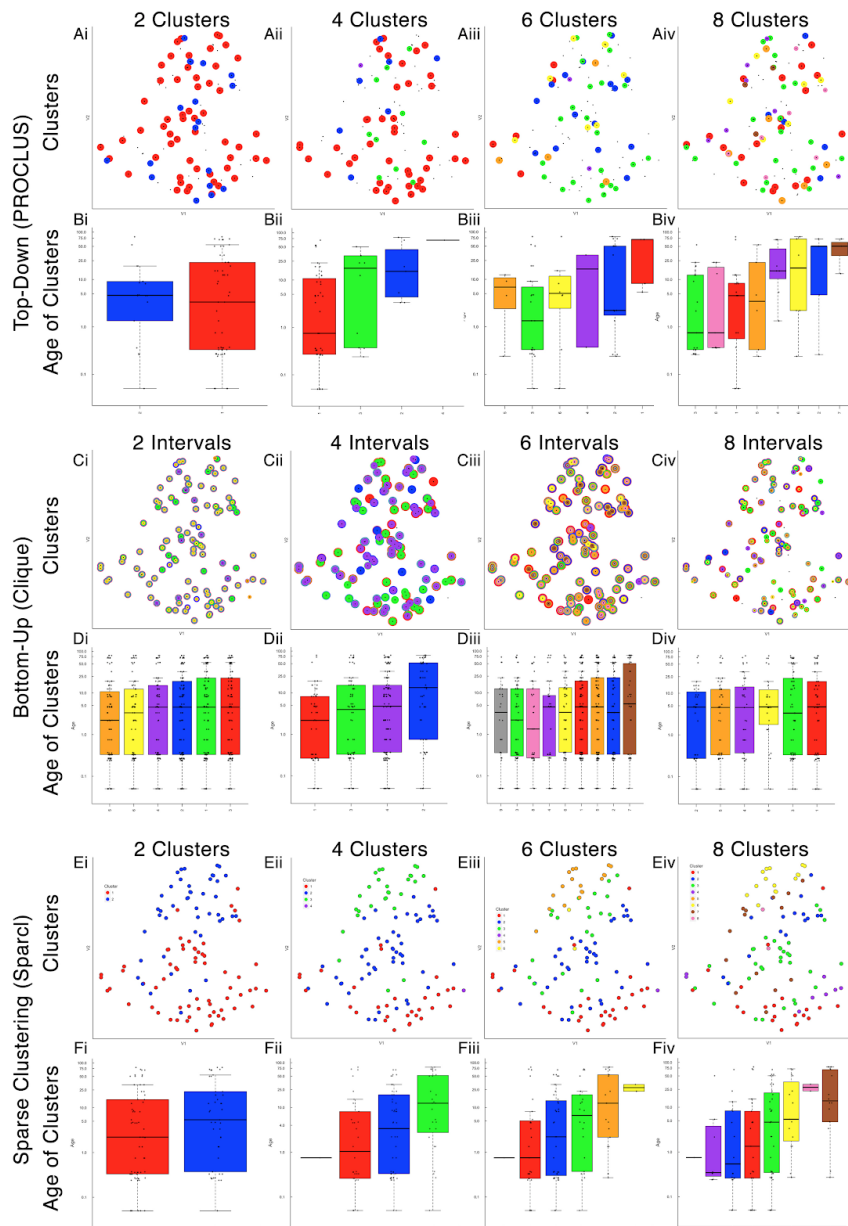


Figure 20. Top-down, bottom-up and sparse subspace clustering.

A-B. Top-down PROCLUS subspace method across range of cluster numbers (2,4,6,8). The clusters are visualized in tSNE representations of the data by color-coding each data point with its cluster identity (Ai-iv) and in histograms showing the median age of the samples in each cluster (Bi-iv). **C-D.** Bottom-up Clique subspace clustering method for a range of 'intervals'. Different clusters are visualized as coloured dots in a tSNE representation of the data (Ci-iv) and as histograms depicting the mean age of the samples (Di-iv). **E-F.** Sparse clustering after varying the inputted k cluster number (2,4,6,8). Different clusters are visualized as coloured dots in a tSNE representation of the data (Ei-iv) and as histograms depicting the mean age of the samples (Fi-iv). The colours in scatterplots and histograms represent the cluster designation for all plots.

In this example, PROCLUS identified clusters but some observations (small grey dots) remained without a cluster designation and were interpreted as outliers (Figure 20A). The outliers remained even after stepping through a range of cluster numbers ($k=2-8$) and some of the clusters had only one or two data points (Figure 20Ai-iii). Furthermore, there was only a weak progression in the median age of the clusters (Figure 20Bi-iii). Thus, the iterative top-down feature identification and cluster border adjustments of PROCLUS performed poorly for analyzing the human visual cortex development data set.

CLIQUE: Next, the bottom-up clustering method CLIQUE was tested to determine how well this iterative approach to building clusters performed with the developmental data.

The *CLIQUE* function from the *subspace* package (Hassani et al. 2015) was used to test clustering with the same data set tested with PROCLUS (`my.data2`). CLIQUE requires an input value for the interval setting (ξ) because the intervals divide each dimension into equal width bins that are searched for dense regions of data points. Here we tested a range of intervals ($\xi=2-8$) that produced 4-9 clusters.

The coding example below (24) used $\xi=2$ as the input interval value and that produced 6 clusters that were visualized in a tSNE plot using `my.clique.tSNE` object (Figure 20 C&D).

```
Clique.intervals2 <- CLIQUE(my.data2,xi=2,tau=0.7) (24)
```

```
#identify the rows in the data for each cluster
rows.2.1<-Clique.intervals2[[1]]$objects
rows.2.2<-Clique.intervals2[[2]]$objects
rows.2.3<-Clique.intervals2[[3]]$objects
rows.2.4<-Clique.intervals2[[4]]$objects
rows.2.5<-Clique.intervals2[[5]]$objects
rows.2.6<-Clique.intervals2[[6]]$objects
```

```
#bind the cluster identity to my.data2
Clique2.1<-cbind(my.data2[c(rows.2.1),c(1:4)],"Cluster"=1) Clique2.2<-cbind(my.data2[c(rows.2.2),c(1:4)],"Cluster"=2)
Clique2.3<-cbind(my.data2[c(rows.2.3),c(1:4)],"Cluster"=3)
Clique2.4<-cbind(my.data2[c(rows.2.4),c(1:4)],"Cluster"=4)
```

```

Clique2.5<-cbind(my.data2[c(rows.2.5),c(1:4)],"Cluster"=5)
Clique2.6<-cbind(my.data2[c(rows.2.6),c(1:4)],"Cluster"=6)

#Create a new data frame that contains the cluster information, and save the clusters as factor
Clique.2.df<- rbind(Clique2.1, Clique2.2, Clique2.3, Clique2.4, Clique2.5, Clique2.6)
Clique.2.df$Cluster<-as.factor(Clique.2.df$Cluster)

#Perform a tSNE analysis to create a 2D representation of the data
my.clique.tSNE<-Rtsne(my.data2, dims = 2, perplexity=25, verbose=TRUE, max_iter = 5000)

#Visualize the clusters using the tSNE information
colours.clus2<-c("#FF0000", "#0000FF", "#00FF00", "#A020F0", "#FFA500", "#FFFF00")
colours.clus2.all <- colours.clus2[as.numeric(Clique.2.df$Cluster)]
cols2 <- c("1" = "#FF0000", "2" = "#0000FF", "3" = "#00FF00", "4" = "#A020F0", "5" = "#FFA500", "6" = "#FFFF00")

ggplot(my.clique.tSNE, aes(V1, V2)) +
  theme(axis.text.x=element_blank(),axis.ticks.x=element_blank(),axis.text.y=element_blank(),axis.ticks.y=element_blank(), panel.background = element_rect(fill = NA, colour = "white"),panel.border = element_blank(), axis.line = element_line(), legend.direction="vertical",legend.position = c(0.1, 0.8),legend.background = element_rect(fill = NA, colour = NA), legend.title.align=0.5)+
  labs(x="V1",y="V2")+
  geom_point(data=Clique2.1,colour="#FF0000",size=8,aes(V1,V2))+
  geom_point(data=Clique2.2,colour="#0000FF",size=7,aes(V1,V2))+
  geom_point(data=Clique2.3,colour="#00FF00",size=6,aes(V1,V2))+
  geom_point(data=Clique2.4,colour="#A020F0",size=5,aes(V1,V2))+
  geom_point(data=Clique2.5,colour="#FFA500",size=4,aes(V1,V2))+
  geom_point(data=Clique2.6,colour="#FFFF00",size=3,aes(V1,V2))+
  geom_point(size=1,shape=20,colour="black")

```

CLIQUE allows data points to be in more than one cluster and to visualize the multi-cluster identities we plotted the data points using concentric color-coded rings. CLIQUE placed all of the data in the developmental data set into multiple overlapping clusters for all of the interval settings ($\xi=2-8$, Figure 20C). That poor partitioning of points resulted in no differences in the median cluster age (Figure 20D). Thus the iterative bottom-up clustering of CLIQUE performed poorly for clustering the developmental data set and did not reveal age-related clustering.

Comparing the top-down PROCLUS and bottom-up CLIQUE methods showed that neither approach was appropriate for analyzing the human visual cortex developmental data set. PROCLUS performed somewhat better because some of the parameters resulted in clusters with a progression in the median cluster age. That better clustering may have been because PROCLUS used a subset of the proteins for each iteration; however, the number of data points treated as outliers was unacceptably high.

SPARCL: We tested a third algorithm, sparse K -means clustering SPACRL (Witten and Tibshirani 2010) that adaptively finds subsets of variables capturing the different dimensions and includes all samples in the clusters. SPARCL searches across multiple dimensions in the data and adjusts the weight of each variable based on their contribution to the clustering. The term ‘sparse’ here refers to the selection of different subsets of proteins to define each cluster, but all samples are assigned to a cluster.

To implement sparse K -means clustering, we used the *Kmeans.sparsecluster* function in the *sparcl* package (Witten and Tibshirani 2013). We explored a range of k clusters between $k=2-9$. The *sparcl* package also includes a function to help determine other input variables such as the boundaries for reweighting the variables (*wbounds*) to produce optimal clustering.

This coding example (25) identifies the optimal *wbounds* setting for $k=2$ clusters:

```
sparcl2.perm<- KMeansSparseCluster.permute(my.data2, K=2, nperms = 50, (25)
wbounds = NULL, silent = FALSE, nvals = 10, centers=NULL)sparcl2.w<-sparcl2.perm$bestw
```

The coding example below calculates sparse clustering for $k=2$ clusters with the *wbounds* found above:

```
sparcl2<-KMeansSparseCluster(my.data2, K=2, wbounds = sparcl2.w, (26)
nstart = 20, silent =FALSE, maxiter=50, centers=NULL)
```

```
#Store the results of the clustering in a dataframe
```

```
sparcl2.clust<-sparcl2[[1]]$Cs
sparcl2.clust<-as.data.frame(sparcl2.clust)
```

```
#Store the rownames as a column for value lookup
```

```
setDT(sparcl2.clust, keep.rownames = TRUE)[]
colnames(sparcl2.clust)[1] <- "Identifier"
colnames(sparcl2.clust)[2] <- "Cluster 2"
sparcl2.clust[,2] <- lapply(sparcl2.clust[,2],as.factor)
```

```
#Perform a tSNE analysis to create a 2D representation of the data
```

```
my.sparcl.tSNE<-Rtsne(my.data2, dims = 2, perplexity=25, verbose=TRUE, max_iter = 5000)
```

```
#Merge the cluster information with the tSNE data frame for visualizing clusters
```

```
full.data<-merge(my.sparcl.tSNE[], sparcl2.clust, by="Identifier")
```

```
colours.clus2<-c("red","blue")
```

```
colours.clus2<-c("#FF0000","#0000FF")
```

```
colours.clus2.all <- colours.clus2[as.numeric(full.data$`Cluster 2`)]
```

```
ggplot(full.data, aes(V1, V2)) +
```

```
  theme(axis.text.x=element_blank(), axis.ticks.x=element_blank(),
axis.text.y=element_blank(),axis.ticks.y=element_blank(),
```

```

panel.background = element_rect(fill = NA, colour = "white"),panel.border = element_blank(),
axis.line = element_line(),
legend.direction="vertical",legend.position = c(0.1, 0.8),
legend.background = element_rect(fill = NA, colour = NA),legend.title.align=0.5)+
scale_color_manual(name="Cluster",values=c(colours.clus2.all),labels=c("1","2"))+ labs(x="V1",y="V2")
+geom_point(size=4,shape=21,colour="black")+
geom_point(size=3.5,aes(colour = `Cluster 2`))

```

RSKC: The clusters found with SPARCL showed good partitioning of the data, and with 4-8 clusters, there was a progression of the median cluster age (Figure 20 E, F). However, some clusters had a small number of data points (e.g. $n=1$). To address that problem we turned to a modified version of the SPARCL algorithm called Robust and Sparse K-means clustering (RSKC) (Kondo et al. 2016). The RSKC algorithm was designed to be robust to the influence of outliers that can drive other algorithms to create clusters of $n=1$. RSKC operates by iteratively omitting outliers from cluster analysis, assigning all remaining samples to clusters, and then reinserting outliers to the analysis by grouping them into the nearest-neighbouring cluster.

We used information from the SPARCL analysis to set the number of clusters to $k=6$ for testing the RSKC method. The *RSKC* function in the *RSKC* package (Kondo et al. 2016) was implemented for this analysis and the code below was used to analyze `my.data2`.

```

sparcl6.robustC<- RSKC(my.data2, 6, alpha=0.1, L1 = 500, nstart = 500, (27)
silent=FALSE, scaling = TRUE, correlation = FALSE)

```

```

#Save the identified clusters for mapping on the tSNE representation as before
robust6C<-sparcl6.robustC$labels
robust6C<- as.factor(robust6C)
sparcl6.robustC$w
avg.data<-cbind(my.data2[,], robust6C)

```

The test of RSKC on the subset of data ($p=7$) gave the best clustering so RSKC was rerun using the full set of 23 proteins. To visualize the 6 clusters from RSKC we multiplied the protein values by the adjusted protein weights from the RSKC clustering algorithm (Figure 22) and used those data as the input to a 2D tSNE plot. The samples were color-coded by the cluster ID to visualize the organization of the clusters (Figure 21A). Next, we ordered the clusters by age from youngest to oldest and plotted those results as a boxplot showing the progression of median cluster age and overlapping ages between the clusters (Figure 21B).

RSKC used all of the data, partitioned all of the samples into a cluster, and none of the clusters had fewer than 3 samples (Figure 21). Thus, RSKC clustering met the criteria we set for selecting a good approach to analyze the visual cortex development data set. Importantly, we analyzed the age progression of the clusters by comparing the observed pattern with a Monte Carlo simulation that randomly assigned the samples into one of the 6 clusters. The age of those randomly assigned clusters showed no progression and they were significantly different from the average age of the observed clusters, making it unlikely that the observed progression in median cluster age (Figure 21B) occurred by chance

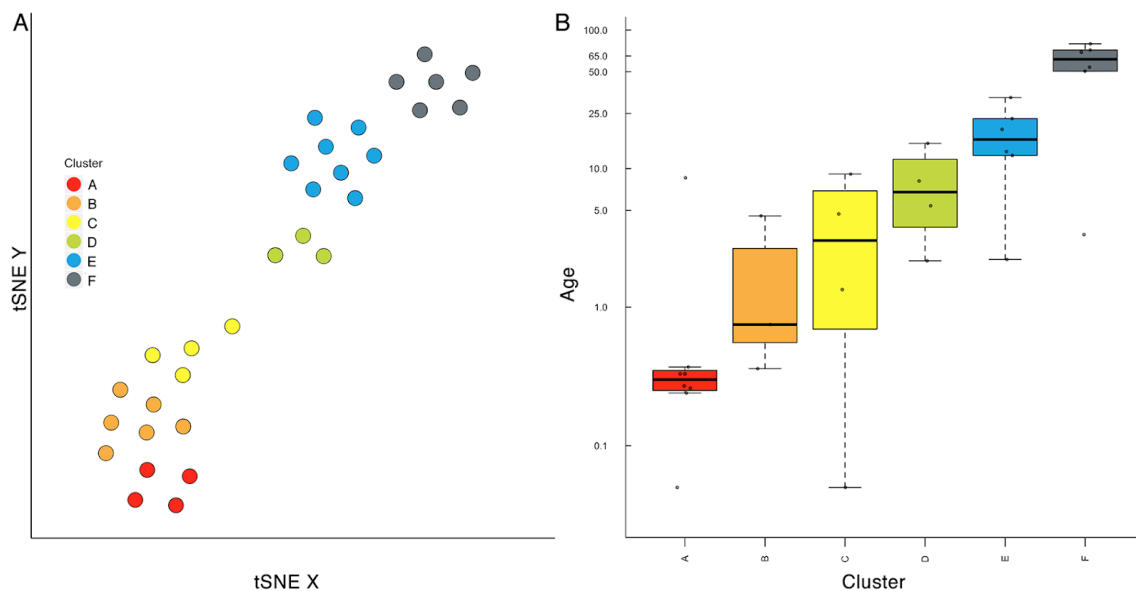


Figure 21. Robust and sparse k-means clustering (RSKC) applied to 23 proteins from the human data set.

A. tSNE plot of the scaled protein data. Sample averages are colored according to cluster results. **B.** Boxplots of cluster age were ordered from youngest (red) to oldest (grey). In both A and B, sample ages were reduced to group averages to reduce crowding

In section 4.4.iii we explain how to explore the RSKC clusters to identify neurobiological features that changed across development.

It is important to note that the WSS metric used in the first workflow to assess the number and quality of the clusters cannot be used with the sparse clustering methods. The lack of a cluster quality metric is because all the data are used with the 4 sparse high-dimensional clustering algorithms, so the number and quality of clusters vary depending on the number of dimensions that are considered. As a result, there is no suitable metric to assess the quality of

clusters in high-dimensions and the different sparse clustering methods must be compared by adjusting the input variables iteratively (Proclus=k, CLIQUE=xi, SPARCL=k, RSKC=k).

4.4.iii) Exploring cluster content

Cluster content was explored with two methods. First, information from the RSKC clustering was used to color-code the samples by their cluster ID and the developmental trajectory was plotted for each protein (Figure 19b,d). Next, the proteins were ordered by their adjusted weights from the RSKC clustering (Figure 22), and the normalized expression of each protein was plotted for the six clusters (Figure 23 & 24).

The second method to study cluster content (Figure 19 i-k) started with identifying features using PCA as described in section 4.3. Then hierarchical clustering was used to order the features and finally, plasticity phenotypes were constructed for each cluster to visualize the neuroplasticity features that change during development of human visual cortex.

Together these approaches to exploring the cluster content provide an understanding of cortical development at the level of individual proteins and higher-level combinations of proteins that define features in the plasticity phenotype.

The following code consults the RSKC object `sparcl6.robustC` to retrieve the weight for each protein and then graphs the proteins in descending order of the weights.

```
#Identify the order of RSKC weights (28)
RSKCvariables<-sparcl6.robustC$weights
RSKCvariables.order<-sort(RSKCvariables,decreasing=TRUE)
RSKCvariables.vector<-order(-RSKCvariables)

#Save the order of RSKC weights as a dataframe
RSKCvariables.order<-data.frame(keyName=names(RSKCvariables.order), value=RSKCvariables.order,
row.names=NULL)

#Plot the weights as a histogram
ggplot(data=RSKCvariables.order,aes(keyName,value))+
  geom_col(colour="black")+
  scale_y_continuous(expand =c(0,0),name="Adjusted variable weights (from RSKC)",lim=c(0,0.3))+
  scale_x_discrete(limits=RSKCvariables.order[,1])+
  theme(axis.line.y=element_line(),axis.line.x=element_line(),panel.grid=element_blank(),
  axis.text.x = element_text(angle=45,hjust =1,size=12),axis.text.y =
element_text(angle=0,vjust=0.5,size=12),
  axis.title.x=element_text(size=14,face="bold"), axis.title.y=element_text(size=14,face="bold"),
  panel.grid.major = element_blank(), panel.grid.minor = element_blank())
```

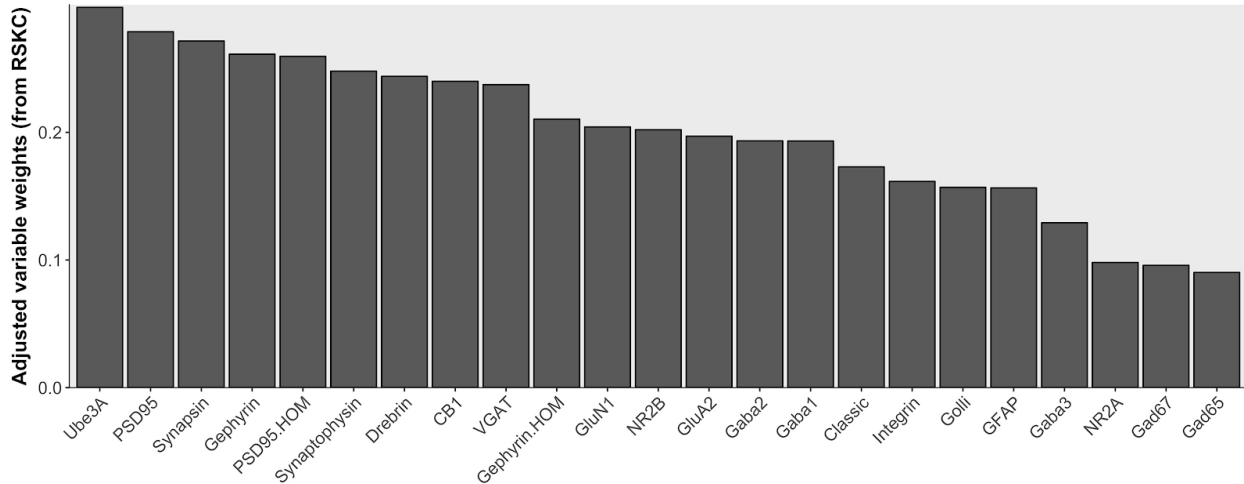


Figure 22. Adjusted weights for the proteins from RSKC.

The proteins are ordered using the adjusted weights from RSKC.

Visualizing the RSKC adjusted weights for the 23 proteins showed an almost 3-fold range in the weighting of the proteins with Ube3A having the maximum and GAD65 the minimum weight (Figure 22). That ordering of the proteins was used along with 2 visualizations of protein expression to explore the influence of different proteins in the clusters. First, we created a parallel coordinate plot for the 6 clusters and 23 proteins that scaled mean protein expression relative to the maximum and minimum cluster average using the *ggparcoord* function in *ggplot2* package (Wickham 2010).

```
ggparcoord(Protein.means,columns=2:24,groupColumn = 1, scale="uniminmax" (29)
,missing="min10",order=RSKCvariables.order,scaleSummary = "mean",
showPoints=FALSE#,alphaLines = 0.25
, mapping=aes(color=as.factor(Group.1)))+
geom_hline(yintercept = 0.5,linetype="dashed",alpha=0.25) +
geom_line(aes(group=factor(Group.1)),size=2) + #somehow works
theme(axis.text.x = element_text(angle = 45,hjust=1),panel.grid.major = element_blank(),
panel.grid.minor = element_blank()+
scale_y_continuous(name="Protein Expression", breaks=c(0,1),labels = c("Min","Max"))+
scale_colour_manual(name = "Cluster",values = ordered6.cols,
breaks=cluster6.order,labels=c("A","B","C","D","E","F"))
```

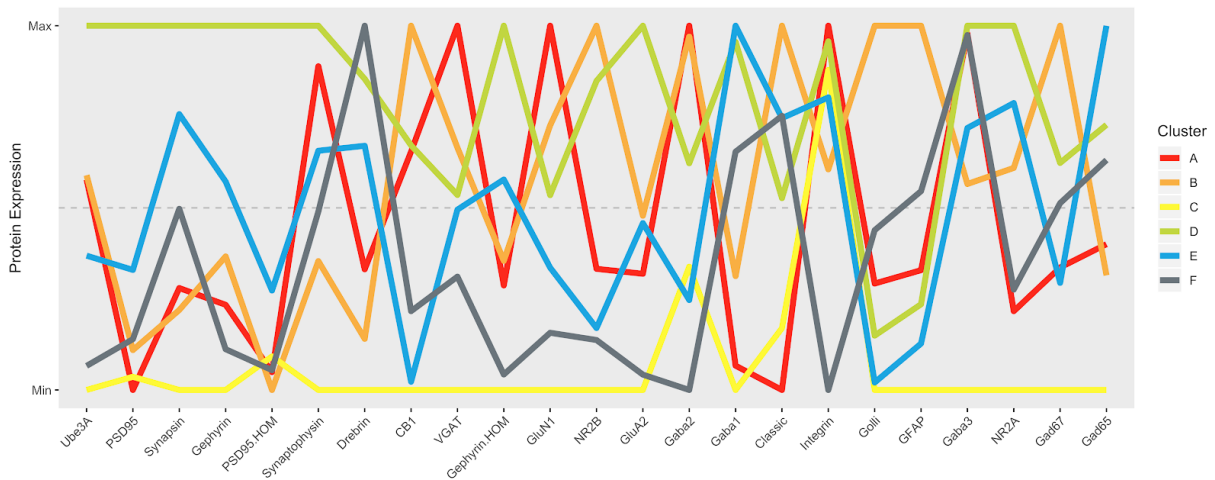


Figure 23. Parallel coordinates of the protein expression in each cluster.

The expression is scaled to the average maximum and minimum expression across all 6 clusters. The colour of the lines is the same conventions for cluster identity as in Figure 21. Proteins were ordered from largest to smallest RSKC weights.

The parallel coordinates plot in Figure 23 showed that the 6 clusters had unique patterns of peaks and valleys in protein expression, and most of the protein peaks were claimed by only one cluster. For example, Cluster D had peak expression for the first 6 proteins (Ube3A, PSD95, Synapsin I, Gephyrin, PSD95HOM and Synaptophysin), then cluster F peaked for Drebrin, cluster B for CB1, cluster A for VGAT and so on. Interestingly, the 4 proteins that had peaks from multiple clusters included the 3 GABA_AR subunits and Integrin β 3.

The information from the parallel coordinates graph can be used to construct a list of protein peaks and valleys for each cluster where those patterns reflect the protein motif for each cluster. Here we visualized the protein motifs for the 6 clusters using the *geom_tile* function in the *gplots* package. The coding for the motif visualization was similar to the method outlined in coding examples (21) and (22) except here it was constructed using the average protein expression.

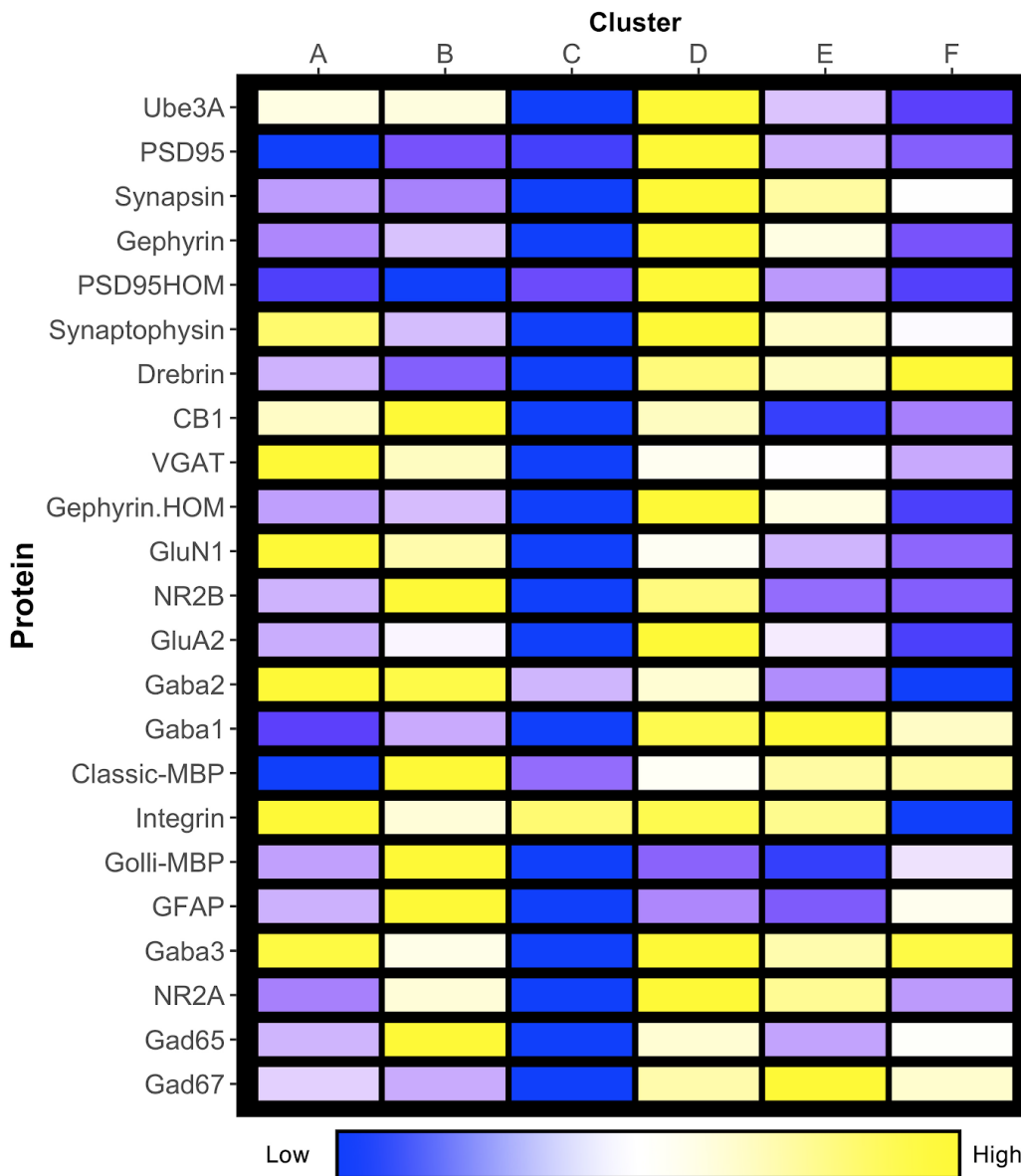


Figure 24. Protein expression motifs for the 6 clusters.

The average protein expression across clusters was scaled from the minimum (blue) to the maximum (yellow). The proteins were ordered according to their RSKC adjusted weights.

Exploring the cluster content with the protein motifs helped to differentiate the groups of clusters that shared protein peaks. For example, the two youngest clusters A and B shared the GABA_Aα₂ peak, but the older clusters D, E, and F shared the GABA_Aα₁ peak. The motifs visualization facilitated the comparison of protein expression within and across clusters since all of the 138 protein averages (6 clusters X 23 proteins) were represented in one figure.

Next, we quantified protein expression in each cluster, plotted those in boxplots and used a bootstrap analysis to determine clusters that had expression significantly above (red boxes) or

below (blue boxes) the median protein expression level. The boxplots for each protein were generated using the *geom_boxplot* function in the *ggplot2* package (Wickham 2010).

```
ggplot(Protein.means, aes(Protein.means,value,fill=robust6C))+ (30)
  geom_boxplot(outlier.colour = NA,aes(group = robust6C))+
  geom_jitter(shape=16, position=position_jitter(0.2),alpha=0.5)+
  scale_fill_manual(name="Cluster Order",values=ordered6.cols,labels=c("A","B","C","D","E","F"))+
  geom_hline(yintercept = 0,linetype="dashed",alpha=0.25) +
  facet_wrap(~variable,scales = "free_y")+
  labs(list(x = paste("Age (Years)"), y = paste("Protein Expression"))) +
  theme_bw()+
  theme(panel.background = element_rect(fill = 'gray95'), axis.text.x = element_blank(),panel.grid.major =
  element_blank(), panel.grid.minor = element_blank())
```

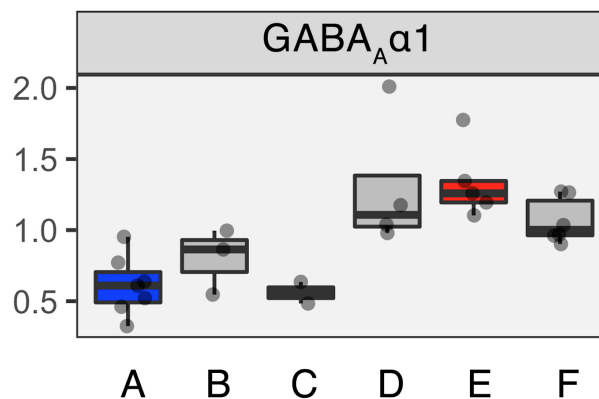


Figure 25. Protein expression per cluster.

Each boxplot represents a different cluster of data points, and the dashed line overlaps balance (0) between each protein. Blue boxes represent clusters with median expression below the lowest 25% of the data, red boxes represent clusters with median expression above the upper 75% of the data, and grey represent those with median expression within the middle 50% of the data.

Using the protein motifs to visualize protein expression by cluster (Figure 24) and the color-coded boxplots to quantify protein expression (Figure 25) helped with efficiently exploring significant patterns in the clusters. That approach, however, did not readily identify combinations of proteins that represent higher-dimensional features in the data set. To explore if high-dimensional features identify age-related changes in the clusters we returned to the use of PCA.

4.4.iv) Candidate high-dimensional feature selection

To identify candidate high-dimensional features in the clusters we applied PCA to the human visual cortex developmental protein data set. The PCA found the significant dimensions and we used those to explore the proteins contributing to those dimensions. Also, we compared

the proteins correlated with PCA dimensions to their adjusted weight from RSKC to uncover the hidden features that supported better clustering with RSKC.

The first step repeats the PCA described for the coding examples (8)-(11) in section 4.3.iii. We used the *PCA* function from the *Factominer* package to analyze and display the percentage of variance explained by each of the 23 dimensions (Figure 26). For this data set, the first 3 dimensions captured >60% of the variance which is often used as a cutoff for identifying the important dimensions.

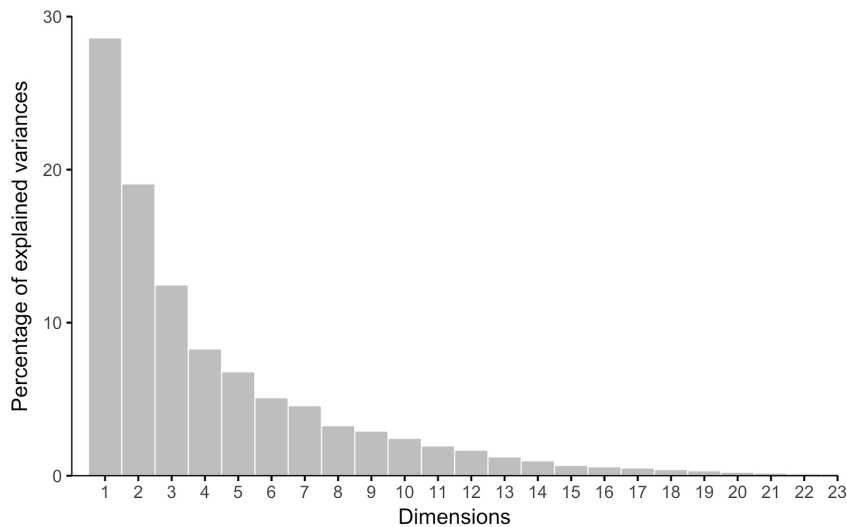


Figure 26. Scree plot of the percentage of explained variance captured by each principal component.

The variance captured by each of the first 3 dimensions is large (>10%), while subsequent dimensions gradually become less. The cumulative variance of the first 3 dimensions is 62%. Typically, a cumulative variance > 60% is an acceptable cutoff for identifying the important dimensions in PCA.

To interpret the representation of each protein on the PC dimensions we calculated pairwise correlations between the vector for each protein and the vector for each of the PC dimensions (Pearson's correlation)(Figure 27A). Next, we determined the quality of representation for each protein on the dimension (\cos^2)(Figure 27B). The R code to calculate and plot those metrics is found in the *FactoMineR* package, and can be called by consulting the *pca* object:

```
var <- get_pca_var(pca)
corrplot(var$cor, is.corr=FALSE, cl.lim=c(-1,1)) #for Pearson's R correlations
corrplot(var$cos2, is.corr=FALSE, cl.lim=c(0,1)) #for cos2
```

(31)

The figures showing the correlations and \cos^2 for each protein with the 23 dimensions used the size and saturation of a circle to represent the strength of the relationship, and the color of the circle indicated the direction for the correlations (Figure 27A, 27B). Inspection of the plots

showed that most of the proteins contributed to the first 3 dimensions but also identified a few proteins that had their most substantial contribution to a higher order dimension. This example helps to illustrate where PCA might lead to dropping variables from subsequent cluster analysis. It is important to note that the workflow described in this section ran PCA and sparse high-dimensional clustering in parallel with each analysis using the full protein data set so that the results from the two approaches could be compared to unpack the higher order features in the data set.

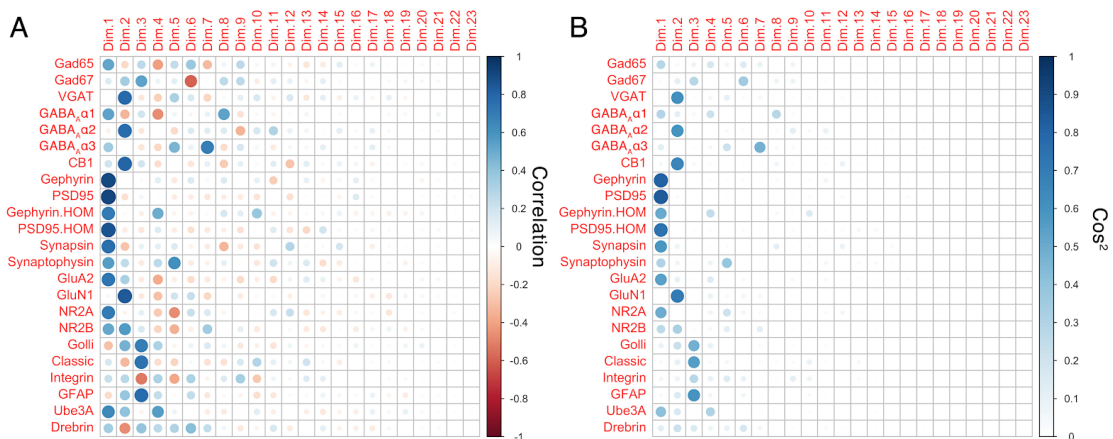


Figure 27. The correlation (A) and \cos^2 (B) matrix showing the relationship between each protein and the 23 principal component dimensions.

(A) The circles in each matrix represent the strength (size and saturation) and direction (colour) of the correlation between proteins and dimensions. (B) The circles represent the goodness-of-fit, \cos^2 for the protein on PC dimensions. Most of the proteins have the strongest correlation and best fit with at least one of the first 3 dimensions (Dim.1, Dim.2, Dim.3).

In this example, the first 3 dimensions were chosen because they captured >60% of the variance in the data (Figure 26), and most of the strong \cos^2 values and Pearson's R correlations (Figure 27). The quality of the representation for each protein on the first 3 dimensions was analyzed by summing up the \cos^2 values and plotting that information as a histogram ranking the protein from lowest to highest \cos^2 value (Figure 28). The following code was used to visualize the sum of \cos^2 for the first 3 dimensions:

```
fviz_cos2(pca, choice = "var", axes = 1:3, color="grey", fill="grey", sort.val="asc")+ (32)
scale_y_continuous(expand=c(0,0), limits=c(0,1))+
geom_hline(yintercept = 0.5, linetype="dashed", alpha=0.25) +
theme(axis.line.y=element_line(), axis.line.x=element_line(), panel.grid=element_blank())
```

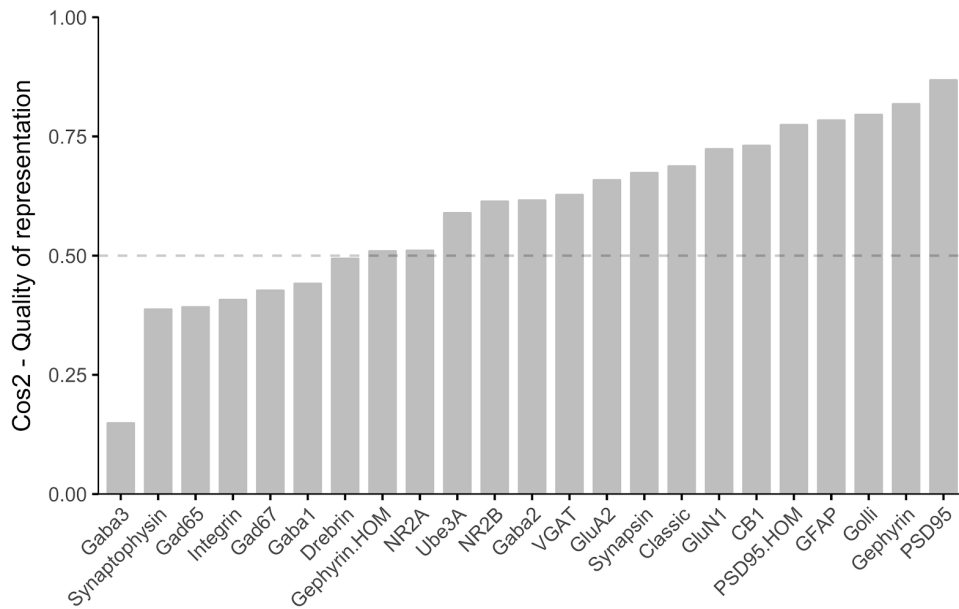


Figure 28. Sum of \cos^2 across the first 3 dimensions.

Across all 23 dimensions, sum of \cos^2 for each protein is 1. Dashed line represents $\cos^2 = 0.5$ cutoff, used for feature selection. 16 proteins fall above that cutoff and 7 fall below. The 7 that fall below can be removed from analysis (feature selection).

The \cos^2 can be plotted for individual dimensions. The example code below (33) uses the parameter `axes` to select the \cos^2 data for dimension 1 (Figure 29).

```
fviz_cos2(pca, choice = "var", axes = 1, color="grey", fill="grey", sort.val="asc"+
scale_y_continuous(expand = c(0,0), limits=c(0,1))+
geom_hline(yintercept = 0.5, linetype="dashed", alpha=0.25) +
theme(axis.line.y=element_line(), axis.line.x=element_line(), panel.grid=element_blank())) (33)
```

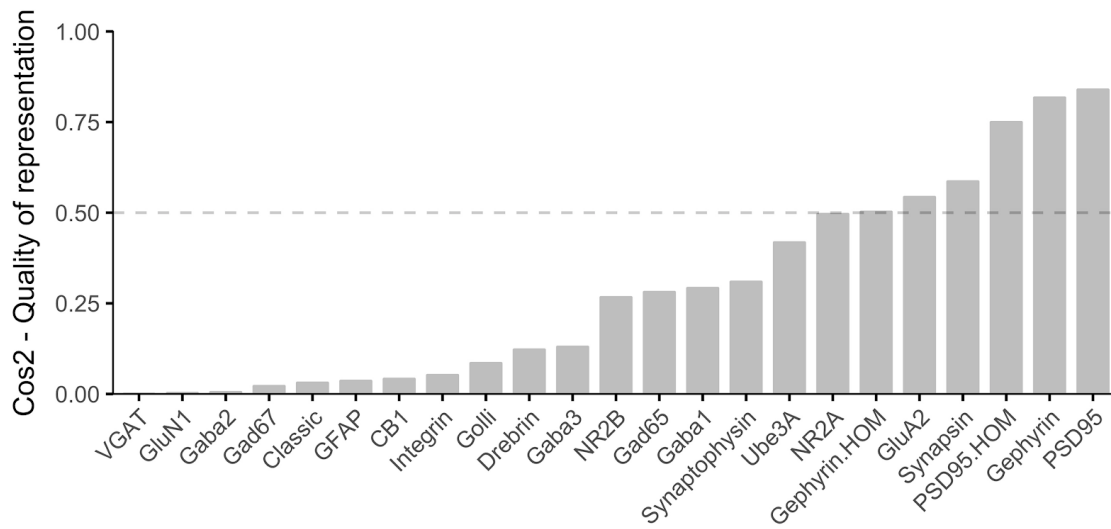


Figure 29. Sum of cos² across dimension 1.

The sum of cos² for each protein in Dimension 1. Dashed line represents cos² = 0.5 cutoff, used for feature selection.

The cos² value (e.g. 0.5) can be used as a cutoff to select a subset of proteins for further analysis but here we used the cos² ranking (high to low) from the first 3 PCs (Figure 28) to compare with the ranking of each protein from the RSKC reweighting (Figure 22). This step was used to identify proteins that RSKC adaptively increased or decreased the weighting (Figure 28) and showed that 5 proteins were increased (Synapsin I, Gephyrin.hom, Drebrin, Ube3A, Synaptophysin) while 4 proteins were decreased by RSKC (Golli-MBP, GFAP, Classic-MBP, GluN2A) (Figure 30). Those differential rankings provided some insight into the proteins that were important for the RSKC clustering but less influential for the PCA. It also illustrated the need for using multiple methods when studying high-dimensional cluster content.

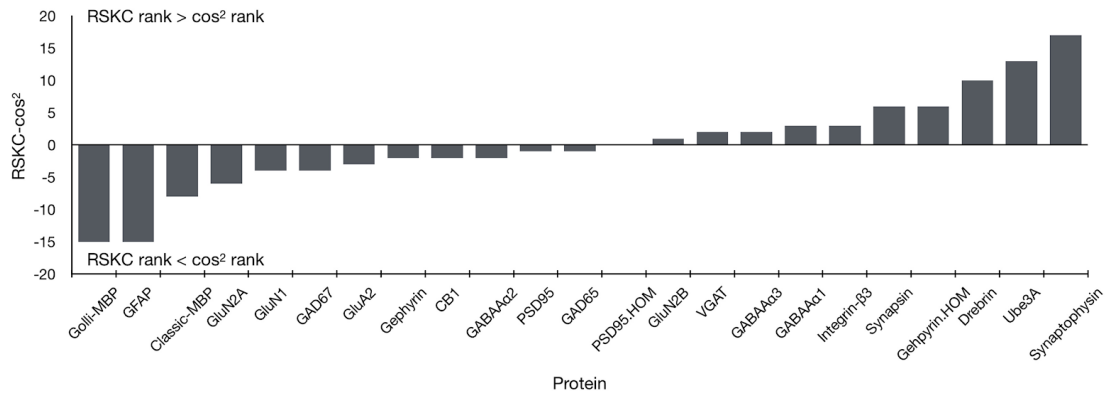


Figure 30. Ranking of proteins using RSKC reweighted values relative to \cos^2 representation.

Positive values on the y-axis indicate a higher ranking using the RSKC reweighted values than with \cos^2 representation, and therefore have greater influence on clusters. Conversely, negative values indicate proteins that were ranked higher by \cos^2 representation than after RSKC reweighting.

Biplots were also used as another approach to visualize the contribution of different proteins to the PC dimensions. The example biplot (Figure 31) showed the vectors for select proteins ($\cos^2 > 0.5$) along dimensions 1 and 2. We used the *fviz_pca_biplot* function from the *FactoMineR* package to superimpose the protein vectors in PCA space.

```
fviz_pca_biplot(invisible="ind",
pca, geom.ind = "point", axes = c(1,2),
labelsize = 5, col.ind = "black",
pointshape = 21, pointsize = 3, addEllipses = FALSE,
col.var = variable.class, gradient.cols = cm.colors, repel=TRUE,
select.var=list(cos2=0.5), arrowsize=0.75,
legend.title = list(fill = expression(paste("Cluster \n Order")),
color = "Feature"),title = "PCA - Biplot Dimensions 1 & 2")+
geom_label_repel(show.legend = FALSE, label.padding = 0.75,
point.padding=0.75, max.iter=5000, force=1000, nudge_x=50) +
theme(panel.background = element_rect(fill = 'gray95'),
legend.position = c(0.9, 0.82),
legend.box="horizontal",panel.grid=element_blank()+
scale_x_continuous(limits=c(-5,7.5),breaks=waiver()+
scale_y_continuous(limits=c(-5,5),breaks=waiver())
```

(34)

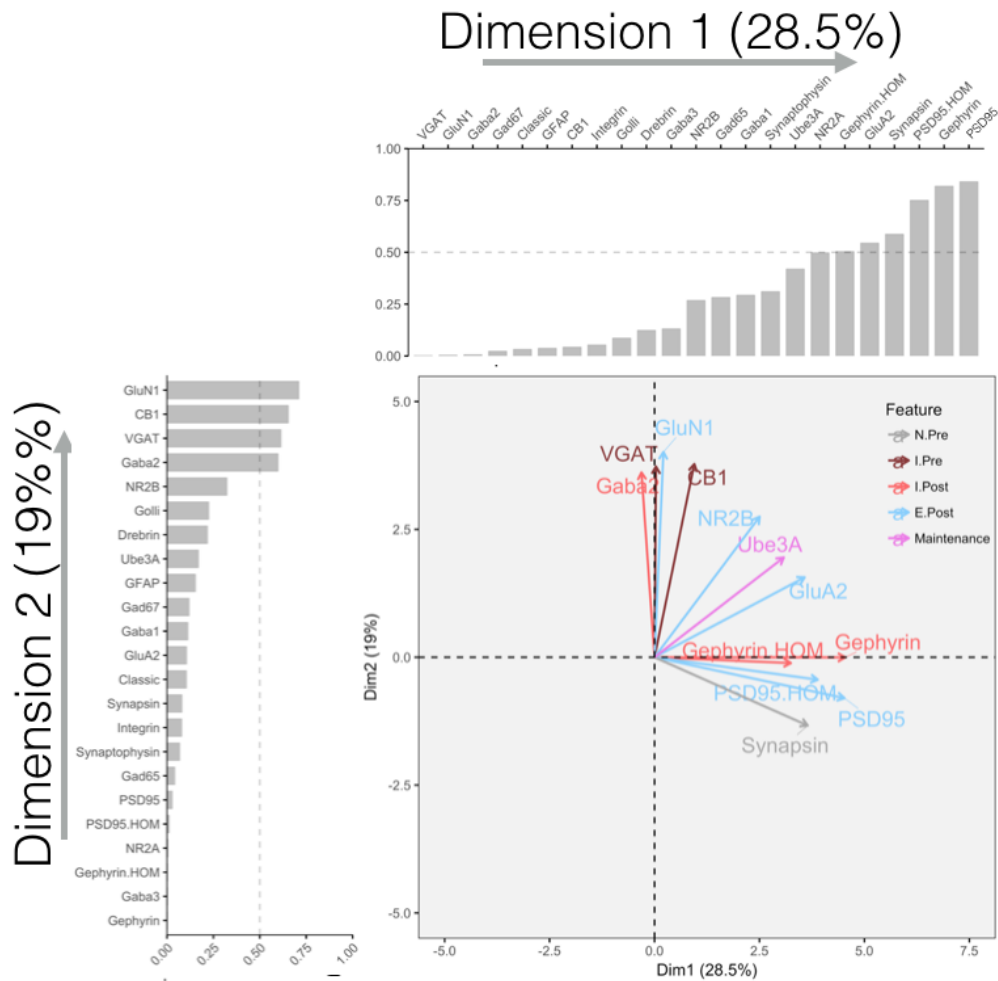


Figure 31. Biplot shows the protein vectors along dimension 1 (horizontal axis) and dimension 2 (vertical axis).

Surrounding histograms depict \cos^2 values for the proteins along dimension 1 (top) and dimension 2 (left). Proteins with a summed \cos^2 above 0.5 (dashed line) across both dimensions are shown. Vector directions marked by arrowheads point in the direction of high protein expression, while low protein expression extends in the opposite direction through the point of origin (not shown). The length of the protein vectors indicates the variance of the protein along the dimension and the angle of the vector indicates the quality of the representation on a dimension. Parallel vectors indicate proteins with similar expression while perpendicular vectors have no relation.

The pair of PC dimensions examined in a biplot can be changed using the values in ‘axes = c(1,2)’ parameter.

The length and angle of the vectors in Figure 31 was informative for identifying the proteins that contribute to each of the PC dimensions. Groups of proteins with similar vectors were correlated while orthogonal vectors indicate little correlation between those proteins. That information was used to guide the selection of proteins for candidate feature.

We also plotted the individual samples onto the biplot by removing the line of code ‘invisible="ind"’. The samples were color-coded by their RSKC cluster ID to visualize those clusters in PCA space (Figure 32). That biplot helped identify the relationship between the 6 clusters PC dimensions 1 and 2. For example, clusters C and D differed along dimension 1 while clusters A and F differed along dimension 2.

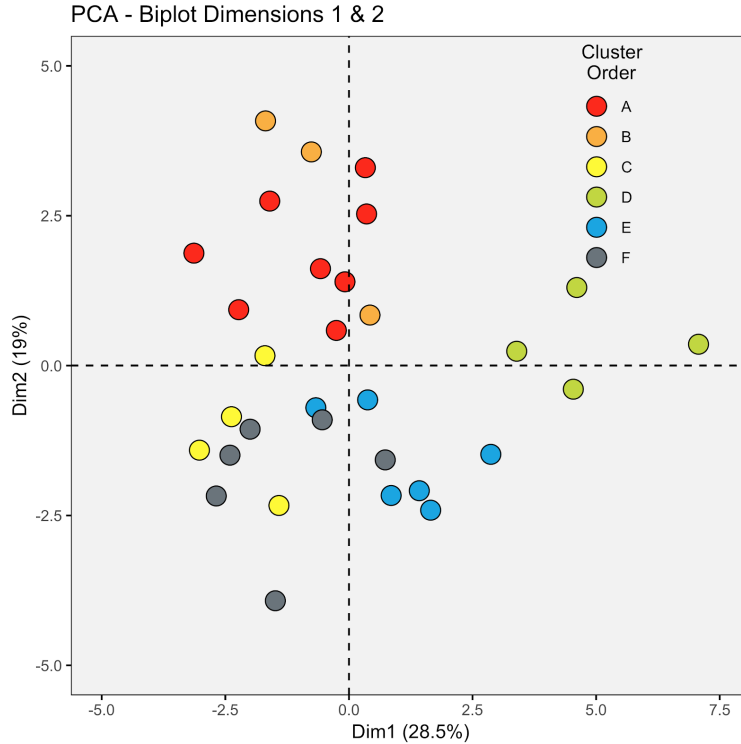


Figure 32. Biplots demonstrate the relationship between proteins and samples.

Biplot of dimension 1 and 2 that shows the individual samples (dots) colour-coded according to the six clusters (A-F) they are grouped in. The axes conventions are the same as in figure 31.

In the next section we use the information gleaned from the \cos^2 , differential RSKC- \cos^2 rankings and biplots about proteins that contribute to high-dimensional features in the data set to help select plasticity features.

4.4.v) Converting protein expression into candidate plasticity features

Here we describe how the basis vectors from PCA and information from the previous section were used to select combinations of proteins for candidate plasticity features. The steps for using the basis vectors to identify candidate features follow those presented in section 4.3.iv but we also included information from the differential RSKC- \cos^2 rankings to ensure that

proteins reweighted by RSKC were appropriately considered for candidate features. Once candidate features were identified, they were validated by correlation with the first 3 PC dimensions.

First, the basis vectors were plotted to show the amplitude of each protein about the PC dimension (example for PC2, Figure 33). The code below plots the basis vector for the second PC:

```
ggplot(data=pca$var$coord[,2], aes(rn, pca.var.coord...2.))+ geom_col(colour="black"+ (35)
scale_y_continuous(expand=c(0,0),name="Amplitude(BasisVector2)",lim=c(-1,1))+
scale_x_discrete(limits=VarCoordDim1$rn)+
theme(axis.line.y=element_line(),axis.line.x=element_line(),panel.grid=element_blank() axis.text.x =
element_text(angle=45,hjust =1,size=12), axis.text.y =
element_text(angle=0,vjust=0.5,size=12), axis.title.x=element_text(size=14,face="bold"),
axis.title.y=element_text(size=14,face="bold"), panel.grid.major
= element_blank(), panel.grid.minor = element_blank())
```

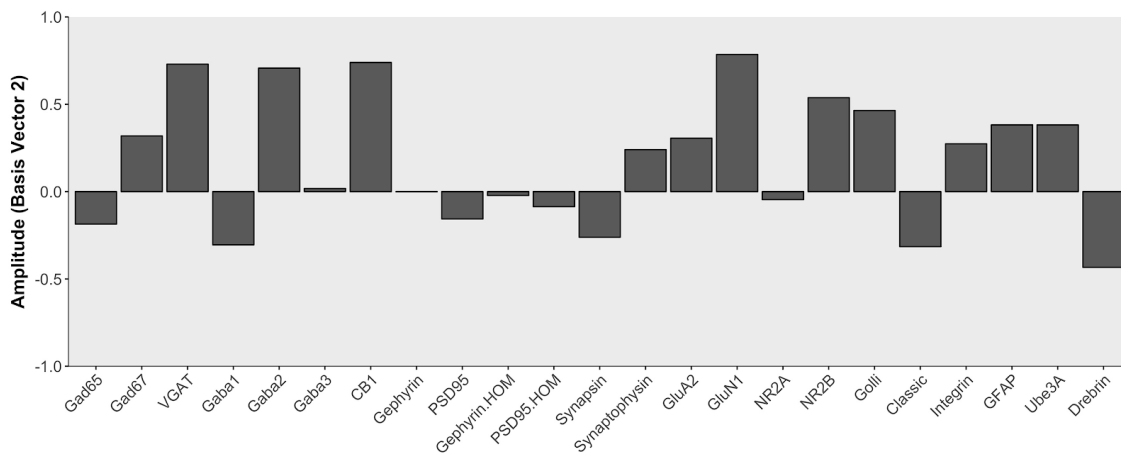


Figure 33. Amplitude of each protein about the second principal component.

Protein amplitudes are obtained from the vectors each protein creates in PCA space. The length of these vectors is plotted about the mean of the basis vector for each PCA dimensions, and the direction (positive or negative) is arbitrarily assigned. Here the basis vector being examined is basis vector 2, and proteins (x-axis) with greater variability about this vector have larger amplitudes, while proteins with less variability about basis vector 2 have smaller amplitudes. When bars move in the same direction, it means proteins change together, and when they move in opposite directions it means protein changes are in opposition.

The basis vector plot illustrated the amplitude and direction that each protein contributed to the PC dimension. We identified proteins with the largest amplitude and pointing in the same direction and summed them. Next, we identified proteins with a large amplitude that were pointing in opposite directions and used them to calculate differential indices. Finally, we used a

targeted approach based on published information about functional pairs or groups of proteins such as the GluN2A:GluN2B balance that regulates NMDAR kinetics (Sun et al. 2017), and LTP (Philpot et al. 2001). Those 3 steps identified combinations of proteins that we called candidate plasticity features.

4.4.vi) Validating plasticity features

After identifying candidate plasticity features, they were calculated from the protein expression and correlated with the each of the 3 PC dimensions using the same the same steps described for the coding example (15).

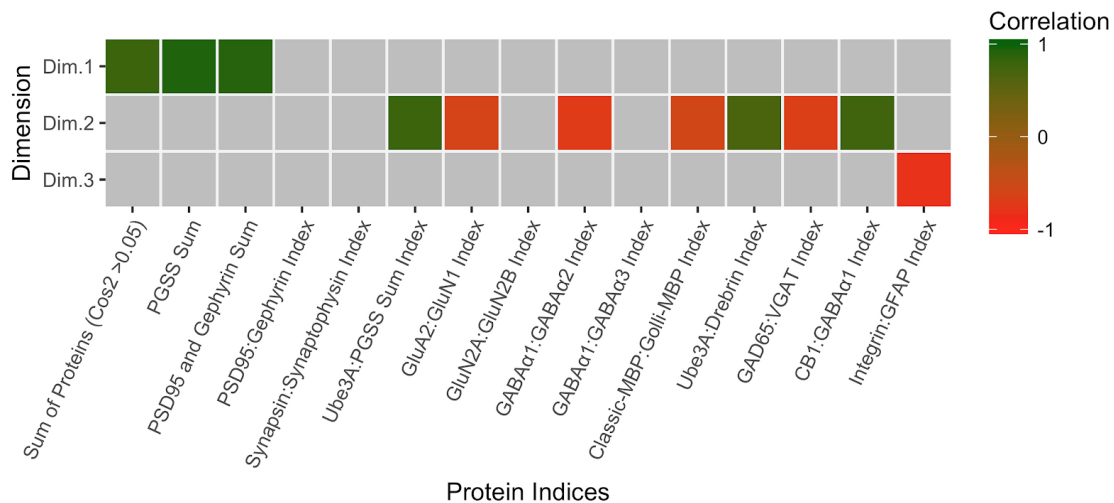


Figure 34. Examination of extracted feature correlation with PCA dimensions.

Significant correlations between the first 3 principal components and protein sums / indices are represented as coloured cells. The colour indicates the magnitude (intensity) and direction (positive=green, negative=red) of significant correlations after Bonferroni correction.

The matrix of correlations between the PC dimensions and candidate plasticity features was inspected paying close attention to features that included proteins differentially weighted by RSKC and PCA (Figure 34). For example, although RSKC reduced the weights of the individual MBP proteins an index calculated using both proteins (Classic-MBP:Golli-MBP) was significantly correlated with PC2 (red). In contrast, RSKC also reduced the weight of GluN2A, but the candidate feature (NR2A:NR2B index) was not correlated with any of the 3 PC dimensions (grey- Figure 34). These two examples demonstrate the importance of validating the candidate features; not all features had significant correlations with a PC dimension.

After exploring the data following the steps above 11 plasticity features were validated for this data set thereby reducing the dimensions from 23 proteins to 11 plasticity features. Furthermore, the steps transformed protein expression into features consistent with combinations of proteins known to regulate plasticity and change during development.

The next step was to use hierarchical clustering with the validated plasticity features to identify the features that had similar patterns of lifespan changes.

4.4.vii) Visualizing feature networks and building plasticity phenotypes

To determine which features had similar patterns of changes across the lifespan we calculated the pairwise correlations between features, ordered those correlations using hierarchical clustering and visualizing the output in a 2D heatmap (Figure 35). The R code used was similar to the heatmap coding example (2)-(6) explained in section 4.3.ii, except a new object called `NewFeatures2` was made with the 11 plasticity features.

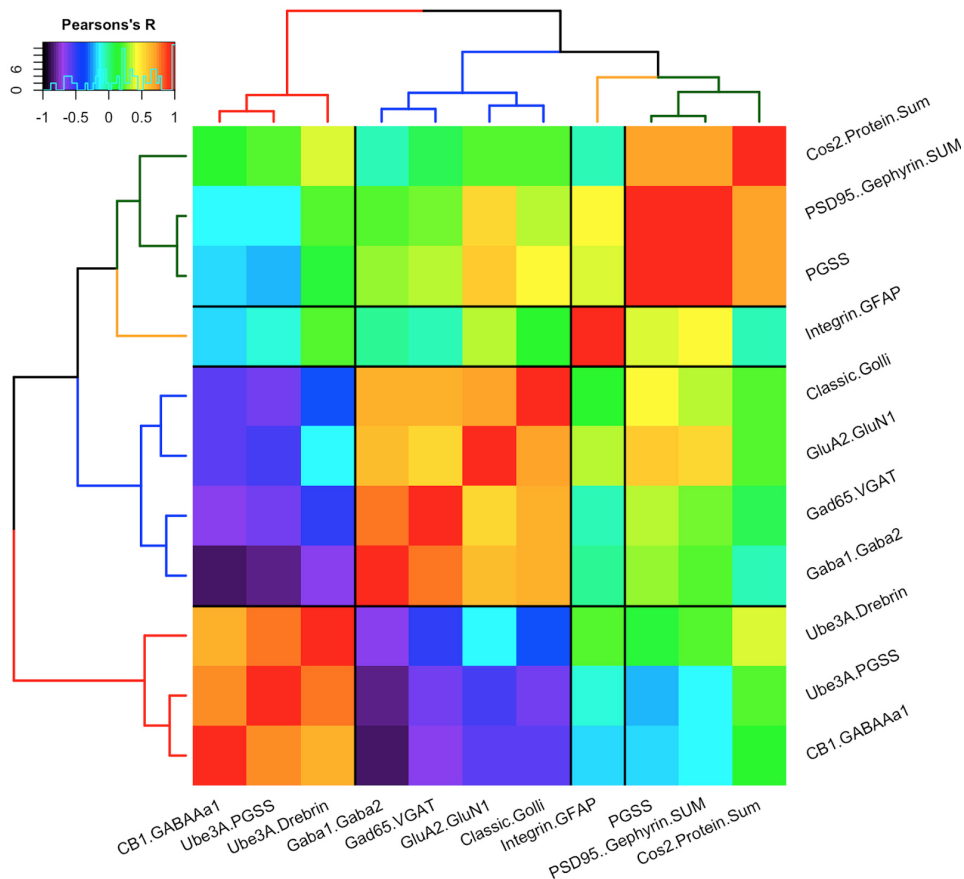
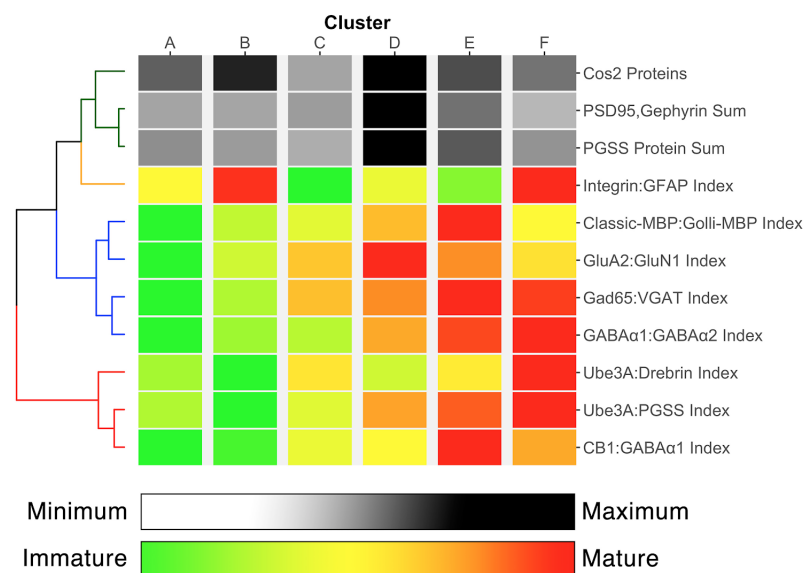


Figure 35. Heatmap of the significant features identified in Figure 34.

Matrix of Pearson's R correlations between the means across 11 plasticity features in each cluster. Clusters were reordered according to the surrounding dendrogram. The dendrogram positioned similar features close together, and moved dissimilar features to the periphery. Inset demonstrates counts across the range of Pearson's correlations, while the color gradient ranges from low negative correlations (blue/black) to high positive correlations (red).

The correlation heatmap identified 4 groups of plasticity features: first, the 3 protein sums were grouped; second, the astrocyte index Integrin:GFAP was on a separate branch; third, Classic:Golli MBP, GluA2:GluN1, Gad65:VGAT, and GABA α 1:GABA α 2 were grouped; finally, markers involved with GABAergic inhibition onto pyramidal neurons that included Ube3A:Drebrin, Ube3A:PGSS, CB1:GABA α 1 indices were separated from the other groups.

The order of the plasticity features found above by hierarchical clustering was used for building the visualization of the plasticity phenotype (Figure 36). The 11 features that create the plasticity phenotype were visualized using the same method described in section 4.3.vii with the R coding examples (21) and (22) except that the object `NewFeatures2` with the 11 plasticity features was the input for this step. Briefly, the code in (21) determines the color scale for each feature and the code in (22) uses those color-codes to create the visualization of the 11 features and 6 clusters.

**Figure 36. Average plasticity phenotype for each of the 6 clusters representing human visual cortical development.**

The order of features in the phenotypes was determined from the dendrogram in Figure 35. Most features transition gradually from an immature to mature state. The progression from light grey to dark grey in the top three bars, and from green to red in the last 8 bars indicate the pace of development.

The plasticity phenotype visualization conveys a substantial amount of information about the development of human visual cortex and helped to identify the features that partitioned samples into one cluster versus another (Figure 36). For example, two features that separated clusters A and B were the Integrin:GFAP index and the sum of \cos^2 proteins. Importantly, because some clusters had overlapping age ranges (e.g. B & C Figure 21), comparing features for those clusters can help to identify neurobiological mechanisms that contribute to heterogeneity during different stages of the lifespan.

4.5 Extensions and Discussion

Here we described two workflows and provided example R code for applying a data-driven approach that uses high-dimensional analyses to study development and plasticity of the visual cortex. The workflows were developed to help with interpreting data sets that include multiple proteins (or genes) and ages or rearing conditions where there are complex patterns of results. Also, we extended previous work by developing steps to build, visualize, and compare plasticity phenotypes that capture the neurobiological features that characterize clusters in the visual cortex data sets.

The workflow in section 4.3 is similar to current approaches applied to study visual cortex that used sequential steps beginning with dimension reduction (e.g. PCA, tSNE) and then cluster analysis (e.g. Carlyle et al. 2017; Luo et al. 2017). We used this to study how different forms of visual experience changed protein expression in visual cortex and added the plasticity phenotype to determine the plasticity features that differentiated among the conditions. The plasticity phenotype is a new way of analyzing visual cortex development and plasticity that can facilitate meaningful interpretation of complex patterns of protein (or gene) changes.

The workflow in section 4.4 separated the cluster analysis and the steps for dimension reduction and feature identification into parallel streams. That change was needed to address the challenges of analyzing the neurobiological development of human visual cortex. Those studies typically use a small number of post-mortem tissue samples (n) but measure many proteins or genes (variables, p) resulting in a $p \sim n$ or $p > n$ data structure that is called sparse. Here we compared a group of sparse high-dimensional cluster analysis methods and determined that a

recent approach, Robust Sparse K-Means Clustering, RSKC (Kondo et al. 2016), did the best job of partitioning the data into age-related clusters. We also described how to use information from both the RSKC and PCA to identify features for constructing the plasticity phenotype to characterize the neurobiological development of human visual cortex.

Both of our workflows build on established methods for high-dimensional data analysis, and each one describes the reasons for applying different approaches for analyzing the data sets. Since research on cluster analysis is a rapidly moving field, we anticipate that new methods, especially for adaptive clustering of sparse data, may perform better than RSKC. The current workflows are flexible and can be adapted to use new algorithms by exchanging a few lines in the example R code. For example, growth mixture models for cluster analysis are being developed that may be more suitable for handling the types of data structures common for studies of human cortical development (Wei et al. 2017).

Identifying clusters and exploring cluster content performed well for the example data set but both workflows need to be tested with other data sets. In particular, extension of the feature selection steps (4.3.iv & 4.4.iv) should include unsupervised methods for identifying features and transforming data. Similarly, RSKC parameters in section 4.4.iii were selected with an exploratory process and manual inspection of cluster results that could be improved once unsupervised methods are developed.

A valuable contribution from this primer is the development and implementation of plasticity phenotypes. In particular, the plasticity phenotype visualization provides an elegant way to facilitate meaningful interpretation of the results in a single 2D plot. It is not clear, however, how well the current method for selecting features for the phenotypes will scale up for studies using larger numbers of proteins or genes. Perhaps additional methods for data reduction will need to be tested to optimize the selection of neurobiological features in larger data sets.

The R package “v1hdexplorer” aggregates the various packages and custom visualization code used in this paper, and is available for download using the function `install_github("balsorjl/v1hdexplorer")`. The custom visualization scripts are included in this document (e.g. coding examples (21) and (22)) for visualizing the plasticity phenotypes.

Supplemental Analysis- Bootstrap analysis using custom R code

To examine the probability that observations in one group (e.g. reverse occlusion-RO) were statistically different from another group (e.g. Normal animals) we performed a one-way bootstrap analysis. First, the observed parameters of the experimental group (RO) were used to create a simulated data set with 1,000,000 points that had the same mean and standard deviation as the observed subset of data. The object `sim.RO` contains the simulated data set of RO samples.

```
sim.RO <- rnorm(1000000, mean.RO, stdev.RO)
```

Next, we modelled *experimental* data of the normal group by drawing, at random, from the *simulated* RO data set (`sim.RO`) the same number of samples as the observed subset of Normal animals (`NNormal`). We calculated the mean of this first experimental subset of data, and replaced all data points in `sim.RO`. This experiment was repeated 100,000 times, and stored in the object `resamples.NormalRO`.

```
resamples.NormalRO <- lapply(1:100000 ,function(i) sample(sim.RO, NNormal, replace = T))
```

Each of these 100,000 experiments were reduced to the experimental mean. This subset of data represent a simulated population of comparisons between Normal and RO animals. We calculated the mean of this simulated population, and saved it as `mean.resamples.NormalRO`.

```
mean.resamples.NormalRO <- sapply(resamples.NormalRO, mean)
```

To determine the probability that the mean of the observed Normal subset of data (`mean.Normal`) came from the observed RO subset of data (`mean.RO`), we compared `mean.Normal` against the population in `mean.resamples.NormalRO`. To calculate the exact probability (p-value) that the observed Normal group (`mean.Normal`) came from the `mean.resamples.NormalRO` population, we calculated the percentage of data points that fall above or below `mean.Normal` in the distribution of data points in `mean.resamples.NormalRO`.

```
Norm.v.RO.pval <- 1-(sum(mean.resamples.NormalRO<mean.Normal)/100000)
```

```
Norm.v.RO.pval<- if (mean.RO<mean.Normal){
  1-(sum(mean.resamples.NormalRO<mean.Normal)/100000)
} else if (mean.RO>mean.Normal) {
  1-(sum(mean.resamples.NormalRO>mean.Normal)/100000)
}
```

In order to compare other conditions against the normal subset of data, adjust the subset of data that is called in place of RO (eg. BD versus Normal). In order to change the direction of the comparison against Normal to be against a different group (eg. MD), exchange the comparator

group for Normal in all of the above statements (eg. BD versus MD). The resultant data can be called into a text file and stored for later use when constructing histograms.

4.6 References

- Adler D. vioplot: Violin plot. R package version 02, URL <http://CRAN.R-project.org/package=vioplot>. 2005.
- Aggarwal CC, Wolf JL, Yu PS, Procopiuc C, Park JS. Fast algorithms for projected clustering. ACM; 1999. pp. 61–72.
- Agrawal R, Gehrke J, Gunopulos D, Raghavan P. Automatic subspace clustering of high dimensional data for data mining applications. Vol. 27. ACM; 1998.
- Artola A, Singer W. Long-term potentiation and NMDA receptors in rat visual cortex. Nature. Nature Publishing Group; 1987 Dec 1;330(6149):649–52.
- Balsor, J., Jones, D. G. & Murphy, K. M. Classification of visual cortex plasticity phenotypes following treatment for amblyopia. In press Neural Plast. 2019
- Beston BR, Jones DG, Murphy KM. Experience-dependent changes in excitatory and inhibitory receptor subunit expression in visual cortex. Front Synaptic Neurosci. 2010;2:138.
- Carlyle BC, Kitchen RR, Kanyo JE, Voss EZ, Pletikos M, Sousa AMM, et al. A multiregional proteomic survey of the postnatal human brain. Nat Neurosci. Nature Publishing Group; 2017 Nov 13;20(12):1787–95.
- Chang W-C. On using principal components before separating a mixture of two multivariate normal distributions. Applied Statistics. JSTOR; 1983;:267–75.
- Donaldson J, Donaldson MJ. Package “tsne.” CRAN Repository. 2010.
- Galili T. dendextend: an R package for visualizing, adjusting and comparing trees of hierarchical clustering. Bioinformatics. 2015 Nov 15;31(22):3718–20.
- Hahsler M, Hornik K, Buchta C. Getting things in order: an introduction to the R package seriation. Journal of Statistical Software. American Statistical Association; 2008;25(3):1–34.
- Harrell FE, Dupont C. Hmisc: harrell miscellaneous. R Package, version. 2008;3(2).
- Hassani M, Kim Y, Choi S, Seidl T. Subspace clustering of data streams: new algorithms and effective evaluation measures. Journal of Intelligent Information Systems. Springer; 2015;45(3):319–35.
- Hastie T, Tibshirani R, Narasimhan B, Chu G. Impute: imputation for microarray data. Bioinformatics. 2001;17(6):520–5.
- Hotelling H. Analysis of a complex of statistical variables into principal components. Journal of educational psychology. Warwick & York; 1933;24(6):417.
- Hoyle DC. Automatic PCA dimension selection for high dimensional data and small sample sizes. Journal of Machine Learning Research. 2008;9(Dec):2733–59.
- Jolliffe IT, Cadima J. Principal component analysis: a review and recent developments. Philos Trans A Math Phys Eng Sci. 2016 Apr 13;374(2065):20150202.

- Kondo Y, Salibian-Barrera M, Software RZJOS. RSKC: An R package for a robust and sparse k-means clustering algorithm. *JSS Journal of Statistical Software*. 2016 Aug;72(5).
- Lakshmi BJ, Shashi M, Madhuri KB. A rough set based subspace clustering technique for high dimensional data. *Journal of King Saud University - Computer and Information Sciences*. Elsevier; 2017 Sep 12.
- Lê S, Josse J, Husson F. FactoMineR: an R package for multivariate analysis. *Journal of Statistical Software*. Los Angeles; 2008;25(1):1–18.
- Luo C, Keown CL, Kurihara L, Zhou J, He Y, Li J, et al. Single-cell methylomes identify neuronal subtypes and regulatory elements in mammalian cortex. *Science*. 2017 Aug 11;357(6351):600–4.
- Maaten LVD, Hinton G. Visualizing Data using t-SNE. *Journal of Machine Learning Research*. 2008;9(Nov):2579–605.
- Minka TP. Automatic choice of dimensionality for PCA. 2001. pp. 598–604.
- Murphy KM, Beston BR, Boley PM, Jones DG. Development of human visual cortex: A balance between excitatory and inhibitory plasticity mechanisms. *Dev Psychobiol*. 2005;46(3):209–21.
- Nowakowski TJ, Bhaduri A, Pollen AA, Alvarado B, Mostajo-Radji MA, Di Lullo E, et al. Spatiotemporal gene expression trajectories reveal developmental hierarchies of the human cortex. *Science*. American Association for the Advancement of Science; 2017 Dec 8;358(6368):1318–23.
- Philpot BD, Sekhar AK, Shouval HZ, Bear MF. Visual Experience and Deprivation Bidirectionally Modify the Composition and Function of NMDA Receptors in Visual Cortex. *Neuron*. Cell Press; 2001 Jan 1;29(1):157–69.
- Pinto JGA, Hornby KR, Jones DG, Murphy KM. Developmental changes in GABAergic mechanisms in human visual cortex across the lifespan. *Front Cell Neurosci*. 2010;4:16.
- Pinto JGA, Jones DG, Williams CK, Murphy KM. Characterizing synaptic protein development in human visual cortex enables alignment of synaptic age with rat visual cortex. *Front Neural Circuits*. 2015;9:3.
- Revelle W. An overview of the psych package. Department of Psychology Northwestern University Accessed on March. Citeseer; 2011;3:2012.
- Siu CR, Balsor JL, Jones DG, Murphy KM. Classic and Golgi Myelin Basic Protein have distinct developmental trajectories in human visual cortex. *Front Neurosci*. 2015 Apr 24;9:1–10.
- Siu CR, Beshara SP, Jones DG, Murphy KM. Development of Glutamatergic Proteins in Human Visual Cortex across the Lifespan. *J Neurosci*. 2017 Jun 21;37(25):6031–42.
- Sun W, Hansen KB, Jahr CE. Allosteric Interactions between NMDA Receptor Subunits Shape the Developmental Shift in Channel Properties. *Neuron*. 2017 Apr 5;94(1):58–64.e3.
- Team R. RStudio: integrated development for R. RStudio, Inc, Boston, MA URL <http://www.rstudio.com>. 2015;42.

- Tibshirani R, Walther G, Hastie T. Estimating the number of clusters in a data set via the gap statistic. *Journal of the Royal Statistical Society: Series B (Statistical Methodology)*. 2001 Jan 1;63(2):411–23.
- Tsumoto T, Hagihara K, Sato H, Hata Y. NMDA receptors in the visual cortex of young kittens are more effective than those of adult cats. *Nature*. Nature Publishing Group; 1987 Jun 1;327(6122):513–4.
- Warnes MGR, Bolker B, Bonebakker L, Gentleman R. Package “gplots.” Various R Programming Tools for Plotting Data. 2016.
- Wei Y, Tang Y, Shireman E, McNicholas PD, Steinley DL. Extending Growth Mixture Models Using Continuous Non-Elliptical Distributions. *arXiv preprint arXiv:170308723*. 2017.
- Wickham H. *ggplot2: elegant graphics for data analysis*. *J Stat Softw*. 2010;35(1):65–88.
- Williams K, Irwin DA, Jones DG, Murphy KM. Dramatic Loss of Ube3A Expression during Aging of the Mammalian Cortex. *Front Aging Neurosci*. 2010;2:18.
- Witten DM, Tibshirani R. A framework for feature selection in clustering. *J Am Stat Assoc*. 2010 Jun 1;105(490):713–26.
- Witten DM, Tibshirani R. *sparcl: Perform sparse hierarchical clustering and sparse k-means clustering*. R Package, version. 2013;1(3).
- Witten, D. M., Tibshirani, R., & Hastie, T. (2009). A penalized matrix decomposition, with applications to sparse principal components and canonical correlation analysis. *Biostatistics*, 10(3), 515-534.

Chapter 5. Classification of visual cortex plasticity phenotypes following treatment for amblyopia

Abstract

Monocular deprivation (MD) during the critical period (CP) has enduring effects on visual acuity and the functioning of the visual cortex (V1). This experience-dependent plasticity has become a model for studying the mechanisms, especially glutamatergic and GABAergic receptors, that regulate amblyopia. Less is known, however, about treatment-induced changes to those receptors and if those changes differentiate treatments that support the recovery of acuity versus persistent acuity deficits. Here we explored the effects of 3 visual treatments started during the CP (n=24, 10 male and 14 female); binocular vision (BV) that promotes good acuity versus reverse occlusion (RO) and binocular deprivation (BD) that causes persistent acuity deficits. We measured recovery of a collection of glutamatergic and GABAergic receptor subunits in V1 and modeled recovery of kinetics for NMDAR and GABA_AR. There was a complex pattern of protein changes that prompted us to develop an unbiased data-driven approach for these high-dimensional data analyses to identify plasticity features and construct plasticity phenotypes. Cluster analysis of the plasticity phenotypes suggests that BV supports adaptive plasticity while RO and BD promote a maladaptive pattern. The RO plasticity phenotype appeared more similar to adults with high expression of GluA2 and the BD phenotypes were dominated by GABA_Aα1, highlighting that multiple plasticity phenotypes can underlie persistent poor acuity. After 2-4 days of BV the plasticity phenotypes resembled normals, but only one feature, the GluN2A:GluA2 balance, returned to normal levels. Perhaps, balancing Hebbian (GluN2A) and homeostatic (GluA2) mechanisms is necessary for the recovery of vision.

Keywords: amblyopia, neuroplasticity, GABA, NMDA, AMPA, phenotype, high-dimensional, treatment, recovery, binocular vision, reverse occlusion, binocular deprivation

5.1 Introduction

Since the earliest demonstrations that monocular deprivation (MD) during a critical period (CP) cause ocular dominance plasticity and acuity loss[1]-[3] this model has been used to deepen our understanding of the neural changes associated with amblyopia. There have been fewer studies, however, about cortical changes associated with the acuity deficits that often persist after treatment for amblyopia[4]-[8]. Here we classified the expression patterns (phenotypes) of a collection of synaptic proteins that regulate experience-dependent plasticity and explored if treatments that promote good versus poor acuity reinstate CP-like plasticity phenotypes in visual cortex (V1).

Many animal studies have highlighted the role of glutamatergic and GABAergic mechanisms for regulating plasticity during the CP[9]-[15]. For example, the subunit composition of AMPA, NMDA, and GABA_A receptors regulate the bidirectional nature of ocular dominance plasticity[16]-[21]. Some of the changes caused by MD include delaying the maturational shift to more GluN2A-containing NMDARs[22], [23], and accelerating the expression of GABA_Aα1-containing GABA_ARs[20], [23]. Together those changes likely decrease signal efficacy and dysregulate the spike-timing dependent plasticity that drives long-term depression (LTD) and weakens deprived eye response[24]. Furthermore, silencing activity engages homeostatic mechanisms that scale the responsiveness of V1 neurons by inserting GluA2-containing AMPAR into the synapse[25]. Importantly, many of the receptor changes have been linked with specific acuity deficits[26], [27] suggesting that visual outcomes may reflect changes to a collection of glutamatergic and GABAergic receptor subunits that together represent a plasticity phenotype for V1.

Animal studies of amblyopia have also identified treatments that promote good versus poor recovery of acuity after MD. For example, reverse occlusion (RO) gives a competitive advantage to the deprived eye that promotes an ocular dominance shift but the acuity recovered by the deprived-eye is transient, and can be lost within hours of introducing binocular vision[6]-[8]. Similarly, closing both eyes after MD to test a form of binocular deprivation therapy (BD) leads to poor acuity in both eyes that does not recover even after months of binocular vision[28]. In contrast, just opening the deprived eye to give binocular vision (BV) after MD appears to engage

cooperative plasticity that promotes both physiological recovery[29] and long-lasting visual recovery in both eyes[27].

Here we quantified expression of glutamatergic and GABAergic receptor subunits in V1 of animals reared with MD and then treated to promote either good visual recovery (BV) or persistent bilateral amblyopia (RO, BD). We compared subunit expression among the treatment groups and with normally developing or MDed animals. Next, we developed an unbiased high-dimensional analysis approach to identify plasticity features in the pattern of subunit expression and to construct plasticity phenotypes. Finally, we used cluster analysis to classify plasticity phenotypes associated with good versus poor acuity and analyzed those to determine which features suggest the recovery of adaptive versus maladaptive plasticity mechanisms.

5.2 Experimental Procedure

Animals & Rearing Conditions

All experimental procedures were approved by the McMaster University Animal Research Ethics Board. We quantified the expression of 7 glutamatergic and GABAergic synaptic proteins in V1 of cats reared with MD from eye opening until 5 weeks of age and then given one of 3 treatments: RO for 18d, BD for 4d, or BV for either short-term (ST-BV, 1hr, 6hrs) or long-term (LT-BV, 1d, 2d or 4d) (n=7, 4 male and 3 female) (Figure 1). The lengths of RO and BD were selected because they have well documented and consistent visual changes that result in poor acuity in both eyes[7], [8], Murphy:1991td [30]. Also, the BV periods were selected to match the lengths used previously to study rapid and dynamic changes caused by MD in both cat and mouse V1 [27], [31], [32]. The raw data collected previously[23] from animals reared with normal binocular vision until 2, 3, 4, 5, 6, 8, 12, 16, or 32 wks of age (n=9 animals, 2 male and 7 female), or MD from eye opening (6-11d) to 4, 5, 6, 9, or 32 wks (n=8 animals, 4 male and 4 female) were used for comparison.

MD was started at the time of eye-opening by suturing together the eyelid margins of one eye (5-0 Coated VICRYL Ethicon P-3) using surgical procedures described previously[8]. Sutures were inspected daily to ensure the eyelids remained closed. At 5 weeks of age, the period of MD was stopped and either BV was started by carefully parting the fused eyelid margins, RO was started by opening the closed eye and closing the open eye or BD was started by closing the open eye. All of these surgical procedures were done using gaseous anesthesia (isoflurane, 1.5-5%, in oxygen) and aseptic surgical techniques.

At the end of the rearing condition animals were euthanized using sodium pentobarbital injection (165mg/kg, IV), and transcardially perfused with cold 0.1M phosphate buffered saline (PBS) (4°C; 80-100 ml/min) until the circulating fluid ran clear. The brain was removed from the skull and placed in cold PBS. A number of tissue samples (2 mm x 2 mm) were taken from the regions of V1 representing the central (C), peripheral (P) and monocular (M) visual fields (Figure 1c). Each tissue sample was placed in a cold microcentrifuge tube, flash frozen on dry ice, and stored in a -80°C freezer.

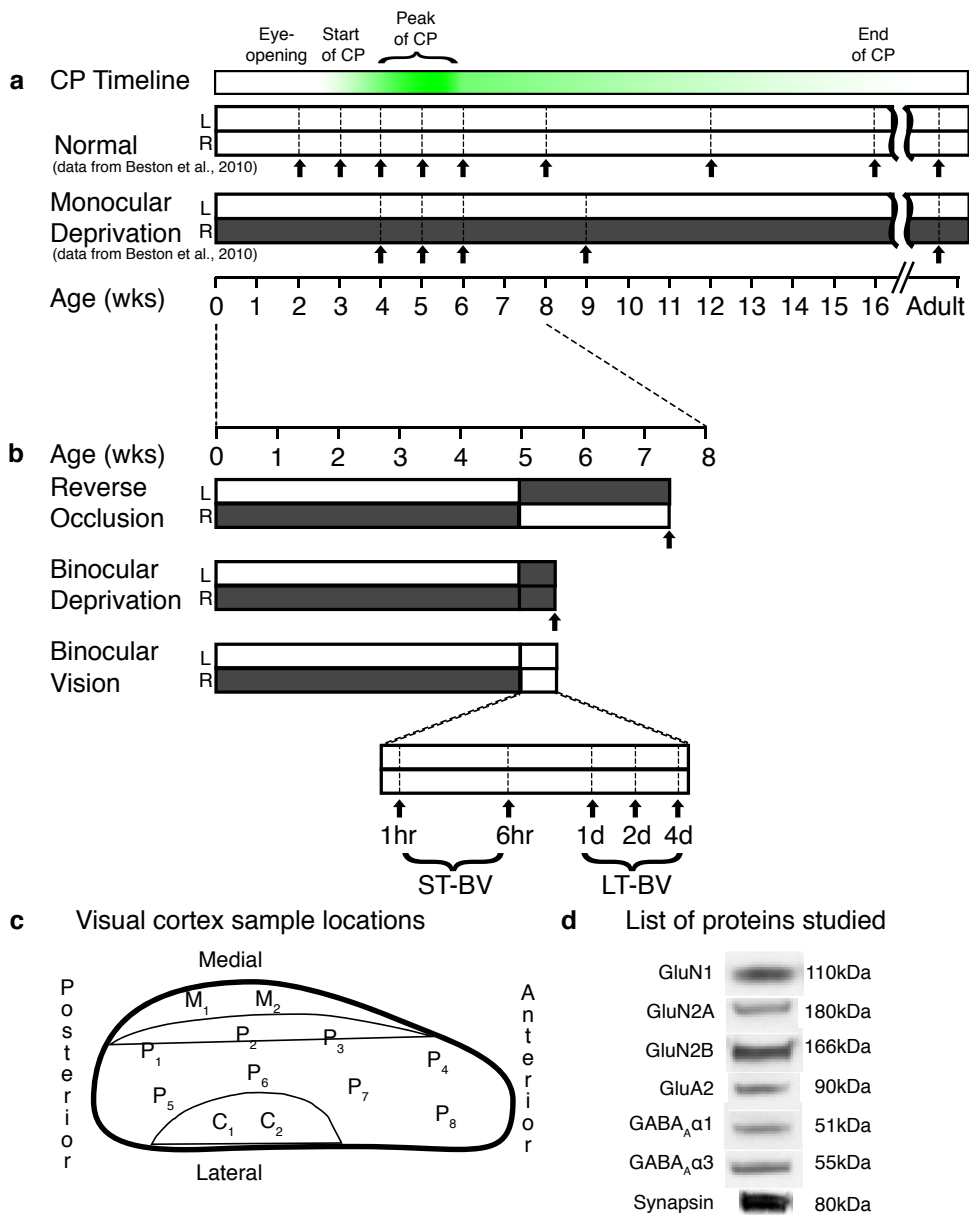


Figure 1. Study design diagram

Timelines for the rearing conditions used in this studied. a. Normal visual experience and monocular deprivation (MD), b. treatment conditions (RO, BD, BV) after MD to 5wks. Filled bars indicate that an eye was closed. Black arrows indicate the age of animals used in the study. A timeline for the critical period (CP) in cat visual cortex[60] highlights the peak of the CP between 4-6 weeks of age. c. Map of the regions in V1 where tissue samples were taken from representing central (C, n=2), peripheral (P, n=8), and monocular (M, n=2) visual fields. d. Representative bands from the Western blots for the 7 proteins quantified in the study and the molecular weights (kDa).

Synaptoneurosome preparation

Synaptoneurosomes were prepared according to a subcellular fractionation protocol [16], [33]. The tissue samples were suspended in 1 ml of cold homogenization buffer (10 mM HEPES, 1 mM EDTA, 2 mM EGTA, 0.5 mM DTT, 10 mg/l leupeptin, 50 mg/l soybean trypsin inhibitor, 100 nM microcystin and 0.1 mM PMSF), and homogenized in a glass-glass Dounce tissue homogenizer (Kontes, Vineland, NJ, USA). Homogenized tissue was passed through a 5 μ m-pore hydrophobic mesh filter (Millipore, Billerica, MA), centrifuged at low-speed (1,000xg) for 20 min, the supernatant was discarded, and the pellet was re-suspended in 1 ml cold homogenization buffer. The sample was centrifuged for 10 min (1000xg), the supernatant was discarded, and the pellet was re-suspended in 100 μ l boiling 1% sodium-dodecyl-sulfate (SDS). Samples were heated for 10 min and then stored at -80°C.

Total protein concentrations were determined for each sample and a set of protein standards using the bicinchoninic acid (BCA) assay (Pierce, Rockford, IL, USA). A linear function was fit to the observed absorbance values of the protein standards relative to their expected protein concentrations. If the fit was less than $R^2=0.99$, the assay was re-done. The slope and the offset of the linear function were used to determine the protein concentration of each sample and then the samples were diluted to 1 μ g/ μ l with sample (M260 Next Gel Sample loading buffer 4x, Amresco) and Laemmli buffer (Cayman Chemical). A control sample was made by combining a small amount from each sample to create an average sample that was run on every gel. Each sample was run twice in the experiment.

Immunoblotting

Synaptoneurosome samples and a protein ladder were separated on 4-20% SDS-PAGE gels (Pierce, Rockford, IL) and transferred to polyvinylidene fluoride (PVDF) membranes (Millipore, Billerica, MA). The blots were blocked in PBS containing 0.05% Triton-x (Sigma, St. Louis, MO) (PBS-T) and 5% skim milk (wt/vol) for 1 hour. Blots were then incubated overnight at 4°C with constant agitation in one of the 7 primary antibodies (Table 1), and washed with PBS-T (Sigma, St. Louis, MO) (3 x 10 min).

Table 1: List of primary antibody concentrations

Antibody	Concentration	Company	Lot Number	Location	RRID
anti-GluN1	1:2000	BD Biosciences Pharmingen	556308	San Diego, CA	RRID:AB_396353
anti-GluN2A	1:2000	Millipore Sigma	24826	Burlington, MA	RRID: AB_95169
anti-GluN2B	1:2000	Millipore Sigma	28629	Burlington, MA	RRID: AB_2112925
anti-GluA2	1:1000	Thermo Fisher		Waltham, MA	RRID: AB_2533058
anti-GABA _A α1	1:500	Santa Cruz Biotechnology	L3102	Santa Cruz, CA	RRID: n/a
anti-GABA _A α3	1:2000	Millipore Sigma		Burlington, MA	RRID: n/a
anti-Synapsin	1:2000	Thermo Fisher		Waltham, MA	RRID: n/a

The appropriate secondary antibody conjugated to horseradish peroxidase (HRP) (1:2000; Cedarlane laboratories LTD, Hornby, ON) was applied to membranes for 1 hour at room temperature, then blots were washed in PBS (3 x 10 min). Bands were visualized using enhanced chemiluminescence (Amersham, Pharmacia Biotech, Piscataway, NJ) and exposed to autoradiographic film (X-Omat, Kodak, Rochester, NY). After each exposure blots were stripped (Blot Restore Membrane Rejuvenation kit (Chemicon International, Temecula, CA, USA)) and probed with the next antibody so each blot was probed for all 7 antibodies (Figure 1d).

Analysis of Protein Expression

The autoradiographic film and an optical density wedge (Oriel Corporation, Baltimore, MD) were scanned (16 bit, AFGA Arcus II, Agfa, Germany), and the bands were identified based on molecular weight. The bands were quantified using densitometry and the integrated grey-level of the band was converted into optical density units (OD) using custom software (MATLAB, The Mathworks, Inc., Natick, Massachusetts). The background density between the lanes was

subtracted from each band and the density of each sample was normalized relative to the control sample run on each gel (sample band density/control band density).

The data were normalized relative to the average expression of the 5wk normal cases and plotted either as histograms to compare expression levels among the 5wk Normal, 5wk MD, RO, and BD animals or as scatterplots to follow expression changes over the 5 different lengths of BV. Table 2 summarizes the number of tissue samples and replication of runs for the 5wk Normal, 5wk MD and recovery conditions across the 3 regions of V1, and 7 proteins that were studied. The data analysis study design is summarized in Figure 2.

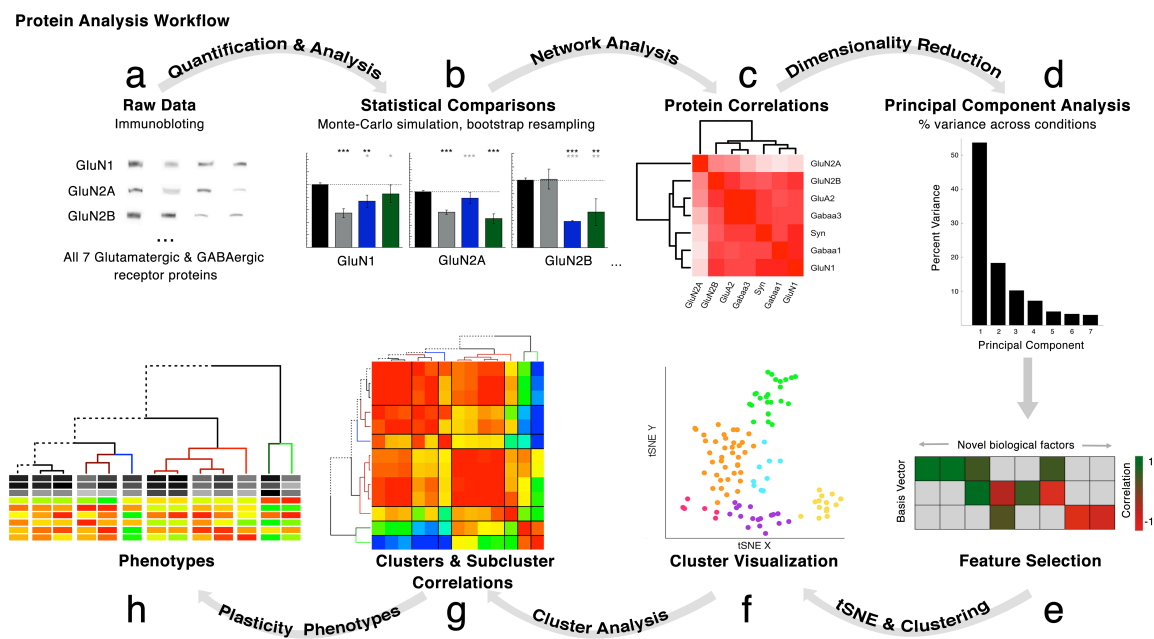


Figure 2. Analysis Workflow

The analysis workflow for data in the study. **a**. Immunoblots were quantified using densitometry, **b**. Statistical comparisons were made using Monte Carlo simulation and bootstrap resampling. **c**. Pairwise correlations were calculated for the 7 proteins for each rearing condition. **d**. Next, a series of steps were done beginning with dimension reduction (PCA), **e**. Feature selection, **f**. Cluster visualization based on the features (tSNE), **g**. Correlation between features or the clusters and subclusters, **h**. Construction and visualization of the plasticity phenotypes for each subcluster.

We analyzed heterogeneity in protein expression within a group by calculating an index of dispersion, the variance-to-mean ratio (VMR), for each protein and rearing condition. Proteins with $VMR < 1$ were classified as under-dispersed, $VMR = 1$ randomly dispersed, and $VMR > 1$ were over-dispersed. We used this measure to compare among groups and assess if a rearing condition changed the variability of protein expression to make the group more or less heterogeneous.

Table 2: The number of animals, cortical tissue pieces, and WB measurements for each condition and V1 region.

Rows summarize the number of runs from the Central (C), Peripheral (P), and Monocular (M) regions of V1 within a rearing condition. The columns list each of the 7 proteins analyzed using Western blotting. Column sums detail the number of runs across rearing conditions and cortical areas. The information for Normal animals is in Table 2-1, and for MD animals is in Table 2-2.

Condition	Number of Animals	Region	Number of Cortical	Number of Western Blot measurements after 2 replications						
				GluN1	GluN2A	GluN2B	GABA _A α1	GABA _A α3	GluA2	Synapsin I
Normal (5wks)		C	2	4	4	4	4	4	4	4
	1	P	8	16	16	16	15	16	16	16
		M	2	4	4	4	4	4	4	4
MD (5wks)		C	3	6	6	6	6	6	6	4
	2	P	9	18	18	18	18	18	18	12
		M	3	5	5	5	5	5	5	4
RO (18d)		C	2	4	4	4	4	4	4	4
	1	P	8	19	19	19	19	19	14	14
		M	2	3	3	3	3	3	2	2
BD (4d)		C	3	6	6	5	6	5	6	5
	1	P	9	18	18	17	16	18	18	17
		M	2	4	4	3	4	4	4	3
ST-BV (1hr, 6hr)		C	4	8	8	8	8	8	8	8
	2	P	16	32	32	32	32	32	32	32
		M	4	8	8	8	8	8	8	7
LT-BV (1d, 2d, 4d)		C	6	12	10	12	11	12	12	10
	3	P	24	43	40	43	43	42	43	40
		M	6	12	12	12	12	12	12	12
SUM				222	217	219	218	220	216	198

Protein Indices

To examine the balance between developmentally and functionally related pairs of glutamatergic and GABAergic receptor subunits, we calculated a set of 3 indices (difference ratios). The indices included: GluA2:GluN1, GluN2B:GluN2A, GABA_Aα3:GABA_Aα1, which

ranged from -1 to 1. The mean and SEM for each index was plotted as either a histogram (5wk Normal, 5wk MD, BD, RO) or scattergram (BV).

Protein Network Analysis

A network analysis of protein expression was done for each rearing condition by calculating the pairwise Pearson's R correlations among the 7 proteins using the *rcorr* function in the *Hmisc* package in R[34]. The networks were visualized as correlation matrices (*heatmap2* function in *gplots*[35]) and the proteins were ordered (dendextend package[36]) using the *seriation* package[37] to place proteins with similar patterns of correlations nearby in the dendrogram. Significant correlations were identified using Bonferroni corrected p-values and indicated by asterisks on the cell in the correlation matrix.

Modeling Population Receptor Decay Kinetics for NMDARs and GABA_ARs

The subunit composition of NMDARs and GABA_ARs determines the decay kinetics of the receptor[36], [37] and so we used that information to build a model for the decay kinetics of a population of receptors for each of the rearing conditions. The decay kinetics of the most common NMDAR composition, triheteromeric receptors containing GluN2A and 2B is 50ms±3ms, while diheteromers NMDARs containing only GluN2B are slower (2B=333ms±17ms) and those containing only GluN2A are faster (2A=36ms±1ms) [36]. The decay kinetics of GABA_ARs with both α1 and α3 subunits is 49ms±23ms while receptors with only the α3 subunit are slower (129.0ms±54.0ms) and only α1 are faster (42.2ms±20.5ms) [37].

We used the relative amounts of GluN2A and 2B, or GABA_Aα1 and α3, as inputs to the model. Receptors containing GluN2A and 2B or GABA_Aα1 and α3 are the most common in the cortex, so the model maximized the number of these pairs which was limited by the subunit with less expression. The remaining proportion of the highly expressed subunit was divided by 2 and used to model the number of pairs for those receptors (2A:2A or 2B:2B; α1:α1 or α3:α3) in the population. The population decay kinetics were then modeled by inserting the relative amounts of the subunits into these formulas:

$$\text{NMDAR kinetics } (([2A:2B] \times 50\text{ms}) + ([2A] \times 36\text{ms}) + ([2B] \times 333\text{ms})) / ([2A:2B] + [2A] + [2B]);$$

$$\text{GABA}_A\text{R kinetics } (([\alpha1:\alpha3] \times 49\text{ms}) + ([\alpha1] \times 42.2\text{ms}) + ([\alpha3] \times 129\text{ms})) / ([\alpha1:\alpha3] + [\alpha1] + [\alpha3]).$$

For example, a sample where GluN2A was 35% and 2B was 65% of the total NMDAR subunit population and would have population kinetics of 135ms.

$$(((0.65-0.35)/2] \times 50\text{ms}) + (((0)/2] \times 36\text{ms}) + ([0.35/2] \times 333\text{ms})) / (((0.65-0.35)] + [(0)/2] + [0.35]) = 135\text{ms}.$$

First, we plotted scattergrams of the average NMDAR and GABA_AR decay kinetics for normal animals and each treatment condition. The development of decay kinetics for normal animals was described using an exponential decay function, while changes in kinetics with increasing lengths of BV were fit by either exponential decay or sigmoidal curves. Next, we compared the relationship between NMDAR and GABA_AR kinetics by plotting both on one graph.

Principal component analysis

We used principal component analysis (PCA) to reduce the dimensionality of the data, identify potential biological features, and create plasticity phenotypes. We applied PCA following procedures we used previously [23], [40], [41] and included data from all of the normal animals and MDs as well as the 3 recovery conditions. We assembled protein expression for GluA2, GluN1, GluN2A, GluN2B, GABA_Aα1, GABA_Aα3, and Synapsin I into an $m \times n$ matrix. The m columns represented the 7 proteins and the n rows were the average protein expression for each of the 12-14 samples from an animal. For a few of the rows data was missing from a single cell and so those samples were omitted for a total of $n=279$ rows in the matrix and 1,953 observations.

The data were centered by subtracting the mean column vector and applying a singular value decomposition (SVD) to calculate the principal components (R Studio). SVD represents the expression of all 7 proteins within a single tissue sample as a vector in high dimensional space and the PCA identifies variance captured by each dimension in that "protein expression space". The first 3 dimensions accounted for 82% of the total variance and were used for the next analyses.

We plotted the basis vectors for the first 3 dimensions (Dim) and used the weight, quality (\cos^2) and directionality of each protein, as well as known protein interactions to help identify potential biological features accounting for the variance. We identified 9 potential features (7

new and 2 indices already analyzed), calculated those features for each sample and correlated each feature with Dim1, Dim2 and Dim3 to create a correlation matrix (see results). The p-values for the correlations were Bonferroni corrected and significant correlations were used to identify features that would be part of the plasticity phenotype. Eight of the features were significantly correlated with at least one of the first 3 dimensions. A measure associated with the E:I balance, was not significantly correlated with the dimensions and so it was not included in the tSNE or cluster analysis. The E:I measure, however, was used for analyzing the composition of the clusters and as a component of the plasticity phenotype because of the importance of the E:I balance for experience-dependent plasticity.

tSNE dimension reduction and cluster analysis

The average expression for the 8 features (Table 3) was compiled into an $m \times n$ matrix, with m columns ($m=8$) representing the significant features and n rows representing each sample from the 3 V1 regions (central, peripheral, monocular) for 5wk Normal, 5wk MD, RO, BD and BV animals ($n=109$). t-distributed stochastic neighbor embedding (t-SNE) was used to reduce this matrix to 2-dimensions (2D). tSNE was implemented in R[42] and the tSNE output was sorted using k-means to assign each sample to a cluster. To determine the optimal number of clusters (k) we calculated the within-groups sum of squares for increasing values of k , fit a single-exponential tau decay function to those data, found the "elbow point" at 4τ which was 6, and used that as the optimal number of clusters. The clusters were visualized by color-coding the dots in the tSNE plot and the composition of the clusters was analyzed.

Table 3: Formulas and Pearson's R correlation between the features and principal components.

The formulas for each identified feature (Fig 3a-c) and PCA identified features (Fig 6j), along with corresponding correlation (R²) values for each of the first 3 principal components. The GluN1:GluA2 and GABA_AR Sum:GlutR Sum were not significantly correlated with any of these 3 components.

Feature	Formula	R ² Dim 1	R ² Dim 2	R ² Dim 3
GluN1:GluA2	$(\text{GluA2} - \text{GluN1}) \div (\text{GluA2} + \text{GluN1})$	0.002	0.075	-0.002
GluN2B: GluN2A	$(\text{GluN2A} - \text{GluN2B}) \div (\text{GluN2A} + \text{GluN2B})$	0.044	-0.421	0.338
GABA _A α3:GABA _A α1	$(\text{GABA}_{\alpha 1} - \text{GABA}_{\alpha 3}) \div (\text{GABA}_{\alpha 1} + \text{GABA}_{\alpha 3})$	-0.176	0.504	0.194
PCA identified Features				
All Protein Sum	$(\text{GluA2} + \text{GluN1} + \text{GluN2A} + \text{GluN2B} + \text{GABA}_{\alpha 1} + \text{GABA}_{\alpha 3} + \text{Synapsin I}) \div 7$	0.983	0.134	0.039
GlutR sum	$(\text{GluA2} + \text{GluN1} + \text{GluN2A} + \text{GluN2B}) \div 4$	0.746	-0.160	0.573
GABA _A R Sum	$(\text{GABA}_{\alpha 1} + \text{GABA}_{\alpha 3}) \div 2$	0.478	0.819	-0.047
GABA _A R Sum:GlutR Sum (EI Index)	$(\text{GlutR Sum} - \text{GABA}_{\alpha 1} \text{ Sum}) \div (\text{GlutR Sum} + \text{GABA}_{\alpha 1} \text{ Sum})$	0.036	-0.064	0.012
GABA _A α1: GluN2A index	$(\text{GluN2A} - \text{GABA}_{\alpha 1}) \div (\text{GluN2A} + \text{GABA}_{\alpha 1})$	0.437	-0.743	-0.070
GluN2B:GluA2	$(\text{GluN2B} - \text{GluA2}) \div (\text{GluN2B} + \text{GluA2})$	0.058	0.209	-0.798
GluN2A:GluA2	$(\text{GluN2A} - \text{GluA2}) \div (\text{GluN2A} + \text{GluA2})$	0.113	-0.172	-0.643

To facilitate analysis of the tSNE clusters we grouped the BV cases into short-term BV (1hr & 6hr) (ST-BV) or long-term BV (1d, 2d, and 4d) (LT-BV), color-coded the samples by rearing condition and used different symbols to indicate the V1 region. For each cluster we annotated the composition based on the rearing condition of the samples to create 'subclusters' (e.g. LT-BV 1) that were used for the next analyses.

We evaluated the similarity/dissimilarity among the subclusters by calculating the pairwise correlations (Pearson's R) between subclusters using the features identified by the PCA as input to the R package *rcorr*. The correlations were visualized in a matrix with the cells color-coded to indicate the strength of the correlation[35]. The order of the subcluster in the matrix was optimized using hierarchical clustering and a dendrogram was created based on the pattern of correlations (using R *dendextend* and *seriation* packages) so that subclusters with strong correlations were nearby in the dendrogram.

Visualization and comparison of plasticity phenotype

The features identified in the PCA analysis were used to indicate the plasticity phenotype for each of the subclusters. In addition to the 8 significant features, the E:I measure was included in the visualization of the plasticity phenotype. The features were color-coded using grey scale for the 3 protein sum features and a color gradient (red = -1, yellow = 0, green = +1) for the 6 protein indices. The plasticity phenotypes were displayed as a stack of color-coded bars with one bar for each feature. For the subclusters, the plasticity phenotypes were ordered by the dendrogram to facilitate comparison among subclusters that were similar versus dissimilar. We also calculated the plasticity phenotypes for the full complement of normally reared and MD animals and displayed those in a developmental sequence to facilitate age-related comparisons with the recovery subclusters. Finally, we did a bootstrap analysis to determine which features of the plasticity phenotypes were different from 5wk normals and used Bonferroni correction to adjust the significance for the multiple comparisons. This analysis was displayed 2 ways: first, each of the 9 feature bands for the dendrogram ordered subclusters was color-coded white if it was not different, red if it was greater, and blue if it was less than 5wk normals; second, boxplots were made to show the value for each of the 9 features and to identify the subclusters that were different from 5wk normals.

A detailed description of the network analysis, PCA, tSNE, clustering and phenotype construction, along with example code for each of these steps can be found in [43].

Statistical analyses

The mean and SEM for each protein and plasticity feature from the 3 regions of V1 was calculated for each rearing condition. We used the bootstrap resampling method because it is a conservative approach to analyzing small sample sizes when standard parametric or non-parametric statistical tests are not appropriate. Here bootstrapping was used to estimate the confidence intervals (CI) for each of the recovery groups and a Monte Carlo simulation was run to determine if the 5wk Normal or 5wk MD groups fell outside those CIs. The statistical software package R was used to simulate normal distributions with 1,000,000 points using the mean and standard deviation from the recovery groups (RO, BD, BV). Next, a Monte Carlo simulation

randomly sampled with replacement from the simulated distribution n times, where n was the number of observations made from the normal or MD group (e.g., $n = 4-19$). The resampling procedure was repeated 100,000 times to determine the 95%, 99% and 99.9% CIs. The recovery group was considered significantly different (e.g., $p < 0.05$, $p < 0.01$ or $p < 0.001$) from the normal and MD group if the mean of those groups fell outside the CI for the recovery group.

Bootstrapping was also used to compare if the recovery subclusters identified by tSNE and k-means clustering were different from normal. When a subcluster was significantly greater than normal ($p < 0.05$) the boxplot was colored red, when it was less than normal ($p < 0.05$) the boxplot was colored blue, and if not it was not different from normal ($p > 0.05$), the boxplot was colored grey.

All of the bootstrap statistical comparisons between protein expression (Table 3-1) indices (Table 4-1) and plasticity features (Table 7-1) are presented in the Supplemental material.

The p-values for the Pearson's correlations were calculated using the rcorr package[34], and the significance levels were adjusted using the Bonferroni correction for multiple comparisons. The Pearson's Rs and p-values for the protein networks (Table 5-1), plasticity features with PCA dimensions (Table 6-1), and association between clusters (Tables 9-1, 9-2) are included in the Supplemental material.

We tested if recovery during BV followed either an exponential decay or sigmoidal pattern by fitting curves to the data using Kaleidagraph (Synergy Software, Reading PA). Significant curve fits were plotted on the graphs to describe the trajectory of recovery.

5.3 Results

Analyzing recovery of synaptic proteins: Synapsin I

We began analyzing the effects of the 3 recovery treatments by comparing expression of a pre-synaptic marker, synapsin I, in the central, peripheral, and monocular regions of cat V1. As we reported previously[23], 5wks MD did not affect expression of synapsin I relative to normals, but RO caused synapsin I expression to double in all regions of V1 (C: 216%±25%, $p<0.0001$; P: 197%±13%, $p<0.0001$; M: 241%±19%, $p<0.0001$) (Figure 3a). In contrast, there was only slightly less than normal synapsin I expression after BD (M: 82%±6%, $p<0.0001$) and 4d-BV (C: 79%±8%, $p<0.0029$).

Analyzing recovery of synaptic proteins: Glutamatergic receptor subunits

Next, we quantified changes in GluA2 and GluN1 expression in V1. Here we found that RO promoted a small increase in GluA2 expression (C: 112%±8%, $p<0.0001$; P: 118%±2%, $p=0.0691$; M: 172%±16%, $p<0.0001$) but a loss of GluN1 (C: 73%±10%, $p=0.0041$; P: 67%±3%, $p<0.0001$; M: 65%±14%, $p=0.0019$, Figure 3c). In contrast, after BD treatment GluA2 was reduced in the binocular regions of V1 (C: 40%±10%, $p<0.0001$; P: 58%±11%, $p<0.0001$).

BV treatment had variable effects on GluA2 similar to the timing of changes seen when short-term (hours) vs long-term (days) MD is started at the peak of the CP [27]. GluA2 expression fluctuated during BV but tended to be slightly below normal levels (Figure 3b). Interestingly, the timing of the fluctuations was the same but in the opposite direction to what we found previously with 1d of MD [27]. After 1d MD there was a decrease but here 1d BV had a transient increase in GluA2.

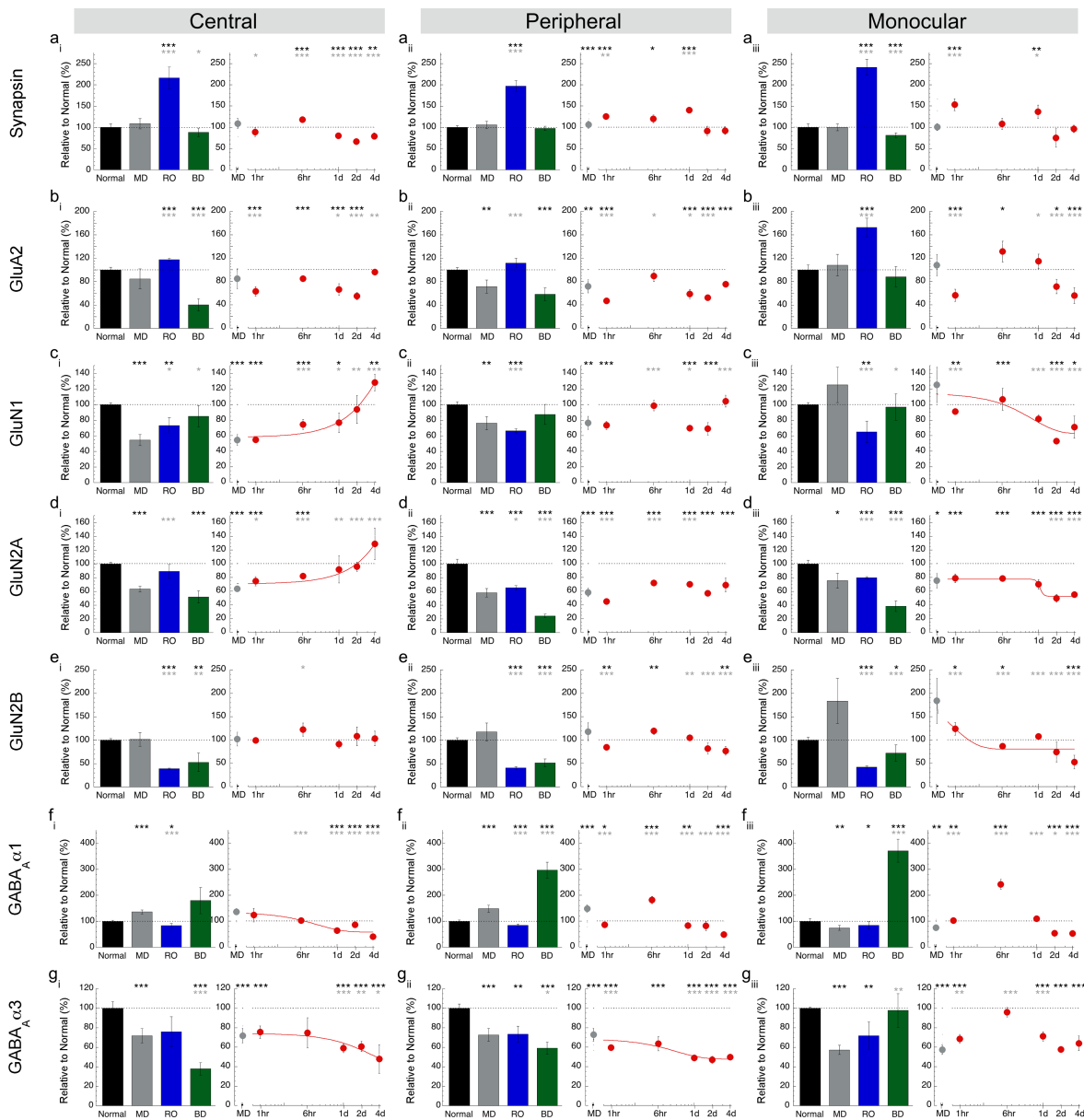


Figure 3. Expression of synaptic proteins in the different regions of visual cortex.

Histograms showing the average expression relative to 5 wk normal animals for the 7 proteins (rows) and 3 regions of V1 (columns), normal 5 wk animals (black bars), animals reared with MD to 5wks (grey bars), and animals treated with either RO (blue bars) or BD (green bars). Scatter plots showing the average protein expression (red dots) after 1hr to 4d of BV treatment. When the trajectory of protein changes during BV treatment was well-defined by a function, curve fits were applied (red line). Error bars represent standard error of the mean (SEM). Black asterisks represent significant differences relative to 5wk normal, and grey asterisks represent significant differences relative to 5wk MD (* $p < 0.05$, ** $p < 0.01$, *** $p < 0.001$). The dotted black line on each graph represents 5wk normal expression. For exact p-values, Pearson's R, and equations for the curve-fits see Table 3-2.

BV treatment had region-specific changes in GluN1 expression with central recovery to above normal levels ($y = 297.43 - 239.58 \cdot \exp(-x/11.61)$, $df=25$, $R^2=0.618$, $p<0.0001$) but below normal levels in the monocular region ($71\% \pm 14\%$, $p=0.0214$).

Next, we analyzed expression of the NMDAR subunits, GluN2A and GluN2B (Figure 3d,e), because they regulate ocular dominance and bidirectional synaptic plasticity in V1[17], [21] as well as receptor kinetics[38]. Similar to our previous study[23], GluN2A expression was reduced after MD across all of V1 (C: $63\% \pm 4\%$, $p<0.0001$; P: $58\% \pm 6\%$, $p<0.0001$; M: $76\% \pm 11\%$, $p=0.0220$). RO promoted modest recovery of GluN2A in the central region ($89\% \pm 10\%$, $p=0.1367$) but BD treatment did not. Instead after BD there was even less GluN2A than MDs in the peripheral ($24\% \pm 2\%$, $p<0.0001$) and monocular regions ($38\% \pm 8\%$, $p<0.0001$). BV promoted recovery of GluN2A in the central region (4d BV: $129\% \pm 23\%$, $p=0.1022$), but not in the other regions.

GluN2B expression was similar to normals after MD [23] but declined after both RO (C: $39\% \pm 1\%$, $p<0.0001$; P: $41\% \pm 3\%$, $p<0.0001$; M: $43\% \pm 2\%$, $p<0.0001$) and BD (C: $53\% \pm 20\%$, $p=0.0085$; P: $52\% \pm 8\%$, $p<0.0001$; M: $72\% \pm 18\%$, $p=0.0354$). BV, however, had little effect on GluN2B expression and after 4d it was similar to normal in the central region, and modestly reduced in peripheral (4dBV: $77\% \pm 9\%$, $p=0.0024$) and monocular regions (4dBV: $53\% \pm 15\%$, $p=0.0007$).

Analyzing recovery of synaptic proteins: GABAergic receptor subunits

Previous studies have shown that GABA_ARs are necessary for opening the CP[44], that GABA_Aα1 regulates patterns of activity needed for ocular dominance plasticity[20] and that GABA_Aα3 and GABA_Aα1 regulate the kinetics of GABA_ARs[39], [45]. For these reasons, we examined how the treatments affected the expression of GABA_Aα1 and GABA_Aα3. We found that BD increased GABA_Aα1 expression (P: $297\% \pm 31\%$, $p<0.0001$; M: $372\% \pm 45\%$, $p<0.0001$) but RO caused a slight decrease (C: $83\% \pm 8\%$, $p=0.0239$; P: $85\% \pm 4\%$, $p=0.0008$; M: $85\% \pm 14\%$, $p=0.0026$). After 4d of BV GABA_Aα1 expression was below normal levels (4d BV C: $40\% \pm 9\%$, $p<0.0001$; P: $48\% \pm 8\%$, $p<0.0001$; M: $51\% \pm 4\%$, $p<0.0001$). There was, however, a transient increase in GABA_Aα1 outside the central region after 6hrs of BV (P: $181\% \pm 14\%$, $p<0.0001$; M: $242\% \pm 19\%$, $p<0.0001$). GABA_Aα3 expression remained below normal levels after both RO and

BV treatments while after BD it was reduced in central and peripheral regions (C: $38\% \pm 6\%$, $p < 0.0001$; P: $59\% \pm 6\%$, $p < 0.0001$). Thus, these results provided preliminary evidence that these treatments do not return normal levels of expression for all 7 proteins in all regions of V1.

Instead, there was an intricate pattern of changes that did not clearly distinguish if a treatment shifted the overall pattern towards normal.

Analyzing heterogeneity in protein expression and comparing among rearing conditions

We were surprised by the complexity in the pattern of protein changes and wondered if there was an abnormally high degree of heterogeneity in the protein expression. To assess heterogeneity, we calculated an index of dispersion (variance-to-mean ratio, VMR) for each protein and condition and used it to determine if the distributions were under-dispersed ($\text{VMR} < 1$), randomly-dispersed ($\text{VMR} = 1$) or over-dispersed ($\text{VMR} > 1$). For 5wk normal and RO conditions all proteins were under-dispersed with VMRs < 0.3 (Supplemental figure 3-1). For the other conditions, the proteins were also under-dispersed except after MD. GluN2B was randomly-dispersed in the monocular region (Supplemental figure 3-1), and GABA_A $\alpha 1$ was over-dispersed centrally after BD and in the monocular region after 4d BV. This analysis did not find increased heterogeneity that might explain the complexity, so we continued to analyze patterns of protein expression starting with pairs of proteins known to have functional interactions.

Analyzing the balance between functionally related pairs of receptor subunits

We calculated a set of indices to assess the effects of recovery treatments on the balance between functionally related pairs of receptor subunits: GluA2:GluN1, GluN2A:GluN2B, and GABA_A $\alpha 1$:GABA_A $\alpha 3$. In normally developing cat V1 the AMPAR:NMDAR balance still favors GluN1 expression at 5wk[23]. MD, however, shifted the balance to favor GluA2 in central (0.06 ± 0.09 , $p = 0.044$) but not in other regions (P: -0.20 ± 0.07 , $p = 0.078$; M: -0.18 ± 0.05 , $p = 0.16$, Figure 4a). RO shifted the balance to favour GluA2 across all of V1 (C: 0.12 ± 0.06 , $p < 0.0001$; P: 0.14 ± 0.04 , $p < 0.0001$; M: 0.29 ± 0.06 , $p < 0.0001$) while BD had the opposite effect shifting to more GluN1 (C: -0.49 ± 0.08 , $p = 0.0002$; P: -0.33 ± 0.04 , $p < 0.0001$). Finally, after 4d of BV the

AMPA:NMDAR favored GluN1 across all of V1 (C: -0.26 ± 0.04 , $p=0.0004$; P: -0.25 ± 0.02 , $p<0.0001$; M: -0.25 ± 0.05 , $p=0.0078$).

The composition of the NMDAR affects experience-dependent plasticity and more GluN2B facilitates, while more GluN2A reduces, plasticity. MD changed the 2A:2B balance to more GluN2B but RO flipped it to more GluN2A (C: 0.28 ± 0.06 , $p<0.0001$; P: 0.28 ± 0.027 , $p<0.0001$; M: 0.31 ± 0.02 , $p<0.0001$)(Figure 4b). BD also shifted the 2A:2B balance to more 2A in the central region (0.14 ± 0.13 , $p=0.0001$) but not the other parts of V1 where it remained at levels similar to the MDs (P: -0.22 ± 0.08 , $p=0.0008$, M: -0.37 ± 0.10). The introduction of BV caused the 2A:2B balance to shift towards normal levels in all of V1 although after 4d of BV the central and peripheral regions were slightly different from normal (C: -0.01 ± 0.05 , $p=0.0002$; P: -0.02 ± 0.04 , $p=0.0003$).

The subunit composition of the GABA_AR also contributes to regulating experience-dependent plasticity in V1 as the developmental addition of GABA_A α 1 is needed for ocular dominance plasticity[20]. Here we found that RO and BD promoted changes in the opposite direction from the 2A:2B balance shifts. RO shifted the α 1: α 3 toward normal levels (C: 0.07 ± 0.14 , $p=0.3087$; P: 0.08 ± 0.04 , $p=0.0083$; M: 0.10 ± 0.04 , $p=0.0008$) while BD shifted it towards even more GABA_A α 1 than found after MD (C: 0.50 ± 0.13 , $p=0.0003$; P: 0.63 ± 0.03 , $p<0.0001$; M: 0.60 ± 0.02 , $p<0.0001$). After 4d of BV the α 1: α 3 balance had shifted back to normal levels in the central and peripheral regions (C: -0.01 ± 0.14 , $p=0.5005$, P: -0.13 ± 0.08 , $p=0.1163$) Thus, both BV and RO shift the α 1: α 3 toward normal levels but only BV shifted the 2A:2B balance toward normal.

Together, the 3 balances highlight region- and treatment-specific changes suggesting that BV may recover closest to 5wk normal balances, however, BV did not simply reinstate normal balances for these pairs of receptor subunits.

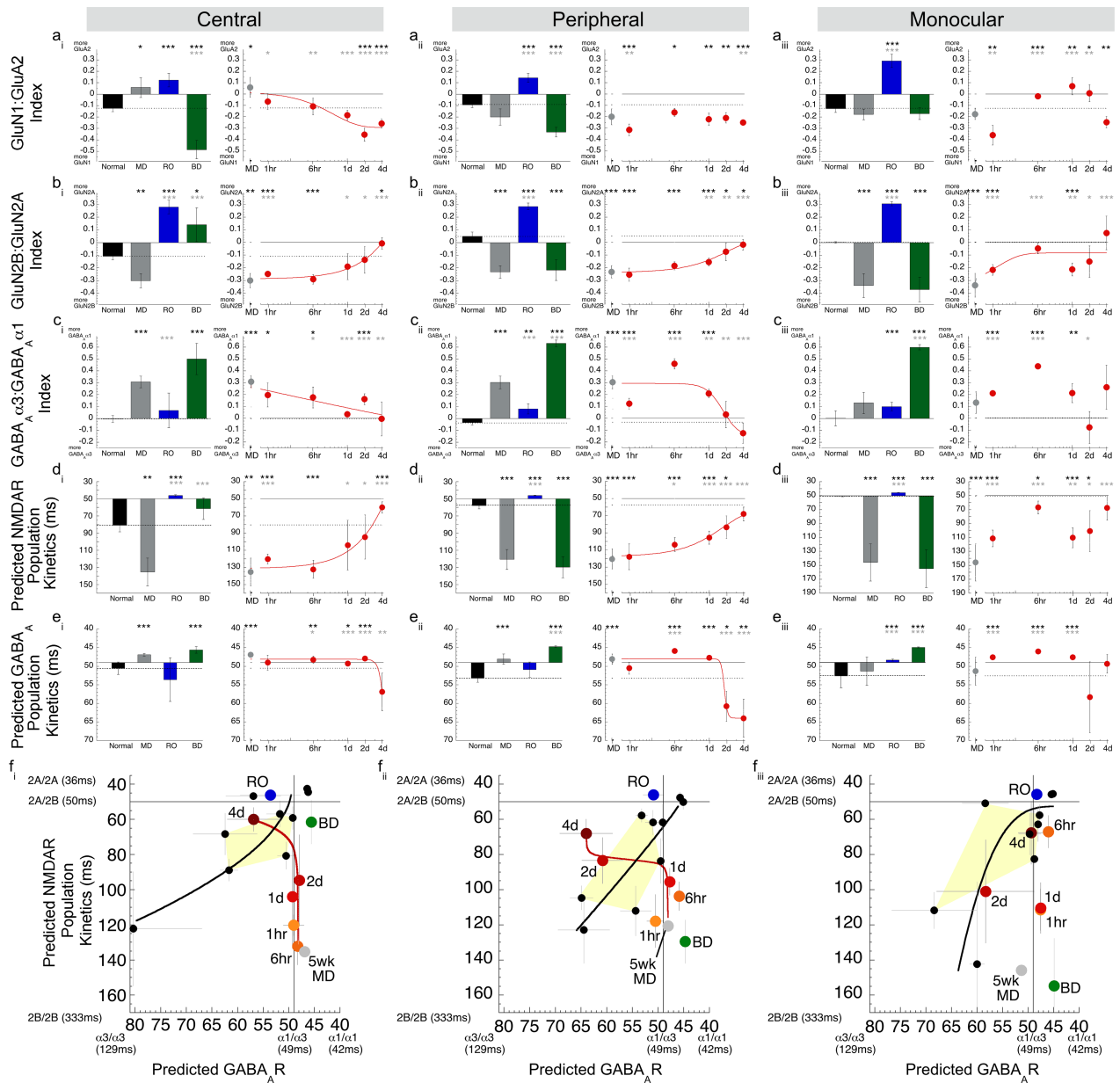


Figure 4. Indices for pairs of receptor subunits and modeling of predicted decay kinetics for a population of NMDARs and GABA_ARs.

Histograms and scatter plots showing the average expression of the 3 receptor subunit indices (**a**:GluN1:GluA2, **b**:GluN2B:GluN2A, **c**:GABA_Aα3:GABA_Aα1) and predicted population kinetics (**d**:NMDAR, **e**:GABA_AR) for the regions of V1 (columns). **f**. The predicted population kinetics are plotted for both GABA_ARs (x-values) and NMDARs (y-values) for normally reared animals age range 2wks-adult with the curve representing the trajectory of the relationship between these features (black dots & line, see Figure 4-1 for normal data). Also, the data are plotted for 5wk MD (grey dot), RO (blue dot), and BD (green dot). The relationship between NMDAR and GABA_AR kinetics during BV treatment for 1hr (orange) to 4d (red) is plotted, and the line uses the functions fit to the data in d and e. The conventions are the same as in Figure 3. For exact p-values, Pearson's R, and equations for the curve-fits see Table 4-2.a.

Modeling NMDAR and GABA_AR population kinetics

The subunit composition of NMDARs and GABA_ARs help to regulate the threshold for experience-dependent plasticity, in part by controlling the receptor kinetics [38], [39]. We used information about receptor kinetics with different subunit compositions to make a model that predicts the average population kinetics and applied it to the rearing conditions studied here. First, we transformed the 2A:2B and $\alpha 1:\alpha 3$ balances into predicted population kinetics (see Methods) and compared among the groups (Figure 4d,e). The pattern of results is necessarily similar to the balances presented above, however, the predicted kinetics suggests a compression of differences between conditions when the balances shift to favor the mature subunits (2A or $\alpha 1$) versus an accentuation of differences to much slower kinetics when the immature subunits (2B or $\alpha 3$) dominated.

To address how treatment induced changes to NMDAR and GABA_AR composition might change the relationship between glutamatergic and GABAergic transmission timing we made XY scatterplots using the predicted kinetics (Figure 4f, 4-2). In addition, we analyzed the normal development to identify the range of kinetics predicted for the peak of the CP (Figure 4-1). During normal development (black line) both balances progressed from slow kinetics at 2wks to faster kinetics through the peak of the CP (Figure 4f- yellow zone, 4-6wks) to reach adult levels. The NMDAR:GABA_AR kinetics for MD, RO and BD fell outside the window predicted for the normal CP, but in different directions. MD had slower NMDAR (C: 135ms±16ms, p=0.0031; P: 121ms±12ms, p<0.0001; M: 146ms±27ms, p=0.0007) but faster GABA_AR kinetics (C: 47ms±0.3ms, p<0.0001; P: 48ms±1ms, p=0.0004; M: 51ms±4ms, p=0.3795), RO had faster NMDAR (C: 46ms±0.8ms, p<0.0001; P: 46ms±0.4ms, p<0.0001; M: 46ms±0.2ms, p<0.0001) but normal CP range for GABA_AR (C: 54ms±6ms, p=0.3015; P: 51ms±2ms, p=0.1586; M: 48ms±0.2ms, p<0.0001), and BD had faster GABA_AR (C: 46ms±0.9ms, p<0.0001; P: 44ms±0.2ms, p<0.0001; M: 45ms±0.2ms, p<0.0001) but normal CP range NMDAR kinetics in the central region only (C: 61ms±12ms, p=0.0836; P: 130ms±12ms, p<0.0001; M: 155ms±27ms, p<0.0001).

The introduction of BV caused a progressive change in the predicted NMDAR:GABA_AR kinetics suggesting an initial speeding up of the NMDAR kinetics over the first 1d to 2d followed by a slowing of the GABA_AR kinetics, especially in the central region.

Taken together, the predicted NMDAR:GABA_AR kinetics suggest differences among the conditions with BV shifting towards a normal CP balance but none of the treatments reinstated normal kinetics. Furthermore, the complexity of the univariate analyses make it difficult to identify individual proteins or balances that differentiate BV treatment from RO and BD. To address this problem, we implemented a set of unbiased, high-dimensional analyses to assess network relationships among the proteins, identify plasticity features, and construct plasticity phenotypes.

Analyzing the pairwise similarity between protein expression profiles

First, we wanted to identify pairs of proteins with similar or opposing expression profiles and compare them among the rearing conditions. For each condition, we collapsed the data from the 3 regions of V1, calculated the matrix of pairwise correlations between the 7 proteins, ordered the protein correlations using a hierarchical dendrogram, and used 2D heatmaps to visualize the correlations (Figure 5). The order of proteins in the dendrogram indicated which ones had similar (e.g. on the same branch of the dendrogram) or different patterns of expression and the color of the cell illustrated the strength of the correlation. For 5wk normal animals (Figure 5a), there were strong positive correlations (red cells) among all proteins except GluN2A, which was weakly correlated and not clustered with the other proteins. A different pattern of correlations was found after MD (Figure 5b); here glutamatergic proteins were weakly, or even negatively correlated (blue cells) with GABA_Aα1, GABA_Aα3, and synapsin I. These results suggest that MD drives a decoupling of these excitatory and inhibitory mechanisms. RO also separated glutamatergic and GABAergic proteins into different clusters at the first branch (Figure 5c); however, the correlations were weaker, suggesting that RO reduced the MD-driven decoupling of these mechanisms. After BD the correlation matrix had mostly positive correlations (Figure 5d) except for synapsin I which was negatively correlated and not clustered with the other proteins. BV treatment highlighted the dynamic nature of this recovery (Figure 5e-i). Just 1hr of BV was enough to change the correlation matrix from the MD pattern, but even

after 4d of BV the correlation matrix still appeared different from the normal 5wk pattern of correlations.

These matrices suggest different patterns of correlations depending on the condition, but this analysis treats each comparison with the same weighting and it is likely that some proteins contribute more than others to the variance in the data. To assess this, we used PCA to identify individual proteins and combinations of proteins that capture the variance in the data and may represent plasticity features reflecting differences among the treatment conditions.

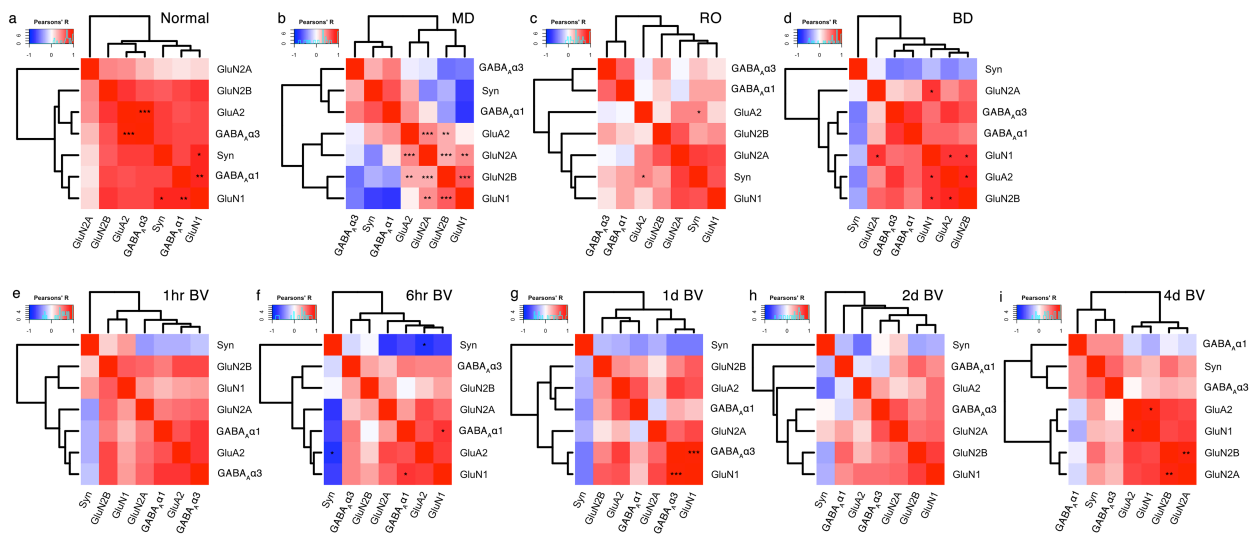


Figure 5. Visualizing pairwise correlations between proteins.

Correlation matrices are plotted showing the strength (saturation) and direction (blue:negative; red:positive) of the pairwise Pearson's R correlations between proteins for each condition **a**. 5wk Normal, **b**. 5wk MD, **c**. RO, **d**. BD, and **e-i**. BV. The order of proteins was determined using hierarchical clustering so proteins with stronger correlations were nearby in the matrix. Significant correlations are denoted by an asterisk (* $p < 0.05$, ** $p < 0.01$, *** $p < 0.001$). For table of Pearson's R values and Bonferroni corrected p-values see Table 5-1.

Using principal component analysis to reduce dimensionality and identify plasticity features

We used PCA to reduce the dimensionality, transform the data and find features that define the covariance among the proteins. An $m \times n$ matrix was made using protein expression, where the m columns were the 7 proteins and the n rows (109) were the tissue samples from all the animals and regions of V1 used in this study. This matrix was analyzed using singular value decomposition (SVD), and the first 3 dimensions explained most of the variance (82%) in the data (Dim1: 54%, Dim2: 18%, Dim3: 10%) (Figure 6a).

To understand which proteins contributed to each dimension we addressed the quality of the representation for each protein using the \cos^2 metric and found that the glutamatergic proteins were well represented by Dim1, GABA_Aα1 by Dim2, and GluA2 and GluN2B by Dim3 but synapsin I and GABA_Aα3 were weakly represented in the first 3 dimensions (Figure 6 b,c). Next, we compared the vectors for each protein (Figure 6 d,f) and the PCA space occupied by the rearing conditions (Figure 6 e,g). The protein vectors show that GluN1, GluN2A, GluN2B, and GluA2 extended along Dim1, GABA_Aα1 along Dim2, and GluA2 and GluN2B were in different directions along Dim3. The PCA space occupied by the conditions suggest some differences: BD was separated on Dim 2 in the same direction as GABA_Aα1, but the center of gravity for the other conditions overlapped the space occupied by normal samples.

The overlap among conditions raised the possibility that higher dimensions may separate the conditions. To begin to assess higher dimensional contributions we examined the basis vectors (Figure 6h) and the correlations between individual proteins and PCA dimensions (Figure 6i) to identify combinations of proteins that might reflect higher dimension features. For example, all proteins had positive amplitudes for the Dim1 basis vector (Figure 6h) and positive correlations with Dim1 (Figure 6i) suggested that protein sums may be higher dimensional features. In addition, weights for GluN2A and GABA_Aα1 on Dim2 were opposite, suggesting that when one protein increased the other decreased and this could be a novel feature of these data. Continuing with this approach we identified 9 putative plasticity features; protein sums (all protein sum, GlutR sum, GABA_AR sum) or indices (GlutR:GABA_AR, GluN2A:GluN2B, GABA_Aα1:GABA_Aα3, GluN2A:GABA_Aα1, GluA2:GluN2B, GluN2A:GluA2). All of the protein sums and 4 of the indices were features not analyzed with the univariate statistics; however, each had a strong biological basis in previous research. For example, the new indices paired the mature GluN2A with the mature GABA_Aα1 or GluA2 subunit, and GluN2B with GluA2 which is known to regulate the development of AMPARs[46]. Finally, we calculated the 9 features and determined if at least one of the first 3 dimensions was correlated with the features (Figure 6j). Only the GlutR:GABA_AR balance was not correlated with any of the first 3 dimensions, but because these mechanisms are related to the E:I balance[47] we included this measure in the next analysis.

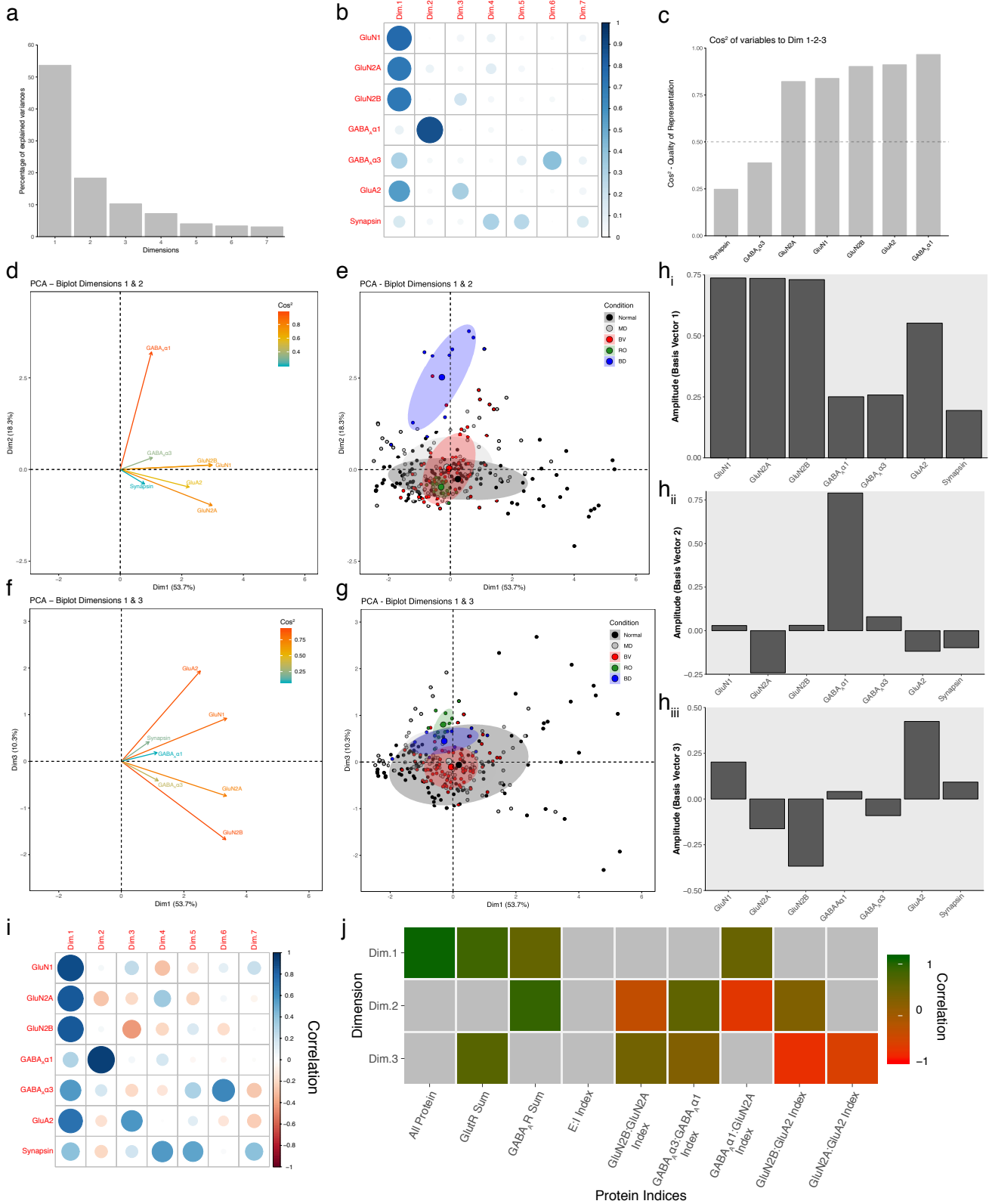


Figure 6. Identifying plasticity features using principal component analysis

a. The percentage of variance captured by each principal component by singular value decomposition (SVD) applied using all of the protein expression data. The first 3 principal components capture 54%, 18% and 10% of the variance, respectively, totalling >80% and thus representing the significant dimensions. **b.** The quality of the representation, \cos^2 , for the proteins is plotted for each dimension (small/white: low \cos^2 ; large/blue: high \cos^2). **c.** The sum of \cos^2 values for the first 3 dimensions for each protein. **d,e.** Biplots of PCA dimensions 1&2 and **f,g.** 1&3. These plots show the vector for each protein (**d,f**) and the data (small dots) plus the average (large dots) for each condition with the best-fitting ellipse (**e,g**). **h.** The basis vectors for dimensions 1-3 showing the amplitude of each protein in the vector. **i.** The strength (circle size) and direction (blue-positive, red-negative) of the correlation (R^2) between each protein and the PCA dimensions. **j.** Correlation between the plasticity features (columns) identified using the basis vectors (see Results) and then PCA dimensions 1-3. Filled cells are significant, bonferroni corrected correlations (green = positive, red = negative). For table of Pearson's R values and significant p-values for these associations see Table 6-1.

We plotted the plasticity features and saw that the GlutR and GABA_AR sums identified differences among the treatment conditions. For example, there was less GlutR in the central region after RO (77%±5%, $p < 0.0001$) and BD (66%±14%, $p = 0.0078$) but normal levels of GlutR after LT-BV (4dBV= 114%±10%, $p = 0.0671$) (Figure 7b). In contrast, GABA_AR decreased for both BV (44%±12, $p < 0.0001$) and RO (80%±7%, $p = 0.0029$) but after BD it either did not change or increased substantially (P: 175%±19, $p < 0.0001$; M: 240%±40, $p < 0.0001$) (Figure 7c). BV caused a shift of the GlutR:GABA_AR to favor GlutR (C: 0.51±0.12, $p = 0.0002$; P: 0.33±0.04, $p < 0.0001$) while BD shifted in the other direction to more GABA_AR (C: -0.22±0.12, $p = 0.0072$; P: -0.45±0.05, $p < 0.0001$; Figure 7d). That pattern was mirrored by the GluN2A:GABA_Aα1 index, with BV shifting to more GluN2A (4dBV C:0.51±0.14, $p = 0.0004$; P: 0.28±0.10, $p = 0.0484$; M:-0.22±0.18, $p = 0.0319$) and BD to more GABA_Aα1 than normal (C: -0.41±0.13, $p = 0.0038$; P: -0.77±0.03, $p < 0.0001$; M: -0.78±0.03, $p < 0.0001$) (Figure 7e). The GluN2B:GluA2 index identified RO as different with substantially more GluA2 (C: 0.40±0.02, $p < 0.0001$; P: 0.43±0.04, $p < 0.0001$; M: 0.55±0.01, $p < 0.0001$; Figure 7f). Together, these features provide some evidence for glutamatergic versus GABAergic differences among the treatment conditions.

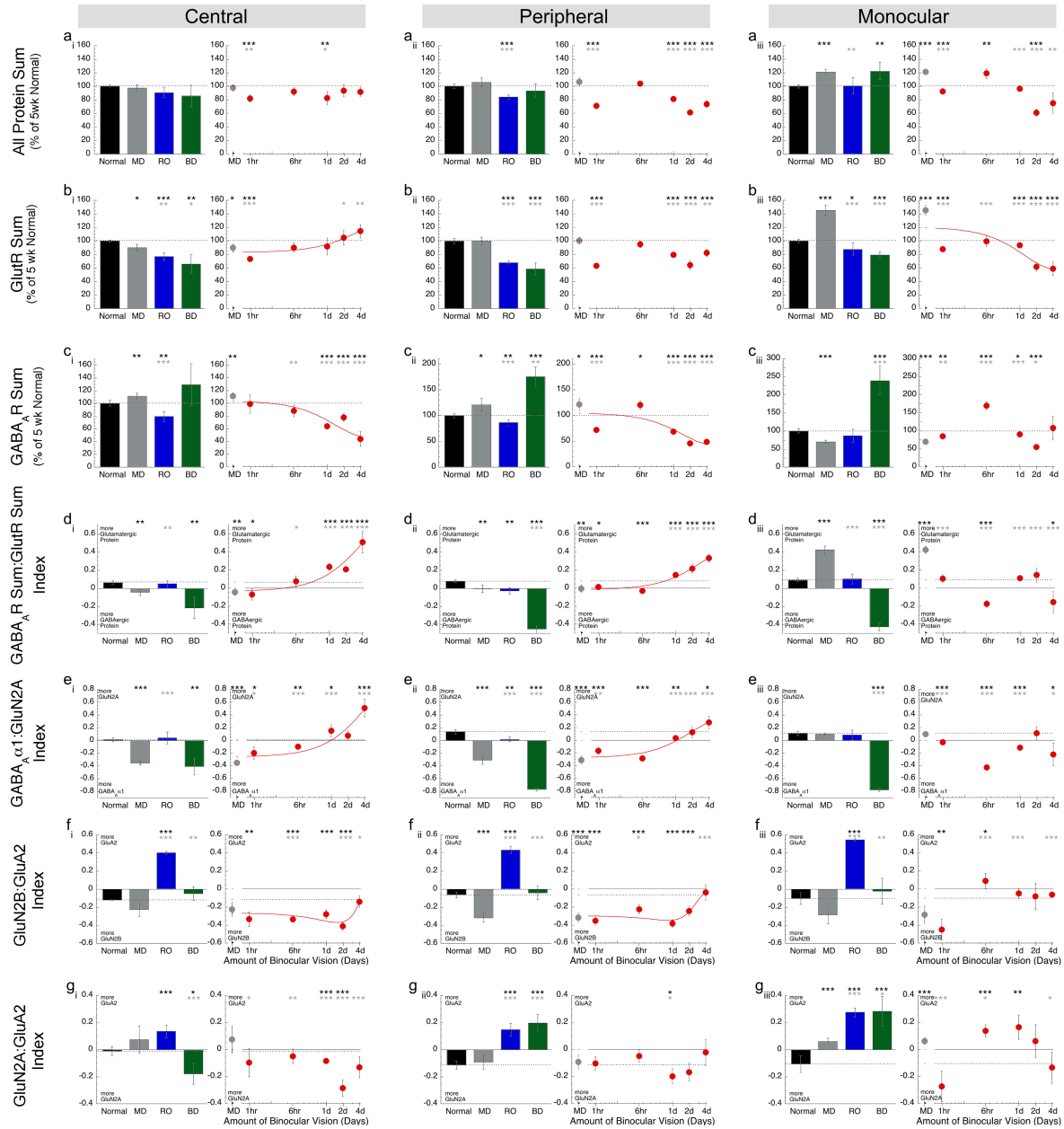


Figure 7. Expression of plasticity features identified using principal component analysis.

Histograms and scatter plots showing the plasticity features (rows)(except GluN2B:GluN2A shown in Fig. 4) that were identified using the PCA basis vectors (Fig. 6j) and plotted for each region of V1 (columns). The conventions are the same as in Figure 3. For exact p-values, Pearson's R, and equations for the curve-fits see Table 7-1.

Using t-SNE to transform and visualize clustering in the pattern of plasticity features

We used t-SNE to transform the plasticity features and visualize them in 2D (Figure 8a), then k-means and the “elbow method” (Figure 8-1) to identify the number of clusters. For these analyses, the BV samples were collapsed into ST-BV (1-6hrs) and LT-BV (1-4d) groups, and the plasticity features were calculated for all samples from the 3 V1 regions.

Six clusters were visualized with t-SNE (Figure 8) and the composition of the clusters was analyzed to determine the V1 regions and rearing conditions in each cluster. Cluster 1 was the largest with 39 samples (C=26%; P=54%; M=21%) and had the greatest number of samples from the central region (Figure 8b,d). Cluster 3 also had samples from central, peripheral and monocular regions while clusters 4, 5, and 6 were dominated by peripheral samples with few or no central region samples. Thus, there was some clustering by V1 region, but more apparent clustering emerged when the samples were color-coded by rearing condition (Figure 8c, d). All but one of the normal samples were in cluster 1, all of the RO samples were in cluster 2, most of the BD samples were in cluster 3 with a few in cluster 6, and most of the MD samples were in clusters 1 or 3. The BV samples, however, were found in 5 of the clusters with the greatest number of BV central samples (83%) grouped with normals in cluster 1.

Further analysis of cluster 1 showed that the majority of LT-BV and ST-BV samples from the central region clustered with the normals (Figure 8d). Interestingly, some of the MD samples were also in cluster 1; however, those samples were from the peripheral and monocular regions which are known to be less affected by MD than the central region[48]. Together, these results show that the data are clustered and that the clustering was driven by both rearing condition and region of V1.

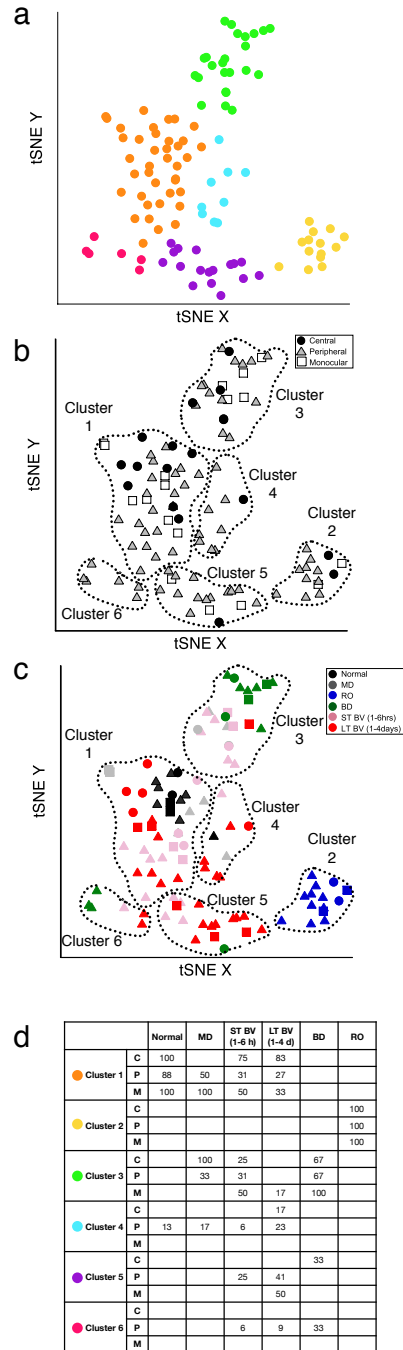


Figure 8. Clustering of samples with similar plasticity features identified using t-Distributed Stochastic Neighbor Embedding (t-SNE) and k-means clustering.

a. Using tSNE to visualize clustering of samples (109 tissue samples from animals reared to 5wk normal, 5wk MD, RO, BD and BV) calculated from k-means analysis of the 8 plasticity features identified by PCA. The optimal number of clusters ($k=6$) was identified by measuring the within groups sum of squares at intervals between 2 and 9 clusters (Figure 8-1) **b.** The content of each cluster was visualized for the region (central, peripheral, monocular) **c.** or treatment condition. **d.** The table summarizes the percentage of samples for each region and condition in Cluster 1-6. For example, 100% of the samples from the central region of V1 in Normal animals were in Cluster 1 while 100% of the samples from all regions of RO were in Cluster 2. This information was used to annotate subclusters based on the cluster membership (1-6), rearing condition, and region of V1.

Correlating plasticity features among subclusters

We annotated the samples in each cluster using the rearing condition and V1 region and used that information to identify 13 subclusters where at least one region per condition had $n \geq 2$ and $>20\%$ of the samples in that cluster (Figure 8d, black font). A correlation matrix was calculated to assess the similarity between subclusters (see Table 9-1 for R values and 9-2 for Bonferroni adjusted p values) and the order of the subclusters in the correlation matrix was optimized by hierarchical clustering so subclusters with similar patterns of features were nearby in the dendrogram. Bonferroni adjusted p value was used to determine the significant correlations ($0.05/78=0.0006$) (Figure 9). This analysis showed that 3 of the 4 LT-BV subclusters (LT-BV 1: $R=0.98$; LT-BV 5: $R=0.98$; LT-BV 4: $R=0.96$) and the MD 1PM subcluster ($R=0.98$) were strongly correlated with normals. The other MD subcluster with central samples (MD 3CP) was on a separate branch of the dendrogram and was strongly correlated with the 3 ST-BV subclusters (ST-BV 1: $R=0.98$; ST-BV 3: $R=0.99$; ST-BV 5: $R=0.98$). The ST-BV subclusters were also correlated with normals (ST-BV 1: $R=0.96$; ST-BV 3: $R=0.94$; ST-BV 5: $R=0.97$), LT-BV 1 (ST-BV 1: $R=0.98$; ST-BV 3: $R=0.94$; ST-BV 5: $R=0.98$), and MD1 (ST-BV 1: $R=0.98$; ST-BV 3: $R=0.94$; ST-BV 5: $R=0.99$) but weaker correlations with LT-BV 4 (ST-BV 1: $R=0.94$; ST-BV 5: $R=0.95$) and no significant correlations with LT-BV 5. RO was correlated with normal ($R=0.96$) but only one of the LT-BV subclusters (LT-BV 5: $R=0.96$) and none of the ST-BV subclusters. The two BD subclusters were correlated ($R=0.94$) but none of the other correlations were significant. The pattern of strong correlations in this matrix and the resulting dendrogram suggested that the subclusters might form 4 groups that have similar plasticity features (1: normal, LT-BV, MDP or M; 2: RO; 3: ST-BV, MDC; 4: BD).

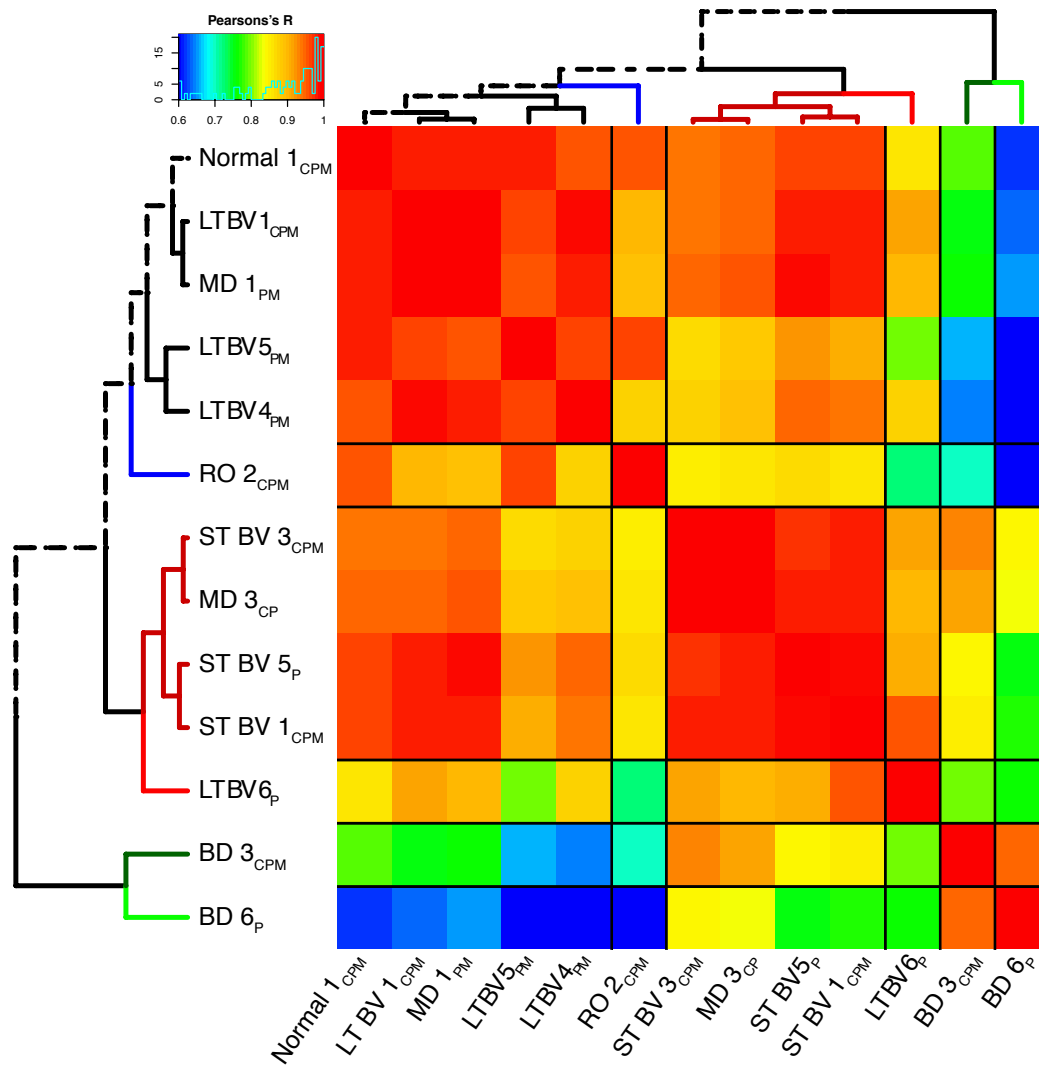


Figure 9. Visualizing pairwise correlations between treatment subclusters.

The matrix is showing the strength (0.6=blue; 1=red) of correlation between the subclusters identified in Fig. 7d and annotated here using the rearing condition, cluster (1-6), and region of V1. Hierarchical clustering was used to order the data so that subclusters with strong correlations were nearby in the matrix. The subclusters formed 5 groups using the height of the dendrogram that is denoted by a change in the color of the dendrogram. The dotted black line in the dendrogram highlights the path to the normal subcluster. The black lines in the matrix identify the 5 groupings of the subclusters. For exact Bonferroni corrected p-values see Table 9-1 and for Pearson's R values see Table 9-2.

Constructing plasticity phenotypes and comparing among the conditions

To compare the pattern of plasticity features among the subclusters we visualized the average for each feature as a color-coded horizontal band, stacked the bands to illustrate the pattern that we called the plasticity phenotype (Figure 10a) and ordered the phenotypes using the same dendrogram as the correlation matrix (Figure 10b). In addition, we visualized the plasticity phenotypes for normal development and MD (using the data from [23]) to compare the treatment subclusters with a broad range of ages that had developed with either normal or abnormal visual experience (Figure 10 c,d).

Inspection of the plasticity phenotypes identified some obvious and other subtler differences among the subclusters (Figure 10b). Indeed, the pattern of red and green bands in the BD phenotypes was different from 5wk normals (Figure 10) and showed the shift to more GABA α 1 and less GluN2A. For the RO subcluster, the light grey bands and number of green bands identified loss of protein expression and a shift to more GluN2A than 2B and more GluA2 than 5wk normals. The RO pattern, however, appeared similar to an older (e.g. 12wk) normally reared animal suggesting that RO may accelerate maturation of these proteins. Thus, these BD and RO treatments led to distinct plasticity phenotypes.

The pattern of red and green bands in the plasticity phenotype for LT-BV and some of the ST-BV subclusters (ST-BV1, ST-BV5) appeared similar to the 5wk normals (Figure 10b) but many of the features were still significantly different from the age-matched normals (Figure 11a, 11-1). Nonetheless, these subclusters had some consistent differences with less GABA α Rs and more GluN2B than 5wk normals. Interestingly, one of the novel features found by PCA, the GluN2A:GluA2 balance, was the only measure where all of the LT-BV subclusters were not different from 5wk normals but both RO and BD were different. Thus, this visualization of the plasticity phenotypes illustrated that the pattern promoted by BV, and LT-BV in particular, was most similar to the normal CP phenotype.

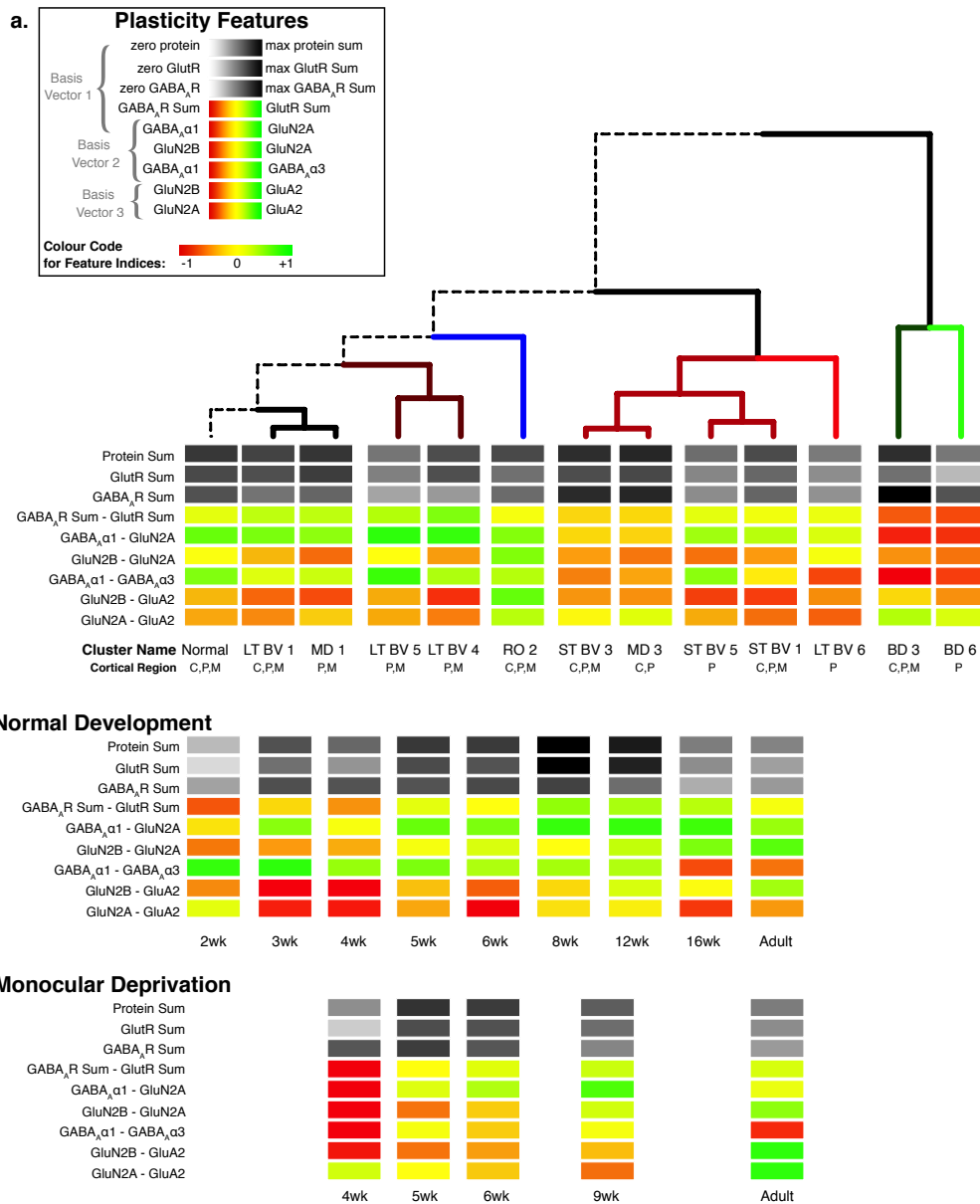


Figure 10. Visualizing the plasticity features and phenotypes for each subclusters

a. We visualized the plasticity features as a stack of color-coded horizontal bars that together comprise the plasticity phenotype. The 3 grey scale bars represent the protein sums and the 6 red-green color-coded bars represent the plasticity indices identified by the PCA. **b.** The plasticity phenotypes were calculated for each subcluster and ordered using the same dendrogram as described in Fig. 9. **c.** For comparison the plasticity phenotypes were calculated using previously published data[23] for normal development (2 - 32 wks) **d.** and animals MDED from eye open until either 4, 5, 6, 9 or 32 wks.

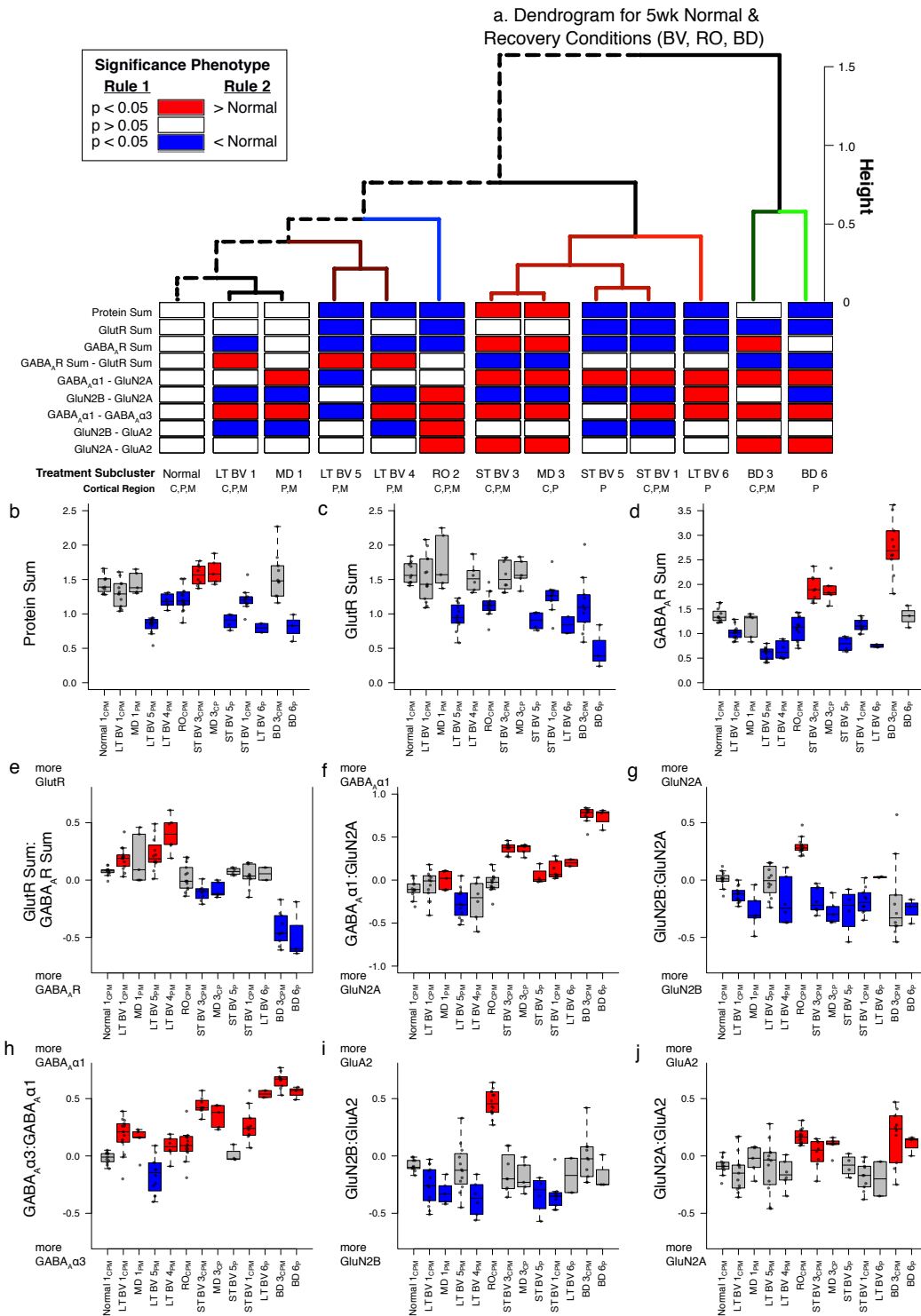


Figure 11. Significant plasticity features

a. We used bootstrap analysis to identify plasticity features that were significantly different from 5wk normal animals and color-coded the horizontal bars red if the feature was >normal and blue if it was <normal (p<0.05). **b-j**. The boxplots show the average protein sum (**b-d**) and an average index value (**e-j**) for each of the subclusters. Boxes were colored red if significantly greater than 5wk normals, blue if significantly less than 5wk normals and grey if not significantly different from 5wk normals. For exact Bonferroni corrected p-values see Table 11-1.

5.4 Discussion

Here we studied a set of glutamatergic and GABAergic receptor subunits in V1 that regulate plasticity and explored classifying the expression patterns for treatments that cause either persistent bilateral amblyopia (RO or BD) or good acuity in both eyes (BV). We found a complex pattern of changes that varied by treatment and region within V1. Analyzing the balances between receptor subunits and modeling kinetics for NMDAR and GABA_AR provided some evidence that BV returns CP-like balances, especially in the central region of V1. Furthermore, applying a new analysis approach using PCA and cluster analysis identified higher dimensional features and subclusters with different plasticity phenotypes for treatments that promote good versus poor recovery of acuity. The LT-BV plasticity phenotypes were closest to the normal CP pattern while the RO phenotype appeared more similar to an older pattern dominated by GluA2. In contrast, the BD phenotypes were dominated by GABA_Aα1 making it distinct from RO and illustrating that multiple plasticity phenotypes can underlie persistent bilateral amblyopia. Finally, the PCA analysis identified an understudied feature, the balance between mature glutamate receptor subunits (GluN2A:GluA2 balance), as a marker that might differentiate treatments supporting good acuity (BV), from those that lead to persistent bilateral amblyopia (RO, BD).

Study design and limitations

The exploratory nature of the design used here was limited because the small number of animals used leaves unanswered how much variation there is in response to the treatments. The visual manipulations (MD, RO, BD, BV), however, are known to cause consistent changes in visual perception [7], [8], [49]-[52], physiology [7], [29], [31], [53], and molecular mechanisms [23], [27], [54]-[59] that have been reliably measured in a number of laboratories using the cat to study visual system plasticity. Thus, this exploration of treatment-induced changes provides a preliminary understanding about the pattern of recovery. These results will be useful for formulating new hypotheses about the links between these proteins and persistent amblyopia as discussed below for the GluN2A:GluA2 balance.

The study design had some strengths including that (i) the animal model has excellent spatial vision, with a central visual field, so we could compare changes in regions of V1 that

represent different parts of the visual field[27], (ii) the treatments were initiated and completed within the CP[60], (iii) there is detailed information about the recovery of physiology for RO and BV[7], [29], [53], [61] and acuity for all 3 treatments[7], [8], [27], [29], [30], (iv) both RO and BD cause persistent bilateral amblyopia[8], [30], and (v) the treatments engage different forms of experience-dependent plasticity (RO: competitive; BD: cooperative with degraded visual input; BV: cooperative with normal visual input).

We observed that only one feature (GluN2A:GluA2 balance) returned to normal after LT-BV treatment raising the hypothesis that it is necessary for good recovery. We were not able to test that question because the molecular tools are not available for manipulating proteins in cat cortex so it will be important to replicate that finding in the mouse and then test the question by directly manipulating those proteins. In addition, a large number of other treatments have been tested to improve recovery after MD, including a brief period of dark-rearing[30], [62], fluoxetine administration[63], perceptual learning[27], [64], or targeting specific molecular mechanisms (e.g., perineuronal nets[65]). Undoubtedly, the timing, length, and type of treatment influences recovery but the conditions used here were necessarily limited because of the labor-intensive nature of this study. Notwithstanding these limitations, the plasticity phenotypes identified RO and BD as different from each other and from normals, but the LT-BV subclusters were remarkably similar to the 5wk normal pattern.

Finally, the design took advantage of the reliability and multiplexing capabilities of Western blotting to obtain a large dataset of plasticity proteins from multiple V1 regions and rearing conditions. Western blotting, however, does not provide information about the cell types, layers, cortical columns, or subcellular localization of these proteins that would reveal which circuits are involved in recovery or persistent amblyopia. Even without that information, the application of high dimensional analyses led to the characterization of features and treatment-based clusters with unique plasticity phenotypes. The phenotyping approach developed here is scalable for studying more proteins or genes, cortical areas, and treatment conditions. Taken together, we think that this approach can be used in other animal models where molecular tools can be combined with visual testing to identify the features and phenotypes necessary for optimal visual recovery.

BV promoted recovery of CP-like plasticity phenotype and identified GluA2:GluN2A as a balance that differentiated BV treatment

We explored BV treatment because it promotes long-lasting recovery of good acuity in both eyes[27] and those findings are similar to promising results of binocular therapies for treating amblyopia in children[66]. Furthermore, there is good physiological recovery with BV[29], [61]. Thus, it was not surprising to find that LT-BV subclusters had the strongest correlations with normals, or that those subclusters had CP-like phenotypes. However, only one of the features, the GluA2:GluN2A balance, returned to normal levels. These findings suggest that it may not be necessary to recapitulate every detail of the normal phenotype to support good visual recovery and that the GluA2:GluN2A balance may be a characteristic feature for tracking functional recovery. Although that balance is not commonly quantified, both proteins are critical components of mechanisms regulating experience-dependent plasticity and that balance might signify the adaptive engagement of multiple plasticity mechanisms. For example, the delayed increase in visual responses during ocular dominance plasticity is part of a homeostatic plasticity mechanism regulated by trafficking GluA2-containing AMPARs into the synapse[67], [68]. Meanwhile, the initiation of ocular dominance plasticity requires GluN2A expression[22], and when GluN2A is deleted or reduced MD does not depress deprived eye responses but instead causes enhancement of activity driven by the open eye[21]. Our finding that LT-BV returned a CP-like GluA2:GluN2A balance suggests that BV may prime GluN2A-dependent Hebbian plasticity to consolidate deprived-eye connections while GluA2-dependent homeostatic plasticity enhances deprived-eye responsiveness without triggering runaway excitation[69]-[73]. Thus, the GluA2:GluN2A balance may reflect the idea that during BV treatment the non-deprived eye acts as a teacher guiding both cooperative and competitive plasticity mechanisms[29].

RO versus BD plasticity phenotypes

Because RO and BD treatments cause persistent bilateral amblyopia[7], [8], [30] we expected these conditions to have abnormal phenotypes. We were surprised, however, to find very different phenotypes for these conditions, showing that more than one plasticity phenotype can account for persistent acuity deficits.

RO samples were in a single cluster dominated by an overabundance of GluA2 and more GluN2A than 2B. Together those changes made the RO phenotype appear more similar to an adult than the CP pattern. The increase in GluA2 was in sharp contrast to the loss after BV treatment, and suggests that RO may scale up AMPAR-dependent homeostatic mechanisms to drive recovery[25] without engaging NMDAR-dependent mechanisms to consolidate those changes[74]. Since AMPAR-mediated homeostasis promotes rapid but transient gains in responsiveness [25], [67], [75]-[78] this might explain the labile acuity recovered with RO[7], [8]. Interestingly, the increase in GluA2 promoted by RO implicates the dense expression of GluA2-containing synapses at feedback connections onto parvalbumin-positive (PV+) neurons[79]. The feedforward connections onto PV+ neurons may also be involved in RO circuit abnormalities because the labile acuity and early shift to GluN2A after RO are similar to changes found in MeCP2 KOs where an abnormally early shift to GluN2A at synapses onto PV+ neurons that halts acuity development[80], [81]. Taken together, these findings provide preliminary evidence that RO may leave behind feedforward (GluN2A subunits) and feedback abnormalities (GluA2) in PV+ neuron circuits in V1.

Although various models of neural plasticity predict that decreasing firing rates will enhance plasticity that idea has not translated to using BD treatment to improve recovery from MD[30]. BD for weeks or months during the CP has a range of effects on V1 including enhancing the appearance of cytochrome oxidase blobs[82], weakening stimulus evoked activity of PV+ neurons[83] and delaying the developmental increase in GAD65 expression [84]. Here we found that a few days of BD treatment caused an abnormal increase in the expression of GABA_Aα1 throughout V1 and a shift to more GluN2A in the central region. GABA_Aα1 receptors are found on pyramidal cell bodies where PV+ neurons synapse and they serve as regulators of ocular dominance plasticity[20] and the window for coincident spike-time dependent plasticity[24]. A recent study has shown that the loss of PV+ activity caused by BD depends on GABA_Aα1 mechanisms and that blocking this subunit increases BD-evoked activity allowing for LTP of PV+ neurons[85]. Our observation of increased GABA_Aα1 expression suggests that BD treatment may further reduce visually evoked activity in V1 that is compounded

by the shift to more GluN2A reducing the availability of NMDA-dependent mechanism needed to consolidate visual recovery.

Modeling recovery of NMDAR and GABA_AR kinetics

Our modeling of population kinetics suggests that different physiological changes accompany the 3 treatments. During normal development the increases in NMDAR and GABA_AR kinetics progress in concert. Physiological studies [86] and our modeling show that this fine balance is decoupled by MD because the delayed shift to GluN2A has slower NMDAR kinetics but the premature increase of GABA_Aα1 has faster GABA_AR kinetics. Neither RO or BD treatment corrected that decoupling and the modeling suggests that those treatments accelerate the shift to faster adult-like kinetics for NMDARs after RO or GABAARs after BD. Modeling the kinetics for BV treatment identified 2 phases of recovery especially in the binocular regions of V1. First, between 0-2 days of BV there was a rapid increase in the predicted NMDAR kinetics that was similar to changes that occur between 2 to 4 weeks of age in normal cats. Second, between 2-4 days of BV there was a slowing of the predicted GABA_AR kinetics and that was opposite to the normal developmental increase in kinetics. These sequential phases of BV treatment do not recapitulate normal development. These results raise the question of whether the BV-driven increase in NMDAR kinetics needs to reach a certain level before triggering the slowing of GABA_AR kinetics to rebalance these mechanisms. This modeling, however, was based on population data about the expression of the receptor subunits and cannot be extrapolated to individual receptors. Nonetheless, the rapid changes with BV treatment suggest that some aspects of normal development may be missed and it will be important to determine what those are.

How might these plasticity phenotypes be used for developing and testing treatments for persistent amblyopia?

The distinct plasticity phenotypes classified for RO and BD treatments provide preliminary evidence that multiple neural changes can account for persistent amblyopia and highlight the need to know which mechanisms to target when trying to engage neuroplasticity mechanisms to improve acuity. Whether the treatment should focus on AMPARs, NMDARs, GABA_ARs or some combination of those receptors will depend on the underlying plasticity phenotype.

Insights into those questions can be addressed in animal models using modern molecular tools and vision testing but translating those findings into treatments for humans will depend on non-invasive ways to determine an individual's plasticity phenotype. For example, magnetic resonance spectroscopy has been used to measure changes in glutamate or GABA concentrations in human V1 after different types of visual experience (e.g. MD[87]) and receptor expression can be quantified by radioligands labeled for SPECT and PET [88]. New molecular imaging techniques hold the promise of greater detail with the ability to measure the concentration of receptor subunits[89]-[91]. That information may be comparable to protein analysis in animals models and suitable for constructing plasticity phenotypes for human V1 to facilitate the translation of new treatments. Furthermore, behavioral paradigms linked with specific plasticity mechanisms (e.g. stimulus-selective response plasticity[92]) may further aid in characterizing human plasticity phenotypes. Thus, selecting a treatment to prevent or correct persistent amblyopia may benefit from in vivo steps to classify an individual's plasticity phenotype.

Conclusions

This exploration of glutamatergic and GABAergic receptor subunit changes in V1 after treatment that promotes either good (BV) or poor (RO, BD) recovery of vision provides a better understanding of the complexity of this problem. Of the treatments studied here, only BV provided evidence for recovery of a CP-like plasticity phenotype in V1. However, only one feature, the GluA2:GluN2A balance, returned to normal levels after BV and that balance is noteworthy because the proteins are regulators of homeostatic and Hebbian plasticity, respectively. The modeling of NMDAR and GABA_AR kinetics suggests two stages for BV recovery: a rapid increase in NMDAR kinetics, followed by slowing of the predicted GABA_AR kinetics which together move that balance into the CP range. We identified features of the plasticity phenotypes that may guide future studies on persistent amblyopia to look for high levels of GluA2 and GluN2A following RO, and high levels of GABA_Aα1 after BD treatment. Finally, the plasticity phenotyping is a good approach for uncovering novel neurobiological features that may be important for recovery of acuity and new treatment targets.

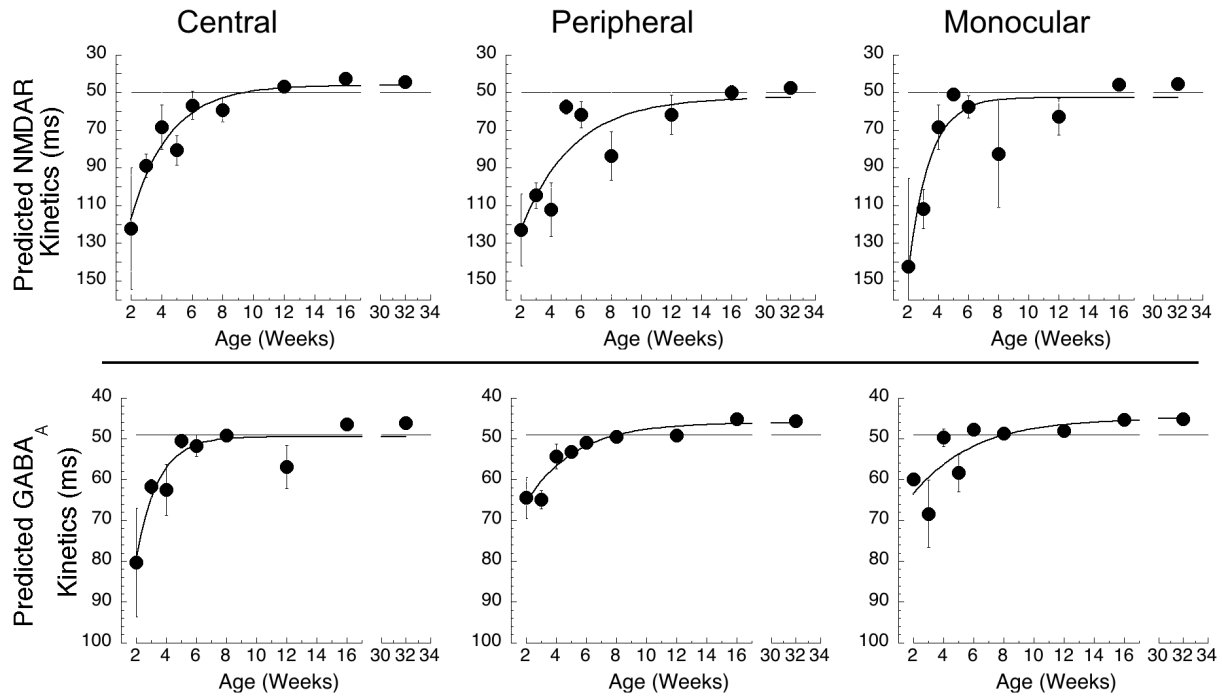


Figure 4-1. Predicted decay kinetics of NMDAR and GABA_AR across normal cat V1 development

Scatterplots of predicted population decay kinetics of each receptor type. Black circles represent the average predicted decay kinetics at each age. Top row of scatterplots show the average kinetics of NMDA receptors across V1 areas. Solid line represents the kinetics of a population of diheteromeric 2A:2B containing NMDARs (50ms). Bottom row shows predicted decay kinetics of GABA receptors across V1 areas. Solid line represents the kinetics of a population of diheteromeric $\alpha 1:\alpha 3$ containing GABA_ARs (49ms). All scatterplots were well defined by an exponential decay curve fit (all $p < 0.0001$).

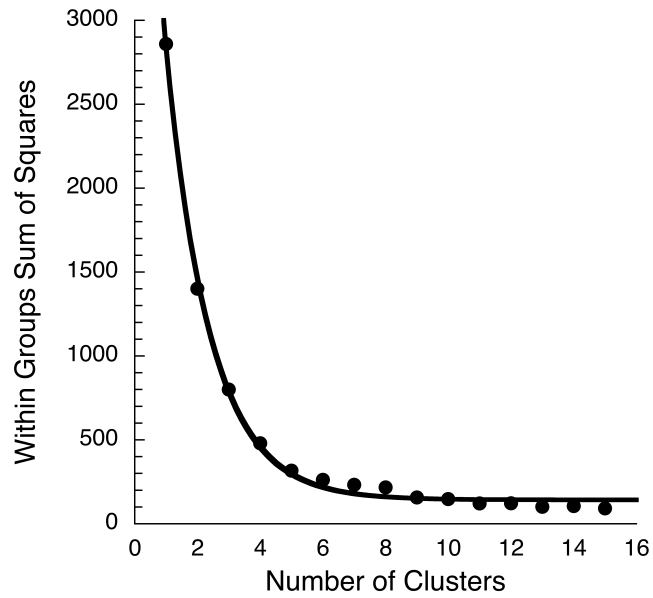


Figure 8-1 Within group sum of squares with variable cluster sizes.

Scatterplot of the within groups sum of squares was measured across a range of clusters between 2 and 15. An exponential decay fit was applied to the data, and 4τ was taken as the point at which changes in cluster number had little effect on the within groups sum of squares. The optimal number of clusters was identified as 6 ($k=6$). This value was used to assign the k-means clusters on tSNE reduced data (Figure 8a).

Weeks BV	Region	GluN1	GluN2A	GluN2B	GABA _A α1	GABA _A α3	GluA2	Syn
2	C	4	4	4	4	4	4	4
	P	16	16	16	16	16	16	16
	M	4	4	4	4	4	4	4
3	C	4	4	4	4	4	4	4
	P	16	16	16	16	16	16	16
	M	4	4	4	4	4	4	4
4	C	4	4	4	4	4	4	4
	P	16	16	16	16	16	16	16
	M	4	4	4	4	4	4	4
5	C	4	4	4	4	4	4	4
	P	16	16	16	15	16	16	16
	M	4	4	4	4	4	4	4
6	C	4	4	4	4	4	4	4
	P	16	16	16	16	16	16	16
	M	4	4	4	4	4	4	4
8	C	6	6	6	6	6	6	6
	P	22	19	22	22	22	22	22
	M	2	2	2	2	2	2	2
12	C	4	4	4	4	4	4	4
	P	16	16	16	16	16	13	16
	M	4	4	4	4	4	4	4
16	C	4	4	4	4	4	4	4
	P	16	16	16	16	16	16	16
	M	4	4	4	4	4	4	4
32	C	4	4	4	4	4	4	4
	P	16	16	16	16	16	16	16
	M	4	4	4	4	4	4	4
SUM		222	219	222	221	222	219	222

Table 2-1. The number of Western blot measurements for each cortical region in Normal animals.

Rows summarize the number of runs from the Central (C), Peripheral (P), and Monocular (M) regions of V1 within each age of animal studied. The columns list each of the 7 proteins analyzed using Western blotting. Column sums detail the number of runs across ages and cortical areas.

Weeks MD	Region	GluN1	GluN2A	GluN2B	GABA _{Aα} 1	GABA _{Aα} 3	GluA2	Syn
4	C	4	4	4	4	4	4	4
	P	16	16	16	16	16	11	16
	M	4	4	4	4	4	2	4
5	C	6	6	6	6	6	6	4
	P	18	18	18	18	18	18	11
	M	4	4	4	4	4	4	4
6	C	8	8	8	8	8	8	8
	P	32	32	32	32	32	32	32
	M	6	6	6	6	6	6	6
9	C	8	8	8	8	8	8	8
	P	36	36	34	34	36	36	31
	M	8	8	8	6	8	8	6
32	C	4	4	4	4	4	4	4
	P	16	16	16	16	16	16	16
	M	2	2	2	2	2	2	2
SUM		172	172	170	168	172	165	156

Table 2-2. The number of Western blot measurements for each cortical region in MD animals.

Rows summarize the number of runs from the Central (C), Peripheral (P), and Monocular (M) regions of V1 within each age of animal studied. The columns list each of the 7 proteins analyzed using Western blotting. Column sums detail the number of runs across ages and cortical areas.

		Central				Curve Fit to BV Data	Peripheral				Curve Fit to BV Data	Monocular				Curve Fit to BV Data
		Vs 5wk Normal		vs. 5wk MD			Vs 5wk Normal		vs. 5wk MD			Vs 5wk Normal		vs. 5wk MD		
		Significance	p-value	Significance	p-value		Significance	p-value	Significance	p-value		Significance	p-value	Significance	p-value	
Synapsin	MD	n.s.	0.2361			n.s.	0.2113			n.s.	0.4861					
	RO	***	0.0000	***	0.0000		***	0.0000	***	0.0000	***	0.0000	***	0.0000		
	BD	n.s.	0.1483	*	0.0123		n.s.	0.2252	n.s.	0.0526	***	0.0001	***	0.0001		
	1hr BV	n.s.	0.1438	*	0.0107		***	0.0000	**	0.0026	***	0.0000	***	0.0000		
	6hr BV	***	0.0000	***	0.0000		*	0.0152	n.s.	0.1051	n.s.	0.2726	n.s.	0.2829		
	1d BV	***	0.0009	***	0.0000		***	0.0000	***	0.0001	**	0.0095	**	0.0095		
	4d BV	***	0.0000	***	0.0000		n.s.	0.1742	n.s.	0.1002	n.s.	0.1263	n.s.	0.1215		
GluA2	MD	n.s.	0.2338			**	0.0085			n.s.	0.3516					
	RO	***	0.0000	***	0.0000		n.s.	0.0691	***	0.0000	***	0.0000	***	0.0000		
	BD	***	0.0000	***	0.0000		***	0.0001	n.s.	0.1110	n.s.	0.2511	n.s.	0.1042		
	1hr BV	***	0.0000	***	0.0006		***	0.0000	***	0.0000	***	0.0000	***	0.0000		
	6hr BV	***	0.0007	n.s.	0.4871		n.s.	0.1370	*	0.0253	*	0.0418	n.s.	0.0760		
	1d BV	***	0.0003	*	0.0106		***	0.0000	*	0.0405	n.s.	0.0912	n.s.	0.2506		
	4d BV	***	0.0000	***	0.0000		***	0.0000	***	0.0000	*	0.0106	***	0.0006		
GluN1	MD	***	0.0000			**	0.0038			n.s.	0.1573					
	RO	**	0.0041	*	0.0104		***	0.0000	***	0.0002	**	0.0019	***	0.0000		
	BD	n.s.	0.1908	*	0.0123		n.s.	0.1753	n.s.	0.1933	n.s.	0.4286	*	0.0292		
	1hr BV	***	0.0000	n.s.	0.0856		***	0.0000	n.s.	0.2717	**	0.0014	***	0.0000		
	6hr BV	***	0.0000	***	0.0001	$y = 297.43-239.58*exp(-x/11.61)$	n.s.	0.4143	***	0.0002	n.s.	0.3155	n.s.	0.0706	$y = 62.45+51.87*exp(-x/0.79)$	
	1d BV	*	0.0294	*	0.0144	$df=25$	***	0.0000	*	0.0366	***	0.0001	***	0.0000	$df=24$	
	4d BV	**	0.0044	***	0.0000	$R^2=0.618$ $p<0.0001$	***	0.0000	n.s.	0.1493	***	0.0000	***	0.0000	$R^2=0.361$ $p=0.0012$	
GluN2A	MD	***	0.0000			***	0.0000			*	0.0220					
	RO	n.s.	0.1367	***	0.0007		***	0.0000	*	0.0142	***	0.0000	***	0.0000		
	BD	***	0.0000	n.s.	0.0923		***	0.0000	***	0.0000	***	0.0000	***	0.0000		
	1hr BV	***	0.0001	*	0.0220		***	0.0000	***	0.0007	***	0.0005	n.s.	0.2953		
	6hr BV	***	0.0001	***	0.0000	$y = 671.85-601.29*exp(-x/39.72)$	***	0.0000	***	0.0000	***	0.0000	n.s.	0.2208	$y = 52.37+(77.48-52.37)/(1+(x/1.06)^{-14.48})$	
	1d BV	n.s.	0.2788	**	0.0065	$df=23$	***	0.0000	***	0.0000	***	0.0000	n.s.	0.1832	$df=24$	
	4d BV	n.s.	0.1022	***	0.0002	$R^2=0.528$ $p<0.0001$	***	0.0000	n.s.	0.4093	***	0.0000	***	0.0000	$R^2=0.422$ $p=0.0003$	
GluN2B	MD	n.s.	0.4587			n.s.	0.1907			n.s.	0.0606					
	RO	***	0.0000	***	0.0000		***	0.0000	***	0.0000	***	0.0000	***	0.0000		
	BD	**	0.0085	**	0.0013		***	0.0000	***	0.0000	*	0.0354	***	0.0000		
	1hr BV	n.s.	0.4438	n.s.	0.3090		**	0.0059	***	0.0000	*	0.0374	***	0.0000		
	6hr BV	n.s.	0.0574	*	0.0384		**	0.0033	n.s.	0.3986	*	0.0172	***	0.0000	$y = 80.23+137.58*exp(-x/0.04)$	
	1d BV	n.s.	0.1647	n.s.	0.0745		n.s.	0.1926	n.s.	0.0050	n.s.	0.0893	***	0.0000	$df=24$	
	4d BV	n.s.	0.3470	n.s.	0.3570		n.s.	0.0574	***	0.0004	n.s.	0.1156	***	0.0000	$R^2=0.396$ $p=0.0006$	
GABA _A α1	MD	***	0.0000			***	0.0007			***	0.0000					
	RO	*	0.0239	***	0.0000		***	0.0008	***	0.0000	**	0.0026	n.s.	0.1754		
	BD	n.s.	0.0977	n.s.	0.1914		***	0.0000	***	0.0000	***	0.0000	n.s.	0.0000		
	1hr BV	n.s.	0.1903	n.s.	0.2725		*	0.0357	***	0.0000	***	0.0002	***	0.0000		
	6hr BV	n.s.	0.2956	***	0.0000	$y = 57.31+77.01*exp(-x/0.47)$	***	0.0000	**	0.0070	***	0.0000	***	0.0000		
	1d BV	***	0.0000	***	0.0000	$df=24$	**	0.0022	***	0.0000	n.s.	0.2356	**	0.0011		
	4d BV	***	0.0006	***	0.0000	$R^2=0.636$ $p<0.0001$	n.s.	0.0562	***	0.0000	***	0.0000	*	0.0179		
GABA _A α3	MD	***	0.0010			***	0.0001			***	0.0000					
	RO	n.s.	0.0614	n.s.	0.3711		**	0.0015	n.s.	0.4668	**	0.0094	n.s.	0.0883		
	BD	***	0.0000	***	0.0000		***	0.0000	*	0.0141	n.s.	0.4510	**	0.0040		
	1hr BV	***	0.0001	n.s.	0.2468		***	0.0000	***	0.0000	***	0.0000	**	0.0031		
	6hr BV	n.s.	0.0524	n.s.	0.4068	$y = 40.25+33.81*exp(-x/2.87)$	***	0.0000	n.s.	0.0917	$y = 47.66+20.83*exp(-x/0.51)$	n.s.	0.2084	***	0.0000	
	1d BV	***	0.0000	***	0.0001	$df=25$	***	0.0000	***	0.0000	$df=91$	***	0.0000	***	0.0007	
	4d BV	***	0.0000	**	0.0047	$R^2=0.211$ $p=0.0159$	***	0.0000	***	0.0000	$R^2=0.163$ $p<0.0001$	***	0.0000	n.s.	0.4088	
	4d BV	***	0.0003	*	0.0229	$p=0.0159$	***	0.0000	0.0000	<0.0001	***	0.0000	n.s.	0.1572		

Table 3-1. Table of p-values comparing protein expression in each treatment condition against 5wk Normal animals and 5wk MD animals.

P-values are presented for each cortical area (columns) and protein (rows). Cortical areas are broken up into comparisons against normal (left) and MD (right). Asterisk color coding matches Figure 3. When a curve fit was applied, the equation, degrees of freedom (df), R² value and exact p-value are listed.

	Pearson's R								Bonferroni Corrected p-value							
	Normal	GluN1	GluN2A	GluN2B	Gabaa1	Gabaa3	GluA2	Syn	GluN1	GluN2A	GluN2B	Gabaa1	Gabaa3	GluA2	Syn	
Swk Normal	GluN1	1.0000	0.1244	0.7605	0.8623	0.6852	0.6861	0.8459								
	GluN2A	0.1244	1.0000	0.4563	0.0831	0.2667	0.4129	0.1248	14.7036	14.7036	0.0857	0.0065	0.2927	0.2887	0.0110	
	GluN2B	0.7605	0.4563	1.0000	0.7056	0.6757	0.7619	0.6297	0.0857	2.8551	2.8551	16.7446	8.4450	3.8260	14.6803	
	Gabaa1	0.8623	0.0831	0.7056	1.0000	0.7158	0.6524	0.6873	0.0065	16.7446	0.2176	0.1857	0.1857	0.4512	0.2839	
	Gabaa3	0.6852	0.2667	0.6757	0.7158	1.0000	0.9535	0.7488	0.2927	8.4450	0.3334	0.1857	0.1857	0.0000	0.1065	
	GluA2	0.6861	0.4129	0.7619	0.6524	0.9535	1.0000	0.7454	0.2887	3.8260	0.0836	0.4512	0.0000		0.1133	
	Syn	0.8459	0.1248	0.6297	0.6873	0.7488	0.7454	1.0000	0.0110	14.6803	0.5924	0.2839	0.1065	0.1133		
Swk MD	GluN1	1.0000	0.4100	0.6353	-0.7834	-0.5047	0.0634	-0.7529			0.0018	0.0002	3.1854	4.6850	0.0736	
	GluN2A	0.4100	1.0000	0.2805	0.1070	-0.0803	0.4764	-0.4470	0.0018		0.0006	15.3799	0.0675	0.0000	5.4053	
	GluN2B	0.6353	0.2805	1.0000	-0.3743	-0.5441	0.2998	-0.2972	0.0002	0.0006		16.0847	2.4495	0.0017	8.5682	
	Gabaa1	-0.7834	0.1070	-0.3743	1.0000	0.5027	0.4173	0.6579	3.1854	15.3799	16.0847		4.9244	9.0319	0.1331	
	Gabaa3	-0.5047	-0.0803	-0.5441	0.5027	1.0000	-0.0448	0.2924	4.6850	0.0675	2.4495	4.9244		0.0689	4.0109	
	GluA2	0.0634	0.4764	0.2998	0.4173	-0.0448	1.0000	0.2912	0.0736	0.0000	0.0017	9.0319	0.0689		0.6893	
	Syn	-0.7529	-0.4470	-0.2972	0.6579	0.2924	0.2912	1.0000	16.8673	5.4053	8.5682	0.1331	4.0109	0.6893		
RO	GluN1	1.0000	0.6894	0.4321	0.3385	0.0863	0.1573	0.6450			0.1339	2.5805	4.9665	16.1523	12.4138	
	GluN2A	0.6894	1.0000	0.6420	-0.0955	-0.0075	0.4625	0.7514	0.1339		0.2794	15.6551	20.5761	2.0130	0.0408	
	GluN2B	0.4321	0.6420	1.0000	0.1985	0.3214	0.0836	0.3557	2.5805	0.2794		10.4227	5.5118	16.3023	4.4506	
	Gabaa1	0.3385	-0.0955	0.1985	1.0000	0.5621	-0.0245	0.3207	4.9665	15.6551	10.4227		0.7652	19.6111	5.5355	
	Gabaa3	0.0863	-0.0075	0.3214	0.5621	1.0000	-0.0713	0.2312	16.1523	20.5761	5.5118	0.7652		16.9808	8.9548	
	GluA2	0.1573	0.4625	0.0836	-0.0245	-0.0713	1.0000	0.4624	12.4138	2.0130	16.3023	19.6111	16.9808		2.0148	
	Syn	0.6450	0.7514	0.3557	0.3207	0.2312	0.4624	1.0000	0.2679	0.0408	4.4506	5.5355	8.9548	2.0148		
BD	GluN1	1.0000	0.7646	0.7614	0.5617	0.5436	0.7744	-0.2661			0.0304	0.0327	0.7683	0.9345	0.0241	
	GluN2A	0.7646	1.0000	0.5647	0.2690	0.1798	0.4188	-0.0405	0.0304		0.7433	7.3989	11.3082	2.8587	18.7055	
	GluN2B	0.7614	0.5647	1.0000	0.5020	0.6689	0.8751	-0.3286	0.0327	0.7433		1.4143	0.1868	0.0009	5.2770	
	Gabaa1	0.5617	0.2690	0.5020	1.0000	0.7619	0.5675	-0.4707	0.7683	7.3989	1.4143		0.0324	0.7197	1.8771	
	Gabaa3	0.5436	0.1798	0.6689	0.7619	1.0000	0.7979	-0.4945	0.9345	11.3082	0.1868	0.0324		0.0131	1.5173	
	GluA2	0.7744	0.4188	0.8751	0.5675	0.7979	1.0000	-0.4630	0.0241	2.8587	0.0009	0.7197	0.0131		2.0049	
	Syn	-0.2661	-0.0405	-0.3286	-0.4707	-0.4945	-0.4630	1.0000	7.5155	18.7055	5.2770	1.8771	1.5173	2.0049		
1hr BV	GluN1	1.0000	0.3855	0.6080	0.2625	0.3749	0.3297	0.3648			4.5343	0.7552	8.6073	4.8274	6.2014	
	GluN2A	0.3855	1.0000	0.5765	0.4831	0.5649	0.5557	-0.3930	4.5343		1.0443	2.3441	1.1682	1.2743	4.3313	
	GluN2B	0.6080	0.5765	1.0000	0.5026	0.6824	0.6945	0.1850	0.7552	1.0443		2.0127	0.3043	0.2562	11.8611	
	Gabaa1	0.2625	0.4831	0.5026	1.0000	0.7756	0.6488	-0.3023	8.6073	2.3441	2.0127		0.0636	0.4717	7.1321	
	Gabaa3	0.3749	0.5649	0.6824	0.7756	1.0000	0.7779	-0.2078	4.8274	1.1682	0.3043	0.0636		0.0607	10.8577	
	GluA2	0.3297	0.5557	0.6945	0.6488	0.7779	1.0000	-0.2947	6.2014	1.2743	0.2562	0.4717	0.0607		7.4014	
	Syn	0.3648	-0.3930	0.1850	-0.3023	-0.2078	-0.2947	1.0000	5.1157	4.3313	11.8611	7.1321	10.8577	7.4014		
6hr BV	GluN1	1.0000	0.5988	0.3296	0.7883	0.4455	0.7283	-0.7436			0.8326	6.2047	0.0487	3.0797	0.1519	
	GluN2A	0.5988	1.0000	0.3423	0.3607	0.2277	0.6980	-0.7610	0.8326		5.7978	5.2382	10.0069	0.2436	0.0849	
	GluN2B	0.3296	0.3423	1.0000	-0.0006	0.3319	0.1969	-0.0005	6.2047	5.7978		20.9706	6.1304	11.3330	20.9738	
	Gabaa1	0.7883	0.3607	-0.0006	1.0000	0.4846	0.6657	-0.7018	0.0487	5.2382	20.9706		2.3178	0.3806	0.2301	
	Gabaa3	0.4455	0.2277	0.3319	0.4846	1.0000	0.4798	-0.1380	3.0797	10.0069	6.1304	2.3178		2.4036	14.0483	
	GluA2	0.7283	0.6980	0.1969	0.6657	0.4798	1.0000	-0.8150	0.1519	0.2436	11.3330	0.3806	2.4036		0.0260	
	Syn	-0.7436	-0.7610	-0.0005	-0.7018	-0.1380	-0.8150	1.0000	0.1170	0.0849	20.9738	0.2301	14.0483	0.0260		
1d BV	GluN1	1.0000	0.6855	0.6145	0.2300	0.9282	0.6501	-0.4983			0.2911	0.7035	9.9149	0.0003	0.4639	
	GluN2A	0.6855	1.0000	0.0939	-0.1271	0.5680	0.2423	-0.3108	0.2911		16.2063	14.5689	1.1342	9.4078	6.8364	
	GluN2B	0.6145	0.0939	1.0000	0.3267	0.4719	0.4137	-0.2796	0.7035	16.2063		6.2991	2.5503	3.8076	7.9555	
	Gabaa1	0.2300	-0.1271	0.3267	1.0000	0.2823	0.6785	-0.4166	9.9149	14.5689	6.2991		7.8546	0.3209	3.7368	
	Gabaa3	0.9282	0.5680	0.4719	0.2823	1.0000	0.7387	-0.4850	0.0003	1.1342	2.5503	7.8546		0.1275	2.3104	
	GluA2	0.6501	0.2423	0.4137	0.6785	0.7387	1.0000	-0.2997	0.4639	9.4078	3.8076	0.3209	0.1275		7.2214	
	Syn	-0.4983	-0.3108	-0.2796	-0.4166	-0.4850	-0.2997	1.0000	2.0834	6.8364	7.9555	3.7368	2.3104	7.2214		
2d BV	GluN1	1.0000	0.5828	0.7563	0.4025	0.5404	0.5221	-0.3177			0.9818	0.0929	4.0868	1.4634	1.7143	
	GluN2A	0.5828	1.0000	0.5211	0.3540	0.6509	0.1215	0.1846	0.9818		1.7288	5.4374	0.4596	14.8432	11.8825	
	GluN2B	0.7563	0.5211	1.0000	0.5761	0.4723	0.2560	-0.3347	0.0929	1.7288		1.0490	2.5424	8.8604	6.0401	
	Gabaa1	0.4025	0.3540	0.5761	1.0000	-0.1227	-0.1081	-0.2650	4.0868	5.4374	1.0490		14.7830	15.4998	8.5092	
	Gabaa3	0.5404	0.6509	0.4723	-0.1227	1.0000	0.3566	0.0017	1.4634	0.4596	2.5424	14.7830		5.3577	20.9110	
	GluA2	0.5221	0.1215	0.2560	-0.1081	0.3566	1.0000	-0.5480	1.7143	14.8432	8.8604	15.4998	5.3577		1.3666	
	Syn	-0.3177	0.1846	-0.3347	-0.2650	0.0017	-0.5480	1.0000	6.6013	11.8825	6.0401	8.5092	20.9110	1.3666		
4d BV	GluN1	1.0000	0.7597	0.7097	-0.2995	0.2312	0.8860	0.2433			0.2266	0.4518	8.4096	10.9292	0.0135	
	GluN2A	0.7597	1.0000	0.9083	-0.1464	0.2666	0.7004	0.3736	0.2266		0.0058	14.4161	9.5874	0.5058	6.0387	
	GluN2B	0.7097	0.9083	1.0000	-0.0472	0.2951	0.7536	0.5582	0.4518	0.0058		18.8348	8.5644	0.2484	1.9639	
	Gabaa1	-0.2995	-0.1464	-0.0472	1.0000	0.4077	-0.1449	0.4367	8.4096	14.4161	18.8348		5.0863	14.4833	4.3467	
	Gabaa3	0.2312	0.2666	0.2951	0.4077	1.0000	0.0029	0.5863	10.9292	9.5874	8.5644	5.0863		20.8653	1.5720	
	GluA2	0.8860	0.7004	0.7536	-0.1449	0.0029	1.0000	0.3818	0.0135	0.5058	0.2484	14.4833	20.8653		5.8017	
	Syn	0.2433	0.3736	0.5582	0.4367	0.5863	0.3818	1.0000	10.4634	6.0387	1.9639	4.3467	1.5720	5.8017		

Table 5-1. Pearson's R values in each treatment condition comparing the strength of association between each protein.

The correlation between each protein within a treatment condition was measured (left), and the observed R values are presented in a matrix. This matrix was reordered in Figure 5 to position high R values nearest one another. The Bonferroni corrected p-values (right) were used to identify the most significant correlations between proteins. P-values <0.05 are colored red to simplify identification of significant correlations.

	All Protein Sum	GlutR sum	GABA _A R Sum	GlutN2B:GluN2A Index	GABA _A α3:GABA _A α1 Index	GABA _A α1:GluN2A Index	GlutN2B:GluA2 Index	GlutN2A:GluA2 Index	GlutR Sum:GABA _A R Sum Index	GlutN2B:GluN2A Index
Dim.1	0.0000	0.0000	0.0000	1.0000	0.0930	0.0000	1.0000	1.0000	1.0000	1.0000
Dim.2	0.7541	0.2225	0.0000	0.0000	0.0000	0.0000	0.0134	0.1211	1.0000	1.0000
Dim.3	1.0000	0.0000	1.0000	0.0000	0.0336	1.0000	0.0000	0.0000	1.0000	1.0000

Table 6-1. Pearson’s R correlations between newly identified plasticity features and PCA dimensions.

The correlation between the PCA scores across all animals, and the first 3 PCA dimensions are presented. P-values of correlations that were significantly correlated after Bonferroni correction are colored red.

		Central				Peripheral				Monocular				
		Vs 5wk Normal		vs. 5wk MD		Curve Fit to BV Data		Vs 5wk Normal		vs. 5wk MD		Curve Fit to BV Data		
		Significance	p-value	Significance	p-value	Significance	p-value	Significance	p-value	Significance	p-value	Significance	p-value	
Total Protein Sum	MD	n.s.	0.3039			n.s.	0.1149			***	0.0000			
	RO	n.s.	0.0963	n.s.	0.1663	***	0.0000	***	0.0000	n.s.	0.4685	**	0.0089	
	BD	n.s.	0.1937	n.s.	0.2379	n.s.	0.2561	n.s.	0.1308	**	0.0077	n.s.	0.4364	
	1hr BV	***	0.0006	**	0.0024	***	0.0000	***	0.0000	***	0.0000	***	0.0000	
	6hr BV	n.s.	0.0825	n.s.	0.1652	n.s.	0.1939	n.s.	0.3297	**	0.0048	n.s.	0.3811	
	1d BV	**	0.0062	*	0.0151	***	0.0000	***	0.0000	n.s.	0.0664	***	0.0000	
	2d BV	n.s.	0.1635	n.s.	0.2675	***	0.0000	***	0.0000	***	0.0000	***	0.0000	
	4d BV	n.s.	0.0965	n.s.	0.1760	***	0.0000	***	0.0000	n.s.	0.0525	**	0.0014	
GlutR Sum	MD	*	0.0270			n.s.	0.4795			***	0.0000			
	RO	***	0.0000	**	0.0078	***	0.0000	***	0.0000	**	0.0277	***	0.0000	
	BD	**	0.0078	*	0.0443	***	0.0000	***	0.0000	***	0.0000	***	0.0000	
	1hr BV	***	0.0000	***	0.0000	***	0.0000	***	0.0000	***	0.0000	***	0.0000	
	6hr BV	n.s.	0.0805	n.s.	0.4991	y = 126.93-44.17*exp(-x/3.15)	n.s.	0.1701	n.s.	0.1937	n.s.	0.4714	***	0.0000
	1d BV	n.s.	0.1737	n.s.	0.4264	df=19	***	0.0000	***	0.0000	***	0.0002	***	0.0000
	2d BV	n.s.	0.2705	*	0.0303	R ² =0.475	***	0.0000	***	0.0000	***	0.0000	***	0.0000
	4d BV	n.s.	0.0671	**	0.0059	p=0.0005	***	0.0003	**	0.0010	***	0.0000	***	0.0000
GABA _A R Sum	MD	**	0.0092			*	0.0157			***	0.0000			
	RO	**	0.0029	***	0.0000	**	0.0085	***	0.0000	n.s.	0.1604	n.s.	0.0923	
	BD	n.s.	0.1868	n.s.	0.2901	***	0.0000	***	0.0067	***	0.0000	***	0.0000	
	1hr BV	n.s.	0.4751	n.s.	0.2013	***	0.0000	***	0.0000	**	0.0031	***	0.0025	
	6hr BV	n.s.	0.1111	**	0.0073	y = 45.02-58.77*exp(-x/1.37)	*	0.0104	n.s.	0.4545	y = 39.14+65.54*exp(-x/1.47)	***	0.0000	
	1d BV	***	0.0000	***	0.0000	df=19	***	0.0000	***	0.0000	df=78	**	0.0217	
	2d BV	***	0.0000	***	0.0000	R ² =0.581	***	0.0000	***	0.0000	R ² =0.360	***	0.0000	
	4d BV	***	0.0000	***	0.0000	p<0.0001	***	0.0000	***	0.0000	p<0.0001	n.s.	0.4082	
GABA _A R Sum:GluR Sum Index	MD	**	0.0014			**	0.0088			***	0.0000			
	RO	n.s.	0.3428	**	0.0060	**	0.0011	n.s.	0.2762	n.s.	0.3866	***	0.0000	
	BD	**	0.0072	n.s.	0.0656	***	0.0000	***	0.0000	***	0.0000	***	0.0000	
	1hr BV	*	0.0161	n.s.	0.3428	*	0.0232	n.s.	0.3166	n.s.	0.3530	***	0.0000	
	6hr BV	n.s.	0.4307	*	0.0274	y = 0.73-0.76*exp(-x/3.37)	***	0.0005	n.s.	0.2605	y = 0.44-0.46*exp(-x/2.68)	***	0.0000	
	1d BV	***	0.0000	***	0.0000	df=19	***	0.0008	***	0.0000	df=78	n.s.	0.2638	
	2d BV	***	0.0000	***	0.0000	R ² =0.716	***	0.0005	***	0.0000	R ² =0.49	n.s.	0.2473	
	4d BV	***	0.0002	***	0.0000	p<0.0001	***	0.0000	***	0.0000	p<0.0001	*	0.0177	
GABA _A α1:GluN2A Index	MD	***	0.0000			***	0.0000			n.s.	0.2515			
	RO	n.s.	0.3777	***	0.0000	**	0.0017	***	0.0000	n.s.	0.3474	n.s.	0.4161	
	BD	**	0.0038	n.s.	0.3288	***	0.0000	***	0.0000	***	0.0000	***	0.0000	
	1hr BV	*	0.0183	*	0.0280	***	0.0000	***	0.0046	***	0.0003	***	0.0002	
	6hr BV	n.s.	0.0014	***	0.0000	y = 0.89-1.15*exp(-x/3.86)	***	0.0000	n.s.	0.1960	y = 0.36-0.63*exp(-x/1.87)	***	0.0000	
	1d BV	*	0.0197	***	0.0000	df=22	**	0.0018	***	0.0000	df=89	***	0.0000	
	2d BV	n.s.	0.1635	***	0.0000	R ² =0.732	n.s.	0.4574	***	0.0000	R ² =0.390	n.s.	0.5014	
	4d BV	***	0.0004	***	0.0000	p<0.0001	*	0.0484	***	0.0000	p<0.0001	*	0.0319	
GlutN2B:GluA2 Index	MD	n.s.	0.1269			***	0.0000			n.s.	0.0502			
	RO	***	0.0000	***	0.0000	***	0.0000	***	0.0000	***	0.0000	***	0.0000	
	BD	n.s.	0.2035	**	0.0060	n.s.	0.3953	***	0.0001	n.s.	0.2542	**	0.0084	
	1hr BV	**	0.0041	n.s.	0.0503	***	0.0000	n.s.	0.2301	**	0.0014	n.s.	0.0559	
	6hr BV	***	0.0000	***	0.0000	y = 1.15-1.52*exp(-x/1.61) ² -5.99*2	***	0.0006	*	0.0282	y = -0.01-0.34*exp(-x/0.83) ² -22.06*2	*	0.0117	
	1d BV	***	0.0007	n.s.	0.0942	df=25	***	0.0000	n.s.	0.0559	df=92	n.s.	0.1674	
	2d BV	***	0.0000	***	0.0000	R ² =0.231	***	0.0005	n.s.	0.0710	R ² =0.16	n.s.	0.4401	
	4d BV	n.s.	0.3750	*	0.0400	p=0.0112	n.s.	0.3682	***	0.0000	p<0.0001	n.s.	0.0505	
GlutN2A:GluA2 Index	MD	n.s.	0.2445			n.s.	0.3563			***	0.0000	n.s.	na	
	RO	***	0.0009	n.s.	0.0535	***	0.0000	***	0.0000	***	0.0000	***	0.0000	
	BD	*	0.0362	***	0.0004	***	0.0000	***	0.0000	***	0.0002	*	0.0125	
	1hr BV	n.s.	0.2076	*	0.0244	n.s.	0.4150	n.s.	0.4175	n.s.	0.0716	***	0.0006	
	6hr BV	n.s.	0.2357	**	0.0027	n.s.	0.0790	n.s.	0.1535	***	0.0000	**	0.0294	
	1d BV	***	0.0000	***	0.0000	*	0.0434	*	0.0127	**	0.0016	n.s.	0.1044	
	2d BV	***	0.0000	***	0.0000	n.s.	0.1986	n.s.	0.1083	n.s.	0.0887	n.s.	0.4977	
	4d BV	n.s.	0.0616	***	0.0007	n.s.	0.1366	n.s.	0.1858	n.s.	0.4026	**	0.0308	

Table 7-1 p-values comparing the each newly identified plasticity feature in treatment conditions against 5wk Normal animals and 5wk MD animals.

p-values are presented for each cortical area (columns) and plasticity feature (rows). Cortical areas are broken up into comparisons against normal (left) and MD (right). Asterisk color coding matches Figure 4. When a curve fit was applied, the equation, degrees of freedom (df), R² value and exact p-value are listed.

	Normal 1	MD 1	ST BV 1	LT BV 1	RO 2	MD 3	ST BV 3	BD 3	LT BV 4	ST BV 5	LT BV 5	LT BV 6	BD 6
Normal 1	1	0.97601795	0.96105886	0.98117	0.95768142	0.94818068	0.94383317	0.78413725	0.95461708	0.96535462	0.98297823	0.85942578	0.62173468
MD 1	0.97601795	1	0.97744298	0.99592531	0.88914347	0.95365077	0.94408703	0.76075697	0.98352939	0.9857111	0.95770586	0.89630038	0.65319854
ST BV 1	0.96105886	0.97744298	1	0.98000413	0.8578434	0.98158073	0.9826135	0.85467041	0.94144785	0.9899475	0.9110114	0.95290107	0.77160096
LT BV 1	0.98117	0.99592531	0.98000413	1	0.90193003	0.94544405	0.94037068	0.75248635	0.98758197	0.97844821	0.96541071	0.91441834	0.63534331
RO 2	0.95768142	0.88914347	0.8578434	0.90193003	1	0.85699952	0.85137272	0.69798422	0.8761915	0.8668415	0.9631905	0.72680318	0.47573671
MD 3	0.94818068	0.95365077	0.98158073	0.94544405	0.85699952	1	0.99775672	0.91971517	0.88803935	0.98380715	0.88099307	0.90030944	0.83242446
ST BV 3	0.94383317	0.94408703	0.9826135	0.94037068	0.85137272	0.99775672	1	0.93098098	0.87805939	0.97593087	0.87093562	0.91606814	0.84324473
BD 3	0.78413725	0.76075697	0.85467041	0.75248635	0.69798422	0.91971517	0.93098098	1	0.84073526	0.84073526	0.94535345	0.96177201	0.94438398
LT BV 4	0.95461708	0.98352939	0.94144785	0.98758197	0.8761915	0.88803935	0.87805939	0.84073526	1	0.94535345	0.96449423	0.87660664	0.52623206
ST BV 5	0.96535462	0.9857111	0.9899475	0.97844821	0.8668415	0.98380715	0.97593087	0.84073526	0.94535345	1	0.92400086	0.90578365	0.75550348
LT BV 5	0.98297823	0.95770586	0.9110114	0.96541071	0.9631905	0.88099307	0.87093562	0.66177201	0.96449423	0.92400086	1	0.79577094	0.47606361
LT BV 6	0.85942578	0.89630038	0.95290107	0.91441834	0.72680318	0.90030944	0.91606814	0.79637235	0.87660664	0.90578365	0.79577094	1	0.76469463
BD 6	0.62173468	0.65319854	0.77160096	0.63534331	0.47573671	0.83242446	0.84324473	0.94438398	0.52623206	0.75550348	0.47606361	0.76469463	1

Table 9-1 Pearson’s R values comparing the strength of association between each treatment subcluster.

The correlation between each sub-cluster was measured and the observed R values are presented in a matrix. This matrix was reordered in Figure 9 to position high R values nearest one another.

	Normal 1	MD 1	ST BV 1	LT BV 1	RO 2	MD 3	ST BV 3	BD 3	LT BV 4	ST BV 5	LT BV 5	LT BV 6	BD 6
Normal	NA	0.00003	0.00014	0.00002	0.00018	0.00033	0.00042	0.02125	0.00023	0.0001	0.00001	0.00623	0.09983
MD 1	0.00003	NA	0.00003	0	0.00313	0.00024	0.00042	0.02839	0.00001	0.00001	0.00018	0.00258	0.07903
ST BV 1	0.00014	0.00003	NA	0.00002	0.00644	0.00002	0.00001	0.00686	0.00008	0	0.00165	0.00025	0.02492
LT BV 1	0.00002	0	0.00002	NA	0.00219	0.00039	0.00051	0.03122	0	0.00002	0.0001	0.00147	0.09049
RO 2	0.00018	0.00313	0.00644	0.00219	NA	0.00655	0.00732	0.05421	0.00431	0.00533	0.00012	0.0411	0.23344
MD 3	0.00033	0.00024	0.00002	0.00039	0.00655	NA	0	0.00122	0.00322	0.00001	0.00385	0.0023	0.01034
ST BV 3	0.00042	0.00042	0.00001	0.00051	0.00732	0	NA	0.00078	0.00413	0.00003	0.00487	0.00139	0.00853
BD 3	0.02125	0.02839	0.00686	0.03122	0.05421	0.00122	0.00078	NA	0.08473	0.00893	0.07385	0.01802	0.00041
LT BV 4	0.00023	0.00001	0.00048	0	0.00431	0.00322	0.00413	0.08473	NA	0.00039	0.00011	0.00427	0.18034
ST BV 5	0.0001	0.00001	0	0.00002	0.00533	0.00001	0.00003	0.00893	0.00039	NA	0.00104	0.00195	0.03017
LT BV 5	0.00001	0.00018	0.00165	0.0001	0.00012	0.00385	0.00487	0.07385	0.00011	0.00104	NA	0.01817	0.23308
LT BV 6	0.00623	0.00258	0.00025	0.00147	0.0411	0.0023	0.00139	0.01802	0.00427	0.00195	0.01817	NA	0.02709
BD 6	0.09983	0.07903	0.02492	0.09049	0.23344	0.01034	0.00853	0.00041	0.18034	0.03017	0.23308	0.02709	NA

Table 9-2 Bonferroni corrected p-values between each treatment subcluster.

The Bonferroni corrected p-values were used to identify the most significant correlations between proteins. P-values less than the Bonferroni corrected level (0.0006) are colored red to simplify identification of significant correlations.

	Comparison	MD 1	LT BV 1	ST BV 1	RO 2	MD 3	ST BV 3	BD 3	LT BV 4	ST BV 5	LT BV 5	LT BV 6	BD 6
All Protein Sum	pvalue	0.000	0.000	0.000	0.000	0.000	0.000	0.000	0.000	0.014	0.000	0.000	0.001
	Asterisk	***	***	***	***	***	***	***	***	*	***	***	***
	color	red	red	red	red	red	red	red	red	red	blue	blue	blue
GlutR Sum	pvalue	0.000	0.000	0.000	0.000	0.000	0.000	0.000	0.000	0.000	0.000	0.039	0.000
	Asterisk	***	***	***	***	***	***	***	***	***	***	*	***
	color	red	red	red	red	red	red	red	red	red	red	red	red
GABA_AR Sum	pvalue	0.003	0.000	0.000	0.000	0.000	0.000	0.000	0.000	0.000	0.000	0.000	0.390
	Asterisk	**	***	***	***	***	***	***	***	***	***	***	n.s.
	color	blue	blue	blue	blue	red	red	red	red	blue	blue	blue	blue
GlutR:GABA_AR Sum	pvalue	0.000	0.000	0.000	0.000	0.000	0.000	0.000	0.000	0.000	0.000	0.000	0.000
	Asterisk	***	***	***	***	***	***	***	***	***	***	***	***
	color	red	red	red	red	red	red	red	blue	red	red	red	red
GABA_Aα3:GluN2A	pvalue	0.000	0.000	0.000	0.000	0.000	0.000	0.000	0.276	0.000	0.419	0.000	0.000
	Asterisk	***	***	***	***	***	***	***	n.s.	***	n.s.	***	***
	color	red	red	red	red	red	red	red	red	white	red	white	red
GluN2B:GluN2A	pvalue	0.002	0.026	0.179	0.000	0.000	0.211	0.302	0.312	0.010	0.000	0.000	0.000
	Asterisk	**	*	n.s.	***	***	n.s.	n.s.	n.s.	**	***	***	***
	color	blue	red	white	red	blue	white	white	white	white	blue	red	red
GABA_Aα3:GABA_Aα1	pvalue	0.000	0.000	0.000	0.021	0.000	0.000	0.000	0.034	0.025	0.000	0.000	0.000
	Asterisk	***	***	***	*	***	***	***	*	*	***	***	***
	color	red	red	red	red	red	red	red	red	red	blue	blue	red
GluN2A:GluA2	pvalue	0.000	0.000	0.000	0.000	0.000	0.000	0.000	0.000	0.000	0.000	0.017	0.000
	Asterisk	***	***	***	***	***	***	***	***	***	***	*	***
	color	red	red	red	red	red	red	red	red	red	red	red	red
GluN2B:GluA2	pvalue	0.000	0.000	0.000	0.000	0.000	0.000	0.000	0.012	0.002	0.000	0.000	0.000
	Asterisk	***	***	***	***	***	***	***	*	**	***	***	***
	color	red	red	red	red	red	red	red	red	red	red	red	red

Table 11-1. p-values for each identified plasticity feature within subclusters compared against the Normal animals from cluster 1.

p-values are presented for the Pearson’s R correlations between each plasticity phenotype and the Normal subcluster. The corresponding significance level is indicated by the text color red if the value was significantly above the normal subcluster, and blue if the value was significantly below, and white if not significantly different.

5.6 References

- [1] T. N. Wiesel and D. H. Hubel, "Single-Cell Responses in Striate Cortex of Kittens Deprived of Vision in One Eye," *J. Neurophysiol.*, vol. 26, no. 6, pp. 1003–1017, Nov. 1963.
- [2] D. H. Hubel and T. N. Wiesel, "The period of susceptibility to the physiological effects of unilateral eye closure in kittens.," *The Journal of Physiology*, vol. 206, no. 2, pp. 419–436, Feb. 1970.
- [3] P. B. Dews and T. N. Wiesel, "Consequences of monocular deprivation on visual behaviour in kittens," *The Journal of Physiology*, vol. 206, no. 2, pp. 437–455, Feb. 1970.
- [4] E. E. Birch, D. R. Stager Sr, J. Wang, and A. O'Connor, "Longitudinal changes in refractive error of children with infantile esotropia," *Eye*, vol. 24, no. 12, pp. 1814–1821, Dec. 2010.
- [5] D. K. Wallace, Pediatric Eye Disease Investigator Group, A. R. Edwards, S. A. Cotter, R. W. Beck, R. W. Arnold, W. F. Astle, C. N. Barnhardt, E. E. Birch, S. P. Donahue, D. F. Everett, J. Felius, J. M. Holmes, R. T. Kraker, M. Melia, M. X. Repka, N. A. Sala, D. I. Silbert, and K. K. Weise, "A randomized trial to evaluate 2 hours of daily patching for strabismic and anisometropic amblyopia in children.," *Ophthalmology*, vol. 113, no. 6, pp. 904–912, Jun. 2006.
- [6] D. E. Mitchell, K. M. Murphy, and M. G. Kaye, "Labile nature of the visual recovery promoted by reverse occlusion in monocularly deprived kittens," *Proc Natl Acad Sci USA*, vol. 81, no. 1, pp. 286–288, Jan. 1984.
- [7] K. M. Murphy and D. E. Mitchell, "Bilateral amblyopia after a short period of reverse occlusion in kittens.," *Nature*, vol. 323, no. 6088, pp. 536–538, Oct. 1986.
- [8] K. M. Murphy and D. E. Mitchell, "Reduced visual acuity in both eyes of monocularly deprived kittens following a short or long period of reverse occlusion.," *Journal of Neuroscience*, vol. 7, no. 5, pp. 1526–1536, May 1987.
- [9] L. N. Cooper and M. F. Bear, "The BCM theory of synapse modification at 30: interaction of theory with experiment," *Nat. Rev. Neurosci.*, vol. 13, no. 11, pp. 798–810, Nov. 2012.
- [10] T. K. Hensch, "Critical period plasticity in local cortical circuits.," *Nat. Rev. Neurosci.*, vol. 6, no. 11, pp. 877–888, Nov. 2005.
- [11] A. Maffei and G. Turrigiano, "The age of plasticity: developmental regulation of synaptic plasticity in neocortical microcircuits.," *Progress in Brain Research*, vol. 169, pp. 211–223, 2008.
- [12] G. B. Smith, A. J. Heynen, and M. F. Bear, "Bidirectional synaptic mechanisms of ocular dominance plasticity in visual cortex," *Philosophical Transactions of the Royal Society B: Biological Sciences*, vol. 364, no. 1515, pp. 357–367, Feb. 2009.
- [13] K. Yashiro and B. D. Philpot, "Regulation of NMDA receptor subunit expression and its implications for LTD, LTP, and metaplasticity," *Neuropharmacology*, vol. 55, no. 7, pp. 1081–1094, Dec. 2008.

- [14] T. K. Hensch and E. M. Quinlan, "Critical periods in amblyopia.," *Vis. Neurosci.*, vol. 35, p. E014, Jan. 2018.
- [15] J. A. Heimel, D. van Versendaal, and C. N. Levelt, "The role of GABAergic inhibition in ocular dominance plasticity.," *Neural Plast.*, vol. 2011, no. 2, pp. 391763–11, 2011.
- [16] E. M. Quinlan, D. H. Olstein, and M. F. Bear, "Bidirectional, experience-dependent regulation of N-methyl-D-aspartate receptor subunit composition in the rat visual cortex during postnatal development.," *Proc Natl Acad Sci USA*, vol. 96, no. 22, pp. 12876–12880, Oct. 1999.
- [17] B. D. Philpot, A. K. Sekhar, H. Z. Shouval, and M. F. Bear, "Visual Experience and Deprivation Bidirectionally Modify the Composition and Function of NMDA Receptors in Visual Cortex," *Neuron*, vol. 29, no. 1, pp. 157–169, Jan. 2001.
- [18] B. D. Philpot, J. S. Espinosa, and M. F. Bear, "Evidence for Altered NMDA Receptor Function as a Basis for Metaplasticity in Visual Cortex," *Journal of Neuroscience*, vol. 23, no. 13, pp. 5583–5588, Jul. 2003.
- [19] A. J. Heynen, B.-J. Yoon, C.-H. Liu, H. J. Chung, R. L. Haganir, and M. F. Bear, "Molecular mechanism for loss of visual cortical responsiveness following brief monocular deprivation," *Nature Publishing Group*, vol. 6, no. 8, pp. 854–862, Aug. 2003.
- [20] M. Fagiolini, J.-M. Fritschy, K. Löw, H. Möhler, U. Rudolph, and T. K. Hensch, "Specific GABAA circuits for visual cortical plasticity.," *Science*, vol. 303, no. 5664, pp. 1681–1683, Mar. 2004.
- [21] K. K. A. Cho, L. Khibnik, B. D. Philpot, and M. F. Bear, "The ratio of NR2A/B NMDA receptor subunits determines the qualities of ocular dominance plasticity in visual cortex.," *Proc. Natl. Acad. Sci. U.S.A.*, vol. 106, no. 13, pp. 5377–5382, Mar. 2009.
- [22] M. Fagiolini, H. Katagiri, H. Miyamoto, H. Mori, S. G. N. Grant, M. Mishina, and T. K. Hensch, "Separable features of visual cortical plasticity revealed by N-methyl-D-aspartate receptor 2A signaling.," *Proc Natl Acad Sci USA*, vol. 100, no. 5, pp. 2854–2859, Mar. 2003.
- [23] B. R. Beston, D. G. Jones, and K. M. Murphy, "Experience-dependent changes in excitatory and inhibitory receptor subunit expression in visual cortex.," *Front Synaptic Neurosci*, vol. 2, p. 138, 2010.
- [24] R. C. Froemke and Y. Dan, "Spike-timing-dependent synaptic modification induced by natural spike trains," *Nature*, vol. 416, no. 6879, pp. 433–438, Mar. 2002.
- [25] M. A. Gainey, J. R. Hurvitz-Wolff, M. E. Lambo, and G. G. Turrigiano, "Synaptic scaling requires the GluR2 subunit of the AMPA receptor.," *J. Neurosci.*, vol. 29, no. 20, pp. 6479–6489, May 2009.
- [26] K. Iny, A. J. Heynen, E. Sklar, and M. F. Bear, "Bidirectional Modifications of Visual Acuity Induced by Monocular Deprivation in Juvenile and Adult Rats," *Journal of Neuroscience*, vol. 26, no. 28, pp. 7368–7374, Jul. 2006.
- [27] K. Williams, J. L. Balsor, S. Beshara, B. R. Beston, D. G. Jones, and K. M. Murphy, "Experience-dependent central vision deficits: Neurobiology and visual acuity.," *Vision Research*, vol. 114, pp. 68–78, Sep. 2015.

- [28] K. R. Duffy, D. H. Bukhamseen, M. J. Smithen, and D. E. Mitchell, "Binocular eyelid closure promotes anatomical but not behavioral recovery from monocular deprivation," *Vision Research*, vol. 114, pp. 151–160, Sep. 2015.
- [29] P. C. Kind, D. E. Mitchell, B. Ahmed, C. Blakemore, T. Bonhoeffer, and F. Sengpiel, "Correlated binocular activity guides recovery from monocular deprivation.," *Nature*, vol. 416, no. 6879, pp. 430–433, Mar. 2002.
- [30] K. R. Duffy and D. E. Mitchell, "Darkness Alters Maturation of Visual Cortex and Promotes Fast Recovery from Monocular Deprivation," *CURBIO*, vol. 23, no. 5, pp. 382–386, Mar. 2013.
- [31] S. D. Faulkner, V. Vorobyov, and F. Sengpiel, "Visual Cortical Recovery From Reverse Occlusion Depends on Concordant Binocular Experience," *J. Neurophysiol.*, vol. 95, no. 3, pp. 1718–1726, Mar. 2006.
- [32] D. S. Schwarzkopf, V. Vorobyov, D. E. Mitchell, and F. Sengpiel, "Brief daily binocular vision prevents monocular deprivation effects in visual cortex.," *Eur J Neurosci*, vol. 25, no. 1, pp. 270–280, Jan. 2007.
- [33] E. B. Hollingsworth, E. T. McNeal, J. L. Burton, R. J. Williams, J. W. Daly, and C. R. Creveling, "Biochemical characterization of a filtered synaptoneurosome preparation from guinea pig cerebral cortex: cyclic adenosine 3':5'-monophosphate- generating systems, receptors, and enzymes," *Journal of Neuroscience*, vol. 5, no. 8, pp. 2240–2253, Aug. 1985.
- [34] F. E. Harrell Jr and M. C. Dupont, "The Hmisc Package," *R Package*, version, pp. 2–0, 2006.
- [35] G. R. Warnes, B. Bolker, L. Bonebakker, R. Gentleman, W. H. A. Liaw, T. Lumley, M. Maechler, A. Magnusson, S. Moeller, and M. Schwartz, "gplots: various R programming tools for plotting data. R package version 2.17. 0," *Computer software*, 2015.
- [36] T. Galili, "dendextend: an R package for visualizing, adjusting and comparing trees of hierarchical clustering.," *Bioinformatics*, vol. 31, no. 22, pp. 3718–3720, Nov. 2015.
- [37] M. Hahsler, K. Hornik, and C. Buchta, "Getting things in order: an introduction to the R package seriation," *Journal of Statistical Software*, vol. 25, no. 3, pp. 1–34, 2008.
- [38] W. Sun, K. B. Hansen, and C. E. Jahr, "Allosteric Interactions between NMDA Receptor Subunits Shape the Developmental Shift in Channel Properties.," *Neuron*, vol. 94, no. 1, pp. 58–64.e3, Apr. 2017.
- [39] M. D. Eyre, M. Renzi, M. Farrant, and Z. Nusser, "Setting the time course of inhibitory synaptic currents by mixing multiple GABA(A) receptor α subunit isoforms.," *J. Neurosci.*, vol. 32, no. 17, pp. 5853–5867, Apr. 2012.
- [40] J. G. A. Pinto, K. R. Hornby, D. G. Jones, and K. M. Murphy, "Developmental changes in GABAergic mechanisms in human visual cortex across the lifespan.," *Front Cell Neurosci*, vol. 4, p. 16, 2010.
- [41] J. G. A. Pinto, D. G. Jones, C. K. Williams, and K. M. Murphy, "Characterizing synaptic protein development in human visual cortex enables alignment of synaptic age with rat visual cortex.," *Front Neural Circuits*, vol. 9, p. 3, 2015.
- [42] J. Donaldson and M. J. Donaldson, "Package 'tsne'," *CRAN Repository*, 2010.

- [43] J. L. Balsor, D. G. Jones, and K. M. Murphy, "A primer on high-dimensional data analysis workflows for studying visual cortex development and plasticity," *bioRxiv*, p. 554378, 2019.
- [44] T. K. Hensch, M. Fagiolini, N. Mataga, M. P. Stryker, S. Baekkeskov, and S. F. Kash, "Local GABA circuit control of experience-dependent plasticity in developing visual cortex.," *Science*, vol. 282, no. 5393, pp. 1504–1508, Nov. 1998.
- [45] K. J. Gingrich, W. A. Roberts, and R. S. Kass, "Dependence of the GABAA receptor gating kinetics on the alpha-subunit isoform: implications for structure–function relations and synaptic transmission.," *The Journal of Physiology*, vol. 489, no. 2, pp. 529–543, Dec. 1995.
- [46] B. J. Hall, B. Ripley, and A. Ghosh, "NR2B Signaling Regulates the Development of Synaptic AMPA Receptor Current," *Journal of Neuroscience*, vol. 27, no. 49, pp. 13446–13456, Dec. 2007.
- [47] D. Keith and A. El-Husseini, "Excitation Control: Balancing PSD-95 Function at the Synapse.," *Front Mol Neurosci*, vol. 1, p. 4, 2008.
- [48] K. M. Murphy, K. R. Duffy, and D. G. Jones, "Experience-dependent changes in NMDAR1 expression in the visual cortex of an animal model for amblyopia," *Vis. Neurosci.*, vol. 21, no. 4, pp. 1–18, Oct. 2004.
- [49] D. E. Mitchell, "The long-term effectiveness of different regimens of occlusion on recovery from early monocular deprivation in kittens.," *Philosophical Transactions of the Royal Society B: Biological Sciences*, vol. 333, no. 1266, pp. 51–79, Jul. 1991.
- [50] K. Burnat, E. Vandenbussche, and B. Zernicki, "Global motion detection is impaired in cats deprived early of pattern vision.," *Behav. Brain Res.*, vol. 134, no. 1, pp. 59–65, Aug. 2002.
- [51] K. Burnat, P. Stiers, L. Arckens, E. Vandenbussche, and B. Zernicki, "Global form perception in cats early deprived of pattern vision.," *NeuroReport*, vol. 16, no. 7, pp. 751–754, May 2005.
- [52] M. Zapasnik and K. Burnat, "Binocular pattern deprivation with delayed onset has impact on motion perception in adulthood.," *Neuroscience*, vol. 255, pp. 99–109, 2013.
- [53] J. A. Movshon, "Reversal of the physiological effects of monocular deprivation in the kitten's visual cortex.," *The Journal of Physiology*, vol. 261, no. 1, pp. 125–174, Sep. 1976.
- [54] L. Chen, N. G. Cooper, and G. D. Mower, "Developmental changes in the expression of NMDA receptor subunits (NR1, NR2A, NR2B) in the cat visual cortex and the effects of dark rearing.," *Molecular Brain Research*, vol. 78, no. 1, pp. 196–200, May 2000.
- [55] S. Jaffer, V. Vorobyov, P. C. Kind, and F. Sengpiel, "Experience-dependent regulation of functional maps and synaptic protein expression in the cat visual cortex.," *Eur J Neurosci*, vol. 35, no. 8, pp. 1281–1294, Apr. 2012.
- [56] L. Cnops, T.-T. Hu, J. Vanden Broeck, K. Burnat, G. Van Den Bergh, and L. Arckens, "Age- and experience-dependent expression of dynamin I and synaptotagmin I in cat visual system.," *J. Comp. Neurol.*, vol. 504, no. 3, pp. 254–264, Sep. 2007.

- [57] L. Cnops, T.-T. Hu, K. Burnat, and L. Arckens, "Influence of binocular competition on the expression profiles of CRMP2, CRMP4, Dyn I, and Syt I in developing cat visual cortex.," *Cereb. Cortex*, vol. 18, no. 5, pp. 1221–1231, May 2008.
- [58] K. Laskowska-Macios, L. Arckens, M. Kossut, and K. Burnat, "BDNF expression in cat striate cortex is regulated by binocular pattern deprivation.," *Acta Neurobiol Exp (Wars)*, vol. 77, no. 3, pp. 199–204, 2017.
- [59] K. Laskowska-Macios, J. Nys, T.-T. Hu, M. Zapasnik, A. Van der Perren, M. Kossut, K. Burnat, and L. Arckens, "Binocular pattern deprivation interferes with the expression of proteins involved in primary visual cortex maturation in the cat.," *Mol Brain*, vol. 8, no. 1, p. 48, Aug. 2015.
- [60] C. R. Olson and R. D. Freeman, "Profile of the sensitive period for monocular deprivation in kittens," *Exp Brain Res*, vol. 39, no. 1, Apr. 1980.
- [61] D. S. Schwarzkopf, V. Vorobyov, D. E. Mitchell, and F. Sengpiel, "Brief daily binocular vision prevents monocular deprivation effects in visual cortex," *Eur J Neurosci*, vol. 25, no. 1, pp. 270–280, 2007.
- [62] E. M. Quinlan, B. D. Philpot, R. L. Huganir, and M. F. Bear, "Rapid, experience-dependent expression of synaptic NMDA receptors in visual cortex in vivo.," *Nat Neurosci*, vol. 2, no. 4, pp. 352–357, Apr. 1999.
- [63] J. F. Maya-Vetencourt, A. Sale, A. Viegi, L. Baroncelli, R. de Pasquale, O. F. O'Leary, E. Castrén, and L. Maffei, "The antidepressant fluoxetine restores plasticity in the adult visual cortex.," *Science*, vol. 320, no. 5874, pp. 385–388, Apr. 2008.
- [64] K. M. Murphy, G. Roumeliotis, K. Williams, B. R. Beston, and D. G. Jones, "Binocular visual training to promote recovery from monocular deprivation," *Journal of Vision*, vol. 15, no. 1, pp. 2–2, 2015.
- [65] D. Carulli, T. Pizzorusso, J. C. F. Kwok, E. Putignano, A. Poli, S. Forostyak, M. R. Andrews, S. S. Deepa, T. T. Glant, and J. W. Fawcett, "Animals lacking link protein have attenuated perineuronal nets and persistent plasticity," *Brain*, vol. 133, no. 8, pp. 2331–2347, Jul. 2010.
- [66] K. R. Kelly, R. M. Jost, Y.-Z. Wang, L. Dao, C. L. Beauchamp, J. N. Leffler, and E. E. Birch, "Improved Binocular Outcomes Following Binocular Treatment for Childhood Amblyopia.," *Invest. Ophthalmol. Vis. Sci.*, vol. 59, no. 3, pp. 1221–1228, Mar. 2018.
- [67] M. E. Lambo and G. G. Turrigiano, "Synaptic and Intrinsic Homeostatic Mechanisms Cooperate to Increase L2/3 Pyramidal Neuron Excitability during a Late Phase of Critical Period Plasticity," *Journal of Neuroscience*, vol. 33, no. 20, pp. 8810–8819, May 2013.
- [68] B.-J. Yoon, G. B. Smith, A. J. Heynen, R. L. Neve, and M. F. Bear, "Essential role for a long-term depression mechanism in ocular dominance plasticity," *Proc Natl Acad Sci USA*, vol. 106, no. 24, pp. 9860–9865, Jun. 2009.
- [69] T. Keck, T. Toyozumi, L. Chen, B. Doiron, D. E. Feldman, K. Fox, W. Gerstner, P. G. Haydon, M. Hübener, H.-K. Lee, J. E. Lisman, T. Rose, F. Sengpiel, D. Stellwagen, M. P. Stryker, G. G. Turrigiano, and M. C. van Rossum, "Integrating Hebbian and homeostatic plasticity: the current state of the field and future research directions,"

- Philosophical Transactions of the Royal Society B: Biological Sciences, vol. 372, no. 1715, p. 20160158, Mar. 2017.
- [70] M. A. Gainey and D. E. Feldman, “Multiple shared mechanisms for homeostatic plasticity in rodent somatosensory and visual cortex.,” *Philos. Trans. R. Soc. Lond., B, Biol. Sci.*, vol. 372, no. 1715, Mar. 2017.
- [71] J. Lisman, “Glutamatergic synapses are structurally and biochemically complex because of multiple plasticity processes: long-term potentiation, long-term depression, short-term potentiation and scaling.,” *Philos. Trans. R. Soc. Lond., B, Biol. Sci.*, vol. 372, no. 1715, Mar. 2017.
- [72] A. X. Yee, Y.-T. Hsu, and L. Chen, “A metaplasticity view of the interaction between homeostatic and Hebbian plasticity.,” *Philos. Trans. R. Soc. Lond., B, Biol. Sci.*, vol. 372, no. 1715, Mar. 2017.
- [73] F. Zenke and W. Gerstner, “Hebbian plasticity requires compensatory processes on multiple timescales.,” *Philos. Trans. R. Soc. Lond., B, Biol. Sci.*, vol. 372, no. 1715, Mar. 2017.
- [74] B. D. Philpot, K. K. A. Cho, and M. F. Bear, “Obligatory Role of NR2A for Metaplasticity in Visual Cortex,” *Neuron*, vol. 53, no. 4, pp. 495–502, Feb. 2007.
- [75] S.-H. Shi, Y. Hayashi, R. S. Petralia, S. H. Zaman, R. J. Wenthold, K. Svoboda, and R. Malinow, “Rapid Spine Delivery and Redistribution of AMPA Receptors After Synaptic NMDA Receptor Activation,” *Science*, vol. 284, no. 5421, pp. 1811–1816, Jun. 1999.
- [76] G. G. Turrigiano, K. R. Leslie, N. S. Desai, L. C. Rutherford, and S. B. Nelson, “Activity-dependent scaling of quantal amplitude in neocortical neurons,” *Nature*, vol. 391, no. 6670, pp. 892–896, Feb. 1998.
- [77] A. Maffei and G. G. Turrigiano, “Multiple Modes of Network Homeostasis in Visual Cortical Layer 2/3,” *Journal of Neuroscience*, vol. 28, no. 17, pp. 4377–4384, Apr. 2008.
- [78] V. Tataavarty, Q. Sun, and G. G. Turrigiano, “How to scale down postsynaptic strength.,” *J. Neurosci.*, vol. 33, no. 32, pp. 13179–13189, Aug. 2013.
- [79] R. N. Kooijmans, M. W. Self, F. G. Wouterlood, J. A. M. Beliën, and P. R. Roelfsema, “Inhibitory interneuron classes express complementary AMPA-receptor patterns in macaque primary visual cortex.,” *J. Neurosci.*, vol. 34, no. 18, pp. 6303–6315, Apr. 2014.
- [80] S. Durand, A. Patrizi, K. B. Quast, L. Hachigian, R. Pavlyuk, A. Saxena, P. Carninci, T. K. Hensch, and M. Fagiolini, “NMDA receptor regulation prevents regression of visual cortical function in the absence of *Mecp2*.,” *Neuron*, vol. 76, no. 6, pp. 1078–1090, Dec. 2012.
- [81] S. B. Mierau, A. Patrizi, T. K. Hensch, and M. Fagiolini, “Cell-Specific Regulation of N-Methyl-D-Aspartate Receptor Maturation by *Mecp2* in Cortical Circuits,” *Biological Psychiatry*, vol. 79, no. 9, pp. 746–754, May 2016.
- [82] K. M. Murphy, K. R. Duffy, D. G. Jones, and D. E. Mitchell, “Development of cytochrome oxidase blobs in visual cortex of normal and visually deprived cats.,” *Cereb. Cortex*, vol. 11, no. 2, pp. 122–135, Feb. 2001.
- [83] B. D. Feese, D. E. Pafundo, M. N. Schmehl, and S. J. Kuhlman, “Binocular deprivation induces both age-dependent and age-independent forms of plasticity in parvalbumin

- inhibitory neuron visual response properties.," *J. Neurophysiol.*, vol. 119, no. 2, pp. 738–751, Feb. 2018.
- [84] Y. Guo, I. V. Kaplan, N. G. Cooper, and G. D. Mower, "Expression of two forms of glutamic acid decarboxylase (GAD67 and GAD65) during postnatal development of the cat visual cortex.," *Brain Res. Dev. Brain Res.*, vol. 103, no. 2, pp. 127–141, Nov. 1997.
- [85] M. C. Bridi, R. de Pasquale, C. L. Lantz, Y. Gu, A. Borrell, S.-Y. Choi, K. He, T. Tran, S. Z. Hong, and A. Dykman, "Two distinct mechanisms for experience-dependent homeostasis," *Nature Publishing Group*, p. 1, 2018.
- [86] A. Maffei, S. B. Nelson, and G. G. Turrigiano, "Selective reconfiguration of layer 4 visual cortical circuitry by visual deprivation.," *Nat Neurosci*, vol. 7, no. 12, pp. 1353–1359, Dec. 2004.
- [87] C. Lunghi, U. E. Emir, M. C. Morrone, and H. Bridge, "Short-term monocular deprivation alters GABA in the adult human visual cortex.," *Curr. Biol.*, vol. 25, no. 11, pp. 1496–1501, Jun. 2015.
- [88] W.-D. Heiss and K. Herholz, "Brain receptor imaging.," *Journal of Nuclear Medicine*, vol. 47, no. 2, pp. 302–312, Feb. 2006.
- [89] J. van der Aart, M. Yaqub, E. J. M. Kooijman, J. Bakker, J. A. M. Langermans, R. C. Schuit, M. B. M. Hofman, J. A. M. Christiaans, A. A. Lammertsma, A. D. Windhorst, and B. N. M. van Berckel, "Evaluation of the Novel PET Tracer [¹¹C]HACH242 for Imaging the GluN2B NMDA Receptor in Non-Human Primates.," *Mol Imaging Biol*, vol. 14, p. 383, Oct. 2018.
- [90] A. Haider, I. Iten, H. Ahmed, A. Müller Herder, S. Gruber, S. D. Krämer, C. Keller, R. Schibli, B. Wünsch, L. Mu, and S. M. Ametamey, "Identification and Preclinical Evaluation of a Radiofluorinated Benzazepine Derivative for Imaging the GluN2B Subunit of the Ionotropic NMDA Receptor.," *J. Nucl. Med.*, p. jnumed.118.212134, Jul. 2018.
- [91] S. D. Krämer, T. Betzel, L. Mu, A. Haider, A. M. Herde, A. K. Boninsegni, C. Keller, M. Szermerski, R. Schibli, B. Wünsch, and S. M. Ametamey, "Evaluation of ¹¹C-Me-NB1 as a Potential PET Radioligand for Measuring GluN2B-Containing NMDA Receptors, Drug Occupancy, and Receptor Cross Talk.," *J. Nucl. Med.*, vol. 59, no. 4, pp. 698–703, Apr. 2018.
- [92] S. F. Cooke and M. F. Bear, "Stimulus-selective response plasticity in the visual cortex: an assay for the assessment of pathophysiology and treatment of cognitive impairment associated with psychiatric disorders.," *Biological Psychiatry*, vol. 71, no. 6, pp. 487–495, Mar. 2012.

Chapter 6. Expression of synaptic and non-neuronal proteins reveal parallel plasticity states across human visual cortex development

Abstract

Perceptual and cognitive development is often described as a series of discrete stages, but recent brain imaging studies suggest continuous development of features such as cortical thickness, area, and volume. This discrepancy between function and structure raises questions about how to link human behaviour with brain development. We have been studying developmental changes in synaptic and non-neuronal proteins in human visual cortex and focusing on mechanisms that mediate experience-dependent plasticity. Typically, our lab and others have analyzed these features by either age-binning or making scatter plots of protein expression. However, both approaches assume an underlying pattern of development. Here we removed these *a priori* assumptions and applied a data-driven approach to characterize the pattern of development in the human visual cortex.

We used robust and sparse k-means clustering algorithm (R package RSKC) to analyze expression of 23 synaptic and non-neuronal proteins in post-mortem tissue samples from human visual cortex (n=31, age range 20 days - 80 years, 13 female, 18 male). These proteins act as triggers or brakes on experience-dependent plasticity and include markers of pre-synaptic function, glutamatergic and GABAergic receptor subunits, receptor anchoring proteins, dendritic spines, myelin, and components of the extracellular matrix. A matrix of protein expression (23 proteins x 403 total runs of Western blotting) was used for the cluster analysis. Importantly, *age* was not included as a variable in the matrix. PCA was also run on the protein matrix to identify features that captured the variance in the data. We visualized developmental changes in the clusters by plotting the balances between sets of proteins that govern synaptic plasticity, which we called '*plasticity features*'. Finally, we created plasticity phenotypes to visualize salient features in each cluster and arranged these phenotypes from youngest to oldest to model human V1 cortical development.

Our analysis revealed a progression of cluster age, but some clusters had overlapping age samples. This overlap between clusters identified a set of parallel "plasticity states" across neighbouring age bins. These findings suggest a new way of thinking about the development of human cortex. At the early and late stages of development, the underlying protein signatures are very homogeneous, and almost all individuals fall into the same cluster. During the middle stages

of development, the underlying protein signatures place individuals into one of a few overlapping states. Deviation into one of these overlapping states may set the course for the rest of cortical development.

6.1 Introduction

Early theories of human development were guided by behavioural observations made by cognitive psychologists, and divide human development into a series of stages (e.g. Piaget 1952, Erikson 1959). As modern technologies such as fMRI, EEG and MRS provided better windows into the living brain, longitudinal analyses of brain structure and function blurred the divisions between developmental stages and suggested that human developmental trajectories progressed along a continuum (Shaw et al., 2008; Grydeland et al., 2013; Mills et al., 2014; Fjell et al., 2015). Unfortunately the resolution of these technologies is relatively poor, and is therefore restricted to analysis of large-scale anatomical changes (MRI) and population responses (EEG), however, a few attempts have been made to link fine neuronal processes with behaviour (Kadosh et al., 2015). More recently, molecular tools have become integrated with developmental neuroscience and an abundance of research is focused on mapping the genomic development of human cortex (eg. <http://www.brainspan.org>, Lister et al., 2013; Nowakowski et al., 2017). One step closer to understanding function, proteomic investigation of human circuits (Carlyle et al., 2017) and systems can be guided by insights from animal models, where numerous examples relate excitatory and inhibitory synaptic proteins to normal function (Froemke and Dan, 2002; Fagiolini et al., 2003; 2004) and synaptic plasticity (Quinlan et al., 1999a; 1999b; Philpot et al., 2001). However, the development of synaptic proteins in human visual cortex, either through discrete stages or continuous trajectories, remains to be elucidated.

Our lab has been studying human brain development by quantifying expression of a collection of synaptic and other neural proteins using a library of postmortem tissue samples (n=31, age= 21 days - 79 years, male/female=18/13) (Siu et al., 2017, Pinto et al., 2010, Williams et al, 2010). The classical approach to interpreting developmental changes is to divide data into discrete age-bins and use either standard (e.g., ANOVA) or modern statistical tests (e.g., bootstrapping simulations) to identify developmental changes. It is becoming more common to plot data and use model-fitting to describe the trajectories of continuous changes (Shaw et al., 2008). Using a combination of these approaches we identified a series of developmental stages in human visual cortex using GABAergic (Pinto et al., 2010), glutamatergic (Siu et al., 2017) and

other synaptic proteins (Pinto et al., 2015). Synthesizing our findings across all of these proteins proves challenging when using age-bins or when defining developmental trajectories.

Here we address this issue by removing a priori assumptions about human brain development and applying modern, data-driven, high-dimensional cluster analysis on the expression profiles of 23 synaptic and non-neuronal proteins. The typical approach to high-dimensional clusters is using subspace or projected clustering algorithms (reviewed in Parsons et al., 2004). However, our data set contains a large number of dimensions relative to the number of observations. Furthermore, we expect certain proteins to better predict the course of human cortical development than others. Therefore, we implemented robust and sparse k-means clustering developed by Witten and Tibshirani (2010: SparCl) and modified by Kondo et al. (2016: RSKC). This high-dimensional clustering algorithm is intended for data sets with many variables (proteins) and uses an adaptive search technique that re-weights all variables according to their impact on cluster formation. After identifying developmental clusters and important proteins, we used a combination of principal component analysis (PCA) and the protein weightings to identify proteins that define each cluster. Finally, we extracted specific plasticity features to better relate protein changes with visual function.

We found 6 clusters of human synaptic protein development stretched along a continuum whereby clusters were distinct and separable at infancy and late adulthood, but intermediate clusters developed in parallel and overlapped in age. Cluster formation was largely driven by a subset of synaptic proteins essential for establishing and maintaining synaptic function, including PSD95, gephyrin, synapsin I, synaptophysin, Ube3A and Drebrin. Surprisingly, intermediate clusters were easily identified by transitions from high to low protein expression, and vice versa. These clusters in the middle of human development therefore appear as a set of parallel "*plasticity states*". These findings suggest a new way of thinking about cortical development where individuals jump between a set of "*plasticity states*" through large and sudden changes in the expression of a few proteins. Early and late stages are marked by a combination of factors related to establishing excitatory/inhibitory balance, structural integrity of neurons and regulating immune response.

6.2 Experimental Procedure

The proteins presented in this paper summarize years of data collection in human cortical tissue. The proteins analyzed, as well as the antibody used, the concentration and supplier are listed in Table 1.

Protein	Antibody concentration and supplier	Citation
GAD65 (glutamic acid decarboxylase 65)	1:500 (Chemicon International, Temecula, CA, USA)	Pinto et al., 2010
GAD67 (glutamic acid decarboxylase 67)	1:1000 (Chemicon International, Temecula, CA, USA)	
VGAT	1:1000 (Synaptic Systems, Göttingen, Germany)	
GABA _A α1	1:500 (Imgenex, San Diego, CA, USA)	
GABA _A α2	1:1000 (Imgenex, San Diego, CA, USA)	
GABA _A α3	1:1000 (Imgenex, San Diego, CA, USA)	
CB1	1:1000 (Cayman, Ann Arbor, MI, USA)	
Gephyrin	1:500 (Chemicon International, Temecula, CA, USA)	Pinto et al., 2015
Gephyrin Homogenate	1:2000 (Millipore, Billerica, MA)	
PSD95 Homogenate	1:32000 (Millipore, Billerica, MA)	
Synapsin I	1:8000 (Invitrogen, Carlsbad, CA)	
Synaptophysin	1:2000 (Sigma-Aldrich, St. Louis, MO);	
GluA2	1:1000 (RRID: AB_2533058, Invitrogen)	Siu et al., 2017
GluN1/NR1	1:4000 (RRID: AB_396353, BD Biosciences PharMingen)	
GluN2A/NR2A	1:1000 (RRID: AB_95169, EMD Millipore)	
GluN2B/NR2B	1:1000 (RRID: AB_2112925, EMD Millipore)	
PSD95	1:16000 (RRID: AB_94278, EMD Millipore)	
Golli-MBP	1:4000 [AB62631] (Abcam, Cambridge, MA, USA).	Siu et al., 2015
Classic-MBP	1:4000 [AB62631] (Abcam, Cambridge, MA, USA).	
Ube3A (E6AP)	(E6AP), 1:1000; (Bethyl Laboratories, Montgomery, TX, USA),	Williams et al., 2010
Integrinβ3	(1:1000 [AB2984], Millipore, Billerica, MA, USA),	Unpublished
GFAP	1:2000 [MAB360](Millipore, Billerica, MA, USA)	
Drebrin	1:1000, [10R-D117A], Fitzgerald Industries International, Acton, MA, USA),	

Table 1: List of proteins included in this chapter.

The antibody used, concentration and supplier are included, along with RRID where applicable. The citation that the data were originally presented in is also included.

Samples and Tissue

Samples from all 31 humans used in this study were from the Brain and Tissue Bank for Developmental Disorders at the University of Maryland (Baltimore, MD, USA). Within 23h of death, human brains were removed and the left occipital lobe was dissected and sectioned into 1cm-thick coronal sections, flash frozen (isopentane and dry ice mixture) and stored at -70°C by Brain and Tissue bank employees. At McMaster, the visual cortex tissue samples were resected on a cold workstation, and visual cortex was identified in the posterior pole of the left occipital lobe according to gyral and sulcal landmarks. Samples were obtained from the superior and inferior calcarine fissure from individuals ranging in age from 20 days to 79 years. The cases used in this study are presented in Table 2.

The study was approved by the McMaster University Research Ethics Board.

Tissue preparation

Using the pattern of gyri and sulci to identify primary visual cortex, small pieces of tissue approximately 50–100 mg were broken off the frozen coronal sections of human cortex. To prepare cortical samples for Western blotting, tissues were transferred to a glass-glass Dounce hand homogenizer (Kontes), resuspended in homogenization buffer (1 ml buffer:50 mg tissue, 0.5 mM DTT, 1 mM EDTA, 2 mM EGTA, 10 mM HEPES, 10 mg/ml leupeptin, 100 nM microcystin, 0.1 mM PMSF, 50 mg/ml soybean trypsin inhibitor), and homogenized until uniform. Due to typical low abundance of synaptic proteins, we performed a synaptosome preparation to enrich synaptic protein expression (Siu et al., 2018). A portion of the homogenate was taken off and set aside, and the remaining whole homogenate was passed through a coarse, 100 μm -pore filter to remove bulk cytosolic entities. The filtered human homogenate was then passed through a fine, 5 μm -pore hydrophilic mesh filter (Millipore). The exception to this was for the four proteins quantified in whole homogenate of human cortex (PSD95HOM, GephyrinHOM, Synapsin I and Synaptophysin). All filtrates were slowly centrifuged (1000xg) for 10 min to separate synaptic fractions into a synaptosome pellet. After removing the supernatant, synaptosome pellets were washed in cold homogenization buffer (1ml), gently vortexed, and slowly centrifuged a second time (1000xg) for 20 minutes. The resultant

synaptosome pellets were resuspended in boiling SDS (1%), heated for 10min, and stored at -80°C.

Age	Sex	Cause of Death	Post-mortem interval (Hours)
20 days	M	Asphyxia	9
20 days	F	Pneumonia	14
86 days	F	Unknown	23
96 days	M	Bronchopneumonia	12
98 days	M	Cardiovascular disorder	16
119 days	M	Bronchopneumonia	22
120 days	M	Pneumonia	23
133 days	M	Accident	16
136 days	F	Pneumonia	11
273 days	M	SIDS	10
1 year 123 days	M	Dehydration	21
2 years 57 days	F	Cardiovascular disorder	21
2 years 75 days	F	Meningitis	11
3 years 123 days	F	Accident	11
4 years 203 days	M	Accident	15
4 years 258 days	M	Accident	17
5 years 144 days	M	Accident	17
8 years 50 days	F	Compressional Asphyxia and Multiple Injuries	20
8 years 214 days	F	Surgical complications	20
9 years 46 days	F	Asthma	20
12 years 164 days	M	Cardiovascular disorder	22
13 years 99 days	M	Asphyxia	5
15 years 81 days	M	Multiple Injuries	16
19 years 76 days	F	Multiple Injuries	16
22 years 359 days	M	Multiple Injuries	4
32 years 223 days	M	Cardiovascular disorder	13
50 years 156 days	M	Cardiovascular disorder	8
53 years 330 days	F	Cardiovascular disorder	5
69 years 110 days	M	Cardiovascular disorder	12
71 years 333 days	F	Multiple medical disorders	9
79 years 181 days	F	Drug Overdose	14

Table 2: Cases used in this study.

Protein measurement and equating protein expression

We used BCA assay to measure total protein expression in all tissue samples, and after normalizing against a set of known standards, we adjust total protein expression across all samples. Aliquots of protein standards (0.25, 0.5, 1.0, 2.0 mg/ml) (BSA protein standards, Bio-Rad Laboratories) and tissue samples (3 μ l x3 wells per sample) were loaded into a 96-well microplate, and each aliquot was suspended in 300 μ l of BCA assay solution. Micro-plates were covered and incubated at 45°C for 45 minutes in order to activate the colorimetric change. Microplates were then transferred to an iMark Microplate Absorbance Reader (Bio-Rad Laboratories), and the scan quantifies the absorbance in each well, which was copied into a Microsoft excel spreadsheet. To validate pipetting accuracy, the average absorbance for each of the 4 protein standards were plotted against known protein expression, and a line of best fit was applied to these data. Only plates with a correlation coefficient of $R^2 > 0.99$ for this line could proceed, those with $R^2 < 0.99$ had to be redone. The average of each tissue sample was normalized to this line of best-fit to determine total protein concentration in each sample, and samples were diluted to 1 μ g/ μ l first with Laemmli buffer (Cayman Chemical) then sample buffer (M260 Next Gel Sample loading buffer 4, Amresco).

Immunoblotting

Protein expression was quantified by separating 20-30 μ g of synaptosome tissue samples on 4%–20% SDS-PAGE, and transferred to PVDF membranes (Immobilon-FLPVDF, EMD Millipore). Between 2-5 runs were performed on samples in this study. Control samples were made by combining a small amount of prepared synaptosomes from each sample within a species, and were run on each gel to facilitate comparisons across membranes.

Membranes were soaked in blocking buffer for 1 h (Odyssey Blocking Buffer 1:1 with PBS) (Li-Cor Biosciences), and transferred to primary antibody and kept cool (4°C) overnight. All antibodies were selected after testing on a multispecies blot that included samples from human, monkey, cat, and rat to ensure that the western blot profile was comparable across species. The blots were washed with PBS-Tween (0.05%PBS-T, Sigma) (3x10 min) and transferred to the appropriate secondary antibody for 1h (25°C), and were again rinsed in PBS-T

(3x10 min). After scanning membranes, antibodies were removed using a Blot Restore Membrane Rejuvenation Kit (EMD Millipore) and membranes were probed again with another antibody.

6.3 Analysis

Protein quantification

All membranes were quantified using densitometry analysis. Membranes were scanned using the Odyssey scanner (Li-Cor Biosciences), the intensity of pixel values within the band were integrated, and the background pixel intensity was subtracted from each lane profile (Odyssey Software version 3.0; Li-Cor Biosciences). To adjust for variations in the width of the band, intensity values were divided by band width for all analyses.

Data Setup

Data was collected through a series of experiments for the following 23 proteins: Glutamic acid decarboxylase (Gad65 and Gad67), vesicular GABA transporter (VGAT), GABA_Aα1, GABA_Aα2, GABA_Aα3, CB1, Gephyrin, post-synaptic density protein 95kDa (PSD95), Gephyrin from homogenate tissue fraction (Gephyrin.HOM), PSD95 from homogenate tissue fraction (PSD95.HOM), Synapsin I, Synaptophysin, GluA2, NR1 (GluN1), GluN2A (NR2A), GluN2B (NR2B), Myelin Basic Protein isoforms (Classic-MBP and Golli-MBP), Integrinβ3 (Integrin), Glial fibrillary acidic protein (GFAP), E3 ubiquitin ligase (Ube3A), Drebrin. Some proteins were quantified more times than others (1-5 runs per protein), resulting in an incomplete $m \times n$ matrix of $m=403$ rows (31 human samples x 13 possible rounds of immunoblotting) x $n=23$ columns (proteins). Multiple rounds of immunoblotting for a given protein were collapsed into the sample average, which condensed the $m \times n$ matrix to $m=31$ rows of human samples x $n=23$ proteins.

Clustering

Data were centered and scaled by subtracting each entry from the column mean and dividing by the corresponding column standard deviation. Sparse k-means clustering was run on the centered data in R (RStudioTeam 2016) using the RSKC package (Kondo et al., 2016). The number of clusters was set to 6 (see results), the number of random initial starting cluster centers

was set to 500, and L1 was increased to allow adjusted weights > 0 for all proteins. Importantly, age was not included in this analysis so clusters were identified based only on protein expression.

The six clusters were ordered from youngest to oldest median age. Cluster ages were visualized using boxplots, and the samples in each cluster were superimposed as individual data points. Protein expression for each cluster were visualized using scatterplots with individual points colored to match the assigned cluster. To describe the trajectory of change in protein expression across developmental stages, scatterplots were fit with a general loess curve, as well as an upper and lower 95% confidence interval. Protein expression was also visualized using boxplots. To describe transitions between sequential clusters we color coded the boxplots. Clusters with a median score greater than 75% of the full range of the data (upper quartile) were coloured red and those with median score less than 25% of the full range of data (lower quartile) were coloured blue.

Important Protein Identification

To assess protein impact on cluster formation, we re-ordered proteins according to their RSKC weights, we converted protein expression to protein maximum and minimum across all proteins and plotted these together on a set of parallel coordinates. Similarly, we created plasticity profiles for each cluster. First color coded gradients were created using the *color_scale_gradient* function in the *ggplot2* package (Wickham, H. 2016). We set the upper and lower limits to match the range of values for protein expression (blue=0 to yellow=maximum expression) and mapping group averages to this RGB space. These values were used to fill the rectangles made in R ggplots.

To identify the most important proteins for forming clusters we performed Principal Component Analysis (PCA) on the same matrix of data. Again sample age was ignored in this analysis. Percentage of explained variance was calculated for each principal component, and the first 3 principal components have a cumulative explained variance $>60\%$, so only these components were used for subsequent analyses.

Cos^2 is a measure of the goodness of fit to each dimension for the representation of a given object (Abdi and Williams, 2010). Cos^2 was calculated for each protein across all 23 dimensions, summed across the first 3 principal components, and ordered from highest total cos^2 to lowest.

Next, PCA biplots were made to demonstrate the impact of each protein on the first 3 dimensions. Important proteins were identified by plotting only variables with $\cos^2 > 0.5$ on each set of axes. Each human sample was superimposed on the same set of dimensions to visualize proteins that determine cluster formation. When high \cos^2 proteins overlapped with clusters, the protein was flagged for follow-up investigation.

Feature Reduction

The list of 23 proteins was reduced to functionally related sets of proteins. These protein sets were identified by examining the amplitudes of individual proteins about the basis vectors, and compared using indices or sums. We refer to these indices and protein sums as plasticity ‘features’. Some of these features have been reported previously, as detailed below:

From Pinto et al., 2010:

$$\text{GAD65:VGAT: } ([\text{GAD65-VGAT}]/[\text{Gad65+VAT}])$$

$$\text{GABA}_{\alpha 1}:\text{GABA}_{\alpha 2}: ([\text{GABA}_{\alpha 1}-\text{GABA}_{\alpha 2}]/[\text{GABA}_{\alpha 1}+\text{GABA}_{\alpha 2}])$$

$$\text{GABA}_{\alpha 1}:\text{GABA}_{\alpha 3}: ([\text{GABA}_{\alpha 1}-\text{GABA}_{\alpha 3}]/[\text{GABA}_{\alpha 1}+\text{GABA}_{\alpha 3}])$$

From Williams et al., 2010:

$$\text{Ube3A:PGSS Sum } ([\text{Ube3A- PGSS Sum}]/[\text{Ube3A+PGSS Sum}])$$

From Pinto et al., 2015:

$$\text{PGSS Sum } ([\text{PSD95HOM} + \text{GephyrinHOM} + \text{Synapsin I} + \text{Synaptophysin}]/4)$$

From Siu et al., 2015:

$$\text{Classic-MBP:Golli-MBP } ([\text{ClassicMBP-GolliMBP}]/[\text{ClassicMBP+GolliMBP}])$$

From Siu et al., 2017:

$$\text{GluA2:GluN1 } ([\text{GluA2-GluN1}]/[\text{GluA2+GluN1}])$$

$$\text{NR2A:NR2B } ([\text{NR2A-NR2B}]/[\text{NR2A+NR2B}])$$

From multiple of Pinto et al., 2010, Williams et al., 2010 and Siu et al., 2017:

$$\text{Synapsin I:Synaptophysin } ([\text{Synapsin I-Synaptophysin}]/[\text{Synapsin I+Synaptophysin}])$$

$$\text{PSD95:Gephyrin } ([\text{PSD95HOM-GephyrinHOM}]/[\text{PSD95HOM+GephyrinHOM}])$$

Novel indices include:

$$\text{Sum of proteins with } \cos^2 > 0.5 \text{ (see figure 4D)}$$

$$\text{PSD95 and Gephyrin Sum: } (\text{PSD95+Gephyrin})/2$$

Ube3A:Drebrin Index: $[\text{Ube3A-Drebrin}]/[\text{Ube3A+Drebrin}]$

CB1:GABA_Aα1 Index: $[\text{CB1-GABA}_{A\alpha 1}]/[\text{CB1+ GABA}_{A\alpha 1}]$

Integrin:GFAP Index: $[\text{Integrin-GFAP}]/[\text{Integrin+ GFAP}]$.

These indices were correlated with PCA results for all of the samples across the 23 dimensions, and significant correlations for these indices were found for all but 4 indices (PSD95:Gephyrin Index, Synapsin I:Synaptophysin Index, NR2A:NR2B Index, and GABA_Aα1:GABA_Aα3 Index). Samples were plotted according to the 6 previously identified clusters in both scatterplots and box plots. Box plots were colored red or blue using the same analysis used to plot protein expression in each cluster. Clusters with a median score greater than 75% of the full range of the data (upper quartile) were coloured red and those with median score less than 25% of the full range of data (lower quartile) were coloured blue.

Correlation matrix was calculated in R using the *corr* function, and visualized using the *heatmap* package. Indices were ordered according to a surrounding dendrogram created using the *dendextend* package. The same dendrogram was used to order the presentation of the color coded indices in the plasticity phenotypes. These were created similar to the protein expression profiles, except the indices of plasticity were mapped such that the minimum side (immature) of an index (typically -1) was set to green, the zero point, where there is balance between proteins in the index, was set to yellow, and the maximum side (mature) of an index (typically +1) was set to red.

Modeling Population Receptor Decay Kinetics for NMDARs and GABA_ARs

In chapter 5, I described the model used to translate expression of receptor subunits into predicted decay kinetics for NMDARs and GABA_ARs. We based our model on population decay kinetics for NMDARs or GABA_ARs measured in two studies (Sun et al., 2017; Eyre et al., 2012). We modelled the decay kinetics for 3 combinations of NMDAR subunit pairings (NR2A only (2A), NR2B only (2B), or NR2A & NR2B (2A:2B)) and for 3 GABA_ARs subunit pairings (GABA_Aα1 only (α1), GABA_Aα3 only (α3) or GABA_Aα1 & GABA_Aα3 (α1:α3)). Observed decay kinetics of NMDARs are 2A=36±1 ms, 2B=333±17 ms, and 2A:2B=50±3 ms (Sun et al., 2017), and decay kinetics for GABA_ARs are α1= 42.2±20.5 ms, α3 = 129.0±54.0 ms and α1:α3 = 49±23 ms (Eyre et al., 2012).

The first assumption of our model is that the expression value from our western blotting is equal to the number of receptor subunits in a tissue sample. We then created a population with 100 receptor subunits and calculated a percentage of receptor subunits in our population. Subunits were assigned to receptors by matching as many pairs of single subunits as possible into triheteromers (2A:2B or $\alpha 1:\alpha 3$) until only one subunit type remained. The remaining subunit pool was paired off into NMDA diheteromers (2A only or 2B only) or GABA_AR diheteromers ($\alpha 1$ only or $\alpha 3$ only).

The relative amounts of NMDAR receptor types (either 2A:2B , 2A only or 2B only) were converted into kinetics according to the formula:

$(([2A:2B] \times 50\text{ms}) + ([2A] \times 36\text{ms}) + ([2B] \times 333\text{ms})) / ([2A:2B] + [2A] + [2B])$. As an example calculation, take a population of receptor subunits containing 75% 2A subunits and 25% 2B subunits would pair off to have 25 x 2A:2B and 25 x 2A only receptors. This would be written:

$$(([0.25] \times 50\text{ms}) + ([0.25] \times 36\text{ms}) + ([0] \times 333\text{ms})) \div ([0.25] + [0.25] + [0]) = 43 \text{ ms.}$$

The formula to calculate the expected GABA_AR decay kinetics is:

$$(([\alpha 1:\alpha 3] \times 49\text{ms}) + ([\alpha 1] \times 42.2\text{ms}) + ([\alpha 3] \times 129\text{ms})) \div ([\alpha 1:\alpha 3] + [\alpha 1] + [\alpha 3]).$$

We plotted the average predicted NMDAR and GABA_AR decay kinetics for all 31 human samples. The changes in predicted decay kinetics were fit with a loess curve, surrounded by a 95% CI band. To compare NMDA and GABA_AR kinetics, both curves were plotted on a shared set of axes. Samples were color coded according to the original cluster designation.

6.4 Results

Sparse High-Dimensional analysis identified 6 clusters

A standard approach to studying developmental data is to group samples into developmental age-bins. Here we applied a different approach to analyzing developmental changes in protein expression by applying robust and sparse k-means clustering (RSKC) across 23 variables that represent the expression of 23 proteins quantified in the primary visual cortex. Importantly, clusters were not influenced by the age of the individuals since age information was omitted from the cluster analysis. Instead, clusters were identified on the basis of protein expression for the 23 protein variables.

To visualize the result of this high-dimensional clustering, we used the adjusted protein values used by the RSKC clustering algorithm as the input data for creating a 2D tSNE plot (Figure 1A). The output from the RSKC method showed a clear progression in the median age of the 6 clusters from the youngest samples in Cluster A to the oldest samples in Cluster F (Figure 1A,B). The 6 clusters identified by RSKC had median ages of 0.3 ± 3.0 yrs, 0.75 ± 2.3 yrs, 3.0 ± 4.1 yrs, 6.8 ± 5.6 yrs, 16.2 ± 10.40 yrs and 61.6 ± 27.5 yrs (Figure 1A). Remarkably, these clusters displayed characteristics of discrete, non-overlapping stages of development in the youngest (Cluster A) and oldest (Cluster F) clusters. Conversely, the 4 intermediate clusters (Clusters B-E) demonstrated greater overlap between stages, suggesting continuous development. No cluster had fewer than 3 samples (Figure 1C), and the variance-to-mean ratio (VMR) of the ages in each cluster steadily declined as the median cluster age increased (Figure 1D). The PMI and sex (Figure 1E,F) did not influence clusters, however it should be noted that the smallest cluster, cluster B, was made entirely of male samples.

We compared the standard binning approach with the results of this cluster analysis (Figure 1G-J). Development can be parsed into any number of age bins, and we use a standard set of age bins (Law et al., 2003, Duncan et al., 2010, Pinto et al., 2010; Williams et al., 2010; Pinto et al., 2015; Siu et al., 2015; 2017): Neonates (<0.3 years), Infants (0.3–1 year), Young children (1–4 years) Older Children(5–11 years), Teenagers (12–20 years), Young Adults (21–55 years) and Older Adults (>55 years) . The number of samples in each bin ranged as high as 6 (young children; 1 to 4), but was never fewer than 3 (older adults; 55+), thus our library of tissue samples

were well distributed across these age bins (Figure 1G). The variability among ages in each age bin, as measured by the variance-to-mean ratio (VMR) was very low (Figure 1H). Other potential factors that could influence age-bin content included the post-mortem interval (PMI) (Figure 1I) and the sex (Figure 1J), but both of these factors were evenly distributed across the age bins.

To demonstrate the differences between binning and clustering samples, the percentage of each cluster was plotted for each age bin (Figure 1K). The youngest two age bins (Neonates and Infants) were comprised mostly of samples that were grouped into Cluster A (red). The third age bin, young children (1 to 4 years) contained samples from 5 different clusters. This age group overlaps with the sensitive period for amblyopia (Epelbaum et al., 1993). The presence of 5 distinct protein signatures in a single age bin highlights the large amount of variability at this stage in development. We have already reported this stage of high inter-individual variability in human V1 development (Pinto et al., 2010; 2015; Siu et al., 2015; 2017), and suspect that some of the susceptibility to amblyopia is due to large fluctuations in individual protein expression we have identified during this stage. For the first time, we report here that this period of high variability in expression creates multiple distinct and identifiable protein signatures that all coexist during this early stage of development.

After this third age bin there were progressively fewer clusters represented within the standard developmental age bins (Figure 1K) from young children (5 to 11 years contains 3 clusters), older children (12 to 20 years contains 2 clusters), young adults (21 to 55 years contains 2 clusters), and older adults (55+ years contains only 1 cluster). The benefit of this approach was highlighted by the sensitivity to different protein signatures across the intermediate levels of development, and in the identification of multiple overlapping protein signatures.

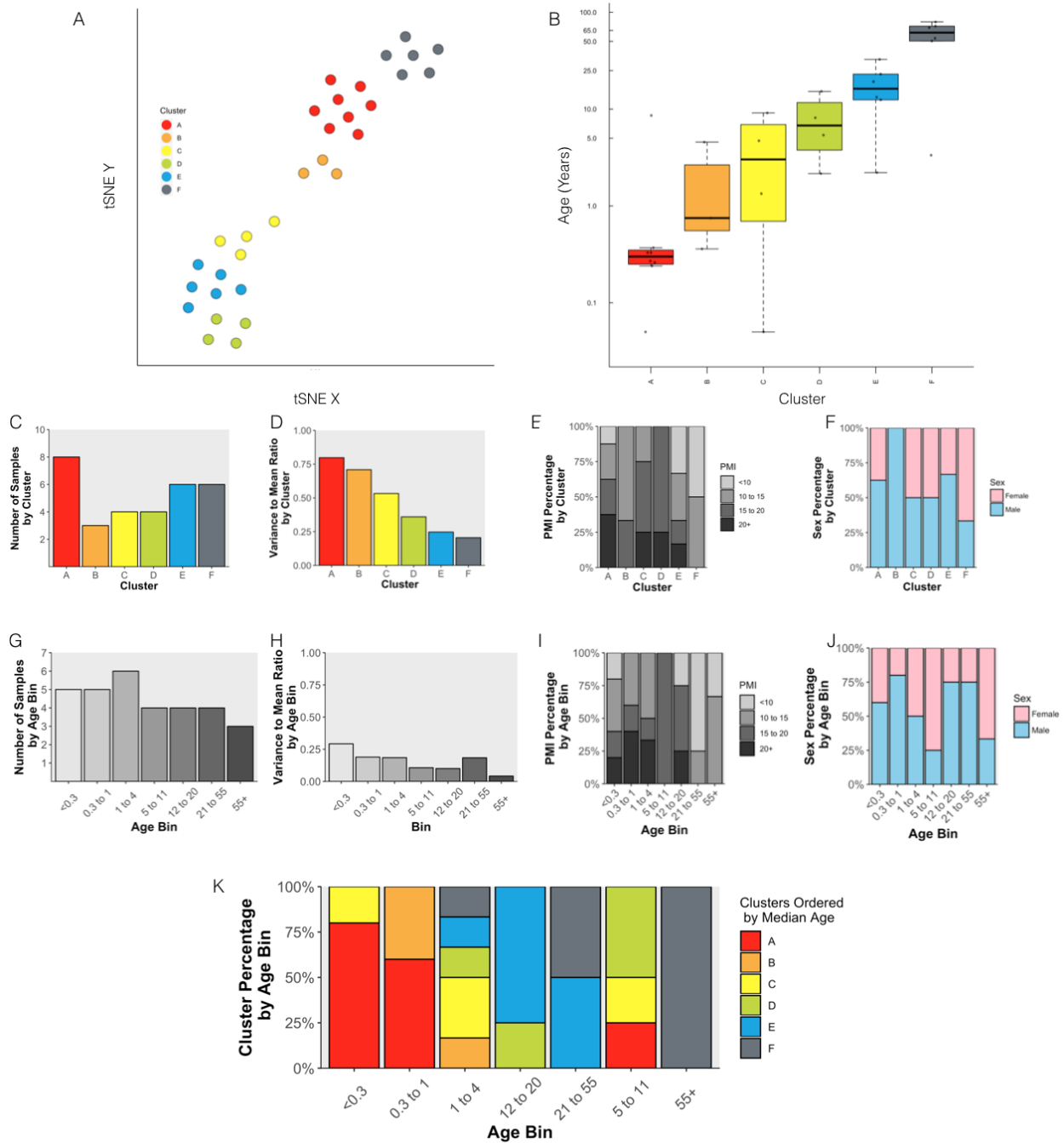


Figure 1. Comparison of samples grouped by RSKC cluster algorithm (A-F) or age bins (G-J).

(A). tSNE plot of the scaled protein data after performing RSKC cluster analysis. Sample averages are colored according to cluster results. (B) Boxplots of cluster age were ordered from youngest (red) to oldest (grey). In both A and B, sample ages were reduced to group averages to reduce crowding. The minimum group size with each method is $n=3$, as demonstrated by the number of individuals in each cluster (C) and in each age bin (G). The variance to mean ratio of the ages for both clusters (D) and age bins (H) show a low dispersion of ages with both approaches. Groups do not appear to be influenced by the post-mortem intervals (PMI) before tissue collection (E,I) or sex (F,J). The percent distribution of clusters across age bins is shown as stacked bar plots (K).

Identifying protein trajectories within and between clusters

To demonstrate changes in protein expression across the lifespan we plotted scatter plots and boxplots of protein expression for each of the identified clusters (Figure 2). As indicated by analysis of samples in each cluster (Figure 1G-J) the youngest and oldest clusters had the most distinct spread of ages of samples, while the middle 4 clusters included samples that overlap in age. Protein expression from birth to adulthood was modelled by fitting loess curves to all of the data points (Figure 2A), which captured protein expression trajectories.

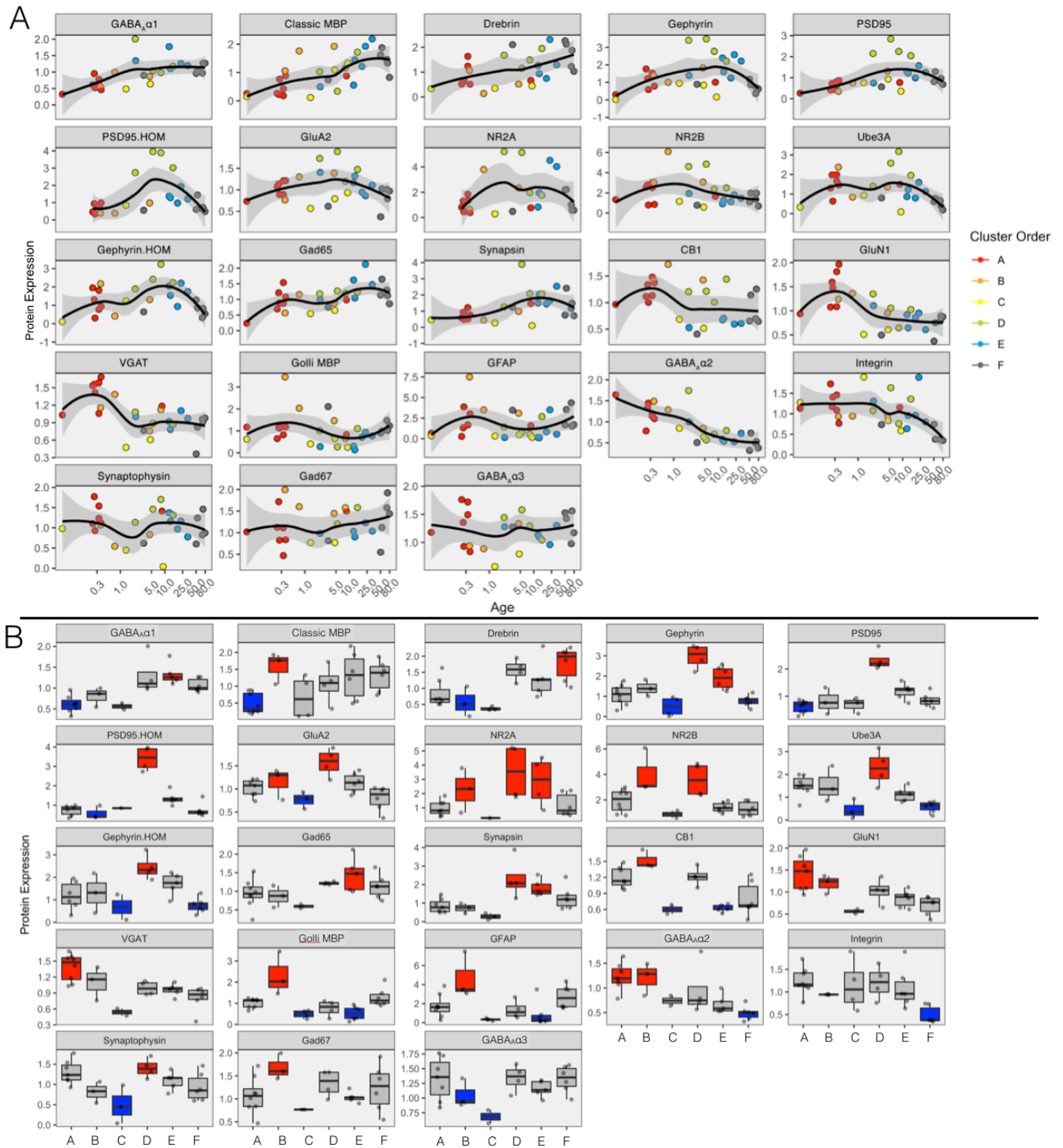


Figure 2. Protein development by age (A) and by cluster (B)

A. Expression of 23 proteins across development, arranged according to similar trajectories. Points are coloured as per the original cluster in Figure 1 G-J. Black loess curves are applied to all of the data, with grey outlines marking 95%CI surrounding each curve. **B.** Boxplots show protein expression within each cluster. Boxplots are colored red when the median expression of a group is greater than the upper quantile of all the data, blue when the median expression of a group is less than the bottom quantile of all data, or grey when the median falls within the middle two quantiles.

Some proteins revealed single clusters that extend outside the 95%CI of a protein-expression curve. Since the identified clusters were grouped by protein expression, and not the other way around, it was likely that identifying the proteins and clusters that ranked high or low relative to other clusters would identify proteins that were important for development. For example many of the proteins (CB1, GluN1, VGAT) had high expression in the youngest cluster (Cluster A- red). The same was true for Cluster D (green points), which identified over-expression of other proteins (Gephyrin, PSD95, GluA2, etc.).

To identify proteins that drove the formation of clusters we analyzed each protein to determine the clusters where the protein was over- (above the upper 75% of expression across all clusters = red) or under-represented (below the lower 25% of expression across all clusters =blue) (Figure 2B). Next we analyzed how the over- versus under-representation of proteins changed between clusters by sorting if the representation of the protein (over vs under) matched the preceding cluster (“Same”), changed from average (middle two quantiles -grey) to over- or under-represented (“Novel”) or “Switched” if clusters went from over- to under-represented between clusters (or vice versa). For example, in the youngest cluster, GluN1, VGAT and GABA_Aα2 were over-represented, but only VGAT changed between the youngest to the second youngest cluster (cluster A to cluster B). Cluster A had under-representation of PSD95, GABA_Aα1, and Classic-MBP. A summary of these categorizations is found in Table 3.

Moving across the remaining clusters from youngest to oldest, Cluster B was identified by over-representation of 7 novel proteins and under-representation of 3 novel proteins (Table 3). The third youngest cluster (C) was defined only by under-represented proteins (17 in total), and interestingly many of these proteins transitioned from over- to under-representation in this cluster (7 in total). The opposite case was true for Cluster D, which was defined by 10 over-represented proteins, many of which switched from a state of under-representation in Cluster C. Cluster C and D therefore were transition states, and despite having samples with large overlap in age, Cluster C and D could be differentiated on the basis of over- versus under-representation of protein. The oldest two clusters (Cluster E and F) were defined by only a few proteins. Cluster E was uniquely marked by over-representation of GABA_Aα1 and Gad65 and under-representation

of CB1 and Golli-MBP. Cluster F had under-representation of Ube3A, Gephyrin Homogenate and GABA_Aα2.

	Age	Quality	Low/High Expression relative to previous cluster			Total
			Same	Novel	Switched	
A	0.3±1.04	High		VGAT, GluN1, GABA _A α2		3
		Low		PSD95, GABA _A α1, Classic-MBP		3
B	0.75±1.34	High	GluN1, GABA _A α2	CB1, NR2B, GluA2, Golli-MBP, GFAP, NR2A, Gad67	Classic-MBP	10
		Low		PSD95.Hom, Drebrin, GABA _A α3		3
C	3.0±2.03	High				0
		Low	GABA _A α3, Drebrin	Ube3A, Gephyrin, Synaptophysin, VGAT, Gephyrin Hom, GABA _A α1, Gad65	CB1, GluN1, NR2B, GluA2, Golli-MBP, GFAP, NR2A, Gad67	17
D	6.8±2.78	High		PSD95, Synapsin, PSD95.Hom, NR2B, NR2A	Ube3A, Gephyrin, Synatophysin, Gephyrin.Hom, GluA2	10
		Low				0
E	16.2 ±4.23	High	Synapsin, Gephyrin, NR2A	GABA _A α1, Gad65		5
		Low		CB1, Golli-MBP		2
F	61.6 ±11.23	High		Drebrin		1
		Low		Ube3A, Gephyrin.Hom, GABA _A α2, Integrin	Gephyrin	5

Table 3: Comparison of protein expression levels against preceding cluster.

First, protein expression was flagged as important if expression was over- (above the upper 75% of expression across all clusters) or under-represented (below the lower 25% of expression) in any cluster. These cluster-identifying proteins were sorted into the above table as “Same” if their expression state (over- vs under-represented) matched the preceding cluster. Clusters were “Novel” if protein expression emerged from a state of non-significance (middle two quantiles -grey) in the preceding cluster. Clusters were “Switched” if they transitioned from over-represented in the preceding cluster to under-represented in the current cluster (or vice versa). The total number of identifying proteins are tallied in the Total column.

RSKC protein weights are cluster-identifying during intermediate stages of development

Classifying proteins into over- and under-represented was a good starting point for identifying the transitions that take place between clusters, but was not necessarily what defined cluster formation. Furthermore, we expected that some proteins should have a greater influence

on the course of development, and therefore should have greater influence on the developmental progression of clusters. One way to determine the proteins with the greatest influence on cluster formation was to inspect the adjusted weights for each protein from the RSKC analysis. The RSKC algorithm identified clusters by adjusting the protein weights so that proteins with a greater contribution to the sparse clustering were given an increased weight, and those that contributed little to clustering were given a reduced weight (Witten and Tibshirani, 2010). Typically, the sparse nature of this approach would set the least important protein weights to zero and removing them from the analysis. We adjusted the L1 parameter, however, so that all proteins had non-zero weight, thereby ensuring that all proteins were included in the analysis. The weights of all proteins were then ordered from largest to smallest (Figure 3A). This highlighted a sigmoidal trend of protein weights, whereby proteins with high and low weights were easily separated, but intermediate proteins remained more or less indistinguishable from one another. Indeed when protein scores were scaled to a local maximum and minimum, and plotted on a shared set of parallel coordinates, cluster-identifying proteins appeared to segregate at the extremes (Figure 3B).

The 6 proteins with the greatest adjusted weights (Ube3A, PSD95, synapsin I, gephyrin, PSD95.Hom, and synaptophysin) easily identified the intermediate Cluster D by over-represented protein expression (Figure 3B- left). Incidentally, 4 of these 6 proteins (PSD95, Synapsin I, Gephyrin and Synaptophysin) were identified in our previous report as a set of structural synaptic proteins useful for mapping the trajectory of V1 synaptic development, and were useful for translating cortical development across species (Pinto et al., 2015). Meanwhile, Ube3A is necessary for experience-dependent maturation of visual cortex (Yashiro et al., 2009).

Conversely, the proteins with the 5 lowest weights, Golli-MBP, GFAP, GABA_Aα3, NR2A, Gad67 and Gad65, identified Cluster C by its unique under-representation of these proteins (Figure 3B- right). These proteins share either immune (Golli-MBP and GFAP) or inhibitory roles (Gad65, Gad67, GABA_Aα3) in cortical function. Neither of these findings were surprising since Cluster C and D were the lowest and highest expressing clusters for most proteins, respectively (Table 3).

This analysis confirmed that proteins were weighted based on protein expression and protein weights are a valuable tool for sorting through the ever-growing list of cluster-identifying proteins. However, since we already flagged those proteins as important, the approach can be employed in lieu of analyzing the relative protein expression (Figure 2B and Table 3). To highlight the pattern of protein expression in the clusters we created a heatmap representing the average expression for each protein (Figure 3C). That analysis demonstrated the contrast between Clusters C and D, and highlighted the many transitions between the clusters.

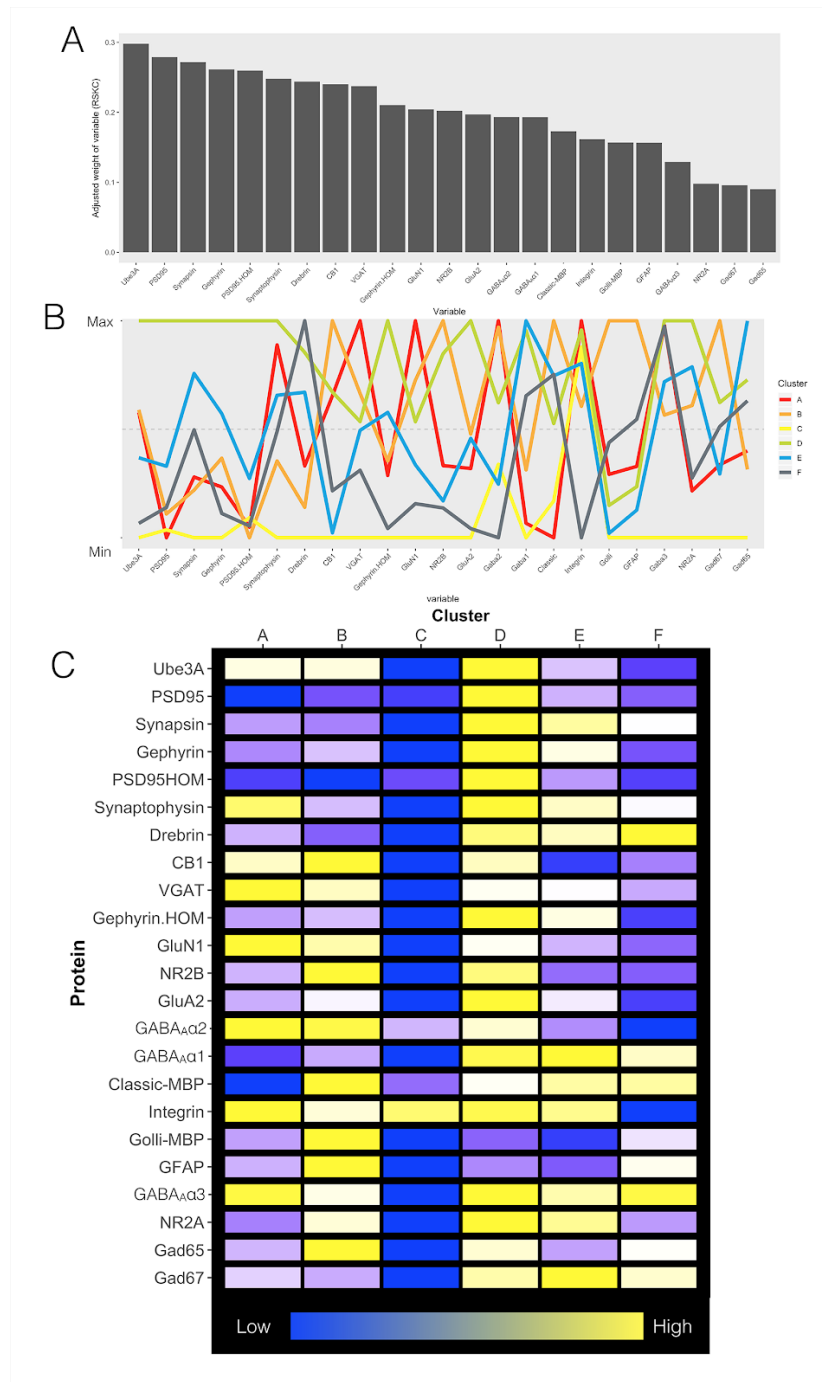


Figure 3. Feature sorting according to sparse clustering.

A. Ranked weightings of proteins assigned by sparse clustering. **B.** Parallel coordinates plot of the mean expression for each protein. Coloured lines indicate cluster. Data were scaled to match protein maximum and minimums across proteins. **C.** Protein phenotypes of the same scaled data. Mean protein expression for each cluster was mapped to a color scale, and maximum and minimum expression of each cluster was set to yellow and blue respectively.

Principal component analysis reveals the remaining cluster-identifying proteins in early and late development

To determine whether any other proteins or combinations of proteins could explain the clusters that formed at the lower and upper limits of human development, we used principal component analysis (PCA). PCA reduced the dimensionality of the data set and identified principal components that explain most of the variance in the data. This restricted the search window for proteins of interest to only a few dimensions. Using that approach we found that the first 3 components captured 28.5%, 19% and 12.4% of the total explained variance respectively, accounting for ~60% of the total cumulative variance (Figure 4A), indicating that these three dimensions contained most of the relevant information in the data set.

We measured the representation of each protein across all 23 protein dimensions using both the correlation with the PCA dimensions (Figure 4B) and \cos^2 (Figure 4C). The correlation between a protein and a PCA dimension estimated the amount of shared information, while \cos^2 estimated the quality of the representation for a protein on a PCA dimension. Since the majority of the large correlations and \cos^2 scores were contained in the first 3 dimensions, we were justified in limiting the search to these dimensions. Proteins with the largest correlations and \cos^2 values on the first dimension included excitatory proteins (GluA2, NR2A, NR2B) as well as markers of synaptic structures (Gephyrin, PSD95, Gephyrin Homogenate, PSD95 homogenate, synapsin I and synaptophysin) and Ube3A. On the second dimension, inhibitory pre- and post-synaptic proteins were well represented (VGAT, GABA_A α 2, CB1) as well as excitatory GluN1, and other support proteins including Golli-MBP, GFAP, Ube3A and Drebrin. The third dimension was mostly dominated by these same support proteins (Golli-MBP, Classic MBP, Integrin, GFAP and drebrin). The sum of the \cos^2 across the first 3 dimensions was plotted, from proteins with the smallest to those with the largest representation (Figure 4D). All but 6 of the proteins had $\cos^2 > 0.5$, confirming that most proteins were well represented on the first 3 dimensions.

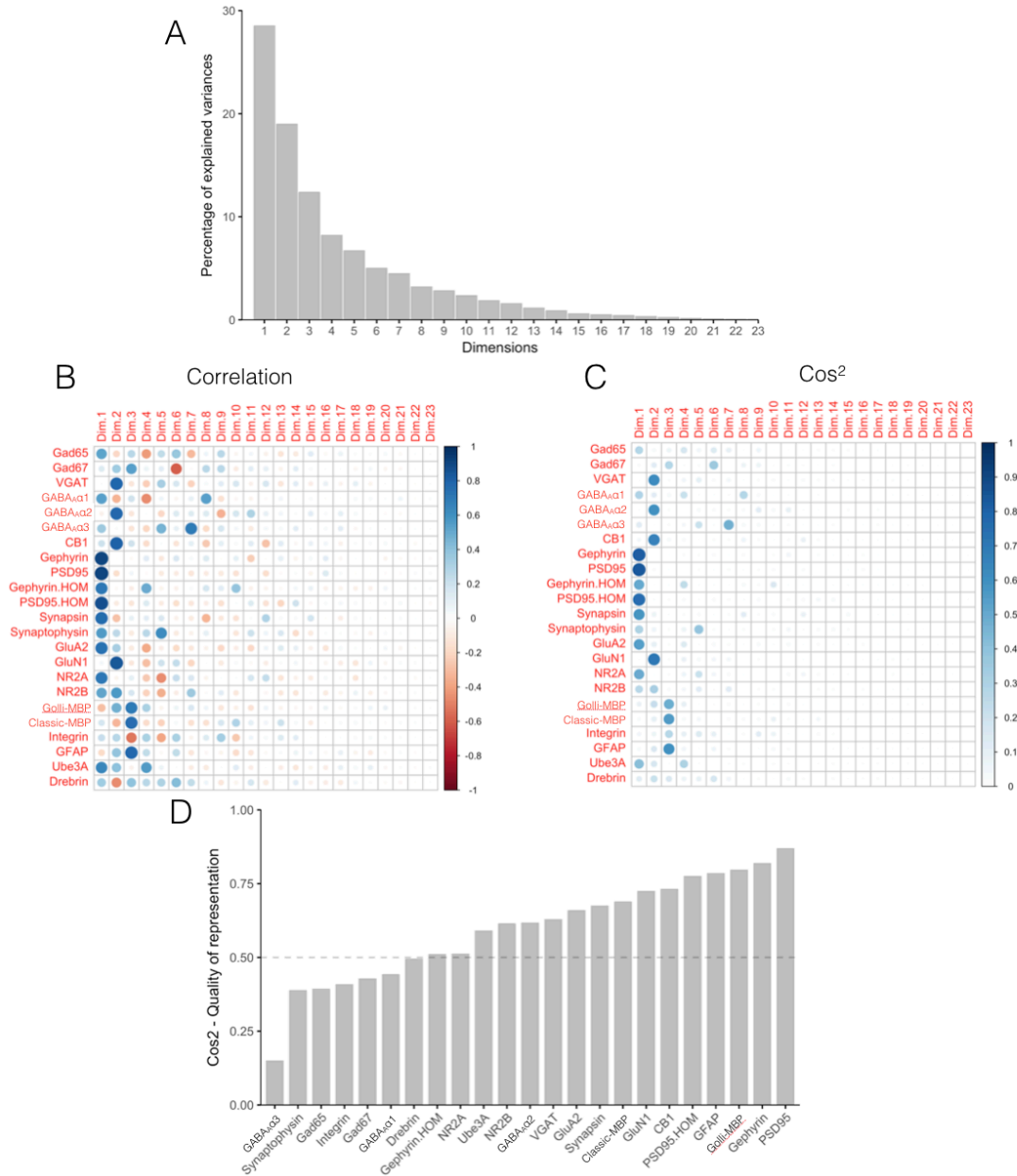


Figure 4. Principal component analysis identifies 3 dimensions of interest.

A. Percent variance identified by all components after singular value decomposition of protein expression. The first 3 principal components capture >60% of the cumulative variance in the data set, and re-sampling the data set determines these three components to contain most of the variance in the system. **B.** Correlation matrix showing the strength (circle size / saturation) and direction (positive=blue, negative=red) of the Pearson's R correlation of each protein represented with each of the principal component dimensions. **C.** Matrix showing the strength (circle size / saturation) and direction (positive=blue, zero=white) of the cos^2 value of each protein represented on each of the principal component dimensions. Most of the proteins have good representation across the first 3 dimensions in both B and C. **D.** Sum of cos^2 across the first 3 dimensions, where the sum of cos^2 for each protein across all 23 dimensions is 1. Dashed line represents $\text{cos}^2 = 0.5$ cutoff, used for reducing number of proteins displayed in subsequent analyses; 16 proteins fall above that cutoff and 7 fall below.

Mapping protein vectors in PCA space highlighted the relative contribution of each protein to development (Figure 5A,C), and when individual samples were superimposed on the same dimensions as the protein vectors, the position of each cluster relative to the protein vectors revealed proteins with the greatest influence on the cluster (Figure 5 B,D). Feature reduction was performed by plotting only proteins with high \cos^2 (>0.5), thereby limiting investigation to only those proteins with a good representation on the most important dimensions (Figure 5 histograms surrounding each plot). On dimensions 1 and 2, which together explain 47.5% of the data, major protein classes of influence include excitatory post-synaptic receptor proteins, inhibitory post-synaptic receptor proteins, inhibitory presynaptic proteins and Ube3a, a synaptic machinery maintenance protein (Figure 5A). The third dimension included more maintenance and structural proteins, including Classic and Golli-MBP, as well as GFAP (Figure 5C).

The key difference with this approach compared with the summary in Table 3 was the sensitivity to small differences in protein expression that were otherwise ignored when data was analyzed on a protein-by-protein basis. The second difference was that importance could be ascribed to each protein vector based on the goodness of representation on a given subset of dimensions (instead of across all dimensions at once), which again increased sensitivity. In addition to the originally identified list of proteins from the first analysis, the PCA and \cos^2 revealed additional proteins for each cluster. The complete list of cluster-identifying proteins is summarized in Table 4.

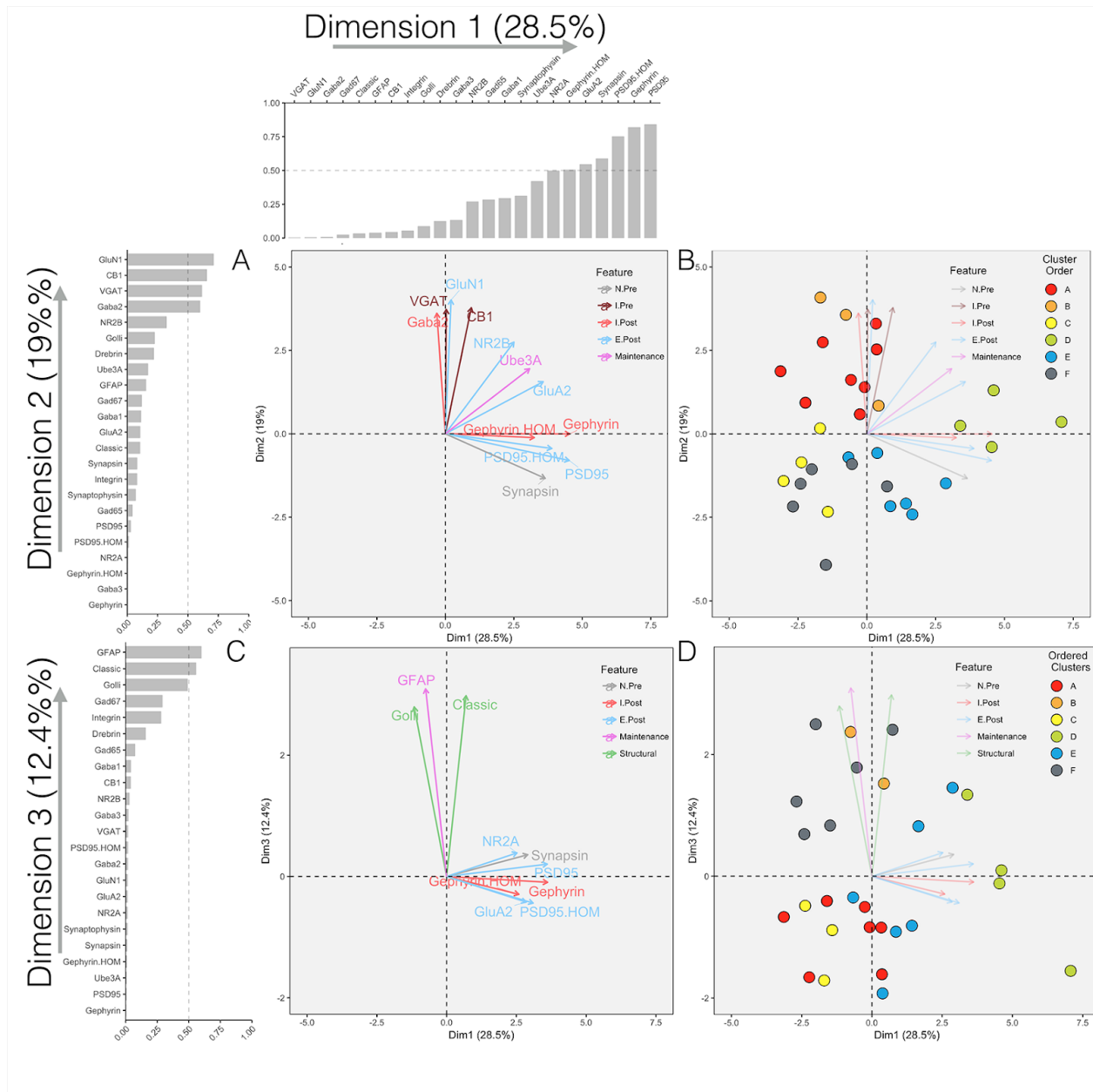


Figure 5. Examination of Principal Component Analysis for feature identification.

A, B. Biplots show protein vectors and individual observations plotted on dimensions 1 and 2. A. Proteins are represented as vectors on both dimension 1 (x-axis) and dimension 2 (y-axis). The length of the vector represents the strength (\cos^2) of the representation of each protein on this set of dimensions. Surrounding histograms depict \cos^2 scores along dimension 1 (top) and dimension 2 (left). Only proteins with a summed \cos^2 above 0.5 (dashed line) across both dimensions are drawn. Vector directions marked by arrowheads point in the direction of high protein expression, while low protein expression extends in the opposite direction through the point of origin. B. Individual observations are plotted as dots on the same dimensions and filled according to the original clusters in Figure 1. Observations near each other in space share similar attributes, observations that overlap with vector arrowheads have high expression of that protein, and observations in the opposite quadrant to a vector have low expression for that protein.

C, D. Plots are the same as in A, B but for dimensions 1 (x-axis) and 3 (y-axis), and applicable histograms are for dimension 1 (top) and dimension 3 (left).

Briefly, Cluster A (youngest median age) was marked by over-representation of CB1 (Figure 5A,B) and under-representation of Classic-MBP, Golli-MBP, and GFAP (Figure 5 C,D). This suggested that early development was characterized by low expression of structural proteins like MBP and maintenance proteins like GFAP. Cluster B on the other hand was easily differentiated from Cluster A on the basis of dimension 3 (Figure 5 C,D), which added over-representation of GFAP, Classic-MBP and Golli-MBP to the list of identifying proteins for Cluster B. This implicates infancy as a stage when non-synaptic, glial and astrocytic systems start to come online. Progression to Cluster C identified under-representation for GluA2, NR2B and Ube3A (Figure 5A,B). As suspected from our earlier analysis (Figure 3), development through Cluster D was accompanied by large increases in expression of many proteins. However, only some of the 17 proteins identified previously were well represented by the first 3 principal components. These include the set of 4 synaptic markers from Pinto et al.(2015)(PSD95, Gephyrin, synapsin I and synaptophysin), as well as the GluA2 subunit of AMPA receptors (Figure 5 B,D). This would suggest that pre-synaptic function (synapsin I, synaptophysin), postsynaptic receptor anchoring (PSD95, Gephyrin) and unsilencing of synapses (GluA2) are emergent factors in this stage. Finally in Cluster E, GFAP, Classic-MBP and Golli-MBP remain under-represented. Curiously, these same 3 proteins increase again in the final Cluster F, at the same time that Ube3A, NR2B and GluA2 decline.

This limited set of cluster-identifying proteins helps ascribe functional changes to each developmental state. Furthermore, it stresses the importance of early and late changes to structural proteins and maintenance proteins. This is in sharp contrast to the subtle increases and decreases that occur for most other synaptic proteins, whether they are excitatory or inhibitory postsynaptic receptors or markers of presynaptic function

Cluster	Age	Quality	D1	D2	D3	All
A	0.3±1.04	High Values		GluN1, CB1, VGAT, GABA α 2		GluN1, CB1, VGAT, GABA α 2
		Low Values			GFAP, Classic-MBP, Golli-MBP	GFAP, Classic-MBP, Golli-MBP
B	0.75±1.34	High Values		GluN1, CB1, VGAT, GABA α 2	GFAP, Classic-MBP, Golli-MBP	GluN1, CB1, VGAT, GABA α 2, GFAP, Classic-MBP, Golli-MBP
		Low Values				
C	3.0±2.03	High Values				
		Low Values	Ube3A, NR2B	GluA2, NR2B	GFAP, Classic-MBP, Golli-MBP	Ube3A, NR2B, GluA2, GFAP, Classic-MBP, Golli-MBP
D	6.8±2.78	High Values	PSD95, Gephyrin, PSD95.Hom, Synapsin, GluA2, Gephyrin.Hom,			PSD95, Gephyrin, PSD95.Hom, Synapsin, GluA2, Gephyrin.Hom,
		Low Values				
E	16.2 ±4.23	High Values				
		Low Values		GluN1, CB1, GABA α 2	GFAP, Golli-MBP	GluN1, CB1, GABA α 2, GFAP, Golli-MBP
F	61.6 ±11.23	High Values			GFAP, Classic-MBP, Golli-MBP	GFAP, Classic-MBP, Golli-MBP
		Low Values	Ube3A, NR2B	GluA2, NR2B		Ube3A, NR2B, GluA2

Table 4: Summary of cluster-identifying proteins across the first 3 PCA dimensions.

Samples in a cluster group together when their coordinates are plotted along principal component dimensions. When clusters align parallel to a protein vector, that protein is flagged as important for determining cluster contents. If the cluster is located at the vector head, then that cluster is reported with high values for that protein. Conversely, if the cluster is located at or behind the vector tail, then that cluster is reported with low values for that protein. High values are indicated in the Quality column, while the dimensions are listed as D1, D2 and D3. Proteins that identify a given cluster are listed in the table.

Feature extraction reveals progressive development between the overlapping plasticity states

To identify combinations of proteins that influenced the clustering we plotted the mean amplitude of each protein about the basis vector for dimensions 1-3 (Figure 6A-C). Across dimension 1, most proteins extend in the same direction, suggesting that the sum of the proteins was the main driver. To investigate if the sum of the proteins represented a meaningful feature,

we calculated a sum of all the well-represented proteins (Sum of Proteins (with $\cos^2 > 0.5$)), a sum of the four synapse markers (Pinto et al., 2015) called PGSS Sum (PSD95, Gephyrin, Synapsin I, Synaptophysin Sum) and a sum of PSD95 and Gephyrin (PSD95 and Gephyrin Sum). All of these sums were significantly correlated with basis vector 1 (Figure 6D), which suggested they were good measures of human V1 development.

Many functionally related pairs of proteins opposed each other about the first 3 basis vectors. These pairs were further examined through the remaining indices that are presented in Figure 6C. Out of the complete list of 12 indices calculated, significant correlations with PCA basis vectors 2 and 3 included the following: Ube3A:PGSS Sum, GluA2:GluN1 Index, GABA_Aα1: GABA_Aα2 Index, Classic-MBP:Golli-MBP Index, GAD65:VGAT Index, Ube3A:Drebrin Index, CB1: GABA_Aα1 Index and Integrin:GFAP Index (Figure 6D). An index of Ube3A to the PGSS set of proteins has been used successfully by our lab (Williams et al., 2010) to model the decline in experience-dependent plasticity regulated by this E3 ubiquitin ligase (Yashiro et al., 2009). The GluA2:GluN1 Index is a proxy for the un-silencing of synapses when AMPAR (GluA2) is inserted into the synapses of otherwise nascent NMDAR-dominated synapses (Isaac et al., 1997; Rumpel et al., 1998), that gradually increases and then decreases across development of human V1 (Siu et al., 2017). The GABA_Aα1:GABA_Aα2 Index is informative of inhibitory control over synapses since the GABA_Aα1, GABA_Aα2 and GABA_Aα3 subunit are all developmentally regulated (Hendrickson et al., 1994; Chen et al., 2001; Bosman et al., 2004; Pinto et al., 2010), and regulate GABA_AR kinetics (Laurie et al., 1992; Gingrich et al., 1995; Eyre et al., 2012). The roles of the two MBP isoforms (Classic-MBP and Golli-MBP) inform about the opposing roles for myelin formation (Jacobs et al., 2005; 2009), compaction (Wake et al., 2011) and the link between the neural and immune systems (Pribyl et al., 1993) across human V1 development (Siu et al., 2015). Finally, the GAD65:VGAT Index informs about the balance between pre-synaptic GABA production and GABA trafficking (Feldblum et al., 1995; McIntire et al., 1997; Sagné et al., 1997).

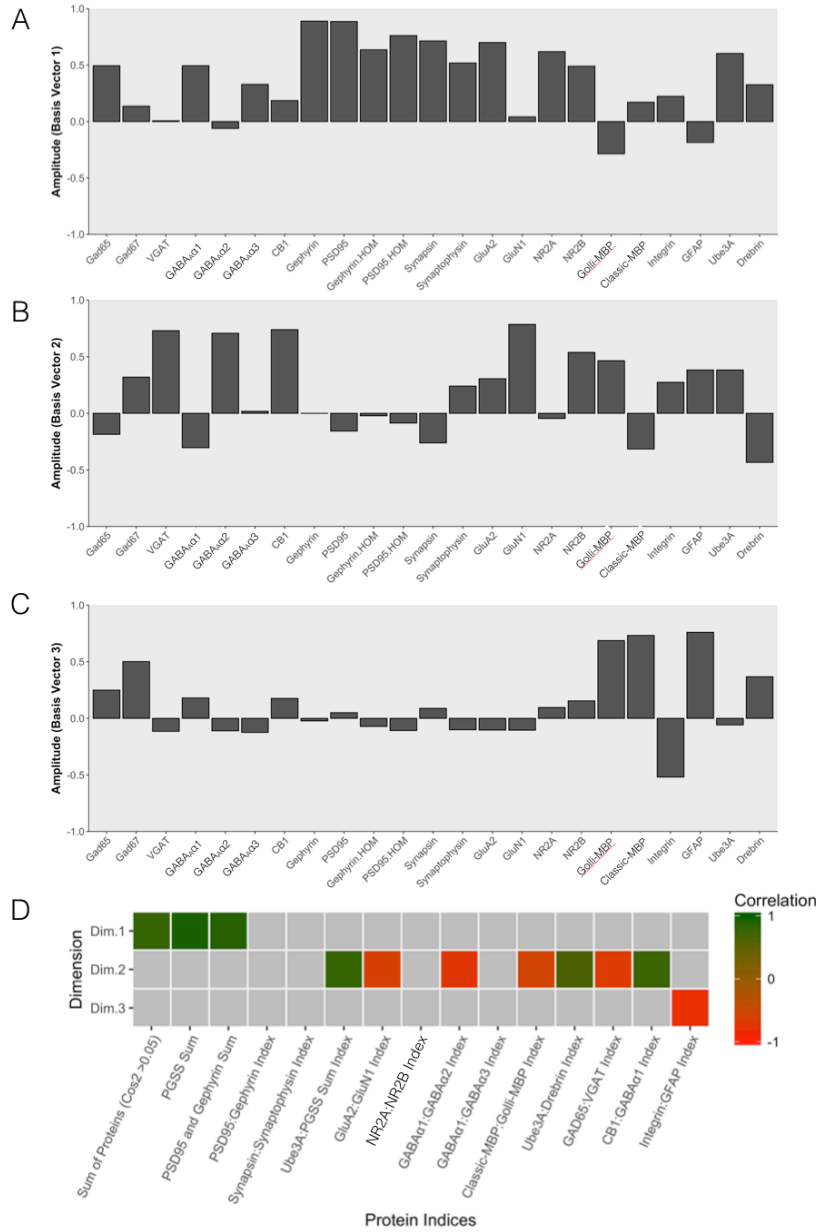


Figure 6. Examination of Principal Component Analysis for feature extraction and reduction.

The influence of each protein on the first A, second B and third C principal components is represented as the relative amplitude about each basis vector. D. Significant correlations between the first 3 principal components and protein sums or indices are represented as coloured cells. The color indicates the magnitude (intensity) and direction (positive=green, negative=red) of significant correlations after Bonferroni correction.

Also, we calculated novel indices that were statistically significant, including the Ube3A:Drebrin Index, which indicates the balance between synaptic protein degradation (DiAntonio and Hicke, 2004) and dendritic spine formation and stability (Hayashi et al., 1996; Hayashi and Shirao, 1999). Ube3A is linked with experience-dependent ocular dominance

plasticity during development (Yashiro et al., 2009) while Drebrin had high expression that decreased toward the end of the critical period in animals (Imamura et al., 1992). To examine the activity-dependent, endocannabinoid regulated GABA release (Sjöström et al., 2003; Jiang et al., 2010) versus mature post-synaptic GABA_A receptors (Hendrickson et al., 1994) we calculated the CB1: GABA_Aα1 Index. Finally, the impact of extracellular matrix protein Integrin (Kramar et al., 2006) versus GFAP (Kaneko et al., 2008) was demonstrated with an Integrin:GFAP Index to address the crosstalk between these two mechanisms (Jones et al., 2011). This index is also informative because integrins regulate expression and function of GABA_AR (Charrier et al., 2010), AMPAR (Cingolani et al., 2008; Pozo et al., 2012) and NMDAR (Bernard-Trifilo et al., 2005; Shi and Ethell, 2006; Michaluk et al., 2009).

Novel biological markers of plasticity across cluster-identified stages

After feature reduction, just like with the analysis of protein expression across clusters (Figure 2A,B) we plotted each index as a series of scatterplots and boxplots for each cluster (Figure 7A,B). The indices were arranged according to basis vector, with metrics correlated with basis vector 1 across the top row, basis vector 2 across the next 3 rows, and the single index from basis vector 3 in the bottom right corner (Figure 7A,B). Each scatterplot was fit with a loess curve to describe the trajectory of change in each index.

All 3 protein sums ($\cos^2 > 0.5$, PGSS Sum and the PSD95 and Gephyrin Sum) started out low, increased until approximately 10 years of age, and then decreased into aging (Figure 7A, top row). The samples that had the highest total proteins were all clustered together in Cluster D (Figure 7B) which was significantly higher than the rest of the data. Conversely, the group that showed the lowest expression across all three of these measures was the oldest Cluster F. These protein sums were reflective of the total available synaptic resources at each stage of development, and it is not surprising that these resources peaked during the period of susceptibility to amblyopia, and gradually declined into adulthood as the available plasticity lessens.

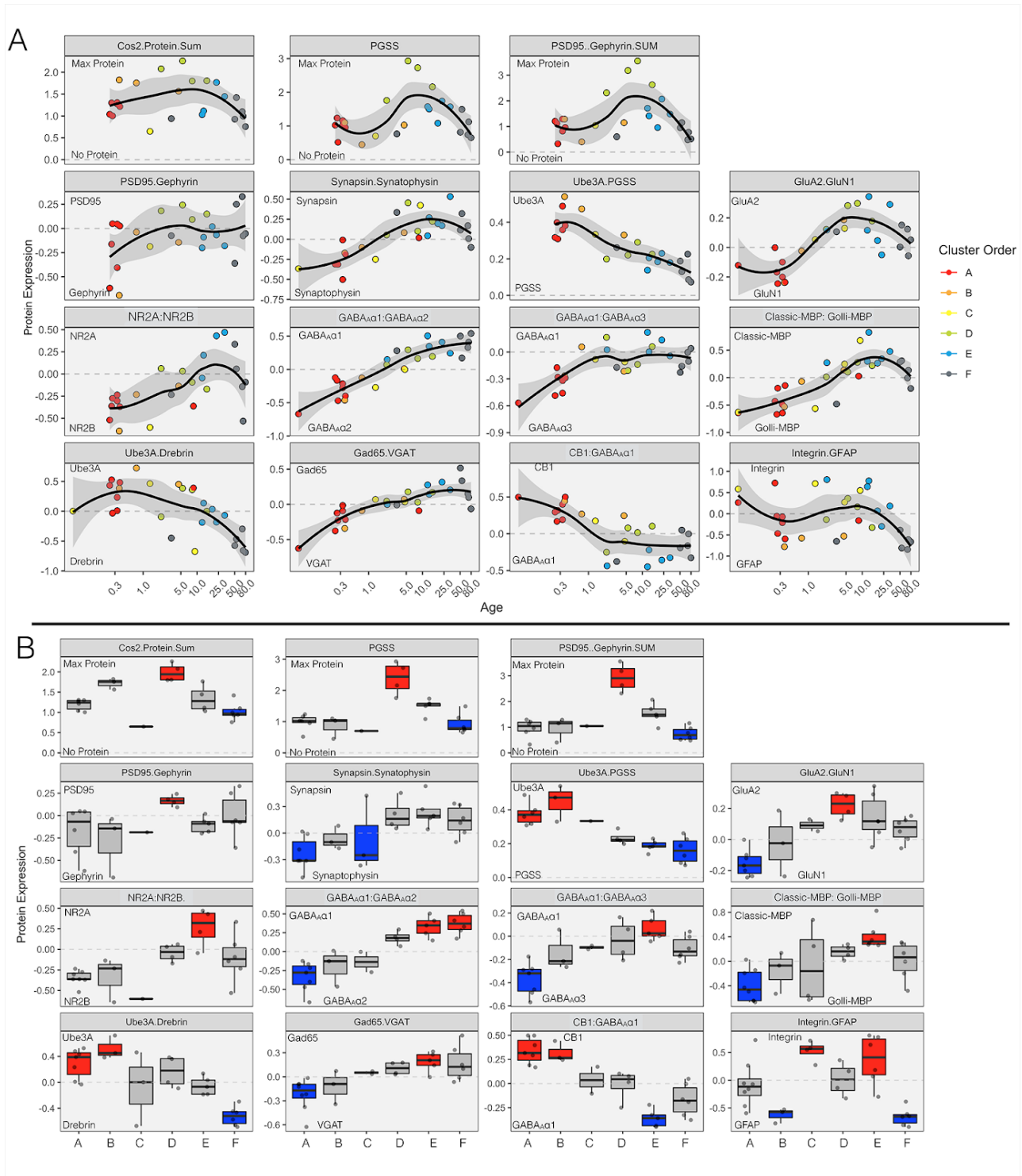


Figure 7. Feature extraction identifies a set of biological features

A. Scatterplots of protein sums and indices with conventions as in Figure 2A. **B.** Boxplots of each cluster are drawn and color coded according to the conventions as described in Figure 2B. Dashed line represents zero or 'balance' between functionally related proteins.

The additional measures that were correlated with basis vectors were indices of functionally related sets of proteins. These indices typically transitioned from a juvenile or immature state to an adult, mature state. Cluster A was typically at either the mature or immature extreme of all indices, and was significantly different from the rest of development on multiple measures. Cluster A favoured synaptophysin over synapsin I, GluN1 over GluA2, the immature subunit in GABA_AR (GABA_Aα1: GABA_Aα3, GABA_Aα1: GABA_Aα2), CB1 over GABA_Aα1, VGAT over Gad65, and had Ube3A over-representation (Ube3A:PGSS sum, Ube3A:Drebrin). Cluster B also had Ube3A over-representation (Ube3A:PGSS sum, Ube3A:Drebrin), favored CB1 over GABA_Aα1 and GFAP over Integrin. Cluster C favored NR2B over NR2A, and Integrin over GFAP.

Aside from having the highest expression of protein sums, Cluster D also favored excitatory PSD95 over inhibitory gephyrin, and favored GluA2 over GluN1. The oldest two clusters, Cluster E and F, contained the extremes of many indices. Cluster E favored the markers of synapses (PSD95, Gephyrin, Synapsin I and Synaptophysin) over Ube3A, the mature NR2A subunit of NMDA receptors, the mature GABA_Aα1 subunit of GABA_AR receptors, Classic-MBP over Golli-MBP, GAD65 over VGAT, and Integrin over GFAP. The oldest Cluster F demonstrated lower protein sums than other clusters across all three protein sums ($\cos^2 > 0.5$, PGSS Sum and then PSD95 and Gephyrin Sum). This cluster also favored PGSS and Drebrin over Ube3A, the mature GABA_Aα1 subunit of GABA_A receptors, and GFAP over integrin.

Systems level plasticity mechanisms are aligned in each cluster

To examine how these features operate as a system, we calculated a correlation matrix between each of the significant features that were correlated with PCA basis vectors. We plotted the results of this correlation analysis in a heatmap (Figure 8), and arranged the order of the correlations according to a surrounding dendrogram. There were 4 main branches to this dendrogram, which identified the groups of indices that change together. The top right corner showed that the protein sums, identified by PCA basis vector 1 ($\cos^2 > 0.5$, PGSS Sum and the PSD95 and Gephyrin Sum) were strongly correlated. The next branch contained a single index, Integrin:GFAP, identified by PCA basis vector 3. The remaining two branches contained all indices that were identified by PCA basis vector 2. These indices could be sorted into ones that

increased from immature to mature (GABA_{AA}1: GABA_{AA}2, Gad65:VGAT, GluA2:GluN1, Classic:Golli-MBP) and ones that decreased from mature to immature (CB1: GABA_{AA}1, Ube3A:PGSS, Ube3A:Drebrin) across development.

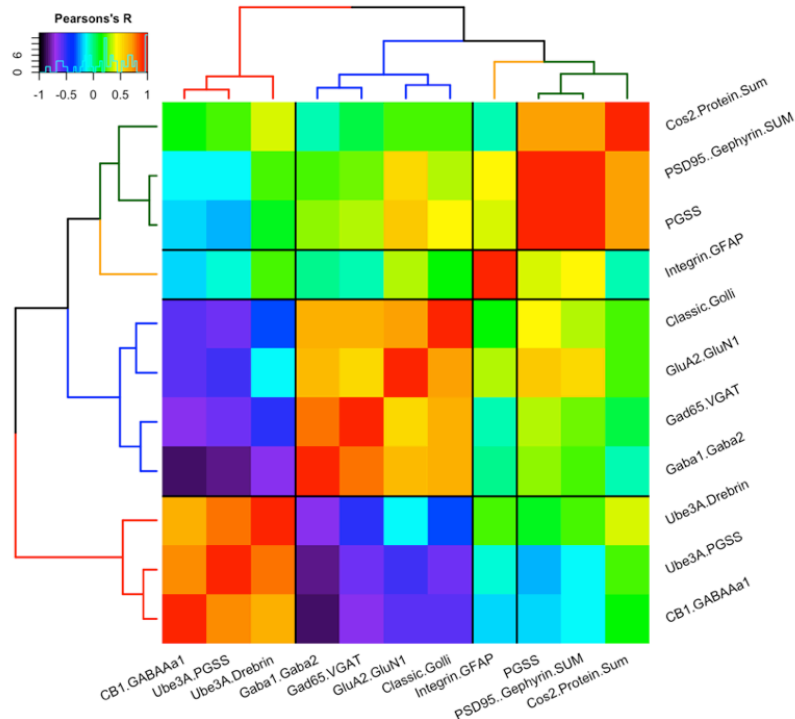


Figure 8. Association between protein sums and functional indices identify developmental changes that emerge during each cluster.

Correlation matrix between protein sums and indices. Pearson's R calculated across the lifespan for each index represents the strength of association (negative= black, purple, blue; positive = green, green, yellow, orange, red) between index and protein sum pairings. Inset indicates distribution of Pearson's R values.

To test this idea we visualized the changes described by each index all at once. We plotted plasticity phenotypes for each cluster, and ordered the phenotypes starting with the cluster that had the youngest median age and progressing to the oldest cluster (Figure 9A-Clusters A-F). The bars representing the features (protein sums and indices) were ordered using the same dendrogram plotted around the correlation matrix (dendrogram in Figure 9A). The first 3 bars represent the protein sums identified by basis vector 1, and span from white (low protein expression) to black (high protein expression). The remaining bars represent the indices, and are color coded to represent one side of each balance as green, and the other side as red (Figure 9).

Aside from the first bar for Integrin:GFAP, most indices were green or yellow across the first 3 clusters (A, B and C). Cluster C began to transition to orange for 2 important indices,

GluA2:GluN1 and Gad65:VGAT. This would suggest that the unsilencing of synapses (as GluN1 overtakes GluA2) and a shift in the readily releasable pool of inhibitory neurotransmitter (as VGAT overtakes Gad65) are beginning to transition in this stage of childhood development. These shifts indicated both excitatory receptors and pre-synaptic inhibitory neurotransmission come online in the early stages of development.

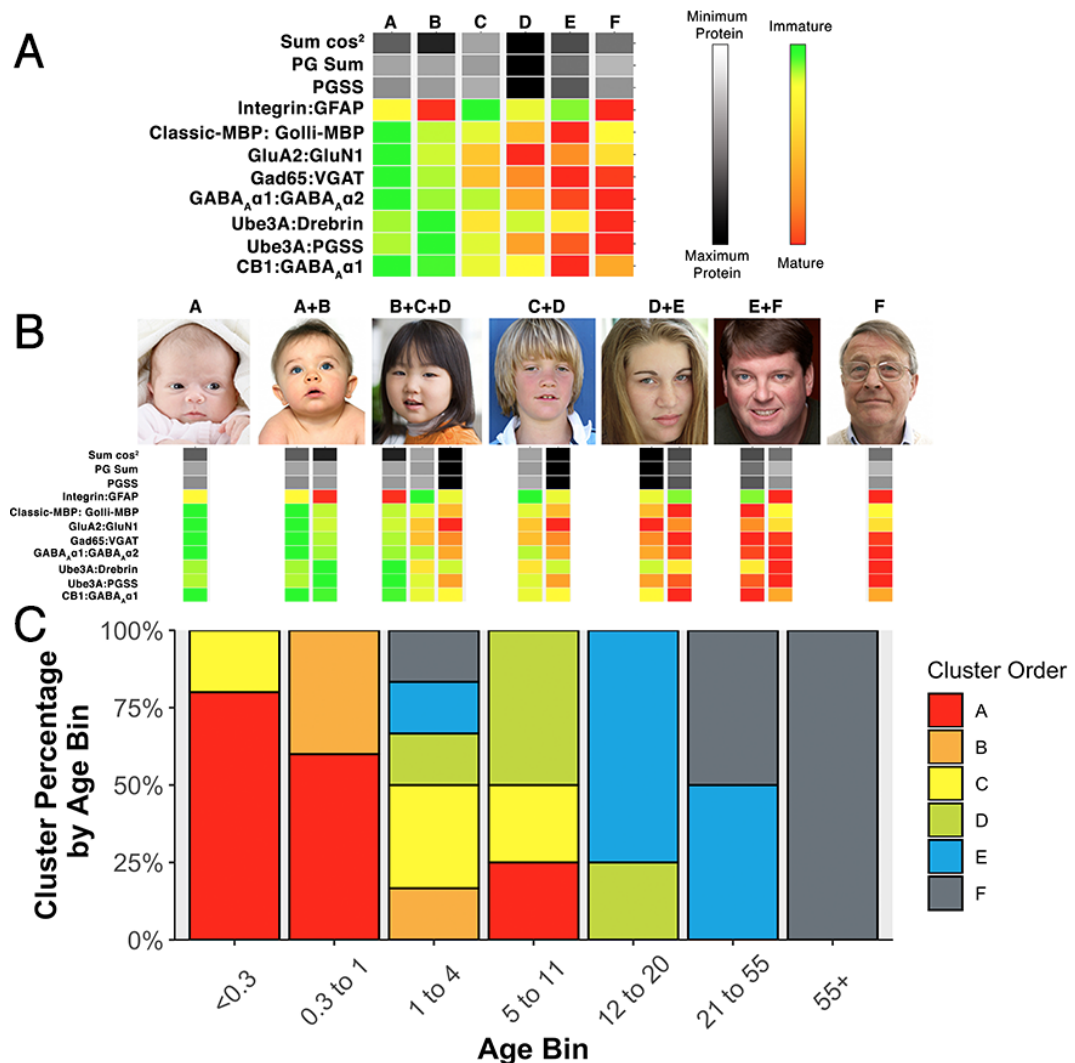


Figure 9. Plasticity motif of indices and protein sums separated by cluster.

A. Mean feature expression for each cluster was mapped to a color scale. Minimum and maximum expression of each cluster was set to grey and black respectively for protein sums (top legend), and immature and mature expression of each cluster was set to green and red respectively for functionally related indices (right side- legend). **B.** Cluster phenotypes were divided amongst the 7 original age-bins typically used for developmental analysis. Neonates (<0.3 years), Infants (0.3–1 year), Young children (1–4 years) Older Children (5–11 years), Teenagers (12–20 years), Young Adults (21–55 years) and Older Adults (>55 years). Clusters that exist in multiple age bins are presented multiple times. **C.** Clusters per age bin, presented here for comparison. Conventions the same as in Figure 1M.

In Cluster D, all three protein sums peak at maximal expression. This indicates high availability of proteins to support plasticity mechanisms. Furthermore, the GluA2:GluN1 transition continued to peak with maximal GluN1 expression. Most other indices were shifting from yellow to orange. A few indices were delayed in the transition (Integrin:GFAP Index, Ube3A:Drebrin and CB1: GABA_Aα1). Cluster E saw total protein sums decrease from the peak in Cluster D, and there were also more indices that reached maximal expression. The oldest cluster, Cluster F, demonstrated even further decreases in protein expression, while the remaining indices shifted to red in this stage.

To visualize the overlap of clusters, we aligned neighbouring cluster phenotypes and repeated the presentation of a phenotype when a cluster was present in more than one age bin (Figure 9B). The percentage of each cluster per age bin showed a good progression from youngest to oldest, but importantly, demonstrated overlap in cluster phenotypes from youngest to oldest age bin.

Modelling receptor kinetics identifies excitatory:inhibitory balance across development

Two indices that did not attain significant correlation with the PCA basis vectors were the NMDAR maturation index (NR2A:NR2B) and the GABA_AR maturation index (GABA_Aα1:GABA_Aα3). These indices are standard balances to investigate in animal models due to the strong link with both visual function (Fagiolini et al., 2003; 2004) and plasticity (Philpot et al., 2001). Both NMDAR and GABA_AR undergo a well-documented substitution in the subunit composition (Laurie et al., 1992; Flint et al., 1997) that is impacted by abnormal early experience (Fagiolini et al., 2003; 2004; Beston et al., 2010). The scatterplots of these indices (Figure 7A) revealed the likely reason for non-significant correlations is that there is a large spread in the 95% CI around the loess plots for these two indices.

To better explain the impact of these receptor subunits on synaptic function, we modelled the predicted receptor decay kinetics of a pool of receptors. The predicted kinetic modelling was based on the observed kinetics in animal models (Eyre et al., 2012; Sun et al., 2017). We plotted the predicted kinetics as scatterplots, and colored the points to match their cluster assignments. The NMDAR kinetics shifted from slow decay speeds to much faster decay into aging (Figure

10A), as the combination of receptor subunits shifted from more 2B to more 2A. Interestingly, the shift to more 2B in old age (Siu et al., 2017) became less pronounced when examining the predicted kinetics as opposed to the expression of receptor subtypes.

The predicted GABA_AR kinetics also transitioned from slow, $\alpha 3:\alpha 3$ to faster $\alpha 1:\alpha 1$ (Figure 10B). The subunit switch in GABA_A receptors in animal models (Beston et al., 2010) and humans (Pinto et al., 2010) suggest this transition in kinetics was to be expected. In order to compare NMDAR and GABA_AR kinetics, the two models were plotted on the same set of axis, with predicted NMDAR kinetics on the y-axis and predicted GABA_AR kinetics on the x-axis (Figure 10C). Youngest points from Cluster A (red) all localized in the bottom left corner of this plot, where both receptor types have slow kinetics. The next oldest Clusters, B and C, had only a few samples and were highly variable. As a result these samples provided a range of predicted kinetics for NMDAR (~100-250ms) and GABA_AR (50-70ms). Cluster D was more tightly regulated and began to transition toward fast NMDAR (~50-100ms) and fast GABA_AR (50-65ms). Cluster E was even more well-regulated with the fastest NMDAR speed (45-55ms) and GABA_AR speed (45-55ms).

A curious trend was noted for the oldest Cluster F, where compact groupings of samples caused the predicted kinetics to regress for both predicted NMDAR (50-200ms) and GABA_AR kinetics (50-65ms). The regression of *both* receptor kinetics suggested that in aging there was a fundamental shift in the function of synapses that enables slower neurotransmission and perhaps greater coincidence detection and LTP.

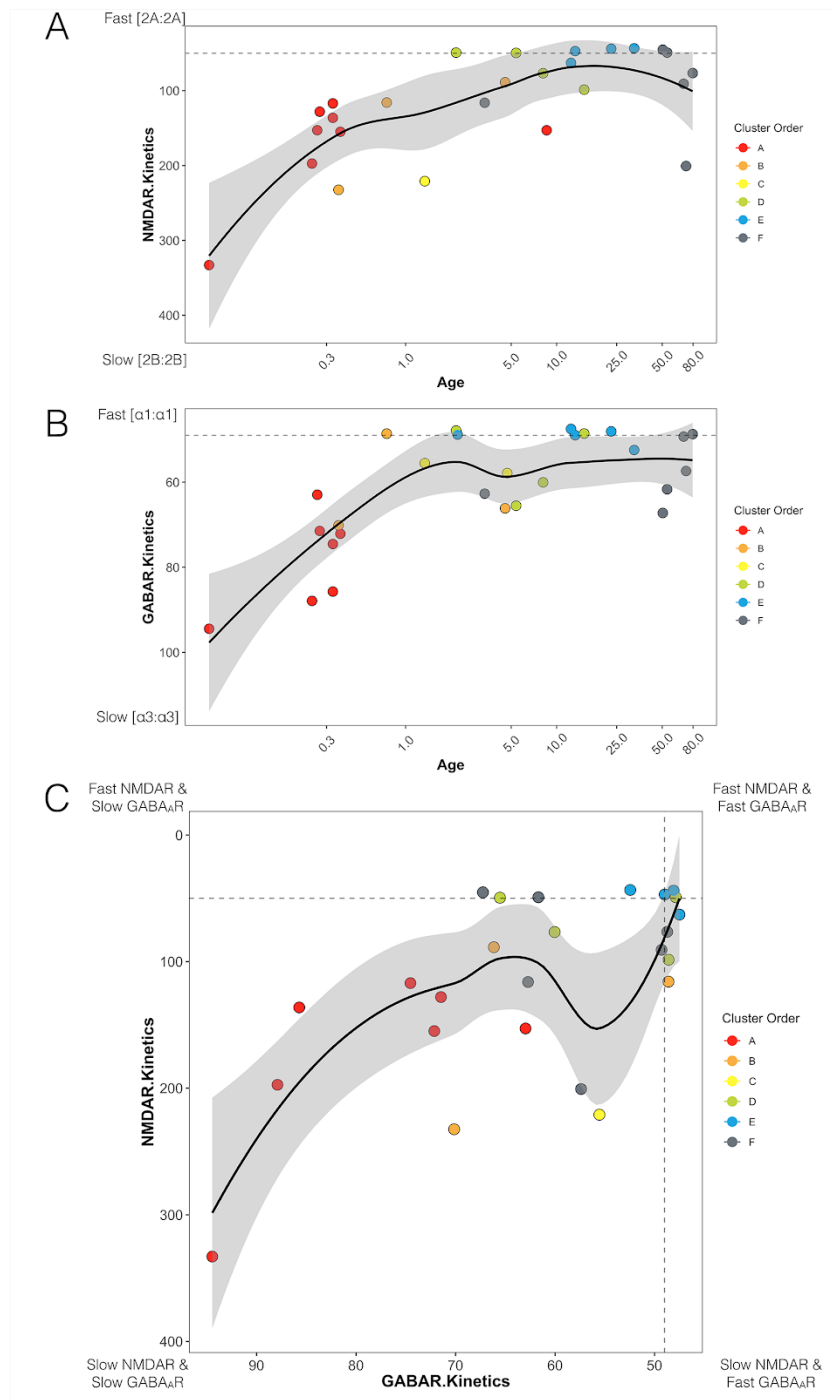


Figure 10. Indices of receptor subunit pairs for NMDAR and GABA_AR predict receptor decay kinetics across development.

A. Average predicted decay kinetics of each individual sample were plotted, and color coded according to cluster. Points were fit with a loss curve, surrounded by 95%CI. Dashed line represents the predicted heterotrimeric decay kinetics [2A:2B]. Predicted GABA_AR decay kinetics across development B. Points were plotted as in A for the predicted GABA_AR decay kinetics. Dashed line represents the predicted heterotrimeric decay kinetics [α 1: α 3]. C. Correlation between predicted decay kinetics of GABA_AR (bottom) and NMDAR (side). Points were plotted as before. Dashed lines represent the same values as in A and B.

6.5 Discussion

Our results show that the neurobiological development of human visual cortex progresses through a series of age-related clusters. The median ages of the clusters were similar to well-known stages of human cognitive and perceptual development. The composition of the clusters, however, did not simply recapitulate discrete age-bins. Samples from the youngest and oldest cases formed discrete age clusters but the clusters representing the rest of the lifespan were a progression of overlapping latent states. For example, the age of the cases in the 4 clusters centered on infants, young children, older children and teenagers overlapped. Since overlap was greatest for clusters centered in childhood, this suggested a period of human development where the synaptic environment in visual cortex has multiple opportunities to diverge into one of many latent brain states. These results expand upon our previous investigations of protein expression in human V1, which identified waves of inter-individual variability in young children (Pinto et al., 2010, Siu et al. 2015, Siu 2018). The current analysis found that the series of 4 overlapping clusters might explain this stage of heightened variability. Despite the overlap in cluster age, there was a clear progression in the expression of plasticity phenotypes across development, with many features of the plasticity phenotype switching from immature to mature as cluster median age increased.

Study design and limitations

There were some limitations to the approach employed here. First, the process of homogenizing cortical tissue in preparation for Western blot analysis destroys valuable information related to the source of proteins, including cell type and cortical layer. Second, even though protein quantification through Western blotting is highly reliable, it does not directly indicate cellular function. With these drawbacks in mind, we restricted our panel of 23 neuronal and non-neuronal proteins to those with well-documented roles in synaptic plasticity and visual function. This allowed us to make more direct comparisons between protein expression and cellular function.

The study design did have multiple strengths, including i) only a small amount of tissue (~20-30 μ g) was required to perform multiple rounds of Western blotting ii) Western blotting let us investigate expression across a large panel of proteins in the same tissue samples and iii)

individuals were sampled across the entirety of the human lifespan. Most importantly, we employed a modern statistical analysis, with techniques borrowed from large scale genomic and proteomic assays that proved sensitive to subtle changes in protein expression. It was only by using this analysis that the 6 latent states of human cortical development could be identified on the basis of the inherent protein signatures of each individual.

Comparison with previous studies

Since the data used here come from 5 studies, it is important to highlight the main differences in biological features using this clustering approach versus those found using standard developmental age bins. We have previously investigated many of these biological features in subsets of these data sets, but only some of these retained significance when examined altogether. For example, the PSD95:Gephyrin, Synapsin:Synaptophysin, GluN2A:GluN2B and GABA_Aα1:GABA_Aα3 features revealed important developmental changes when examined previously (Pinto et al., 2010; 2015, Williams et al., 2010 and Siu et al., 2017) but failed to achieve significance in the current analysis. The reason for the lack of significance in the current study is that the current PCA basis vectors are created using contributions from all 23 proteins, which would produce a very different set of basis vectors than in the original studies. Therefore, these features that failed to attain significant correlations in the current analysis simply did not map onto the updated set of PCA basis vectors (Figure 5, 6). Closer examination of these features in Figure 7 shows that many of the ones that fail to retain significance have a large 95% CI, including GluN2A:GluN2B and GABA_Aα1:GABA_Aα3. It is possible that these features do not provide as tight regulation of human cortical development as some of the other features that were well correlated with PCA basis vectors.

Some features that have previously been examined were well mapped onto the current set of PCA basis vectors and retained significance. These include GABA_Aα1:GABA_Aα2, Gad65:VGAT (Pinto et al., 2010), Ube3A:PGSS Sum (Williams et al., 2010), PGSS Sum (Pinto et al., 2015), Classic-MBP:Golli-MBP (Siu et al., 2015), GluA2:GluN1 (Siu et al., 2017). For many of these features we have previously noted large variability, especially early in development. Parsing the data into clusters reduced the within cluster variability, and instead revealed greater between cluster variability. For example, the PGSS sum used in Pinto et al.,

2015 now shows that the peak in development where this protein sum reaches a maximum arises from a single cluster that contained all the samples with high protein sums, while the two neighbouring clusters had much lower protein sum expression.

Finally, new features that were identified as significant in the current study include the Sum of proteins with $\cos^2 > 0.5$, PSD95 and Gephyrin Sum, Ube3A:Drebrin, CB1:GABA α 1 and Integrin:GFAP. A brief explanation of these features follows.

Identification of new features

The analysis of human cortical development revealed several new features that highlight the differences between latent brain states. Specifically, the three protein sum measurements (Sum of proteins with $\cos^2 > 0.5$, PG Sum and PGSS Sum) highlighted an early developmental period during childhood that encompassed the overlapping states. For example, the third state (median age = 3.0 ± 2.03 years) was closest in median age to young children (1-4 years) and demonstrated under-representation of protein expression, while the fourth state (median age = 6.8 ± 2.78 years) was closest in median age to older children (5-11 years), and demonstrated protein over-representation. Protein over-representation may be related to the PSD95 peak that coincides with the end of the critical period in both rodents and humans (Pinto et al., 2015, Siu et al., 2018). Taken together, the variability across the 4 overlapping states indicated a period of heightened protein dynamics. The variability in protein sum expression could represent dynamic fluctuations between overlapping states or fluctuations in protein expression within an individual. The idea of large changes in protein expression levels of human cells is not uncommon, and expression levels have been found to fluctuate after just a few hours (Sigal et al., 2006). The repeated sampling of tissue samples used in our methodology revealed low variability within an individual, suggest that these dynamics highlight changes between individuals belonging to the different clusters.

We identified a period late in development, during the final latent state (Cluster F = 61.6 ± 27.5 yrs), where several indices regress from the mature end of an index toward the immature end. For example, Classic-MBP:Golli-MBP reverted in favor of more Golli-MBP suggesting heightened immune response (Pribyl et al., 1993, Paez et al., 2007, 2011, 2012) and increased immune response could indicate active glial and astrocytic presence. The GluA2:GluN1 reverted

back to more GluN1 which decreases synapse efficacy (Liao et al. 2001, Huang et al., 2015), would prolong excitatory impulses in post-synaptic cells since the kinetics of these receptors are much longer than the kinetics for AMPAR (Gainey et al., 2009). The shift in these features likely preserves synapse integrity by causing a regression of these indices to become more neuroprotective.

The notion of prolonged receptor kinetics was supported by our model of receptor kinetics for NMDA and GABA_A receptors across development using values from animal studies (Eyre and Nusser 2012, Sun et al., 2017). This analysis revealed a steady progression of predicted receptor kinetics from slow early in development to reach a peak in the teenage to young adult years, before slowing again in older adults. This final state with older adults had slow predicted receptor kinetics affecting both the excitatory and inhibitory receptors. In animal studies, slow receptor kinetics typically transforms synaptic environments to become receptive to experiential changes (Bridi et al., 2018, Kirkwood et al., 1996). If one only considered this measure then it suggests a period late in development where the visual cortex might be more susceptible to either long-term potentiation or depression. However, if that were the case then we would have expected the oldest and youngest samples to be in the same cluster and they are not. Furthermore, if cortical aging shifts to a period of heightened plasticity then it has devastating implications for any visual insult that manifests in old age. This includes the formation of cataracts, which could result in lasting visual impairments that persist even after corrective action is taken.

Benefits of multiple latent brain states

Our finding of a developmental series of overlapping brain states does not uncover whether individuals oscillate between brain states, or if brain states are a characteristic belonging to each individual. If individuals can *jump* between states, this would provide an avenue to rapidly and dramatically change protein expression in response to different synaptic environments. The central dogma of biology predicts that protein expression follows RNA expression, and proteogenomic studies have indeed reported a wide range of correlations between RNA expression and protein expression depending on the state of the system (Gry et al., 2009, Ruggles et al., 2017, Liu et al., 2016). At steady-state, when there are few overlapping states, protein levels are well-predicted by RNA expression, but during state transitions the RNA-protein

correspondence drops (Liu et al., 2016). Indeed, in the human cortex before childhood and adolescence, the correspondence between cortical gene expression and protein levels is high (Beveridge et al., 2013, Breen et al., 2018), meaning that fluctuations in RNA expression would be matched by fluctuations in protein expression. The high variability in protein expression during these states is likely matching changes in RNA expression.

There is a decrease in RNA-protein correspondence, however, from the middle stages of development and onward (Beveridge et al., 2013, Breen et al., 2018). This means that as development proceeds into aging there are fewer state transitions, but RNA-protein correspondence decreases. We suggest that during these later states, the post-transcriptional machinery that protects against variations in RNA fails to balance over- or under-representation of proteins, as suggested by Beveridge et al. (2013). As a result, a secondary protective system likely becomes activated that converges on oligodendrocytic and myelinating processes (Breen et al., 2018), creating an over-representation of immune-system proteins in the latest stages of life. We demonstrate this via regressions in the Integrin:GFAP and Classic-MBP:Golli-MBP indices toward the immature GFAP and Golli-MBP, respectively, in the older adults cluster (Cluster F).

Conclusions

This investigation of 23 synaptic and non-neuronal proteins in human V1 across the lifespan revealed plasticity features and phenotypes that are useful for describing human development. These plasticity phenotypes represent 6 latent states that begin as a distinct and non-overlapping during the early, neonatal period of development, then become heterogeneous and demonstrate developmental overlap through childhood and the teenage years, before separating into distinct states into aging. The overlapping states during childhood and adolescence represent high variability in protein expression in response to changes in visual experience. The discrete states demonstrated by older adults (Cluster F) displayed a regression to juvenile-like states of plasticity for both immune-related plasticity features and predicted kinetics.

6.6 References

- Abdi H, Williams LJ (2010) Principal component analysis. *Wiley Interdisciplinary Reviews: Computational Statistics* 2:433–459.
- Bernard-Trifilo JA, Kramar EA, Torp R, Lin C-Y, Pineda EA, Lynch G, Gall CM (2005) Integrin signaling cascades are operational in adult hippocampal synapses and modulate NMDA receptor physiology. *Journal of Neurochemistry* 93:834–849.
- Beston BR, Jones DG, Murphy KM (2010) Experience-dependent changes in excitatory and inhibitory receptor subunit expression in visual cortex. *Front Synaptic Neurosci* 2:138.
- Beveridge, N. J., Santarelli, D. M., Wang, X., Tooney, P. A., Webster, M. J., Weickert, C. S., & Cairns, M. J. (2013). Maturation of the human dorsolateral prefrontal cortex coincides with a dynamic shift in microRNA expression. *Schizophrenia bulletin*, 40(2), 399-409.
- Bosman LWJ, Rosahl TW, Brussaard AB (2004) Neonatal development of the rat visual cortex: synaptic function of GABA_A receptor α subunits. *The Journal of Physiology* 545:169–181.
- Breen, M. S., Ozcan, S., Ramsey, J. M., Wang, Z., Ma'ayan, A., Rustogi, N., ... & Bahn, S. (2018). Temporal proteomic profiling of postnatal human cortical development. *Translational psychiatry*, 8(1), 267.
- Bridi, M. C., de Pasquale, R., Lantz, C. L., Gu, Y., Borrell, A., Choi, S. Y., ... & Lee, H. K. (2018). Two distinct mechanisms for experience-dependent homeostasis. *Nature neuroscience*, 21(6), 843.
- Carlyle BC, Kitchen RR, Kanyo JE, Voss EZ, Pletikos M, Sousa AMM, Lam TT, Gerstein MB, Sestan N, Nairn AC (2017) A multiregional proteomic survey of the postnatal human brain. *Nat Neurosci* 20:1787–1795.
- Charrier C, Machado P, Tweedie-Cullen RY, Rutishauser D, Mansuy IM, Triller A (2010) A crosstalk between β 1 and β 3 integrins controls glycine receptor and gephyrin trafficking at synapses. *Nature Publishing Group* 13:1388–1395.
- Chen L, Yang C, Mower GD (2001) Developmental changes in the expression of GABA_A receptor subunits (α 1, α 2, α 3) in the cat visual cortex and the effects of dark rearing. *Molecular Brain Research* 88:135–143.
- Cingolani LA, Thalhammer A, Yu LMY, Catalano M, Ramos T, Colicos MA, Goda Y (2008) Activity-Dependent Regulation of Synaptic AMPA Receptor Composition and Abundance by β 3 Integrins. *Neuron* 58:749–762.
- DiAntonio A, Hicke L (2004) Ubiquitin-dependent regulation of the synapse. *Annu Rev Neurosci* 27:223–246.
- Duncan, C. E., Webster, M. J., Rothmond, D. A., Bahn, S., Elashoff, M., & Weickert, C. S. (2010). Prefrontal GABA_A receptor α -subunit expression in normal postnatal human development and schizophrenia. *Journal of psychiatric research*, 44(10), 673-681.

- Epelbaum M, Milleret C, Buisseret P, Dufier JL (1993) The sensitive period for strabismic amblyopia in humans. *Ophthalmology* 100:323–327.
- Erikson, E. H. (1959). *Identity and the life cycle: Selected papers*.
- Eyre MD, Renzi M, Farrant M, Nusser Z (2012) Setting the time course of inhibitory synaptic currents by mixing multiple GABA(A) receptor α subunit isoforms. *J Neurosci* 32:5853–5867.
- Fagiolini M, Fritschy J-M, Löw K, Möhler H, Rudolph U, Hensch TK (2004) Specific GABAA circuits for visual cortical plasticity. *Science* 303:1681–1683.
- Fagiolini M, Katagiri H, Miyamoto H, Mori H, Grant SGN, Mishina M, Hensch TK (2003) Separable features of visual cortical plasticity revealed by N-methyl-D-aspartate receptor 2A signaling. *Proc Natl Acad Sci USA* 100:2854–2859.
- Feldblum S, Dumoulin A, Anoaï M, Sandillon F, Privat A (1995) Comparative distribution of GAD65 and GAD67 mRNAs and proteins in the rat spinal cord supports a differential regulation of these two glutamate decarboxylases in vivo. *J Neurosci Res* 42:742–757.
- Fjell AM et al. (2015) Development and aging of cortical thickness correspond to genetic organization patterns. *Proc Natl Acad Sci USA* 112:15462–15467.
- Flint AC, Maisch US, Weishaupt JH, Kriegstein AR, Monyer H (1997) NR2A subunit expression shortens NMDA receptor synaptic currents in developing neocortex. *Journal of Neuroscience* 17:2469–2476.
- Froemke RC, Dan Y (2002) Spike-timing-dependent synaptic modification induced by natural spike trains. *Nature* 416:433–438.
- Gainey, M. A., Hurvitz-Wolff, J. R., Lambo, M. E., & Turrigiano, G. G. (2009). Synaptic scaling requires the GluR2 subunit of the AMPA receptor. *Journal of Neuroscience*, 29(20), 6479-6489.
- Gingrich KJ, Roberts WA, Kass RS (1995) Dependence of the GABAA receptor gating kinetics on the alpha-subunit isoform: implications for structure–function relations and synaptic transmission. *The Journal of Physiology* 489:529–543.
- Gry, M., Rimini, R., Strömberg, S., Asplund, A., Pontén, F., Uhlén, M., & Nilsson, P. (2009). Correlations between RNA and protein expression profiles in 23 human cell lines. *BMC genomics*, 10(1), 365.
- Grydeland H, Walhovd KB, Tamnes CK, Westlye LT, Fjell AM (2013) Intracortical Myelin Links with Performance Variability across the Human Lifespan: Results from T1- and T2-Weighted MRI Myelin Mapping and Diffusion Tensor Imaging. *Journal of Neuroscience* 33:18618–18630.
- Hayashi K, Ishikawa R, Ye LH, He XL, Takata K, Kohama K, Shirao T (1996) Modulatory role of drebrin on the cytoskeleton within dendritic spines in the rat cerebral cortex. *Journal of Neuroscience* 16:7161–7170.

- Hayashi K, Shirao T (1999) Change in the shape of dendritic spines caused by overexpression of drebrin in cultured cortical neurons. *J Neurosci* 19:3918–3925.
- Hendrickson A, March D, Richards G, Erickson A, Shaw C (1994) Coincidental appearance of the $\alpha 1$ subunit of the gaba-a receptor and the type ibenzodiazepine receptor near birth in macaque monkey visual cortex. *International Journal of Developmental Neuroscience* 12:299–314.
- Huang, X., Stodieck, S. K., Goetze, B., Cui, L., Wong, M. H., Wenzel, C., ... & Schlüter, O. M. (2015). Progressive maturation of silent synapses governs the duration of a critical period. *Proceedings of the National Academy of Sciences*, 201506488.
- Imamura K, Shirao T, Mori K, Obata K (1992) Changes of drebrin expression in the visual cortex of the cat during development. *Neurosci Res* 13:33–41.
- Isaac JT, Crair MC, Nicoll RA, Malenka RC (1997) Silent synapses during development of thalamocortical inputs. *Neuron* 18:269–280.
- Jacobs EC, Pribyl TM, Kampf K, Campagnoni C, Colwell CS, Reyes SD, Martin M, Handley V, Hiltner TD, Readhead C, Jacobs RE, Messing A, Fisher RS, Campagnoni AT (2005) Region-Specific Myelin Pathology in Mice Lacking the Golli Products of the Myelin Basic Protein Gene. *Journal of Neuroscience* 25:7004–7013.
- Jacobs EC, Reyes SD, Campagnoni CW, Givogri MI, Kampf K, Handley V, Spreuer V, Fisher R, Macklin W, Campagnoni AT (2009) Targeted Overexpression of a Golli-Myelin Basic Protein Isoform to Oligodendrocytes Results in Aberrant Oligodendrocyte Maturation and Myelination. *ASN NEURO* 1:AN20090029.
- Jiang B, Huang S, de Pasquale R, Millman D, Song L, Lee H-K, Tsumoto T, Kirkwood A (2010) The maturation of GABAergic transmission in visual cortex requires endocannabinoid-mediated LTD of inhibitory inputs during a critical period. *Neuron* 66:248–259.
- Jones EV, Bernardinelli Y, Tse YC, Chierzi S, Wong TP, Murai KK (2011) Astrocytes control glutamate receptor levels at developing synapses through SPARC-beta-integrin interactions. *J Neurosci* 31:4154–4165.
- Kadosh KC, Krause B, King AJ, Near J, Kadosh RC (2015) Linking GABA and glutamate levels to cognitive skill acquisition during development. *Hum Brain Mapp* 36:4334–4345.
- Kaneko M, Stellwagen D, Malenka RC, Stryker MP (2008) Tumor Necrosis Factor- α Mediates One Component of Competitive, Experience-Dependent Plasticity in Developing Visual Cortex. *Neuron* 58:673–680.
- Kirkwood, A., Rioult, M. G., & Bear, M. F. (1996). Experience-dependent modification of synaptic plasticity in visual cortex. *Nature*, 381(6582), 526.
- Kondo Y, Salibian-Barrera M, Software RZJOS (2016) RSKC: An R package for a robust and sparse k-means clustering algorithm. *JSS Journal of Statistical Software* 72.
- Kramar EA, Lin B, Rex CS, Gall CM, Lynch G (2006) Integrin-driven actin polymerization consolidates long-term potentiation. *Proc Natl Acad Sci USA* 103:5579–5584.

- Laurie DJ, Wisden W, Seeburg PH (1992) The distribution of thirteen GABAA receptor subunit mRNAs in the rat brain. III. Embryonic and postnatal development. *Journal of Neuroscience* 12:4151–4172.
- Law, A. J., Weickert, C. S., Webster, M. J., Herman, M. M., Kleinman, J. E., & Harrison, P. J. (2003). Expression of NMDA receptor NR1, NR2A and NR2B subunit mRNAs during development of the human hippocampal formation. *European journal of neuroscience*, 18(5), 1197-1205.
- Liao, D., Scannevin, R. H., & Huganir, R. (2001). Activation of silent synapses by rapid activity-dependent synaptic recruitment of AMPA receptors. *Journal of Neuroscience*, 21(16), 6008-6017.
- Lister R et al. (2013) Global epigenomic reconfiguration during mammalian brain development. *Science* 341:1237905.
- Liu, Y., Beyer, A., & Aebersold, R. (2016). On the dependency of cellular protein levels on mRNA abundance. *Cell*, 165(3), 535-550.
- McIntire SL, Reimer RJ, Schuske K, Edwards RH, Jorgensen EM (1997) Identification and characterization of the vesicular GABA transporter. *Nature* 389:870–876.
- Michaluk P, Mikasova L, Groc L, Frischknecht R, Choquet D, Kaczmarek L (2009) Matrix metalloproteinase-9 controls NMDA receptor surface diffusion through integrin beta1 signaling. *J Neurosci* 29:6007–6012.
- Mills KL, Lalonde F, Clasen LS, Giedd JN, Blakemore S-J (2014) Developmental changes in the structure of the social brain in late childhood and adolescence. *Soc Cogn Affect Neurosci* 9:123–131.
- Nowakowski TJ, Bhaduri A, Pollen AA, Alvarado B, Mostajo-Radji MA, Di Lullo E, Haeussler M, Sandoval-Espinosa C, Liu SJ, Velmeshev D, Ounadjela JR, Shuga J, Wang X, Lim DA, West JA, Leyrat AA, Kent WJ, Kriegstein AR (2017) Spatiotemporal gene expression trajectories reveal developmental hierarchies of the human cortex. *Science* 358:1318–1323.
- Paez PM, Cheli VT, Ghiani CA, Spreuer V, Handley VW, Campagnoni AT (2012) Golli myelin basic proteins stimulate oligodendrocyte progenitor cell proliferation and differentiation in remyelinating adult mouse brain. *Glia* 60:1078–1093.
- Paez PM, Fulton D, Spreuer V, Handley V, Campagnoni AT (2011) Modulation of Canonical Transient Receptor Potential Channel 1 in the Proliferation of Oligodendrocyte Precursor Cells by the Golli Products of the Myelin Basic Protein Gene. *Journal of Neuroscience* 31:3625–3637.
- Paez PM, Spreuer V, Handley V, Feng J-M, Campagnoni C, Campagnoni AT (2007) Increased expression of golli myelin basic proteins enhances calcium influx into oligodendroglial cells. *J Neurosci* 27:12690–12699.
- Parsons L, Haque E, Liu H (2004) Subspace clustering for high dimensional data: a review. *ACM SIGKDD Explorations Newsletter* 6:90–105.

- Philpot BD, Weisberg MP, Ramos MS, Sawtell NB, Tang Y-P, Tsien JZ, Bear MF (2001) Effect of transgenic overexpression of NR2B on NMDA receptor function and synaptic plasticity in visual cortex. *Neuropharmacology* 41:762–770.
- Piaget, J., & Cook, M. (1952). *The origins of intelligence in children* (Vol. 8, No. 5, p. 18). New York: International Universities Press.
- Pinto JGA, Hornby KR, Jones DG, Murphy KM (2010) Developmental changes in GABAergic mechanisms in human visual cortex across the lifespan. *Front Cell Neurosci* 4:16.
- Pinto JGA, Jones DG, Williams CK, Murphy KM (2015) Characterizing synaptic protein development in human visual cortex enables alignment of synaptic age with rat visual cortex. *Front Neural Circuits* 9:3.
- Pozo K, Cingolani LA, Bassani S, Laurent F, Passafaro M, Goda Y (2012) $\beta 3$ integrin interacts directly with GluA2 AMPA receptor subunit and regulates AMPA receptor expression in hippocampal neurons. *Proc Natl Acad Sci USA* 109:1323–1328.
- Pribyl TM, Campagnoni CW, Kampf K, Kashima T, Handley VW, McMahon J, Campagnoni AT (1993) The human myelin basic protein gene is included within a 179-kilobase transcription unit: expression in the immune and central nervous systems. *Proc Natl Acad Sci USA* 90:10695–10699.
- Quinlan EM, Olstein DH, Bear MF (1999a) Bidirectional, experience-dependent regulation of N-methyl-D-aspartate receptor subunit composition in the rat visual cortex during postnatal development. *Proc Natl Acad Sci USA* 96:12876–12880.
- Quinlan EM, Philpot BD, Huganir RL, Bear MF (1999b) Rapid, experience-dependent expression of synaptic NMDA receptors in visual cortex in vivo. *Nat Neurosci* 2:352–357.
- Ruggles, K. V., Krug, K., Wang, X., Clauser, K. R., Wang, J., Payne, S. H., ... & Mani, D. R. (2017). Methods, tools and current perspectives in proteogenomics. *Molecular & Cellular Proteomics*, 16(6), 959-981.
- Rumpel S, Hatt H, Gottmann K (1998) Silent Synapses in the Developing Rat Visual Cortex: Evidence for Postsynaptic Expression of Synaptic Plasticity. *Journal of Neuroscience* 18:8863–8874.
- Sagné C, Mestikawy El S, Isambert M-F, Hamon M, Henry J-P, Giros B, Gasnier B (1997) Cloning of a functional vesicular GABA and glycine transporter by screening of genome databases. *FEBS Letters* 417:177–183.
- Shaw P, Kabani NJ, Lerch JP, Eckstrand K, Lenroot R, Gogtay N, Greenstein D, Clasen L, Evans A, Rapoport JL, Giedd JN, Wise SP (2008) Neurodevelopmental Trajectories of the Human Cerebral Cortex. *Journal of Neuroscience* 28:3586–3594.
- Shi Y, Ethell IM (2006) Integrins control dendritic spine plasticity in hippocampal neurons through NMDA receptor and Ca^{2+} /calmodulin-dependent protein kinase II-mediated actin reorganization. *J Neurosci* 26:1813–1822.

- Sigal, A., Milo, R., Cohen, A., Geva-Zatorsky, N., Klein, Y., Liron, Y., ... & Alon, U. (2006). Variability and memory of protein levels in human cells. *Nature*, 444(7119), 643.
- Siu CR, Balsor JL, Jones DG, Murphy KM (2015) Classic and Golli Myelin Basic Protein have distinct developmental trajectories in human visual cortex. *Front Neurosci* 9:1–10.
- Siu CR, Beshara SP, Jones DG, Murphy KM (2017) Development of Glutamatergic Proteins in Human Visual Cortex across the Lifespan. *J Neurosci* 37:6031–6042.
- Siu, C. R., & Murphy, K. M. (2018). The development of human visual cortex and clinical implications. *Eye and brain*, 10, 25.
- Sjöström PJ, Turrigiano GG, Nelson SB (2003) Neocortical LTD via coincident activation of presynaptic NMDA and cannabinoid receptors. *Neuron* 39:641–654.
- Sun W, Hansen KB, Jahr CE (2017) Allosteric Interactions between NMDA Receptor Subunits Shape the Developmental Shift in Channel Properties. *Neuron* 94:58–64.e3.
- Wake H, Lee PR, Fields RD (2011) Control of Local Protein Synthesis and Initial Events in Myelination by Action Potentials. *Science* 333:1647–1651.
- Wickham, H. (2016). *ggplot2: elegant graphics for data analysis*. Springer.
- Williams K, Irwin DA, Jones DG, Murphy KM (2010) Dramatic Loss of Ube3A Expression during Aging of the Mammalian Cortex. *Front Aging Neurosci* 2:18.
- Witten DM, Tibshirani R (2010) A framework for feature selection in clustering. *J Am Stat Assoc* 105:713–726.
- Yashiro K, Riday TT, Condon KH, Roberts AC, Bernardo DR, Prakash R, Weinberg RJ, Ehlers MD, Philpot BD (2009) Ube3a is required for experience-dependent maturation of the neocortex. *Nat Neurosci* 12:777–783.

Chapter 7. General Discussion

7.1 Summary of main findings

In this thesis I have contributed to advancements in the areas of synaptic plasticity mechanisms as they pertain to animal models, our understanding of the course of human cortical development, and in identifying potential targets for amblyopia therapy. I have done this by using modern approaches to studying questions. In the first part of this thesis (Chapters 2, 3 and 4), I presented new techniques for studying the central visual pathway. My most significant contributions addressed two gaps in the literature. First, using the cat animal model I identified the plasticity phenotypes that distinguished treatments promoting good versus poor recovery from amblyopia (Chapter 5). Second, using human postmortem tissue and modern high-dimensional data analyses I characterized the neurobiological development of human visual cortex from birth to older adults as a series of stages with overlapping phenotypic states (Chapter 6).

In Chapter 2, I combined classic neural tracing techniques and unfolding and flattening tissues, with fluorescent tracers and tissue clearing to easily, affordably and efficiently image stages of the cat central visual pathway. The approach showed the patchy pattern of retinal afferents in the superior colliculus. That pattern was first proposed by Ann Graybiel in 1970, and subsequently was only partially been demonstrated by Illing in 1989 using a single tracer injection. Here I used two different fluorescent labels that were easily visualized in every slice of the cat SC, I confirmed the waxing and waning pattern in SC as true interdigitation and demonstrate clear interdigitation of ipsilateral and contralateral afferents in the cat LGN (Chapter 2). The benefit of my approach was that every single section was easily and rapidly reacted to reveal label extending from both eyes. I also confirmed that these labels remained in cleared tissue, however because we imaged through the entire depth of cleared tissue, the utility of these labels in cleared subcortical and cortical structures leaves something to be desired. This anterograde labeling method was cheap, rapid and provided a high-resolution way to visualize projections from both eyes in multiple stages along the central visual pathway.

In Chapter 3, I modernized the classic fractionation protocol for producing synaptoneurosomes by introducing semi-automated steps for the homogenization and filtration of samples. The protocol is amenable for use in animal as well as human cortical tissues. The main

benefit of this protocol was increased reliability, and the three additional benefits were the increased synaptoneurosome yield and decreased preparation time and cost over traditional manual hand-preparations. This method for procuring synaptoneurosome was high throughput and semi-automated, and with some modifications, the process could become fully automated. This would save researchers valuable time and manpower in their experiments.

In Chapter 4, I describe the development of two workflows for the high-dimensional analyses that I used throughout the remainder of this thesis. This resource proved extremely valuable in identifying expression patterns across multiple proteins that were otherwise obscured by standard parametric analyses (eg. ANOVA, t-tests). Tissue preparations such as those outlined in chapter 3 simplified data acquisition, and when coupled with genomic assays or shotgun proteomics, large data sets are becoming commonplace for systems neuroscientists. Identifying patterns in high dimensional data sets is a challenge faced by many researchers. As such, Chapter 4 serves as a valuable tool for any neuroscientist with a multivariate data set who is having difficulties identifying patterns of change.

In the second part of this thesis (Chapter 5 and 6) I employed the data analyses outlined in Chapter 4. My protein analysis workflow has proven extremely useful in classifying plasticity phenotypes following various treatments for amblyopia, as well as in analyzing the course of human development. In Chapter 5 I used this pipeline to identify the plasticity phenotypes of reverse occlusion, the classic treatment for amblyopia therapy. I also identified synaptic changes following BD and BV, two of the modern approaches to treating amblyopia in animals. I identified the course of recovery in important synaptic proteins for restoring good BV. The plasticity phenotyping approach that I created was a novel and useful tool for understanding the complexity of experience-dependent plasticity. For example, the GluA2:GluN2A balance represented the balance between homeostatic and Hebbian plasticity, and we showed that this was crucial for good visual recovery. All of these findings offered much needed insight for the failures of RO as a treatment for amblyopia, and a potential explanation for the recent successes of binocular treatments.

In chapter 6 I employed a data-driven approach to quantifying a panel of 23 synaptic and non-neuronal proteins in the human visual cortex across development. The main finding from

this project was that human development proceeds through a series of 6 overlapping stages. The earliest and latest of these stages were discrete from neighbouring stages and showed the least amount of overlap with other stages. The intervening 4 stages had a high degree of overlap and contained samples with a protein signature that varied between the 4 stages. In particular, this explained the high variability often associated with young children and could explain the variable efficacy of amblyopia treatments in young children. My series of high-dimensional analyses allowed me to identify the proteins that drove the bulk of development in each of the stages. Finally, I identified a set of functional indices that identified potential targets for amblyopia therapy in the future. Unlike results following standard statistical analyses, the combination of clustering and phenotyping employed in this chapter captured the complexity of human brain changes across the lifespan.

7.2 Methodological Approach

There were several considerations associated with translation between animal models and human patients. The first is the use of proper animal models that share the amblyopia visual phenotype being measured. Non-human primates were an attractive animal model for studying amblyopia because of homologies between their visual system and humans, including the specialized retinal fovea, overlapping binocular visual fields, as well as the existence of primary and higher order visual cortical areas. However, some carnivores like the cat are even more attractive candidates for studying the development of amblyopia because they share many of these important qualities but are also less cost prohibitive. Importantly, cats have an area centralis that imbues them with specialized central vision, and cats demonstrate lasting visual deficits that resemble the human phenotype after early MD (Williams et al., 2015) and reverse occlusion (Murphy and Mitchell, 1986). Rodents on the other hand, score much worse on many visual abilities, including having low visual acuity compared to cats, monkeys and humans. Rodents also lack an area of specialized central vision and ocular dominance columns, which made direct comparison with the amblyopia phenotype difficult. Rodents do however, have cells in a binocular region of visual cortex, and these cells respond preferentially to one eye over the other and after MD there is an increase in the number of binocular cells that respond to the non-deprived eye (Dräger, 1978). Thanks to the compatibility of rodents with powerful tools that

manipulate genetics, rodents have been instrumental in identifying neurobiological mechanisms that initiate and terminate the visual CP (Hensch et al., 1998; Fagiolini et al., 2003; 2004). Together all of these animal models form the bridge for translation from molecular to behavioural amblyopia, and each has their own attractive qualities for comparing neuroplasticity mechanisms across species.

The second challenge was in employing a methodological approach that could map neuroplasticity changes following maladaptive cortical development across species. Measuring visual acuity was an obvious first choice, since this is an easily observable phenotype of amblyopia. As previously indicated, the various choices of animal model cover a wide range of visual acuities progressing from lower order mammals like rodents (grating acuity $\sim 1\text{c/deg}$) to excellent acuity in macaques (grating acuity $\sim 30\text{c/deg}$). Training animal models however, is time consuming, and it is notoriously difficult to restrict acuity changes to a specific mechanism or region of visual cortex.

Luckily, the neuroscientist molecular toolbox is expanding, and the advent of physiological probes that measure visually evoked post-synaptic currents and optical imaging of intrinsic signals have improved temporal and spatial resolution. Using these techniques scientists have identified expanded geniculo-cortical axon terminals (Antonini and Stryker, 1993; 1996), expanded dendritic spines and greater internalization of spines after MD (Mataga et al., 2004; Oray et al., 2004). Combining this increased resolution with the power of genetic manipulation in rodents even allows for advanced techniques like calcium responses of single cells in-vivo (e.g. Jaepel et al., 2017). However, recording physiological shifts in ocular dominance is not viable in humans. Furthermore, post-mortem anatomy is laborious and notoriously difficult in human tissues, thus rendering scaling across species of either physiological or anatomical investigations difficult.

In this thesis I chose to investigate synaptic proteins since they lay at the intersection between synaptic structure and function. There were many advantages to studying synaptic proteins. The foremost advantage was that synaptic proteins execute synaptic plasticity mechanisms, including ocular dominance plasticity. Secondly, most of these proteins could reliably be measured across many species, and they serve as good predictors of synaptic function

(eg. Quinlan et al., 1999b). The intersection between structural and physiological consequences of MD are the synaptic proteins that execute excitatory and inhibitory transmission in V1, mediated by activation of AMPAR, NMDAR and GABA_AR proteins, to name a few. Measuring the expression of these proteins remains one of the best alternatives to further our understanding of the mechanisms underlying amblyopia in both animal models and humans.

The third challenge was in aligning development across species. Typically, alignment is done by matching reproductive stages in each species. For aligning the development of the visual system, this was not the most useful tool considering differing lengths of gestation, age at eye-opening and other developmental differences between species. Next, one might choose the identification of the visual CP. In cats the window of susceptibility to the effects of early monocular deprivation identifies 4-6 weeks as the peak of the CP (Olson and Freeman, 1980). Visual milestones such as CP in animals, and the window of susceptibility to amblyopia in humans (Lewis and Maurer, 2005), provided comparable proxies for age alignment (Pinto et al., 2015). Recent efforts use multiple proxies for aligning neurodevelopment, including developmental milestones such as birth, gestation, eye opening, opening of CP and close of CP, as well as hundreds of other shared stages of neural development amongst higher mammals (Clancy et al., 2001; Workman et al., 2013). The issue with this approach was the assumption that a single age can be used to align the entirety of cortical development, across both cortical and subcortical structures. Within our own lab we have demonstrated different rates of cortical development for different regions in rats, monkeys and humans (Pinto et al., 2013; Williams et al., 2010). To further complicate the matter, there is a disconnect between the development of structure and function in human visual cortex. Anatomical milestones such as synapse density and horizontal connections quickly mature over the first few years of life (Huttenlocher et al., 1982; Burkhalter et al., 1993), but visual abilities take much longer (Lewis and Maurer, 2005; Owsley, 2011). Anatomical bases for translation are therefore not good proxies for interspecies comparison of the visual system, and developmental milestones are likely region-specific.

Therefore, an optimal approach to uncover the neural bases of amblyopia treatments, and to address transient recovery following treatment, had to address all three challenges outlined here. First, a suitable animal model must be used for making comparisons with human amblyopia. In

this thesis I present multiple analyses of the cat central visual pathway. Second, a method must be used that is scalable across species to humans. In this thesis I investigated synaptic protein expression using Western blotting since synaptic proteins could be quantified in both cat and human cortex. Third, a technique must be used that enables unbiased comparison across species. In chapter 4, I outline the series of high-dimensional analysis that combined many protein variables to define development of cat and human visual cortex based solely on proteins that govern ocular dominance plasticity.

7.3 Significance

New views of binocular treatment for amblyopia

The shortcomings of RO as a treatment for amblyopia have been a perplexing puzzle for clinicians and neuroscientists alike for a long while. Recently, this has prompted a shift in treatments towards binocular approaches (Birch, 2013). Even though this was not a new idea (Mitchell, 1991; Kind et al., 2002; Faulkner et al., 2006; Schwarzkopf et al., 2007), it has taken a while for this idea to permeate into testing new treatments in animal models of amblyopia. As an example, the recent success of dark exposure might seem like an attractive candidate treatment based on matched stimulation to both eyes (He et al., 2013; Duffy and Mitchell, 2013). The improvements after dark exposure however, only persist when accompanied by visual training paradigms, and practically speaking this is not easily adaptable for human trials. Instead, manipulating binocular visual experience by opening both eyes after treating amblyopia seems to be a more attractive alternative. Binocular treatments that provided matched stimulation to both eyes demonstrate acceptable acuity recovery (Hess et al., 2010; Knox et al., 2012; Kelly et al., 2018), and binocular perceptual learning has also seen success, even in adults (Levi and Li, 2009). Even animal models have shown acuity improvements following BV (Williams et al., 2015). The likely reason for the success of these treatments is that the good eye is able to adequately ‘teach’ the poor eye when provided enough stimulation.

The significance of the findings from my classification of plasticity phenotypes following recovery treatments for amblyopia (Chapter 5) suggest that the type of intervention after fixing the monocular occlusion in amblyopic children matters greatly, not only in the first few days, but

even the first few hours. Indeed, reports of improved recovery soon after cataract removal in young children suggest these first few days are crucial (Maurer, 1999). More importantly, my findings identify some of those important plasticity mechanisms employed during these early interval of BV (1hr - 4d), including the GluA2:GluN2A balance. We interpreted these results as a critical interplay between homeostatic and Hebbian plasticity mechanisms that take place immediately following removal of MD. By modelling the course of recovery using predicted receptor kinetics we identified a series of changes in the first 4d of BV that restored the synaptic environment of these animals to the peak of the CP. For example, the immediate response (hours) affected glutamatergic mechanisms and the delayed response (days) affected GABAergic mechanisms. Using this knowledge, we can begin to predict the impact of different treatments over these intervals, as well as the effect of instituting RO or BD. This is important since future behavioural interventions will likely require some combination of BV+RO or BV+BD.

Secondly, my analysis in chapters 4 and 5 provided a system-level analysis across multiple plasticity mechanisms. This analysis was instrumental in the suggested explanations for the failures of treatments that have provided only temporary recovery from the effects of MD, including RO and BD. RO employs temporary AMPAR-dominated homeostatic recovery mechanisms while BD causes premature, regional shifts in GABAergic mechanisms. High dimensional analyses such as these are clearly very powerful for identifying system effects that have otherwise been missed with uni-dimensional comparisons.

Stages of human development

My analysis of human visual cortical development supported the fundamental shift in the way neuroscientist are thinking about neurodevelopment. Standard analyses process data into age bins of development (e.g. Siu et al., 2017) or use linear models to track the course of human development (e.g. Miller et al., 2012). Neither approach is incorrect, but they both omit a large amount of information in the data by restricting data to one class or another. Instead, in Chapter 6, I analyzed the data across all protein dimensions at once and used high-dimensional clustering to identify similarity among the samples based on the underlying patterns in the network of protein expression. This approach revealed a series of 6 stages of human development, similar to

the ones explained in Siu et al., 2017, except that these stages were not heterogenous, and demonstrate a fair degree of developmental overlap.

Early and late stages of human development were relatively homogeneous and did not overlap with neighbouring developmental states. Conversely, the 4 middle stages represented a succession of overlapping phenotypes. Together these findings demonstrated that the human lifespan was marked by expression of a set of key proteins early and late in development, but during the middle stages protein expression was more heterogeneous. The plasticity phenotypes were useful for identifying significant plasticity features that defined each of these stages.

The notion of brain states have been found to influence everything from visual processing (Reynolds and Chelazzi, 2004) to the balance between excitation and inhibition in the cortex (Zhou et al., 2014). If deviations to different states occurred on a temporally finite scale, such as over the course of a few months or years, it is not surprising that when examining expression of individual proteins in children we identified states of high and low inter-individual variability in post-mortem human visual cortex (Pinto et al., 2010; Siu et al., 2015; 2017). Time and again our lab has identified this period of high variability early in development, and it is sometimes difficult to reconcile with the high reliability of our protein assays. I have shown that this variability originates from multiple overlapping plasticity phenotypes that complement the standard age-binning approach to analyzing human brain development.

In early developing human cortex, before childhood and adolescence, there is high correspondence between cortical gene expression and protein levels (Beveridge et al., 2014, Breen et al., 2018), meaning that fluctuations in RNA and protein expression are well conserved in response to environmental changes. I proposed that this variability might explain the difficulty in providing lasting recovery to amblyopic children through patching therapy, since the cortex of young children can exist in any of the 4 overlapping states that we identified. I proposed future treatment strategies should target *multiple* plasticity mechanisms in order to correct as many immature or premature plasticity features as possible, similar to the combined treatment strategies tested in animal models (Faulkner et al., 2006). As previously discussed, I also propose combined administration of different visual manipulations, however they should focus on

matched binocular experience (e.g. BD + BV), since only these manipulations correct plasticity features to normal developmental levels in animal models.

I also identify a period of regression to juvenile forms of plasticity in late adulthood. I showed this by the regressions of the Integrin:GFAP and Classic-MBP:Golli-MBP indices toward the immature GFAP and Golli-MBP, respectively. This might represent a period of rejuvenation where the cortex is once again susceptible to experience-dependent changes, but cannot compensate for these changes, supported by the notion that there is decreased correlation between RNA and protein levels in aging (Beveridge et al., 2014, Breen et al., 2018). Instead, I propose that the cortex compensates by shifting the immune system into a protective state that favors glial proteins (GFAP) and other immune interactions (Golli-MBP). This offers a message of hope for rescuing the declining acuity in old age. Since other plasticity mechanisms, such as the GluN2A:GluN2B balance also shift toward a more juvenile-like state in aging, these findings offer a cautionary tale in that even brief visual insult (e.g. the formation of cataracts) could cause lasting and damaging changes.

7.4 Future Directions

Animal models

There are many future directions for this work, not the least of which involves an extension of the treatment paradigms for amblyopia therapies. Due to the restraints imposed by the size of cat litters, we were only able to test a certain number of intervention lengths. For example the reverse occlusion length (18 days) was chosen as the optimal amount of RO because it provides the most recovery from the physiological effects of MD (Movshon, 1976a). However, just as we tested various intervals of treatment for MD (Beston et al., 2010) and BV (Chapter 5) in order to track the progression of recovery, so too should RO be tested across a range of intervals. Binocular deprivation should also be tested across a range of intervals, but this intervention should be modified to test the effect of dark rearing, since there are subtle differences in the amount of recovery noted for the difference between complete darkness and eyelid closure (Duffy et al., 2015). Examining the time-course of recovery would pinpoint the exact molecular changes that occur after RO and BD.

It would also be interesting to confirm the predicted receptor decay kinetics suggested by my models. Recording electrical activity in cat V1 has been used since Hubel and Wiesel identified the effects of MD on cortical neurons. Now the relative contributions of AMPA, NMDA and GABA_A receptors can be reliably separated and quantified (Monyer et al., 1994; Flint et al., 1997). It would be useful to measure the changes in receptor kinetics in response to the various treatments for amblyopia examined in Chapter 5. This would not only confirm the physiological impact of each treatment on cortical function, but also confirm the utility of my model in extending quantifications of protein expression to actual synaptic function.

I would also suggest that combined amblyopia treatments be examined, similar to how reverse occlusion and binocular experience were used to identify the benefits of BV for good recovery (Faulkner et al., 2006), or how binocular training and patching therapy have been used in conjunction to promote good recovery from amblyopia (Li et al., 2013). Since we identified robust treatment effects for RO in the predicted kinetics of the system, it is feasible to use the blueprint for recovery after BV to design and administer RO after different amounts of BV to directly target CP-like plasticity. More specifically, we suggest that a few hours or days of dark exposure can rescue the effects of RO and BD by targeting multiple plasticity mechanisms that become shifted to an abnormal state after these treatments.

Translating Animal findings to humans

An avenue for translation between animal models of amblyopia and understanding human cortical development is to compare the protein expression in developing cats with expression of the same proteins in developing humans. It is essential to understand the normal course of development in animal models as well as in humans so that effective translation can take place. To address this question, I would first identify which proteins and plasticity features undergo similar developmental changes between species. Then combining this information with my recent observations of the effects of different treatment paradigms in cats, I could use this information to more accurately guide future amblyopia treatments. For example, creating a correlation matrix between the two data sets (cats and humans) would identify which proteins covary across development. Second, performing high-dimensional clustering techniques such as those outlined in Chapter 4 would reveal shared developmental stages between the two species. Using these two

approaches I could identify which stages across development share underlying patterns in protein expression. Finally, I would use PCA to identify biological features of interest and I could compare plasticity phenotypes across both species. Together, these analyses would reveal any plasticity mechanisms that are preserved across development in both species, similar to the techniques outlined in Luo et al., 2017.

Human neurobiology

The work presented here quantifying the panel of proteins in human visual cortex represents over a decade of careful tissue collection, processing and analysis. It is important to not only verify the trajectories demonstrated by each protein, but also to expand this collection to include all proteins involved in visual system plasticity. Unpublished observations from our lab has corroborated the expression patterns of many of the proteins in Chapter 6 in a separate data set of gene expression in human visual cortex collected by the Allen brain institute (<http://portal.brain-map.org/>). This data set contains many more genes of interest, and it would be extremely valuable to map the development of human V1, and other cortical areas, to better understand human development.

A common critique of the variability in our young samples might be that the variability is a result of measurement error or low sample size. I examined the idea of measurement error in my previous publication measuring inter-individual variability using an antibody against two protein isoforms of MBP (Classic and Golli) (Siu et al., 2015). In that study, only one protein isoform demonstrates a wave of early variability, while the other remains constant. Since both isoforms were detected with the same antibody, that control demonstrated the reliability of the inter-individual variability. Furthermore, Pinto et al. (2015) analyzed anchoring proteins for excitatory and inhibitory receptors (PSD95 and Gephyrin) in the same set of samples, and identified two different waves on heterogeneity. Notwithstanding these findings, increasing the number of samples would help address any concerns over sample variability, as well as provide more data for parsing the 6 developmental stages.

Human amblyopia therapy

It is clear that a powerful approach to treating amblyopia is visual manipulations and binocular vision. However there is still a disconnect in our understanding of the neurobiological mechanisms that give rise to amblyopia and how they change during treatment. This is valuable information that can first be discovered and tested in animal models (Chapter 5) and then should be translated to human therapies.

It would also be beneficial to see more biologically inspired therapies make it to clinical trials. The evidence is growing for pharmaceutical interventions for amblyopia. Many new approaches are uncovering potential targets to reinstate CP-plasticity (e.g. Shepherd and Bear, 2011). However, the gap between animal findings and human trials will persist unless these interventions are tested in suitable animal models and tested in a manner that can be adapted for use in humans. This disconnect between behavioural and pharmaceutical interventions is beneficial for pushing our understanding of the visual system, but it continues to create a further divide between possible treatments.

Utilizing analyses such as the ones implemented in my thesis enables personalized medicine for amblyopia patients and aging individuals. Performing assays of cortical protein expression gives an estimate of the plasticity state in an individual. Comparing these against the course of normal development could give an indication of the errors that exist in an amblyopic or aging visual system, and would limit the search for treatment to a subset of plasticity features.

References

- Agetsuma M, Hamm JP, Tao K, Fujisawa S, Yuste R (2018) Parvalbumin-Positive Interneurons Regulate Neuronal Ensembles in Visual Cortex. *Cereb Cortex* 28:1831–1845.
- Anderson PA, Olavarria J, Van Sluyters RC (1988) The overall pattern of ocular dominance bands in cat visual cortex. *Journal of Neuroscience* 8:2183–2200.
- Antonini A, Fagiolini M, Stryker MP (1999) Anatomical correlates of functional plasticity in mouse visual cortex. *J Neurosci* 19:4388–4406.
- Antonini A, Gillespie DC, Crair MC, Stryker MP (1998) Morphology of single geniculocortical afferents and functional recovery of the visual cortex after reverse monocular deprivation in the kitten. *Journal of Neuroscience* 18:9896–9909.
- Antonini A, Stryker MP (1993) Rapid remodeling of axonal arbors in the visual cortex. *Science* 260:1819–1821.
- Antonini A, Stryker MP (1996) Plasticity of geniculocortical afferents following brief or prolonged monocular occlusion in the cat. *J Comp Neurol* 369:64–82.
- Bavelier D, Levi DM, Li RW, Dan Y, Hensch TK (2010) Removing Brakes on Adult Brain Plasticity: From Molecular to Behavioral Interventions. *Journal of Neuroscience* 30:14964–14971.
- Bear MF, Kleinschmidt A, Gu QA, Singer W (1990) Disruption of experience-dependent synaptic modifications in striate cortex by infusion of an NMDA receptor antagonist. *Journal of Neuroscience* 10:909–925.
- Beattie EC, Stellwagen D, Morishita W, Bresnahan JC, Ha BK, Zastrow Von M, Beattie MS, Malenka RC (2002) Control of synaptic strength by glial TNFalpha. *Science* 295:2282–2285.
- Beston BR, Jones DG, Murphy KM (2010) Experience-dependent changes in excitatory and inhibitory receptor subunit expression in visual cortex. *Front Synaptic Neurosci* 2:138.
- Beveridge, N. J., Santarelli, D. M., Wang, X., Tooney, P. A., Webster, M. J., Weickert, C. S., & Cairns, M. J. (2013). Maturation of the human dorsolateral prefrontal cortex coincides with a dynamic shift in microRNA expression. *Schizophrenia bulletin*, 40(2), 399-409.
- Bhola R, Keech RV, Kutschke P, Pfeifer W, Scott WE (2006) Recurrence of amblyopia after occlusion therapy. *Ophthalmology* 113:2097–2100.
- Birch EE (2013) Progress in Retinal and Eye Research. *Progress in Retinal and Eye Research* 33:67–84.
- Birch EE, Holmes JM (2010) The clinical profile of amblyopia in children younger than 3 years of age. *J AAPOS* 14:494–497.
- Birch EE, Li SL, Jost RM, Morale SE, La Cruz De A, Stager D, Dao L, Stager DR (2015) Binocular iPad treatment for amblyopia in preschool children. *J AAPOS* 19:6–11.

- Birch EE, Stager DR Sr. (2006) Long-Term Motor and Sensory Outcomes After Early Surgery for Infantile Esotropia. *Journal of American Association for Pediatric Ophthalmology and Strabismus* 10:409–413.
- Birch EE, Stager DR Sr., Berry P, Leffler J (2004) Stereopsis and long-term stability of alignment in esotropia. *Journal of AAPOS* 8:146–150.
- Blakemore C, Van Sluyters RC (1974) Reversal of the physiological effects of monocular deprivation in kittens: further evidence for a sensitive period. *The Journal of Physiology* 237:195–216.
- Blakemore, C. O. L. I. N., Garey, L. J., & Vital-Durand, F. (1978). The physiological effects of monocular deprivation and their reversal in the monkey's visual cortex. *The Journal of Physiology*, 283(1), 223-262.
- Bonnert TP, McKernan RM, Farrar S, le Bourdellès B, Heavens RP, Smith DW, Hewson L, Rigby MR, Sirinathsinghji DJ, Brown N, Wafford KA, Whiting PJ (1999) theta, a novel gamma-aminobutyric acid type A receptor subunit. *Proc Natl Acad Sci USA* 96:9891–9896.
- Bosman, L. W., Rosahl, T. W., & Brussaard, A. B. (2002). Neonatal development of the rat visual cortex: synaptic function of GABAA receptor α subunits. *The Journal of physiology*, 545(1), 169-181.
- Bowering ER, Maurer D, Lewis TL, Brent HP (1993) Sensitivity in the nasal and temporal hemifields in children treated for cataract. *Invest Ophthalmol Vis Sci* 34:3501–3509.
- Bowering ER, Maurer D, Lewis TL, Brent HP (1997) Constriction of the visual field of children after early visual deprivation. *J Pediatr Ophthalmol Strabismus* 34:347–356.
- Breen, M. S., Ozcan, S., Ramsey, J. M., Wang, Z., Ma'ayan, A., Rustogi, N., ... & Bahn, S. (2018). Temporal proteomic profiling of postnatal human cortical development. *Translational psychiatry*, 8(1), 267.
- Briggs F, Kiley CW, Callaway EM, Usrey WM (2016) Morphological Substrates for Parallel Streams of Corticogeniculate Feedback Originating in Both V1 and V2 of the Macaque Monkey. *Neuron* 90:388–399.
- Burkhalter A, Bernardo KL, Charles V (1993) Development of local circuits in human visual cortex. *Journal of Neuroscience* 13:1916–1931.
- Cabungcal J-H, Steullet P, Kraftsik R, Cuenod M, Do KQ (2013a) Early-life insults impair parvalbumin interneurons via oxidative stress: reversal by N-acetylcysteine. *Biological Psychiatry* 73:574–582.
- Cabungcal J-H, Steullet P, Morishita H, Kraftsik R, Cuenod M, Hensch TK, Do KQ (2013b) Perineuronal nets protect fast-spiking interneurons against oxidative stress. *Proc Natl Acad Sci USA* 110:9130–9135.
- Carmignoto, G., & Vicini, S. (1992). Activity-dependent decrease in NMDA receptor responses during development of the visual cortex. *Science*, 258(5084), 1007-1011.

- Cardin JA, Carlén M, Meletis K, Knoblich U, Zhang F, Deisseroth K, Tsai L-H, Moore CI (2009) Driving fast-spiking cells induces gamma rhythm and controls sensory responses. *Nature* 459:663–667.
- Carulli D, Pizzorusso T, Kwok JCF, Putignano E, Poli A, Forostyak S, Andrews MR, Deepa SS, Glant TT, Fawcett JW (2010) Animals lacking link protein have attenuated perineuronal nets and persistent plasticity. *Brain* 133:2331–2347.
- Casagrande VA (1994) A third parallel visual pathway to primate area V1. *Trends Neurosci* 17:305–310.
- Casagrande VA, Diamond IT (1974) Ablation study of the superior colliculus in the tree shrew (*Tupaia glis*). *J Comp Neurol* 156:207–237.
- Casagrande VA, Harting JK, Hall WC, Diamond IT, Martin GF (1972) Superior colliculus of the tree shrew: a structural and functional subdivision into superficial and deep layers. *Science* 177:444–447.
- Casagrande VA, Yazar F, Jones KD, Ding Y (2007) The morphology of the koniocellular axon pathway in the macaque monkey. *Cereb Cortex* 17:2334–2345.
- Chatterjee S, Callaway EM (2003) Parallel colour-opponent pathways to primary visual cortex. *Nature* 426:668–671.
- Chen WS, Bear MF (2007) Activity-dependent regulation of NR2B translation contributes to metaplasticity in mouse visual cortex. *Neuropharmacology* 52:200–214.
- Chen, L., Yang, C., & Mower, G. D. (2001). Developmental changes in the expression of GABAA receptor subunits ($\alpha 1$, $\alpha 2$, $\alpha 3$) in the cat visual cortex and the effects of dark rearing. *Molecular brain research*, 88(1-2), 135-143.
- Choong YF, Lukman H, Martin S, Laws DE (2004) Childhood amblyopia treatment: psychosocial implications for patients and primary carers. *Eye* 18:369–375.
- Chua B, Mitchell P (2004) Consequences of amblyopia on education, occupation, and long term vision loss. *Br J Ophthalmol* 88:1119–1121.
- Clancy B, Darlington RB, Finlay BL (2001) Translating developmental time across mammalian species. *NEUROSCIENCE* 105:7–17.
- Cleland BG, Harding TH, Tulunay-Keesey U (1979) Visual resolution and receptive field size: examination of two kinds of cat retinal ganglion cell. *Science* 205:1015–1017.
- Conley M, Fitzpatrick D (1989) Morphology of retinogeniculate axons in the macaque. *Vis Neurosci* 2:287–296.
- Cooper LN, Bear MF (2012) The BCM theory of synapse modification at 30: interaction of theory with experiment. *Nat Rev Neurosci* 13:798–810.
- Crair MC, Ruthazer ES, Gillespie DC, Stryker MP (1997) Relationship between the ocular dominance and orientation maps in visual cortex of monocularly deprived cats. *Neuron* 19:307–318.

- Curcio CA, Sloan KR, Kalina RE, Hendrickson AE (1990) Human photoreceptor topography. *J Comp Neurol* 292:497–523.
- Cynader M, Berman N (1972) Receptive-field organization of monkey superior colliculus. *J Neurophysiol* 35:187–201.
- Daw NW (1998) Critical Periods and Amblyopia. *Arch Ophthalmol* 116:502–505.
- del Río MR, DeFelipe J (1994) A study of SMI 32-stained pyramidal cells, parvalbumin-immunoreactive chandelier cells, and presumptive thalamocortical axons in the human temporal neocortex. *J Comp Neurol*.
- Derrington, A. M., Krauskopf, J., & Lennie, P. (1984). Chromatic mechanisms in lateral geniculate nucleus of macaque. *The Journal of physiology*, 357(1), 241-265.
- Dews PB, Wiesel TN (1970) Consequences of monocular deprivation on visual behaviour in kittens. *The Journal of Physiology* 206:437–455.
- Dityatev A, Schachner M, Sonderegger P (2010) The dual role of the extracellular matrix in synaptic plasticity and homeostasis. *Nat Rev Neurosci* 11:735–746.
- Djurisic M, Vidal GS, Mann M, Aharon A, Kim T, Ferrao Santos A, Zuo Y, Hübener M, Shatz CJ (2013) PirB regulates a structural substrate for cortical plasticity. *Proc Natl Acad Sci USA* 110:20771–20776.
- Dräger UC (1978) Observations on monocular deprivation in mice. *J Neurophysiol* 41:28–42.
- Duffy KR, Bukhamseen DH, Smithen MJ, Mitchell DE (2015) Binocular eyelid closure promotes anatomical but not behavioral recovery from monocular deprivation. *Vision Research* 114:151–160.
- Duffy KR, Fong M-F, Mitchell DE, Bear MF (2018) Recovery from the anatomical effects of long-term monocular deprivation in cat lateral geniculate nucleus. *J Comp Neurol* 526:310–323.
- Duffy KR, Mitchell DE (2013) Darkness Alters Maturation of Visual Cortex and Promotes Fast Recovery from Monocular Deprivation. *CURBIO* 23:382–386.
- Eaton NC, Sheehan HM, Quinlan EM (2016) Optimization of visual training for full recovery from severe amblyopia in adults. *Learn Mem* 23:99–103.
- Ellemberg D, Lewis TL, Maurer D, Brent HP (2000) Influence of monocular deprivation during infancy on the later development of spatial and temporal vision. *Vision Research* 40:3283–3295.
- Erikson EH (1959) Identity and the life cycle: Selected papers.
- Erreger K, Dravid SM, Banke TG, Wyllie DJA, Traynelis SF (2005) Subunit-specific gating controls rat NR1/NR2A and NR1/NR2B NMDA channel kinetics and synaptic signalling profiles. *The Journal of Physiology* 563:345–358.

- Eyre MD, Renzi M, Farrant M, Nusser Z (2012) Setting the time course of inhibitory synaptic currents by mixing multiple GABA(A) receptor α subunit isoforms. *J Neurosci* 32:5853–5867.
- Fagiolini, M., & Hensch, T. K. (2000). Inhibitory threshold for critical-period activation in primary visual cortex. *Nature*, 404(6774), 183.
- Fagiolini M, Fritschy J-M, Löw K, Möhler H, Rudolph U, Hensch TK (2004) Specific GABAA circuits for visual cortical plasticity. *Science* 303:1681–1683.
- Fagiolini M, Katagiri H, Miyamoto H, Mori H, Grant SGN, Mishina M, Hensch TK (2003) Separable features of visual cortical plasticity revealed by N-methyl-D-aspartate receptor 2A signaling. *Proc Natl Acad Sci USA* 100:2854–2859.
- Faulkner SD, Vorobyov V, Sengpiel F (2006) Visual Cortical Recovery From Reverse Occlusion Depends on Concordant Binocular Experience. *J Neurophysiol* 95:1718–1726.
- Flint AC, Maisch US, Weishaupt JH, Kriegstein AR, Monyer H (1997) NR2A subunit expression shortens NMDA receptor synaptic currents in developing neocortex. *Journal of Neuroscience* 17:2469–2476.
- Freeman RD, Olson C (1982) Brief periods of monocular deprivation in kittens: effects of delay prior to physiological study. *J Neurophysiol* 47:139–150.
- Friedman DS, Repka MX, Katz J, Giordano L, Ibrionke J, Hawse P, Tielsch JM (2009) Prevalence of amblyopia and strabismus in white and African American children aged 6 through 71 months the Baltimore Pediatric Eye Disease Study. *Ophthalmology* 116:2128–34.e1–2.
- Gainey MA, Hurvitz-Wolff JR, Lambo ME, Turrigiano GG (2009) Synaptic scaling requires the GluR2 subunit of the AMPA receptor. *J Neurosci* 29:6479–6489.
- Gandhi NJ, Katnani HA (2011) Motor functions of the superior colliculus. *Annu Rev Neurosci* 34:205–231.
- Gao TY et al. (2018) Effectiveness of a Binocular Video Game vs Placebo Video Game for Improving Visual Functions in Older Children, Teenagers, and Adults With Amblyopia: A Randomized Clinical Trial. *JAMA Ophthalmol* 136:172–181.
- Giffin F, Mitchell DE (1978) The rate of recovery of vision after early monocular deprivation in kittens. *The Journal of Physiology* 274:511–537.
- Gingrich KJ, Roberts WA, Kass RS (1995) Dependence of the GABAA receptor gating kinetics on the alpha-subunit isoform: implications for structure-function relations and synaptic transmission. *The Journal of Physiology* 489 (Pt 2):529–543.
- Gordon, J. A., & Stryker, M. P. (1996). Experience-dependent plasticity of binocular responses in the primary visual cortex of the mouse. *Journal of Neuroscience*, 16(10), 3274-3286.
- Grafstein, B. (1971). Transneuronal transfer of radioactivity in the central nervous system. *Science*, 172(3979), 177-179.

- Grant S, Moseley MJ (2011) Amblyopia and Real-World Visuomotor Tasks. *Strabismus* 19:119–128.
- Graybiel, A. M. (1975). Anatomical organization of retinotectal afferents in the cat: An autodiographic study. *Brain Research*, 96(1), 1-23.
- Greifzu, F., Pielecka-Fortuna, J., Kalogeraki, E., Krempler, K., Favaro, P. D., Schlüter, O. M., & Löwel, S. (2014). Environmental enrichment extends ocular dominance plasticity into adulthood and protects from stroke-induced impairments of plasticity. *Proceedings of the National Academy of Sciences*, 111(3), 1150-1155.
- Gu QA, Bear MF, Singer W (1989) Blockade of NMDA-receptors prevents ocularity changes in kitten visual cortex after reversed monocular deprivation. *Brain Res Dev Brain Res* 47:281–288.
- Guillery RW, Kaas JH (1971) A study of normal and congenitally abnormal retinogeniculate projections in cats. *J Comp Neurol* 143:73–100.
- Guillery RW, Sherman SM (2002) Thalamic relay functions and their role in corticocortical communication: generalizations from the visual system. *Neuron* 33:163–175.
- Gunton KB (2013) Advances in amblyopia: what have we learned from PEDIG trials? *Pediatrics* 131:540–547.
- Hamos, J. E., Van Horn, S. C., Raczkowski, D., & Sherman, S. M. (1987). Synaptic circuits involving an individual retinogeniculate axon in the cat. *Journal of Comparative Neurology*, 259(2), 165-192.
- Harting JK, Hall WC, Diamond IT, Martin GF (1973) Anterograde degeneration study of the superior colliculus in *Tupaia glis*: evidence for a subdivision between superficial and deep layers. *J Comp Neurol* 148:361–386.
- Hartshorne JK, Germine LT (2015) When Does Cognitive Functioning Peak? The Asynchronous Rise and Fall of Different Cognitive Abilities Across the Life Span. *Psychol Sci* 26:433–443.
- He H-Y, Hodos W, Quinlan EM (2006) Visual deprivation reactivates rapid ocular dominance plasticity in adult visual cortex. *J Neurosci* 26:2951–2955.
- Hendrickson A, March D, Richards G, Erickson A, Shaw C (1994) Coincidental appearance of the alpha 1 subunit of the GABA-A receptor and the type I benzodiazepine receptor near birth in macaque monkey visual cortex. *Int J Dev Neurosci* 12:299–314.
- Hendrickson A, Wilson ME, Toyne MJ (1970) The distribution of optic nerve fibers in *Macaca mulatta*. *Brain Res* 23:425–427.
- Hendry SH, Huntsman MM, Viñuela A, Möhler H, de Blas AL, Jones EG (1994) GABAA receptor subunit immunoreactivity in primate visual cortex: distribution in macaques and humans and regulation by visual input in adulthood. *Journal of Neuroscience* 14:2383–2401.

- Hendry SH, Reid RC (2000) The koniocellular pathway in primate vision. *Annu Rev Neurosci* 23:127–153.
- Hendry SH, Yoshioka T (1994) A neurochemically distinct third channel in the macaque dorsal lateral geniculate nucleus. *Science* 264:575–577.
- Hensch, T. K., Fagiolini, M., Mataga, N., Stryker, M. P., Baekkeskov, S., & Kash, S. F. (1998). Local GABA circuit control of experience-dependent plasticity in developing visual cortex. *Science*, 282(5).
- Hensch TK, Quinlan EM (2018) Critical periods in amblyopia. *Vis Neurosci* 35:E014.
- Herrmann K (1996) Differential distribution of AMPA receptors and glutamate during pre- and postnatal development in the visual cortex of ferrets. *J Comp Neurol* 375:1–17.
- Hess RF, Mansouri B, Thompson B (2010) A new binocular approach to the treatment of amblyopia in adults well beyond the critical period of visual development. *Restor Neurol Neurosci* 28:793–802.
- Hess RF, Mansouri B, Thompson B (2011) Restoration of binocular vision in amblyopia. *Strabismus* 19:110–118.
- Hess RF, Pointer JS (1985) Differences in the neural basis of human amblyopia: the distribution of the anomaly across the visual field. *Vision Research* 25:1577–1594.
- Hess RF, Thompson B (2015) Amblyopia and the binocular approach to its therapy. *Vision Research* 114:4–16.
- Heynen AJ, Yoon B-J, Liu C-H, Chung HJ, Haganir RL, Bear MF (2003) Molecular mechanism for loss of visual cortical responsiveness following brief monocular deprivation. *Nature Publishing Group* 6:854–862.
- Hollmann M, Hartley M, Heinemann S (1991) Ca²⁺ permeability of KA-AMPA-gated glutamate receptor channels depends on subunit composition. *Science* 252:851–853.
- Holmes JM (2018) Lessons From Recent Randomized Clinical Trials of Binocular Treatment for Amblyopia. *JAMA Ophthalmol* 136:181–183.
- Holmes JM, Beck RW, Kraker RT, Astle WF, Birch EE, Cole SR, Cotter SA, Donahue S, Everett DF, Hertle RW, Keech RV, Paysse E, Quinn GF, Repka MX, Scheiman MM, Pediatric Eye Disease Investigator Group (2004) Risk of amblyopia recurrence after cessation of treatment. *Journal of AAPOS* 8:420–428.
- Holmes JM, Beck RW, Kraker RT, Cole SR, Repka MX, Birch EE, Felius J, Christiansen SP, Coats DK, Kulp MT, Pediatric Eye Disease Investigator Group (2003a) Impact of patching and atropine treatment on the child and family in the amblyopia treatment study. *Arch Ophthalmol* 121:1625–1632.
- Holmes JM, Kraker RT, Beck RW, Birch EE, Cotter SA, Everett DF, Hertle RW, Quinn GE, Repka MX, Scheiman MM, Wallace DK, Pediatric Eye Disease Investigator Group (2003b) A randomized trial of prescribed patching regimens for treatment of severe amblyopia in children. *Ophthalmology* 110:2075–2087.

- Holmes JM, Manh VM, Lazar EL, Beck RW, Birch EE, Kraker RT, Crouch ER, Erzurum SA, Khuddus N, Summers AI, Wallace DK, Pediatric Eye Disease Investigator Group (2016) Effect of a Binocular iPad Game vs Part-time Patching in Children Aged 5 to 12 Years With Amblyopia: A Randomized Clinical Trial. *JAMA Ophthalmol* 134:1391–1400.
- Hu F, Strittmatter SM (2004) Regulating axon growth within the postnatal central nervous system. *Semin Perinatol* 28:371–378.
- Hubel DH, LeVay S, Wiesel TN (1975) Mode of termination of retinotectal fibers in macaque monkey: an autoradiographic study. *Brain Res* 96:25–40.
- Hubel, D. H., & Wiesel, T. N. (1962). Receptive fields, binocular interaction and functional architecture in the cat's visual cortex. *The Journal of physiology*, 160(1), 106-154.
- Hubel DH, Wiesel TN (1970) The period of susceptibility to the physiological effects of unilateral eye closure in kittens. *The Journal of Physiology* 206:419–436.
- Huttenlocher, P. R., de Courten, C., Garey, L. J., & Van der Loos, H. (1982). Synaptogenesis in human visual cortex—evidence for synapse elimination during normal development. *Neuroscience letters*, 33(3), 247-252.
- Illing RB (1989) The mosaic of the uncrossed retinal projection in the superior colliculus of the cat. *Exp Brain Res* 74:641–644.
- Jacobs GH (2008) Primate color vision: a comparative perspective. *Vis Neurosci* 25:619–633.
- Jaepel J, Hübener M, Bonhoeffer T, Rose T (2017) Lateral geniculate neurons projecting to primary visual cortex show ocular dominance plasticity in adult mice. *Nature Publishing Group* 20:1708–1714.
- Jones MW, French PJ, Bliss TV, Rosenblum K (1999) Molecular mechanisms of long-term potentiation in the insular cortex in vivo. *J Neurosci* 19:RC36.
- Jones, K. R., Spear, P. D., & Tong, L. I. L. L. I. A. N. (1984). Critical periods for effects of monocular deprivation: differences between striate and extrastriate cortex. *Journal of Neuroscience*, 4(10), 2543-2552.
- Kaas JH, Harting JK, Guillery RW (1974) Representation of the complete retina in the contralateral superior colliculus of some mammals. *Brain Res* 65:343–346.
- Kaas JH, Huerta MF, Weber JT, Harting JK (1978) Patterns of retinal terminations and laminar organization of the lateral geniculate nucleus of primates. *J Comp Neurol* 182:517–553.
- Kaneko M, Stellwagen D, Malenka RC, Stryker MP (2008) Tumor Necrosis Factor- α Mediates One Component of Competitive, Experience-Dependent Plasticity in Developing Visual Cortex. *Neuron* 58:673–680.
- Kaplan E, Shapley RM (1986) The primate retina contains two types of ganglion cells, with high and low contrast sensitivity. *Proc Natl Acad Sci USA* 83:2755–2757.
- Kelly KR, Jost RM, Dao L, Beauchamp CL, Leffler JN, Birch EE (2016) Binocular iPad Game vs Patching for Treatment of Amblyopia in Children: A Randomized Clinical Trial. *JAMA Ophthalmol* 134:1402–1408.

- Kelly KR, Jost RM, La Cruz De A, Birch EE (2015) Amblyopic children read more slowly than controls under natural, binocular reading conditions. *Journal of AAPOS* 19:515–520.
- Kelly KR, Jost RM, Wang Y-Z, Dao L, Beauchamp CL, Leffler JN, Birch EE (2018) Improved Binocular Outcomes Following Binocular Treatment for Childhood Amblyopia. *Invest Ophthalmol Vis Sci* 59:1221–1228.
- Kind PC, Mitchell DE, Ahmed B, Blakemore C, Bonhoeffer T, Sengpiel F (2002) Correlated binocular activity guides recovery from monocular deprivation. *Nature* 416:430–433.
- Kirkwood A, Bear MF (1994a) Hebbian synapses in visual cortex. *Journal of Neuroscience* 14:1634–1645.
- Kirkwood A, Bear MF (1994b) Homosynaptic long-term depression in the visual cortex. *Journal of Neuroscience* 14:3404–3412.
- Klein C, Evrard HC, Shapcott KA, Haverkamp S, Logothetis NK, Schmid MC (2016) Cell-Targeted Optogenetics and Electrical Microstimulation Reveal the Primate Koniocellular Projection to Supra-granular Visual Cortex. *Neuron* 90:143–151.
- Kleinschmidt, A., Bear, M. F., & Singer, W. (1987). Blockade of "NMDA" receptors disrupts experience-dependent plasticity of kitten striate cortex. *Science*, 238(4825), 355-358.
- Kleppe, I. C., & Robinson, H. P. (1999). Determining the activation time course of synaptic AMPA receptors from openings of colocalized NMDA receptors. *Biophysical journal*, 77(3), 1418-1427.
- Knox PJ, Simmers AJ, Gray LS, Cleary M (2012) An exploratory study: prolonged periods of binocular stimulation can provide an effective treatment for childhood amblyopia. *Invest Ophthalmol Vis Sci* 53:817–824.
- Kovács I, Kozma P, Fehér Á, Benedek G (1999) Late maturation of visual spatial integration in humans. *Proc Natl Acad Sci USA* 96:12204–12209.
- Kuffler SW (1953) Discharge patterns and functional organization of mammalian retina. *J Neurophysiol* 16:37–68.
- Lambo ME, Turrigiano GG (2013) Synaptic and Intrinsic Homeostatic Mechanisms Cooperate to Increase L2/3 Pyramidal Neuron Excitability during a Late Phase of Critical Period Plasticity. *Journal of Neuroscience* 33:8810–8819.
- Lane RH, Allman JM, Kaas JH (1971) Representation of the visual field in the superior colliculus of the grey squirrel (*Sciurus carolinensis*) and the tree shrew (*Tupaia glis*). *Brain Res* 26:277–292.
- Lee BB, Virsu V, Creutzfeldt OD (1983) Linear signal transmission from prepotentials to cells in the macaque lateral geniculate nucleus. *Exp Brain Res* 52:50–56.
- LeVay, S., Stryker, M. P., & Shatz, C. J. (1978). Ocular dominance columns and their development in layer IV of the cat's visual cortex: a quantitative study. *Journal of Comparative Neurology*, 179(1), 223-244.

- Levi DM, Li RW (2009) Perceptual learning as a potential treatment for amblyopia: A mini-review. *Vision Research* 49:2535–2549.
- Levi DM, Polat U (2005) Neural plasticity in adults with amblyopia. *Proc Natl Acad Sci USA* 93:1–5.
- Levi DM, Polat U, Hu YS (1997) Improvement in Vernier acuity in adults with amblyopia. Practice makes better. *Invest Ophthalmol Vis Sci* 38:1493–1510.
- Lewis TL, Maurer D (2005) Multiple sensitive periods in human visual development: Evidence from visually deprived children. *Dev Psychobiol* 46:163–183.
- Li J, Thompson B, Deng D, Chan LYL, Yu M, Hess RF (2013) Dichoptic training enables the adult amblyopic brain to learn. *Curr Biol* 23:R308–R309.
- Li RW, Levi DM (2004) Characterizing the mechanisms of improvement for position discrimination in adult amblyopia. *Journal of Vision* 4:7–7.
- Li RW, Provost A, Levi DM (2007) Extended perceptual learning results in substantial recovery of positional acuity and visual acuity in juvenile amblyopia. *Invest Ophthalmol Vis Sci* 48:5046–5051.
- Li RW, Young KG, Hoenig P, Levi DM (2005) Perceptual learning improves visual performance in juvenile amblyopia. *Invest Ophthalmol Vis Sci* 46:3161–3168.
- Lind GE, Mou T-C, Tamborini L, Pomper MG, De Micheli C, Conti P, Pinto A, Hansen KB (2017) Structural basis of subunit selectivity for competitive NMDA receptor antagonists with preference for GluN2A over GluN2B subunits. *Proc Natl Acad Sci USA* 114:E6942–E6951.
- Lund JS, Lund RD, Hendrickson AE, Bunt AH, Fuchs AF (1975) The origin of efferent pathways from the primary visual cortex, area 17, of the macaque monkey as shown by retrograde transport of horseradish peroxidase. *J Comp Neurol* 164:287–303.
- Lund RD (1972a) Synaptic patterns in the superficial layers of the superior colliculus of the monkey, *Macaca mulatta*. *Exp Brain Res* 15:194–211.
- Lund RD (1972b) Anatomic studies on the superior colliculus. *Invest Ophthalmol* 11:434–441.
- Luo, C., Keown, C. L., Kurihara, L., Zhou, J., He, Y., Li, J., ... & Bui, B. (2017). Single-cell methylomes identify neuronal subtypes and regulatory elements in mammalian cortex. *Science*, 357(6351), 600-604.
- Martin PR, White AJ, Goodchild AK, Wilder HD, Sefton AE (1997) Evidence that blue-on cells are part of the third geniculocortical pathway in primates. *Eur J Neurosci* 9:1536–1541.
- Masland RH (2012) The Neuronal Organization of the Retina. *Neuron* 76:266–280.
- Mataga N, Mizuguchi Y, Hensch TK (2004) Experience-dependent pruning of dendritic spines in visual cortex by tissue plasminogen activator. *Neuron* 44:1031–1041.
- Maurer D (1999) Rapid Improvement in the Acuity of Infants After Visual Input. *Science* 286:108–110.

- Maurer D, Lewis TL (2001) Visual acuity: the role of visual input in inducing postnatal change. *Clinical Neuroscience Research* 1:1–9.
- Maurer D, McKee SP (2018) Classification and diversity of amblyopia. *Vis Neurosci* 35:E012.
- Maya-Vetencourt JF, Sale A, Viegi A, Baroncelli L, de Pasquale R, O'Leary OF, Castrén E, Maffei L (2008) The antidepressant fluoxetine restores plasticity in the adult visual cortex. *Science* 320:385–388.
- McBain HB, Au CK, Hancox J, MacKenzie KA, Ezra DG, Adams GGW, Newman SP (2014) The impact of strabismus on quality of life in adults with and without diplopia: a systematic review. *Survey of Ophthalmology* 59:185–191.
- McGee AW, Yang Y, Fischer QS, Daw NW, Strittmatter SM (2005) Experience-driven plasticity of visual cortex limited by myelin and Nogo receptor. *Science* 309:2222–2226.
- Michael CR (1988) Retinal afferent arborization patterns, dendritic field orientations, and the segregation of function in the lateral geniculate nucleus of the monkey. *Proc Natl Acad Sci USA* 85:4914–4918.
- Mitchell D, Gingras G (1998) Visual recovery after monocular deprivation is driven by absolute, rather than relative, visually evoked activity levels. *Curr Biol* 8:R897.
- Mitchell DE (1988) The extent of visual recovery from early monocular or binocular visual deprivation in kittens. *The Journal of Physiology* 395:639–660.
- Mitchell DE (1991) The long-term effectiveness of different regimens of occlusion on recovery from early monocular deprivation in kittens. *Philosophical Transactions of the Royal Society B: Biological Sciences* 333:51–79.
- Mitchell DE, Cynader M, Movshon JA (1977) Recovery from the effects of monocular deprivation in kittens. *J Comp Neurol* 176:53–63.
- Mitchell DE, MacKinnon S (2002) The present and potential impact of research on animal models for clinical treatment of stimulus deprivation amblyopia. *Clin Exp Optom* 85:5–18.
- Mitchell DE, MacNeill K, Crowder NA, Holman K, Duffy KR (2016) Recovery of visual functions in amblyopic animals following brief exposure to total darkness. *The Journal of Physiology* 594:149–167.
- Mitchell DE, Murphy KM, Kaye MG (1984) Labile nature of the visual recovery promoted by reverse occlusion in monocularly deprived kittens. *Proc Natl Acad Sci USA* 81:286–288.
- Montey, K. L., & Quinlan, E. M. (2011). Recovery from chronic monocular deprivation following reactivation of thalamocortical plasticity by dark exposure. *Nature Communications*, 2, 317.
- Montey, K. L., Eaton, N. C., & Quinlan, E. M. (2013). Repetitive visual stimulation enhances recovery from severe amblyopia. *Learning & Memory*, 20(6), 311-317.
- Monyer H, Burnashev N, Laurie DJ, Neuron BS (1994) Developmental and regional expression in the rat brain and functional properties of four NMDA receptors. *Advances in carbohydrate chemistry*.

- Monyer, H., Sprengel, R., Schoepfer, R., Herb, A., Higuchi, M., Lomeli, H., ... & Seeburg, P. H. (1992). Heteromeric NMDA receptors: molecular and functional distinction of subtypes. *Science*, 256(5060), 1217-1221.
- Movshon JA (1976a) Reversal of the behavioural effects of monocular deprivation in the kitten. *The Journal of Physiology* 261:175–187.
- Movshon JA (1976b) Reversal of the physiological effects of monocular deprivation in the kitten's visual cortex. *The Journal of Physiology* 261:125–174.
- Movshon JA, Dürsteler MR (1977) Effects of brief periods of unilateral eye closure on the kitten's visual system. *J Neurophysiol* 40:1255–1265.
- Murphy KM, Duffy KR, Jones DG (2004) Experience-dependent changes in NMDAR1 expression in the visual cortex of an animal model for amblyopia. *Vis Neurosci* 21:653–670.
- Murphy, K. M., Jones, D. G., & Van Sluyters, R. C. (1995). Cytochrome-oxidase blobs in cat primary visual cortex. *Journal of Neuroscience*, 15(6), 4196-4208.
- Murphy KM, Mitchell DE (1986) Bilateral amblyopia after a short period of reverse occlusion in kittens. *Nature* 323:536–538.
- Murphy KM, Mitchell DE (1987) Reduced visual acuity in both eyes of monocularly deprived kittens following a short or long period of reverse occlusion. *Journal of Neuroscience* 7:1526–1536.
- Murphy, K. M., Roumeliotis, G., Williams, K., Beston, B. R., & Jones, D. G. (2015). Binocular visual training to promote recovery from monocular deprivation. *Journal of vision*, 15(1), 2-2.
- Nelson BA, Gunton KB, Lasker JN, Nelson LB, Drohan LA (2008) The psychosocial aspects of strabismus in teenagers and adults and the impact of surgical correction. *J AAPOS* 12:72–76.e1.
- O'Connor AR, Birch EE, Anderson S, Draper H, FSOS Research Group (2010) The functional significance of stereopsis. *Invest Ophthalmol Vis Sci* 51:2019–2023.
- Olson CR, Freeman RD (1980) Profile of the sensitive period for monocular deprivation in kittens. *Exp Brain Res* 39.
- Oray S, Majewska A, Sur M (2004) Dendritic spine dynamics are regulated by monocular deprivation and extracellular matrix degradation. *Neuron* 44:1021–1030.
- Owsley C (2011) Aging and vision. *Vision Research* 51:1610–1622.
- Packwood EA, Cruz OA, Rychwalski PJ, Keech RV (1999) The psychosocial effects of amblyopia study. *Journal of AAPOS* 3:15–17.
- Philpot BD, Espinosa JS, Bear MF (2003) Evidence for Altered NMDA Receptor Function as a Basis for Metaplasticity in Visual Cortex. *Journal of Neuroscience* 23:5583–5588.

- Philpot BD, Sekhar AK, Shouval HZ, Bear MF (2001) Visual Experience and Deprivation Bidirectionally Modify the Composition and Function of NMDA Receptors in Visual Cortex. *Neuron* 29:157–169.
- Piaget, J., & Cook, M. (1952). *The origins of intelligence in children* (Vol. 8, No. 5, p. 18). New York: International Universities Press.
- Pinto JGA, Hornby KR, Jones DG, Murphy KM (2010) Developmental changes in GABAergic mechanisms in human visual cortex across the lifespan. *Front Cell Neurosci* 4:16.
- Pinto, J. G., Jones, D. G., & Murphy, K. M. (2013). Comparing development of synaptic proteins in rat visual, somatosensory, and frontal cortex. *Frontiers in neural circuits*, 7, 97.
- Pinto JGA, Jones DG, Williams CK, Murphy KM (2015) Characterizing synaptic protein development in human visual cortex enables alignment of synaptic age with rat visual cortex. *Front Neural Circuits* 9:3.
- Pizzorusso T (2002) Reactivation of Ocular Dominance Plasticity in the Adult Visual Cortex. *Science* 298:1248–1251.
- Pizzorusso, T., Medini, P., Landi, S., Baldini, S., Berardi, N., & Maffei, L. (2006). Structural and functional recovery from early monocular deprivation in adult rats. *Proceedings of the National Academy of Sciences*, 103(22), 8517-8522.
- Polat U, Ma-Naim T, Belkin M, Sagi D (2004) Improving vision in adult amblyopia by perceptual learning. *Proc Natl Acad Sci USA* 101:6692–6697.
- Polyak S (1957) *The vertebrate visual system: its origin, structure, and function and its manifestations in disease with an analysis of its role in the life of animals and in the origin of man; preceded by a historical review of investigations of the eye, and of the visual pathways and centers of the brain.* University of Chicago Press.
- Polyak SL (1941) *The retina.*
- Pouille F, Scanziani M (2001) Enforcement of temporal fidelity in pyramidal cells by somatic feed-forward inhibition. *Science* 293:1159–1163.
- Quinlan EM, Olstein DH, Bear MF (1999a) Bidirectional, experience-dependent regulation of N-methyl-D-aspartate receptor subunit composition in the rat visual cortex during postnatal development. *Proc Natl Acad Sci USA* 96:12876–12880.
- Quinlan EM, Philpot BD, Hugarir RL, Bear MF (1999b) Rapid, experience-dependent expression of synaptic NMDA receptors in visual cortex in vivo. *Nat Neurosci* 2:352–357.
- Rahi JS, Cumberland PM, Peckham CS (2006) Does amblyopia affect educational, health, and social outcomes? Findings from 1958 British birth cohort. *BMJ* 332:820–825.
- Ramoas AS, Mower AF, Liao D, Jafri SI (2001) Suppression of cortical NMDA receptor function prevents development of orientation selectivity in the primary visual cortex. *J Neurosci* 21:4299–4309.

- Repka MX, Beck RW, Holmes JM, Birch EE, Chandler DL, Cotter SA, Hertle RW, Kraker RT, Moke PS, Quinn GE, Scheiman MM (2003) A randomized trial of patching regimens for treatment of moderate amblyopia in children. *Arch Ophthalmol* 121:603–611.
- Repka MX, Cotter SA, Beck RW, Kraker RT, Birch EE, Everett DF, Hertle RW, Holmes JM, Quinn GE, Sala NA, Scheiman MM, Stager DR, Wallace DK, Pediatric Eye Disease Investigator Group (2004) A randomized trial of atropine regimens for treatment of moderate amblyopia in children. *Ophthalmology* 111:2076–2085.
- Repka MX, Wallace DK, Beck RW, Kraker RT, Birch EE, Cotter SA, Donahue S, Everett DF, Hertle RW, Holmes JM, Quinn GE, Scheiman MM, Weakley DR (2005) Two-year follow-up of a 6-month randomized trial of atropine vs patching for treatment of moderate amblyopia in children. *Arch Ophthalmol* 123:149–157.
- Reynolds, J. H., & Chelazzi, L. (2004). Attentional modulation of visual processing. *Annu. Rev. Neurosci.*, 27, 611-647.
- Roorda A, Metha AB, Lennie P, Williams DR (2001) Packing arrangement of the three cone classes in primate retina. *Vision Research* 41:1291–1306.
- Richardson, D. S., & Lichtman, J. W. (2015). Clarifying tissue clearing. *Cell*, 162(2), 246-257.
- Roorda A, Williams DR (1999) The arrangement of the three cone classes in the living human eye. *Nature* 397:520–522.
- Rumpel S, Hatt H, Gottmann K (1998) Silent Synapses in the Developing Rat Visual Cortex: Evidence for Postsynaptic Expression of Synaptic Plasticity. *Journal of Neuroscience* 18:8863–8874.
- Sale, A., Berardi, N., & Maffei, L. (2009). Enrich the environment to empower the brain. *Trends in neurosciences*, 32(4), 233-239.
- Sawada M, Kondo N, Suzumura A, Marunouchi T (1989) Production of tumor necrosis factor- α by microglia and astrocytes in culture. *Brain Res* 491:394–397.
- Sawtell, N. B., Frenkel, M. Y., Philpot, B. D., Nakazawa, K., Tonegawa, S., & Bear, M. F. (2003). NMDA receptor-dependent ocular dominance plasticity in adult visual cortex. *Neuron*, 38(6), 977-985.
- Schwarzkopf DS, Vorobyov V, Mitchell DE, Sengpiel F (2007) Brief daily binocular vision prevents monocular deprivation effects in visual cortex. *Eur J Neurosci* 25:270–280.
- Self, M. W., Kooijmans, R. N., Supèr, H., Lamme, V. A., & Roelfsema, P. R. (2012). Different glutamate receptors convey feedforward and recurrent processing in macaque V1. *Proceedings of the National Academy of Sciences*, 109(27), 11031-11036.
- Sengpiel F (2014) Plasticity of the visual cortex and treatment of amblyopia. *Curr Biol* 24:R936–R940.
- Seung HS, Sümbül U (2014) Neuronal cell types and connectivity: lessons from the retina. *Neuron* 83:1262–1272.
- Schatz, C. J., & Stryker, M. P. (1978). Ocular dominance in layer IV of the cat's visual cortex and the effects of monocular deprivation. *The Journal of Physiology*, 281(1), 267-283.

- Shatz CJ (1983) The prenatal development of the cat's retinogeniculate pathway. *Journal of Neuroscience* 3:482–499.
- Shepherd JD, Bear MF (2011) New views of Arc, a master regulator of synaptic plasticity. *Nature Publishing Group* 14:279–284.
- Simons K (2005) Amblyopia characterization, treatment, and prophylaxis. *Survey of Ophthalmology* 50:123–166.
- Siu CR & Murphy KM (2018) The development of human visual cortex and clinical implications. *Eye Brain* 10:25–36.
- Siu CR, Balsor JL, Jones DG, Murphy KM (2015) Classic and Golgi Myelin Basic Protein have distinct developmental trajectories in human visual cortex. *Front Neurosci* 9:1–10.
- Siu CR, Beshara SP, Jones DG, Murphy KM (2017) Development of Glutamatergic Proteins in Human Visual Cortex across the Lifespan. *J Neurosci* 37:6031–6042.
- Sjöstrand J, Olsson V, Popovic Z, Conradi N (1999) Quantitative estimations of foveal and extra-foveal retinal circuitry in humans. *Vision Research* 39:2987–2998.
- Smith GB, Heynen AJ, Bear MF (2009) Bidirectional synaptic mechanisms of ocular dominance plasticity in visual cortex. *Philosophical Transactions of the Royal Society B: Biological Sciences* 364:357–367.
- Solomon SG, Lennie P (2007) The machinery of colour vision. *Nat Rev Neurosci* 8:276–286.
- Sommeijer, J. P., Ahmadlou, M., Saiepour, M. H., Seignette, K., Min, R., Heimel, J. A., & Levelt, C. N. (2017). Thalamic inhibition regulates critical-period plasticity in visual cortex and thalamus. *Nature neuroscience*, 20(12), 1715-1721.
- Spillmann L (2014) Receptive fields of visual neurons: the early years. *Perception* 43:1145–1176.
- Steinberg RH, Reid M, Lacy PL (1973) The distribution of rods and cones in the retina of the cat (*Felis domesticus*). *J Comp Neurol* 148:229–248.
- Stellwagen D, Malenka RC (2006) Synaptic scaling mediated by glial TNF- α . *Nature* 440:1054–1059.
- Stephany, C. É., Ma, X., Dorton, H. M., Wu, J., Solomon, A. M., Frantz, M. G., ... & McGee, A. W. (2018). Distinct circuits for recovery of eye dominance and acuity in murine amblyopia. *Current Biology*, 28(12), 1914-1923.
- Stewart CE, Moseley MJ, Stephens DA, Fielder AR (2004) Treatment dose-response in amblyopia therapy: the Monitored Occlusion Treatment of Amblyopia Study (MOTAS). *Invest Ophthalmol Vis Sci* 45:3048–3054.
- Stodieck SK, Greifzu F, Goetze B, Schmidt K-F, Löwel S (2014) Brief dark exposure restored ocular dominance plasticity in aging mice and after a cortical stroke. *Exp Gerontol* 60:1–11.
- Stone J (1978) The number and distribution of ganglion cells in the cat's retina. *J Comp Neurol* 180:753–771.

- Sun W, Hansen KB, Jahr CE (2017) Allosteric Interactions between NMDA Receptor Subunits Shape the Developmental Shift in Channel Properties. *Neuron* 94:58–64.e3.
- Swindale NV, Vital-Durand F, Blakemore C (1981) Recovery from monocular deprivation in the monkey. III. Reversal of anatomical effects in the visual cortex. *Proc R Soc Lond, B, Biol Sci* 213:435–450.
- Syken J, Grandpre T, Kanold PO, Shatz CJ (2006) PirB restricts ocular-dominance plasticity in visual cortex. *Science* 313:1795–1800.
- Tailby C, Solomon SG, Lennie P (2008a) Functional asymmetries in visual pathways carrying S-cone signals in macaque. *J Neurosci* 28:4078–4087.
- Tailby C, Szmajda BA, Buzás P, Lee BB, Martin PR (2008b) Transmission of blue (S) cone signals through the primate lateral geniculate nucleus. *The Journal of Physiology* 586:5947–5967.
- Tigges J, O'Steen WK (1974) Termination of retinofugal fibers in squirrel monkey: a re-investigation using autoradiographic methods. *Brain Res* 79:489–495.
- Tigges M, Tigges J (1970) The retinofugal fibers and their terminal nuclei in *Galago crassicaudatus* (primates). *J Comp Neurol* 138:87–101.
- Tovar KR, McGinley MJ, Westbrook GL (2013) Triheteromeric NMDA receptors at hippocampal synapses. *J Neurosci* 33:9150–9160.
- Trachtenberg, J. T., Trepel, C., & Stryker, M. P. (2000). Rapid extragranular plasticity in the absence of thalamocortical plasticity in the developing primary visual cortex. *Science*, 287(5460), 2029-2032.
- Tropea D, Majewska AK, Garcia R, Sur M (2010) Structural dynamics of synapses in vivo correlate with functional changes during experience-dependent plasticity in visual cortex. *J Neurosci* 30:11086–11095.
- Tsirlin I, Colpa L, Goltz HC, Wong AM (2015) Behavioral training as new treatment for adult amblyopia: a meta-analysis and systematic review. *Invest Ophthalmol Vis Sci* 56:4061–4075.
- Turrigiano GG, Nelson SB (2004) Homeostatic plasticity in the developing nervous system. *Nat Rev Neurosci* 5:97–107.
- Tusa RJ, Palmer LA, Rosenquist AC (1978) The retinotopic organization of area 17 (striate cortex) in the cat. *J Comp Neurol* 177:213–235.
- van de Graaf ES, van der Sterre GW, van Kempen-du Saar H, Simonsz B, Looman CWN, Simonsz HJ (2007) Amblyopia and Strabismus Questionnaire (A&SQ): clinical validation in a historic cohort. *Graefes Arch Clin Exp Ophthalmol* 245:1589–1595.
- Vedamurthy I, Nahum M, Huang SJ, Zheng F, Bayliss J, Bavelier D, Levi DM (2015) A dichoptic custom-made action video game as a treatment for adult amblyopia. *Vision Research* 114:173–187.

- Wake H, Lee PR, Fields RD (2011) Control of Local Protein Synthesis and Initial Events in Myelination by Action Potentials. *Science* 333:1647–1651.
- Wallace DK, Pediatric Eye Disease Investigator Group, Edwards AR, Cotter SA, Beck RW, Arnold RW, Astle WF, Barnhardt CN, Birch EE, Donahue SP, Everett DF, Felius J, Holmes JM, Kraker RT, Melia M, Repka MX, Sala NA, Silbert DI, Weise KK (2006) A randomized trial to evaluate 2 hours of daily patching for strabismic and anisometropic amblyopia in children. *Ophthalmology* 113:904–912.
- Wässle H, Grünert U, Röhrenbeck J, Boycott BB (1990) Retinal ganglion cell density and cortical magnification factor in the primate. *Vision Research* 30:1897–1911.
- Wässle H, Illing RB (1980) The retinal projection to the superior colliculus in the cat: A quantitative study with HRP. *J Comp Neurol* 190:333–356.
- Webber AL, Wood J (2005) Amblyopia: prevalence, natural history, functional effects and treatment. *Clin Exp Optom* 88:365–375.
- Webber AL, Wood JM, Gole GA, Brown B (2008) The effect of amblyopia on fine motor skills in children. *Invest Ophthalmol Vis Sci* 49:594–603.
- Webber AL, Wood JM, Thompson B (2016) Fine Motor Skills of Children With Amblyopia Improve Following Binocular Treatment. *Invest Ophthalmol Vis Sci* 57:4713–4720.
- Whiting PJ, Bonnert TP, McKernan RM, Farrar S, le Bourdellès B, Heavens RP, Smith DW, Hewson L, Rigby MR, Sirinathsinghji DJ, Thompson SA, Wafford KA (1999) Molecular and functional diversity of the expanding GABA-A receptor gene family. *Annals of the New York Academy of Sciences* 868:645–653.
- Wiesel TN, Hubel DH (1963) Single-Cell Responses in Striate Cortex of Kittens Deprived of Vision in One Eye. *J Neurophysiol* 26:1003–1017.
- Wiesel TN, Hubel DH (1965) Comparison of the effects of unilateral and bilateral eye closure on cortical unit responses in kittens. *J Neurophysiol* 28:1029–1040.
- Wiesel TN, Hubel DH (1966) Spatial and chromatic interactions in the lateral geniculate body of the rhesus monkey. *J Neurophysiol* 29:1115–1156.
- Wiesel TN, Hubel DH, Lam DM (1974) Autoradiographic demonstration of ocular-dominance columns in the monkey striate cortex by means of transneuronal transport. *Brain Res* 79:273–279.
- Williams K, Balsor JL, Beshara S, Beston BR, Jones DG, Murphy KM (2015) Experience-dependent central vision deficits: Neurobiology and visual acuity. *Vision Research* 114:68–78.
- Williams K, Irwin DA, Jones DG, Murphy KM (2010) Dramatic Loss of Ube3A Expression during Aging of the Mammalian Cortex. *Front Aging Neurosci* 2:18.
- Woodruff G, Hiscox F, Thompson JR, Smith LK (1994) Factors affecting the outcome of children treated for amblyopia. *Eye (Lond)* 8 (Pt 6):627–631.

- Workman AD, Charvet CJ, Clancy B, Darlington RB, Finlay BL (2013) Modeling transformations of neurodevelopmental sequences across mammalian species. *J Neurosci* 33:7368–7383.
- Wu C, Hunter DG (2006) Amblyopia: diagnostic and therapeutic options. *American Journal of Ophthalmology* 141:175–184.
- Yoon B-J, Smith GB, Heynen AJ, Neve RL, Bear MF (2009) Essential role for a long-term depression mechanism in ocular dominance plasticity. *Proc Natl Acad Sci USA* 106:9860–9865.
- Yashiro, K., Corlew, R., & Philpot, B. D. (2005). Visual deprivation modifies both presynaptic glutamate release and the composition of perisynaptic/extrasynaptic NMDA receptors in adult visual cortex. *Journal of Neuroscience*, 25(50), 11684-11692.
- Yu H, Majewska AK, Sur M (2011) Rapid experience-dependent plasticity of synapse function and structure in ferret visual cortex in vivo. *Proc Natl Acad Sci USA* 108:21235–21240.
- Zhou M, Liang F, Xiong XR, Li L, Li H, Xiao Z, Tao HW, Zhang LI (2014) Scaling down of balanced excitation and inhibition by active behavioral states in auditory cortex. *Nature Publishing Group* 17:841–850.
- Zhou, Y., Huang, C., Xu, P., Tao, L., Qiu, Z., Li, X., & Lu, Z. L. (2006). Perceptual learning improves contrast sensitivity and visual acuity in adults with anisometric amblyopia. *Vision research*, 46(5), 739-750.